Diss. ETH No. 14424

Cold Firn and Ice in the Monte Rosa and Mont Blanc Areas: Spatial Occurrence, Surface Energy Balance and Climatic Evidence

A dissertation submitted to the
SWISS FEDERAL INSTITUTE OF TECHNOLOGY ZURICH
for the degree of
Doctor of Natural Science

presented by
Stephan Suter
Dipl. Natw. ETH
born 25 April 1969
citizen of Kölliken (AG)

accepted on the recommendation of
Prof. Dr. H.-E. Minor, examiner
Prof. Dr. A. Ohmura, co-examiner
Dr. M. Hoelzle, co-examiner
Prof. Dr. M. Kuhn, co-examiner

2001

Contents

Contents 1

List of Figures 5

List of Tables 9

List of Symbols 11
Latin Letters 11
Greek Letters 14

Abstract 15

Zusammenfassung 17

Résumé 19

1 Introduction 21
1.1 The EU-Project ALPCLIM 21
1.2 Cold Firn and Ice in the Alps 22
1.3 Energy-Balance Studies on Mountain Glaciers 24

2 Objectives 25

3 Site Description and Field Observations 27
3.1 General Overview 27
3.2 Mont Blanc Area 27
3.2.1 Site Description 27
3.2.2 Previous Studies 29
3.2.3 Field Observations 29
3.3 Monte Rosa Area 30
3.3.1 Site Description 30
3.3.2 Previous Studies 31
3.3.3 Field Observations 33

4 Energy Balance at Seserjoch, Monte Rosa 35
4.1 Theoretical Background 35
4.1.1 Radiative Fluxes 35
4.1.2 Turbulent Fluxes 37
4.1.3 Subsurface- or Ground Heat Flux 43
4.1.4 Melt and Re-freezing 43
4.2 Energy-Balance Station 44
4.2.1 General Setting 44
4.2.2 Instruments and Calibration 46
4.3 Data Analysis and Results 49
4.3.1 Wind Direction 50
4.3.2 Wind Velocity 50
4.3.3 Air Temperature 51

4.3.4 Relative Humidity . . . 52
4.3.5 Shortwave Radiation . . . 52
4.3.6 Albedo . . . 53
4.3.7 Longwave Radiation . . . 54
4.3.8 Surface Temperature . . . 56
4.3.9 Snow Accumulation and Ablation . . . 56
4.4 Energy Balance . . . 57
4.4.1 Net Radiation . . . 57
4.4.2 Turbulent Fluxes . . . 58
4.4.3 Subsurface- or Ground Heat Flux . . . 65
4.4.4 Melt and Re-freezing . . . 68
4.4.5 Energy Balance and Residual Heat Flux . . . 70
4.5 Conclusions . . . 75

5 Spatial Occurrence of Cold Firn **77**
5.1 Objectives and General Proceeding . . . 77
5.2 Data Acquisition and Analysis . . . 77
5.2.1 Steam Drilling . . . 77
5.2.2 Methodology . . . 78
5.2.3 Data Analysis . . . 83
5.3 Results . . . 86
5.3.1 Mont Blanc Area . . . 86
5.3.2 Monte Rosa Area . . . 89
5.4 Statistical Analysis and Models . . . 92
5.4.1 Theoretical Background . . . 92
5.4.2 Further Input Data . . . 93
5.4.3 Simple Linear Regression . . . 94
5.4.4 Multiple Linear Regression . . . 95
5.4.5 Distribution Models . . . 97
5.5 Conclusions . . . 103

6 Borehole Thermometry **107**
6.1 Theoretical Background . . . 107
6.1.1 Thermal Processes in a Cold Glacier . . . 107
6.1.2 Analytical Solutions . . . 113
6.1.3 Numerical Solutions . . . 115
6.2 Site Selection . . . 124
6.3 Data Acquisition and Analysis . . . 125
6.3.1 Boreholes . . . 125
6.3.2 Methodology of the Temperature Measurements . . . 125
6.3.3 Data Analysis . . . 127
6.4 Results and Comparison with other Climate Records . . . 128
6.4.1 Mont Blanc Area . . . 128
6.4.2 Monte Rosa Area . . . 133
6.5 Conclusions . . . 148

7 A Coupled Energy-Balance/Firn-Temperature Model **151**
7.1 Introduction . . . 151
7.2 Spatial Energy-Balance Model . . . 151
7.2.1 Model Description . . . 151
7.2.2 Resulting Energy Balance . . . 157
7.2.3 Discussion . . . 158
7.2.4 Simplification . . . 160
7.3 Firn-Temperature Model . . . 160
7.3.1 Seserjoch . . . 160
7.3.2 Colle Gnifetti . . . 161
7.3.3 Monte Rosa Study Area . . . 161
7.4 Scenarios . . . 161
7.4.1 Seserjoch . . . 162
7.4.2 Colle Gnifetti . . . 163
7.4.3 Monte Rosa Study Area . . . 163
7.5 Conclusions . . . 165

8 Conclusions and Perspectives **169**

A Field Data **173**
A.1 Mont Blanc Area . . . 173
A.2 Monte Rosa Area . . . 174

References **175**

Curriculum Vitae **185**

Acknowledgements **187**

Seite Leer /
Blank leaf

List of Figures

3.1 General overview of the location of the Mont Blanc and Monte Rosa study areas in the Alps . . . 27
3.2 Overview of the Mont Blanc Massif . . . 28
3.3 Overview of the Mont Blanc study area . . . 29
3.4 Overview of the Monte Rosa region . . . 31
3.5 Overview of the Monte Rosa study area . . . 32
4.1 Data-communication system of the energy-balance station . . . 45
4.2 Instrumentation of the energy-balance station . . . 46
4.3 Wind direction at Seserjoch . . . 50
4.4 Wind speed at Seserjoch . . . 50
4.5 Air temperature at Seserjoch and comparison with surrounding stations 51
4.6 Relative humidity at Seserjoch . . . 52
4.7 Shortwave radiation and albedo at Seserjoch . . . 53
4.8 Shortwave radiation and diurnal albedo at Seserjoch . . . 54
4.9 Longwave radiation at Seserjoch . . . 55
4.10 Surface Temperatures at Seserjoch . . . 56
4.11 Accumulation and ablation at Seserjoch . . . 57
4.12 Net radiation at Seserjoch . . . 58
4.13 Sensible heat flux measured with the sonic anemometer at Seserjoch . 59
4.14 Mean wind-speed, temperature- and humidity profiles at Seserjoch . . 61
4.15 Sensible and latent heat flux derived from the profile method . . . 62
4.16 Sensible and latent heat flux derived from the bulk method . . . 63
4.17 Sensible and latent heat flux derived from the Bowen-ratio method . 64
4.18 Comparison between sonic-derived sensible heat flux and other methods 65
4.19 Comparison of daily mean values of sensible and latent heat flux . . . 66
4.20 Accumulation, change of temperature gradient and ground heat flux at Seserjoch . . . 67
4.21 Surface temperatures and daily residual heat flux from August, 1999 showing melt events . . . 68
4.22 Surface and air temperatures, net radiation and residual heat flux from two days in August . . . 70
4.23 Energy balance at Seserjoch on June 26, 1999 . . . 72
4.24 Energy balance at Seserjoch from November 1 to November 2, 1999 . 73
4.25 Energy balance at Seserjoch from May, 1999 to April, 2000 . . . 74
5.1 Steam drilling at the 4807 m high Mont Blanc summit . . . 78
5.2 Linear extrapolation of borehole temperatures . . . 85
5.3 Measured 18-m temperatures in the Mont Blanc area from 1998 (single values) . . . 87
5.4 Measured 18-m temperatures in the Mont Blanc area from 1998 (grid values) . . . 88
5.5 Measured 18-m temperatures in the Monte Rosa area from 1999 (single values) . . . 89
5.6 Measured 18-m temperatures in the Monte Rosa area from 1999 (grid values) . . . 90

5.7 Extrapolated accumulation in the Monte Rosa area from June, 1999 to May, 2000 91
5.8 Observed MAFTs as a function of elevation 94
5.9 Observed MAFTs as a function of elevation and aspect 95
5.10 Observed MAFTs as a function of elevation and potential direct solar radiation 97
5.11 Statistically simulated MAFTs for the Mont Blanc and Monte Rosa study areas 102
5.12 Statistically simulated cold-firn distribution in the Zermatt region . . 103
6.1 Thermal processes at the boundaries of and within a cold glacier . . . 107
6.2 Measured air- and surface temperatures at Seserjoch 108
6.3 Wind-pumping event at Dôme du Goûter, Mont Blanc area 112
6.4 Penetration depth of seasonal temperature variations in cold firn for pure heat conduction 114
6.5 Calculated englacial steady-state profiles with different values for net mass balance and ground heat flux 115
6.6 Numerically calculated penetration depth of seasonal temperature-variations in cold firn 117
6.7 Velocity-depth and age-depth distribution in a 100 m deep glacier . . 118
6.8 Deviations from steady-state temperatures for three vertical velocity models and arrival time at depth of 1 % of the surface perturbation . 118
6.9 Arrival time at depth of 1 % of a surface perturbation exerted during 30 years or 1 year 119
6.10 Thermal evolution of a glacier to a linear surface-temperature increase within 20 years until steady state is reached again 120
6.11 Effect of simulated latent heat on a steady-state temperature profile for different durations of surface melt and penetration depths of the 0 °C front 121
6.12 Effect of latent heat release on a steady-state temperature profile for different durations of surface melt and melt-energy inputs 123
6.13 Effect of the melt-signal distribution over the melting period on englacial temperature profiles for different melt-energy inputs 124
6.14 Age-depth distribution for two sites in the Mont Blanc area 128
6.15 Measured and calculated firn temperatures and temperature gradients at Col du Dôme, Mont Blanc area 129
6.16 Measured englacial temperatures and temperature gradients at Dôme du Goûter, Mont Blanc area 130
6.17 Measured and extrapolated temperature profile, calculated steady-state situation and transient temperature profiles at Dôme du Goûter, Mont Blanc area 131
6.18 MAAT-series from Jungfraujoch and from 16 high-level stations of the Alps 133
6.19 Age-depth distribution for various sites in the Monte Rosa area . . . 134
6.20 Measured englacial temperatures and temperature gradients at Colle Gnifetti, Monte Rosa area 134
6.21 Measured and calculated (steady-state) temperature profiles at Colle Gnifetti, Monte Rosa area 135

6.22 Measured englacial temperatures and temperature gradients at Seserjoch, Monte Rosa area . . . 137
6.23 Observed and parameterized thermal diffusivities κ and thermal conductivities K at Seserjoch . . . 138
6.24 Controlled simulation of the englacial firn temperatures at Seserjoch, Monte Rosa . . . 139
6.25 Measured and extrapolated temperature profile, calculated steady-state situation and transient temperature profiles at Seserjoch, Monte Rosa area . . . 141
6.26 Measured firn temperatures and temperature gradients in a firn basin on Grenzgletscher, Monte Rosa area . . . 143
6.27 Measured firn temperatures, temperature gradients and calculated steady-state situations at four saddle- or dome sites in the Monte Rosa area . . . 144
6.28 MAAT-series from Jungfraujoch and from 16 high-level stations of the Alps . . . 146
6.29 Melt-layer frequency at Colle Gnifetti, Monte Rosa . . . 147
6.30 $\delta^{18}O$ record at Colle Gnifetti, Monte Rosa . . . 147
7.1 Comparison between observed and modeled global radiation at Seserjoch . . . 153
7.2 Comparison between observed and parameterized surface temperature and longwave incoming radiation at Seserjoch . . . 154
7.3 Comparison between observed and parameterized sensible and latent heat flux at Seserjoch . . . 155
7.4 Relation between daily mean surface temperature and melt-energy flux at Seserjoch . . . 156
7.5 Difference between model-derived and observed surface temperatures at Seserjoch . . . 157
7.6 Modeled daily mean surface temperatures and melt input for the Monte Rosa study area on August 1, 1999 . . . 158
7.7 Modeled daily mean surface temperatures for the Monte Rosa study area on December 6, 1999 . . . 159
7.8 Daily mean air temperatures from the Colle del Lys station from 1997 to 2000 . . . 162
7.9 Observed and modeled future firn- and ice temperatures at Seserjoch 163
7.10 Observed and modeled future firn- and ice temperatures at Colle Gnifetti . . . 164
7.11 Evolution of the cold-firn occurrence in the Monte Rosa study area under conditions of global warming . . . 165

Seite Leer /
Blank leaf

List of Tables

4.1 Characteristics of the radiation instruments 47
4.2 Characteristics of the instruments for turbulent fluxes 48
4.3 Characteristics of the snow-height and the snow-temperature instruments 49
4.4 Summary of the monthly and yearly sum of melt days, melt duration and melt-energy input at Seserjoch 69
4.5 Summary of the monthly and yearly mean energy-balance fluxes at Seserjoch 75
5.1 Statistical results of the simple linear regression 94
5.2 Statistical results of the multiple linear regression 96
5.3 Lower boundaries of cold firn occurrence as a function of aspect . . . 97
5.4 Lower boundaries of cold firn occurrence as a function of potential direct solar radiation 98
5.5 Lower boundaries of cold firn occurrence as a function of aspect and slope 98
5.6 Lower boundaries of cold firn occurrence as a function of aspect and accumulation index 99
5.7 Lower boundaries of cold firn occurrence as a function of potential direct solar radiation and accumulation index 99
5.8 Lower boundaries of cold firn occurrence as a function of aspect, slope and accumulation index 100
5.9 Lower boundaries of cold firn occurrence as a function of potential direct solar radiation, slope and accumulation index 101

Seite Leer /
Blank leaf

List of Symbols

Latin Letters

Symbol	Description	Units
a_λ	Extinction Coefficient	1/m
A_0	Parameter of the Ice Flow Law	$4.9{\cdot}10^{-25}$ 1/(Pa$^3\cdot$ s) for -10 °C
b	Surface Accumulation of the Glacier	m/s
c_a	Specific Heat Capacity of Air at Constant Pressure	J/(kg·K)
c_i	Specific Heat Capacity of Ice	J/(kg·K)
cl	Cloud-Cover Fraction	
C_{PIR}	Sensitivity Factor of a Pyrgeometer	V/W·m^{-2}
e	Water-Vapour Pressure	Pa
e_s	Saturation Water-Vapour Pressure	Pa
f_C	Heat Production due to Firn Compaction	W/m^3
f_D	Heat Production due to Ice Deformation	W/m^3
F_s	Hemispherical Fraction of the Sky	Fraction of π
F_t	Hemispherical Fraction of the Terrain	Fraction of π
g	Acceleration due to Gravity	9.81 m/s^2
G	Global or Total Shortwave Incoming Radiation	W/m^2
G_b	Basal Heat Flux	W/m^2
G_i	Englacial Heat Flux	W/m^2
h	Altitude above Sea Level or Glacier Thickness	m
H	Sensible Heat Flux	W/m^2
$I(\lambda)$	Monochromatic Irradiance at Wavelength λ	W/(m^{2}sr)
k	von Kármán Constant	0.41
K	Thermal Conductivity	W/(m·K)
K_i	Thermal Conductivity of Snow, Firn or Ice	W/(m·K)
K_r	Thermal Conductivity of Rock	2.5 - 3.3 W/(m·K)
$K\uparrow$	Shortwave Outgoing Radiation	W/m^2
$K\downarrow$	Shortwave Incoming Radiation	W/m^2
K_H	Eddy Diffusivity for Heat Exchange	m^2/s
K_{LE}	Eddy Diffusivity for Water-Vapour Exchange	m^2/s
l	Coefficient of Thermal Expansion	1/°C
L	Obukhov Length	m
$L\uparrow$	Longwave Outgoing Radiation	W/m^2
$L\downarrow$	Longwave Incoming Radiation	W/m^2
LE	Latent Heat Flux (Evaporation, Condensation and Sublimation)	W/m^2
LM	Latent Heat Flux due to Re-freezing Meltwater in the Snow Cover	W/m^2 or W/m^3
L_f	Latent Heat of Fusion for Water	334'000 J/kg at 0 °C
L_s	Latent Heat of Sublimation for Water	2'835'000 J/kg at 0 °C
L_v	Latent Heat of Vaporization for Water	2'501'000 J/kg at 0 °C

Symbol	Description	Units
$\vec{m}_w$	Mass Flux of Water	kg/(s·m^2) or kg/(s·m^3)
mol_a	Molar Mass of (Dry) Air	0.028966 kg/mol
mol_w	Molar Mass of Water	0.018015 kg/mol
M	Heat Flux due to Surface Melt or Re-freezing of Water	W/m^2
n	Dimensionless Exponent of the Ice Flow Law	1-3
p	Air Pressure	Pa
p_0	Standard Air Pressure at Sea Level	101'325 Pa
P	Period	s
q	Specific Humidity	kg water/kg air
$\overline{q}$	Time-Averaged Specific Humidity	kg water/kg air
q'	Fluctuating Specific Humidity	kg water/kg air
q_*	Scaling Parameter for Humidity	kg water/kg air
Q	Energy Input per Unit Length	J/m
r	Distance or Radius	m
R	Net Radiation	W/m^2
R_g	Universal Gas Constant	8.31441 J/(mol·K)
Ri	Gradient Richardson Number	
Ri_b	Bulk Richardson Number	
R_T	Resistance	Ω
RH	Relative Humidity	%
$\Re_\lambda$	Reflectance of Snow	
S	Subsurface Heat Flux	W/m^2
t	Time	s
T	Temperature	°C or K
T_0	Mean or Reference Air Temperature at Sea Level	288.15 K
$\overline{T}$	Time-Averaged Temperature	°C or K
T'	Fluctuating Temperature	°C or K
T_a	Air Temperature	°C or K
T_b	Starting Temperature	°C or K
T_f	Final Temperature	°C or K
T_s	Surface Temperature	°C or K
u	Horizontal Wind Velocity	m/s
$\overline{u}$	Time-Averaged Horizontal Wind Velocity	m/s
u'	Fluctuating Horizontal Wind Velocity	m/s
u_*	Scaling Parameter for Wind Velocity (Friction Velocity)	m/s
U	Voltage	V
$\vec{v}$	Vector of Wind or Glacier Flow Velocity	m/s
w	Vertical Wind-Velocity Component	m/s
$\overline{w}$	Time-Averaged Vertical Wind-Velocity Component	m/s
w'	Fluctuating Vertical Wind-Velocity Component	m/s

Symbol	Description	Units
z	Height above the Surface or Depth below the Surface	m
z_q	Log-Mean Height for Humidity	m
z_t	Log-Mean Height for Temperature	m
z_u	Log-Mean Height for Wind Velocity	m
z_{0q}	Surface Roughness Length for Humidity	m
z_{0t}	Surface Roughness Length for Temperature	m
z_{0u}	Surface Roughness Length for Wind	m

Greek Letters

Symbol	Description	Units
α	Surface Albedo or Slope	% or °
β	Bowen Ratio	
γ	Mean Air-Temperature Lapse Rate	K/m
Γ	Dry-Adiabatic Lapse Rate	K/m
ϵ_a	Longwave Atmospheric Emissivity	
ϵ_{body}	Body Emissivity of a Pyrgeometer	
ϵ_{dome}	Dome Emissivity of a Pyrgeometer	
ϵ_s	Longwave Emissivity of Snow or Firn	
$\dot{\epsilon}_{xz}$	Strain Rate in the xz-plane	1/s
θ	Potential Temperature	°C or K
$\overline{\theta}$	Time-Averaged Potential Temperature	°C or K
θ'	Fluctuating Potential Temperature	°C or K
θ_*	Scaling Parameter for (Potential) Temperature	°C or K
κ	Thermal Diffusivity	m^2/s
λ	Wavelength	μm
Λ	Scale-depth Parameter of Density Increase	1/m
μ	Density Ratio	
ν	Kinematic Viscosity	m^2/s
ρ	Density	kg/m^3
ρ_a	Air Density	kg/m^3
ρ_0	Air Density at 288.15 K and at 1 atm	$1.225\,kg/m^3$
ρ_f	Firn Density	kg/m^3
ρ_s	Snow Density	kg/m^3
σ	Stefan-Boltzmann Constant	$5.67032{\cdot}10^{-8}\,W/(m^2{\cdot}K^4)$
τ	Time Constant or Shear Stress	s or Pa
τ_{dome}	Dome Transmissivity of a Pyrgeometer	
τ_{xz}	Shear Stress in the xz-plane	Pa
ϕ	Phase Shift	
ϕ_m	Stability Function for Momentum	
ϕ_h	Stability Function for Heat	
ϕ_q	Stability Function for Water Vapour	
ω	Angular Frequency	1/s

Abstract

Little knowledge exists to date on the complex glacier-atmosphere interactions leading to the formation of cold firn on high-elevation Alpine glaciers. Although cold firn and ice is not a wide-spread phenomenon on Alpine glaciers, it is of importance for many glaciological problems and has a major impact on glaciers as an environmental and climatic archive.

The present study is a contribution to a better and more quantitative understanding of the atmospheric and glaciological processes in cold firn areas. The study is divided into four main parts dealing with the atmosphere-ground interactions (surface energy-balance), the distribution of cold firn in space (spatial occurrence of cold firn), the thermometric evidence of observed firn- and ice-temperature profiles in terms of a climate signal (borehole thermometry) and the energy balance and the (future) englacial thermal conditions in space (coupled spatial energy-balance/firn-temperature model).

The atmospheric impact was investigated with the help of an energy-balance study at the cold 4300 m high Seserjoch firn saddle, Monte Rosa area (Italy and Switzerland). Measurements of short- and longwave radiation, wind speed and wind direction, air temperature, air humidity, snow height and snow- and firn temperatures were carried out between September, 1998 and August, 2000. A one-year time series of energy-balance measurements covering the period from May, 1999 to April, 2000 shows that the net radiation and turbulent heat fluxes are the major contribution to the energy balance. The heat fluxes due to surface melt in summer and re-freezing events (re-freezing of meltwater at the surface or rime accretion) have to be taken into account. Their precise magnitude is difficult to interpret as these fluxes also comprise the instrumental and methodological errors of the energy-balance calculation. Single surface melt events and the prevailing meteorological conditions favouring or preventing surface melt could be identified by precise high-resolution surface-temperature measurements.

Near-surface firn temperatures were measured in 22 steam-drilled boreholes in the summit region of Mont Blanc (France and Italy) between 3800 and 4800 m a.s.l. in June, 1998, and in 31 boreholes in the Monte Rosa area (Italy and Switzerland) between 3900 and 4500 m a.s.l. in May/July 1999. Borehole temperatures were sampled with removable thermistor chains to a depth of 22 m. The temperatures at 18 m depth ranged between temperate conditions and approximately -15 °C. The thermal distribution pattern of cold firn suggests a strong influence of solar radiation and turbulent heat exchange. During the melt season in summer, these energy fluxes mainly determine the melt-energy input into the snow and firn and, thereby, the observed near-surface firn temperatures. Mean annual air temperature is of secondary importance for the spatial distribution pattern, although the observed mean annual firn temperatures generally increase with decreasing elevation. A statistical analysis of the measured firn temperatures revealed that the parameters elevation, potential direct solar radiation, slope and accumulation are able to explain more than 80 % of the variation of the mean annual firn temperatures. The aspect-dependent lower boundaries for cold firn in the Mont Blanc and Monte Rosa areas range between

3500 and 3700 m a.s.l. on north-facing and between 3800 and 4100 m a.s.l. on south-facing slopes.

Theoretical calculations, using a one-dimensional time-dependent thermo-mechanical firn-temperature model including the effect of latent heat originating from surface melt, show that the englacial thermal regime is extremely sensitive to the magnitude and duration of surface melt and that melt events perturb the pure surface-temperature signal, considerably. A typical surface-temperature perturbation penetrates a 100 m thick glacier within 18 to 30 years, only. Therefore, the possible time horizon for surface-temperature reconstructions using englacial temperature profiles is limited to a few centuries at best. Englacial temperature profiles were measured with an absolute accuracy of ± 0.01–0.03°C in a 29 m deep borehole at Seserjoch (4300 m a.s.l., Monte Rosa area), in a 25 m deep borehole at the saddle point of Colle Gnifetti (4450 m a.s.l., Monte Rosa area) and in a 40 m deep borehole on top of Dôme du Goûter (4300 m a.s.l., Mont Blanc area). These records suggest a surface-temperature increase on the order of 0.5–1 °C for the last decade.

A spatial energy-balance model was coupled with a one-dimensional thermal firn-temperature model and applied to the Monte Rosa study area. Although the energy-balance model yielded some encouraging results, the errors in the calculated surface temperature turned out to be too large for a direct application in a coupled energy-balance/firn-temperature model. A simplified formulation of the upper boundary condition in terms of surface temperature and melt-energy input is proposed and coupled with the firn-temperature model. The model is considered robust enough to give a statement on the future thermal evolution of the cold firn saddles of Seserjoch and Colle Gnifetti.

Zusammenfassung

Wenig ist bis heute bekannt über die komplexen Austauschprozesse zwischen Gletscher und Atmosphäre, welche zur Bildung von kaltem Firn auf hochgelegenen Alpengletschern führen. Obwohl kalter Firn und kaltes Eis nicht ein weitverbreitetes Phänomen für Alpengletscher darstellt, ist es doch für viele glaziologische Fragestellungen wichtig und hat einen grossen Einfluss auf Gletscher als Umwelt- und Klimaarchiv.

Die vorliegende Arbeit versteht sich als Beitrag zu einem verbesserten quantitativen Verständnis der atmosphärischen und glaziologischen Prozesse in kalten Firngebieten. Die Studie ist in vier Hauptteile gegliedert, welche sich mit den Wechselwirkungen zwischen der Atmosphäre und dem Untergrund (Oberflächenenergiebilanz), der Verbreitung von kaltem Firn im Raum (räumliche Verbreitung von kaltem Firn), der thermometrischen Aussage beobachteter Firn- und Eistemperaturprofile im Sinne eines Klimasignals (Bohrlochthermometrie) und der Energiebilanz und den (zukünftigen) thermischen Bedingungen des Gletschers im Raum (gekoppeltes räumliches Energiebilanz-/Firntemperaturmodell) befassen.

Der Einfluss der Atmosphäre wurde mit Hilfe einer Energiebilanzstudie am 4300 m hohen, kalten Firnsattel des Seserjochs (Monte Rosa, Italien und Schweiz) untersucht. Messungen der kurz- und langwelligen Strahlung, der Windgeschwindigkeit und -richtung, der Lufttemperatur, der Luftfeuchte, der Schneehöhe und der Schnee- und Firntemperaturen wurden zwischen September 1998 und August 2000 durchgeführt. Eine einjährige Energiebilanzmessreihe von Mai 1999 bis April 2000 zeigt, dass die Nettostrahlung und die turbulenten Wärmeflüsse den Hauptanteil der Energiebilanz ausmachen. Die Wärmeflüsse aufgrund der Oberflächenschmelze im Sommer und von Wiedergefrierprozessen (Wiedergefrieren von Schmelzwasser oder Rauhreifbildung) können nicht vernachlässigt werden. Ihre exakte Grössenordnung ist schwierig zu bestimmen, da diese Flüsse auch die instrumentellen und methodischen Fehler der Energiebilanzberechnung beinhalten. Präzise, hochaufgelöste Oberflächentemperaturmessungen ermöglichten es, einzelne Oberflächenschmelzereignisse und die vorherrschenden meteorologischen Bedingungen zu identifizieren, welche Oberflächenschmelze begünstigen oder verhindern.

Oberflächennahe Firntemperaturen wurden in 22 Dampfbohrlöchern in der Gipfelregion des Mont Blanc (Frankreich und Italien) zwischen 3800 und 4800 m ü. M. im Juni 1998 und in 31 Dampfbohrlöchern im Monte Rosa Gebiet (Italien und Schweiz) zwischen 3900 und 4500 m ü. M. im Mai/Juli 1999 gemessen. Die Bohrlochtemperaturen wurden mit Hilfe mobiler Thermistorenketten bis in eine Tiefe von 22 m aufgezeichnet. Die Temperaturen in 18 m Tiefe variierten zwischen temperierten Bedingungen und ungefähr -15 °C. Das Verbreitungsmuster von kaltem Firn legt einen starken Einfluss der Sonneneinstrahlung und des turbulenten Wärmeaustausches nahe. Während der Schmelzperiode im Sommer bestimmen diese Energieflüsse hauptsächlich den Schmelzenergieeintrag in den Schnee und Firn und damit die beobachteten, oberflächennahen Firntemperaturen. Die mittlere Jahrestemperatur der Luft ist eher zweitrangig für das räumliche Verbreitungsmuster, obwohl die beobachteten mittleren Firntemperaturen im allgemeinen mit abnehmender Höhe

zunehmen. Eine statistische Auswertung gemessener Firntemperaturen hat gezeigt, dass die Parameter Höhe, potentielle Direktstrahlung, Hangneigung und Akkumulation mehr als 80 % der Variation der mittleren Firntemperaturen erklären können. In den Mont Blanc und Monte Rosa Gebieten schwanken die expositionsabhängigen Untergrenzen für kalten Firn zwischen 3500 und 3700 m ü. M. in Nord- und 3800 und 4100 m ü. M. in Südhängen.

Theoretische Berechnungen mit Hilfe eines eindimensionalen, zeitabhängigen, thermomechanischen Firntemperaturmodells, welches den Einfluss der latenten Wärme durch wiedergefrierendes Schmelzwasser berücksichtigt, zeigen, dass die Temperaturverteilung im Gletscher extrem empfindlich auf den Umfang und die Dauer der Oberflächenschmelze reagiert und dass Oberflächenschmelzereignisse das reine Oberflächentemperatursignal empfindlich stören. Eine typische Oberflächentemperaturstörung hat einen 100 m dicken Gletscher innerhalb von nur 18 bis 30 Jahren durchquert, was im besten Fall zu einem möglichen Zeithorizont für Oberflächentemperaturrekonstruktionen mit Hilfe von Bohrlochtemperaturprofilen von einigen Jahrhunderten führt. Bohrlochtemperaturprofile wurden mit einer absoluten Genauigkeit von ± 0.01–0.03°C in einem 29 m tiefen Bohrloch am Seserjoch (4300 m ü. M., Monte Rosa Gebiet), in einem 25 m tiefen Bohrloch im Sattelpunkt des Colle Gnifetti (4450 m ü. M., Monte Rosa Gebiet) und in einem 40 m tiefen Bohrloch auf dem Gipfel des Dôme du Goûter (4300 m ü. M., Mont Blanc Gebiet) gemessen. Die Bohrlochtemperaturprofile zeigen dabei eine Erhöhung der Oberflächentemperatur in der Grössenordnung von 0.5–1 °C für das letzte Jahrzehnt.

Ein räumliches Energiebilanzmodell wurde mit einem eindimensionalen thermischen Firntemperaturmodell gekoppelt und auf das Monte Rosa Studiengebiet angewendet. Obwohl das Energiebilanzmodell einige vielversprechende Resultate lieferte, hat es sich gezeigt, dass die Fehler in der errechneten Oberflächentemperatur zu gross waren für eine direkte Anwendung in einem gekoppelten Energiebilanz-/Firntemperaturmodell. Eine vereinfachte Formulierung der oberen Randbedingung im Sinne der Oberflächentemperatur und des Schmelzenergieeintrages wird vorgeschlagen und mit dem Firntemperaturmodell gekoppelt. Das Modell wird als soweit robust betrachtet, um eine Aussage über die zukünftige thermische Entwicklung der kalten Firnsättel am Seserjoch und am Colle Gnifetti machen zu können.

Résumé

Jusqu'à présent, il existe peu de connaissances relatives à l'interaction complexe entre l'atmosphère et le glacier qui mène à la formation de névé froid sur les glaciers de hautes altitudes dans les Alpes. Bien qu'on ne trouve le névé froid et la glace froide que sporadiquement dans les Alpes, ils interviennent dans divers problèmes glaciologiques et sont d'une grande importance en tant qu'archives environnementales et climatiques.

La présente étude vise à une meilleure compréhension quantitative des processus atmosphériques et glaciologiques dans les régions de névé froid. Elle est divisée en quatre chapitres principaux traitant de l'interaction entre l'atmosphère et le sol (bilan énergétique de surface), de la distribution du névé froid dans l'espace (distribution spatiale du névé froid), de l'évidence thermométrique des profils de température observés dans le névé et la glace sous l'angle d'un signal climatique (thermométrie des forages) et du lien entre le bilan énergétique et les conditions thermiques (futures) du glacier dans l'espace (modèle couplé du bilan énergétique et de la température du névé).

L'impact des conditions atmosphériques a été étudié à l'aide d'une analyse du bilan énergétique du névé froid au col du Seserjoch à 4300 m d'altitude, dans la région du Mont-Rose (Italie et Suisse). Des mesures de rayonnement d'ondes courtes et longues, de vitesse et de direction du vent, de température et d'humidité de l'air, de hauteur et de température de la neige et du névé ont été effectuées entre septembre 1998 et août 2000. Une série de mesures du bilan énergétique sur la période de mai 1999 à avril 2000 montre que le rayonnement net et les flux de chaleur turbulente contribuent majoritairement au bilan énergétique. Mais le flux de chaleur provenant de la fonte de neige en surface en été et les cas de regel (regel de l'eau de fonte à la surface, accrétion de givre) ne peuvent être négligés. Les valeurs de ces flux sont difficiles à interpréter à cause des erreurs de mesures et de méthodologies du calcul du bilan énergétique. Des mesures à haute résolution des températures de surface en été permettent d'identifier des cas isolés de fonte en surface, et de mettre en évidence les conditions météorologiques favorisant ou empêchant la fonte en surface.

Des températures du névé proches de la surface ont été mesurées dans 22 forages à vapeur dans la région sommitale du Mont-Blanc (France et Italie) entre 3800 et 4800 m d'altitude en juin 1998 ainsi que dans 31 forages à vapeur dans la région du Mont-Rose entre 3900 et 4500 m d'altitude en mai et en juillet 1999. Elles ont été mesurées à l'aide de chaînes de thermistances amovibles jusqu'à une profondeur de 22 m. En 1999, les températures à 18 m de profondeur variaient entre des conditions tempérées et environ -15 °C. La distribution spatiale du névé froid suggère une forte influence du rayonnement solaire et des échanges de chaleur turbulente sur les températures à 18 m. Durant la période de fonte en été, ces flux d'énergie constituent le principal apport d'énergie de fonte dans la neige et le névé et déterminent les températures observées proches de la surface du névé. La température moyenne annuelle de l'air est de moindre importance pour la distribution spatiale, bien qu'en général les températures moyennes annuelles observées du névé augmentent lorsque l'altitude diminue. Une analyse statistique des températures mesurées dans le névé

montre que les paramètres altitude, rayonnement solaire potentiel direct, pente et accumulation expliquent plus de 80 % de la variation des températures moyennes annuelles du névé. Dans les régions du Mont-Blanc et du Mont-Rose, les limites inférieures de névé froid varient entre 3500 et 3700 m d'altitude sur les versants nord et entre 3800 et 4100 m d'altitude sur les versants sud.

Des calculs théoriques de la température du névé ont été effectués à l'aide d'un modèle thermomécanique unidimensionnel dépendant du temps et incluant les effets de chaleur latente émanant de la fonte de neige. Ils montrent que le régime thermique du glacier est extrêmement sensible à l'importance et à la durée de la fonte en surface et que les cas de fonte perturbent considérablement le signal pur de température de surface. Une perturbation typique de la température de surface se déplace à travers un glacier de 100 m d'épaisseur en 18 à 30 ans seulement. Ainsi, les profils de température du glacier permettent une reconstitution des températures de surface au mieux pour les derniers siècles. Des profils de température du glacier ont été établis avec une précision absolue de ± 0.01–$0.03\,^{\circ}\mathrm{C}$ dans un forage de 29 m au Seserjoch (4300 m, région du Mont-Rose), dans un forage de 25 m au point culminant du Colle Gnifetti (4450 m, région du Mont-Rose) ainsi que dans un forage de 40 m au sommet du Dôme du Goûter (4300 m, région du Mont-Blanc). Ces données suggèrent une augmentation de la température de surface de l'ordre de 0.5 à $1\,^{\circ}\mathrm{C}$ pour la dernière décennie.

Un modèle spatial de bilan énergétique a été couplé avec un modèle thermique unidimensionnel des températures de névé et appliqué à la région du Mont-Rose. Bien que le modèle de bilan énergétique ait fourni des résultats encourageants, les erreurs sur la température de surface sont trop grandes pour une application directe dans un modèle couplé. Une formulation simplifiée des conditions aux limites supérieures de température de surface et d'apport d'énergie de fonte est proposée et est utilisée dans le modèle de température du névé. Le modèle ainsi simplifié est considéré assez robuste pour faire une prévision de l'évolution thermique future du névé froid aux cols du Seserjoch et du Colle Gnifetti.

1 Introduction

As changes in the highly sensitive ecosystem of the Alps may soon exceed the limits of historical and Holocene variability, improved knowledge on past and present environmental changes is of fundamental interest. Regional patterns of man-induced climate changes and their impact on the social and economic development of the Alpine countries have to be assessed. The loss in reliability on the historically collected empirical data basis must be replaced by improved process understanding combined with robust models applicable to existing environments under conditions of fast climate change. High-altitude glaciers offer a unique environmental archive documenting past and ongoing changes with high resolution. Thus, it is of major interest to open, analyse and document this archive, offering a variety of environmental parameters in space and time as probably no other natural archive does.

1.1 The EU-Project ALPCLIM

The present study was made within the framework of the EU-Project *ALPCLIM* (*Environmental and Climate Records from High-Elevation Alpine Glaciers*). The project was launched to collect, analyse, interpret and synthesize the wide variety of environmental and climate information from high-elevation Alpine glaciers in a collaboration of eight Institutes from Germany, France, Italy, Austria and Switzerland. The principal objectives were

1. exploitation of Alpine glacier archives for climate-related records (water isotopes, aerosol and trace gases);
2. evaluation and validation of these records in view of their reliability, representativeness and inherent net atmospheric signals finally leading to
3. basic prospects on the potential of Alpine glacier archives for various paleoenvironmental and climatic studies.

The project was divided into four work packages:

1. Ice-Core Data Acquisition
2. Ice-Core Data Evaluation
3. Glacio-Meteorology
4. High-Alpine Climatology Study

Each work package was subdivided into several activities. The relevant work package for this study (Glacio-Meteorology) included the activities on

a. spatial distribution of cold-firn areas;
b. climatic evidence of englacial temperature records;
c. low-altitude ice archives.

The VAW/ETH-part of the project presented in this study dealt with the two first activities, namely the spatial distribution, surface energy balance and climatic evidence of cold high-elevation Alpine glaciers (see Section 2).

1.2 Cold Firn and Ice in the Alps

Cold glaciers are defined as firn- and ice bodies showing negative temperatures as a whole and over a minimum time period of one year. If the entire glacier is at pressure-melting point, they are said to be *temperate*. Many existing glaciers are neither cold nor temperate throughout. Temperate parts often occur at the glacier bed or in the accumulation area. Such ice bodies are called *polythermal* (eg Paterson, 1994). In the accumulation area, the following zones can be distinguished according to the occurrence and penetration depth of surface meltwater:

- the *recrystallization zone* (Shumskii, 1964) or the *dry-snow zone* (Müller, 1962), where even in summer no surface melt occurs due to a very low *mean annual air temperature* (MAAT);
- the *recrystallization-infiltration zone* (Shumskii, 1964) or the *percolation zone A* (Müller, 1962), where melt only takes place in the uppermost annual layer of the snow or firn;
- the *cold-infiltration zone* (Shumskii, 1964) or the *percolation zone B* (Müller, 1962), where meltwater penetrates through several annual layers of the firn and
- the *temperate-firn zone*, where penetrating meltwater warms the entire firn body to 0 °C.

In the first three zones, cold ice is formed in the accumulation area. The situation in the ablation area is often more complicated as other factors – besides local climate – determine the existence or absence of cold ice, such as glacier dynamics, hypsography and glacier thickness. Thus, cold ice in the ablation area is either the result of cold-ice advection from the accumulation area (eg Blatter, 1987) or of a local cooling due to special microclimatic conditions at the glacier surface, eg when the glacier snout ends in the permafrost zone (eg Haeberli, 1976).
In order to quantify firn- and ice temperatures, a *mean annual firn temperature (MAFT)* and a *mean annual ice temperature (MAIT)* can be defined, respectively. Seasonal surface-temperature fluctuations are normally reflected within the uppermost 10–20 m of the firn and ice. Englacial temperatures measured to this depth are called *near-surface firn- and ice temperatures* adapting the concept by Hooke et al. (1983). The MAFT or MAIT is found at a depth where the seasonal temperature fluctuations vanish or – in practice – where they are within the accuracy range of the measurement. In the dry-snow zone, the MAFT is very close to the observed surface- or air temperature. In the recrystallization-infiltration and cold-firn zones, the MAFT is normally higher than the observed surface and air temperatures due to latent heat within the upper snow and firn layers released by penetrating and refreezing surface meltwater. As a consequence of a surface temperature which cannot rise above 0 °C and radiative cooling during night, the surface temperatures of cold firn are deeper than the observed air temperatures on average. Thus, care must be taken if temperature reconstructions from borehole-temperature profiles (as a result of a surface-temperature history) are interpreted in terms of air-temperature changes. In ablation areas, the MAIT can be both higher and lower than the MAAT, mainly depending on (snow-) insulation and meltwater effects (Hooke et al., 1983).

Attention must be paid to sites with strong firn- or ice advection and to steep slopes and topographic depressions in the cold-firn zone. In this zone, lateral advection of meltwater can alter the mean in-situ thermal conditions.
Mean annual firn and ice temperatures are mainly a result of the energy- and mass balance at the glacier surface. Important parameters affecting the mean annual firn and ice temperatures are MAAT, radiation flux, rate and seasonality of accumulation/ablation, volume of penetrating and re-freezing meltwater in firn areas, topographic location (depression or ridge) and wind effects. Some of these parameters are closely interconnected like, eg topography, wind effects and snow deposition. Other parameters which can influence the near-surface thermal regime are glacier flow velocity, extension and characteristics of the catchment basin (eg deposition of cold snow by avalanche activity), intensity of friction at the glacier bed and ice deformation, ground heat flux and occurrence of crevassed zones (eg Paterson, 1994; Suter et al. 2001).
Negative firn- and ice temperatures are of relevance in glacio-climatological studies for the following reasons:

- they are linked to the parameters of the ice flow law (eg Paterson, 1994);
- they can be considered a key parameter for detecting global warming or cooling trends (see eg, Robin, 1983, Zotikov, 1986, Haeberli, 1990; Haeberli and Funk, 1991; MacAyeal et al., 1991; Fischer et al., 1995; Cihlar et al., 1997; Lüthi, 2000). In glacierized polar and high-mountain regions, negative firn- and ice temperatures can be interpreted in terms of natural thermographs with a pronounced long-term memory function as they reflect the surface-temperature conditions of the past. Observed temperature profiles from polar ice caps, for instance, clearly indicate a warming trend for the 20th century (Robin, 1983);
- steep hanging glaciers entirely or partly frozen to their beds are stabilized (Alean, 1985; Haeberli et al., 1989; Wagner, 1996; Lüthi and Funk, 1997);
- they can significantly influence the mass-balance evolution of a glacier (eg Greuell and Oerlemans, 1986; Konzelmann and Braithwaite, 1995) and are of importance in mass-balance/sea-level scenarios (Meier, 1984);
- they are essential for glaciological trace-element investigations. Cold firn and ice ensure an optimum embedding and conservation medium for natural trace elements like terrestrial and cosmic dusts, marine salts, isotopes and gases as well as anthropogenic contributions such as soot particles, (exhaust) gases, organic compositions and numerous radio-active isotopes (eg, Wagenbach, 1989; Haeberli and Stauffer, 1994).

For a long time it was assumed that glaciers in the Alps were generally temperate, although Vallot (1893 and 1913) already observed cold firn in the Mont Blanc Massif at the end of the 19th and at the beginning of the 20th century. Only in the 1950s, the discussion about cold firn and ice in the Alps was reanimated by investigations in the Monte Rosa (Fisher, 1953; 1954; 1955 and 1963) and Jungfrau areas (Haefeli and Brentani, 1955). Lliboutry et al. (1976) and Haeberli (1976) were among the first who systematically assessed the distribution of cold firn and ice in the Alps. In the past, extensive firn- and ice-temperature measurements took predominately

place at locations of specific practical or scientific interest in connection with construction work (eg Haefeli and Brentani, 1955; Haeberli et al., 1979), glacier-risk prevention (Lüthi and Funk, 1997) and high-alpine core drillings (eg Oeschger et al., 1977; Alean et al., 1983; Haeberli and Funk, 1991; Vincent et al., 1997). A scheme for the spatial distribution of cold firn and ice was outlined by Hooke et al. (1983) including near-surface temperatures of alpine and polar regions and by Haeberli and Alean (1985) focusing on firn- and ice temperatures from the Alps. An altitude- and aspect-dependent statistical model on the distribution of cold firn and ice in accumulation areas of the Alps has recently been developed by Suter et al. (2001).
The potential of borehole-temperature records for paleo-temperature reconstructions (*borehole thermometry*) has recently been discovered and was successfully applied to temperature records from Greenland (Dahl-Jensen and Johnsen, 1986) and Antarctica (Ritz, 1989; MacAyeal et al., 1991; Salamatin et al., 1994; Dahl-Jensen et al., 1999) using forward approaches or sophisticated inverse modeling based on control or Monte-Carlo methods.
Modern techniques like terrestrial or airborne radar (eg Bamber, 1989; Bjørnsson et al., 1996; Ødegård et al., 1997) and remote sensing (eg West et al., 1996) have been developed and applied to map the thermal structure of glaciers.

1.3 Energy-Balance Studies on Mountain Glaciers

The near-surface thermal regime of cold firn and ice can only be fully understood by means of an energy-balance study. Modern energy-/mass-balance investigations (measurements and modeling) have mostly neglected the near-surface temperature regime, although the assumption of a steady 0 °C surface temperature during the melt season may lead to substantial errors (Greuell and Oerlemans, 1986). Glacier melt in cold ablation areas is significantly reduced resulting in lower degree-day factors (melt index according to the sum of positive degree days of the air temperature) as the warming of cold ice represents a substantial heat sink (Konzelmann and Braithwaite, 1995).
Energy-balance studies over snow go back to the 1930s and 1940s, already (Sverdrup, 1936; Wilson, 1941). A series of modern energy-balance (component-) measurements and modelings was carried out for alpine glaciers (eg Föhn, 1973; La Casinière, 1974; Martin, 1975; Wagner, 1979 and 1980; Escher-Vetter 1985a and 1985b; Funk 1985; Oerlemans 1992, van de Waal et al. 1992; Arnold et al., 1996; Hock and Noetzli, 1997; Hock, 1999; Oerlemans, 2001) most of them in connection with mass-balance and glacier-melt/discharge investigations on temperate valley glaciers.
Index methods like BTS-measurements (*B*ottom *T*emperature of the Winter *S*now Cover) at the snow-ice or snow-firn interface in end-winter and snow-depth measurements were carried out to obtain possible climatological and topographic proxy-parameters for detecting cold firn and ice (Ødegård et al. 1992; Suter, 1995; Lütschg, 2000).
Physically-based energy-balance models, including all energy-balance components, were successfully applied to complex alpine topography for simulating spring snow melt (Plüss, 1997; Fierz et al., 1997), glacier melt (Brock et al., 2000), permafrost occurrence (Hoelzle et al., 2001) or were used to model the snow cover evolution for avalanche forecasting (Brun et al., 1989; Lehning et al., 1999).

2 Objectives

The objectives of the present study can be summarized as follows:

- Better and more quantitative understanding of the spatial occurrence of cold firn and ice in high-altitude areas of the Alps (Mont Blanc and Monte Rosa areas) and development of a statistical distribution model for cold firn based on proxy-parameters.
- Detailed energy- and mass-balance study over cold firn to isolate the relevant energy- and mass fluxes and determination of the upper boundary condition in terms of surface temperature and melt-energy flux.
- Assessment of the climatic evidence of englacial borehole-temperature records as a short- and mid-term surface- and air-temperature signal as compared to other climatic signals like air-temperature records from weather stations and ice-core records.
- Coupling of the surface energy balance with the thermal regime of the firn and ice by connecting an areal energy-balance model with a one-dimensional firn-temperature model including heat diffusion, heat advection and latent heat.

Seite Leer /
Blank leaf

3 Site Description and Field Observations

3.1 General Overview

Figure 3.1 shows the location of the Mont Blanc and Monte Rosa study areas and of the weather stations used for this study. The study areas are described in Sections 3.2 (Mont Blanc) and 3.3 (Monte Rosa).
The weather stations at Jungfraujoch (3580 m a.s.l.), at Grand St. Bernard (2478 m a.s.l.) and at Zermatt (1638 m a.s.l.) are operated by the *Swiss Meteorological Institute (SMA)*, whereas the station at Gornergrat (3135 m a.s.l.) is operated by both the SMA and the *Swiss Federal Institute of Snow- and Avalanche Research (SFISAR)*.

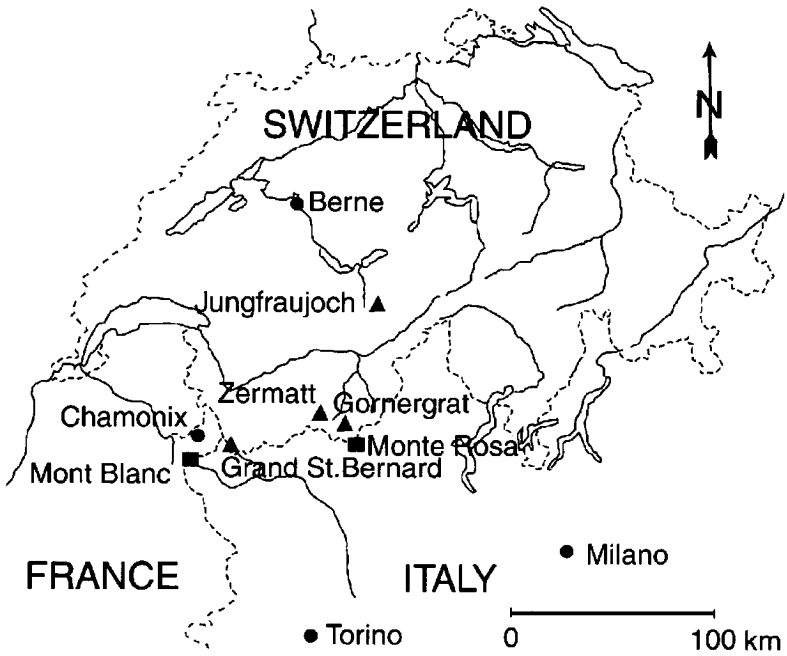

Figure 3.1: General overview of the location of the Mont Blanc and Monte Rosa study areas in the Alps. The study areas of the Mont Blanc and Monte Rosa are denoted with a square; the weather stations used for this study with a triangle.

3.2 Mont Blanc Area

3.2.1 Site Description

The *Mont Blanc Massif* is built up by a massive granite body and culminates in the firn- and ice-covered 4807 m high summit of Mont Blanc; highest peak of the European Alps. The massif in the boundary region of Italy, France and Switzerland is bordered by the French Val Montjoie to the west and Val de Chamonix to the north, the Italian Val Veni and Val Ferret to the south and the Swiss Val Ferret to the east. The massif is about 15 km in width and 40 km in length. Its marked appearance is not only due to the relatively small dimensions, but also to the large difference in height of almost 4000 m between the valley floors and the culmination.

The area is heavily glacierized and the largest valley glaciers are Ghiacciaio del Miage in Italy, Mer de Glace and Glacier d'Argentière in France and Glacier de Saleina in Switzerland (Figure 3.2).
The actual study area (45° 50' 30" N, 6° 51' 00" E) has a size of about 3 km^2 and is situated to the north of the Mont Blanc summit. It stretches from about 3800

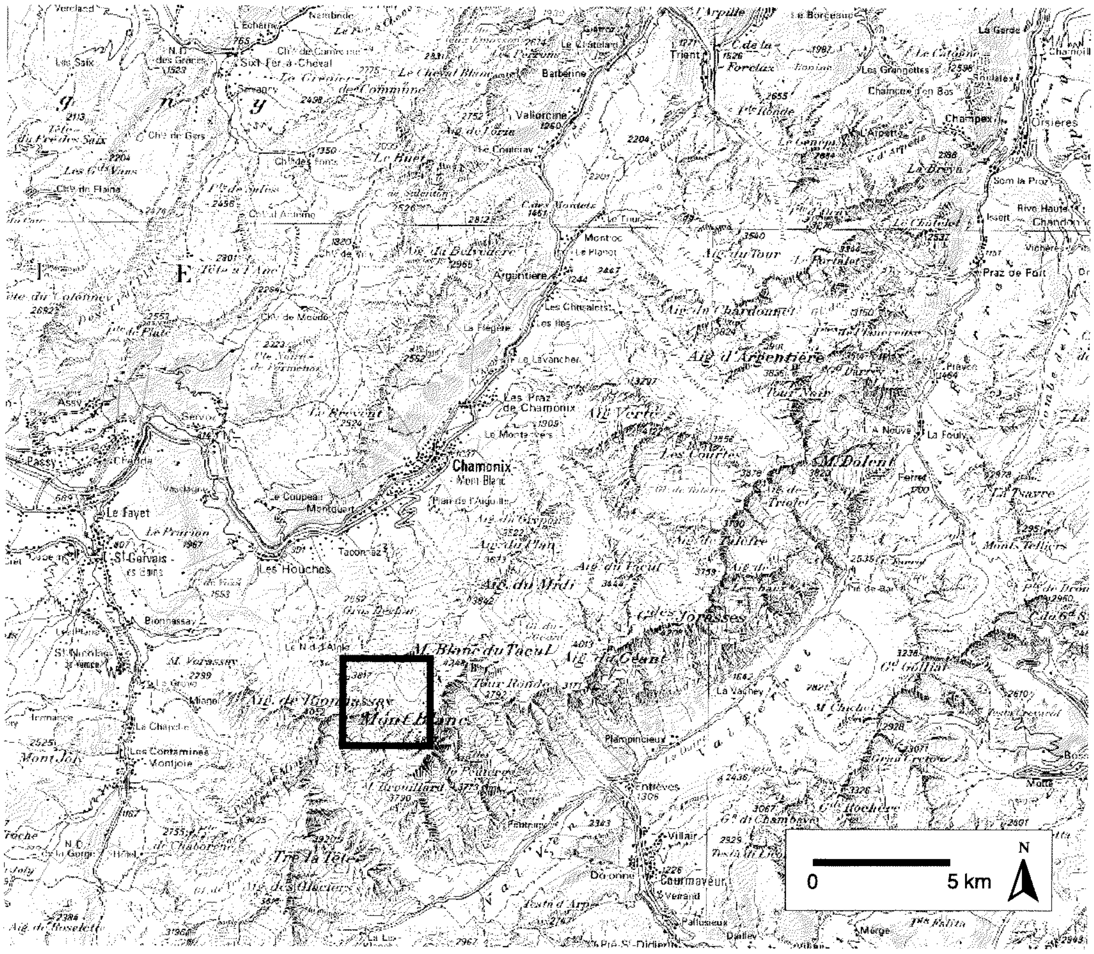

Figure 3.2: Overview of the Mont Blanc Massif. The study area is marked with a rectangle. Map: PM200 ©Swiss Federal Office of Topography.

to 4800 m a.s.l. and comprises the accumulation areas of Glacier de Bionnassay, Glacier de Taconnaz and Glacier des Bossons as well as the summits of Mont Blanc, 4807 m a.s.l. and Dôme du Goûter, 4304 m a.s.l. (Figure 3.3).
The climate of the investigated area is characterized by almost persistent negative air temperatures, very high wind speeds as the massif is fully exposed to the (north-)westerlies and, therefore, high precipitation rates. Due to the generally high wind speeds, the accumulation shows a wide spatial variability and can be found between 0.2 m of water equivalent (w.e.) per year at very wind-exposed sites (personal communication from S. Preunkert, 2001) and 4 m w.e./a at wind-protected sites (Vincent et al., 1997). The observed firn- and ice depths are found between a few meters and up to about 40 m at exposed crests and domes and between 120 and more than 200 m at saddles and basins (Suter, 1993; Vincent et al., 1997).

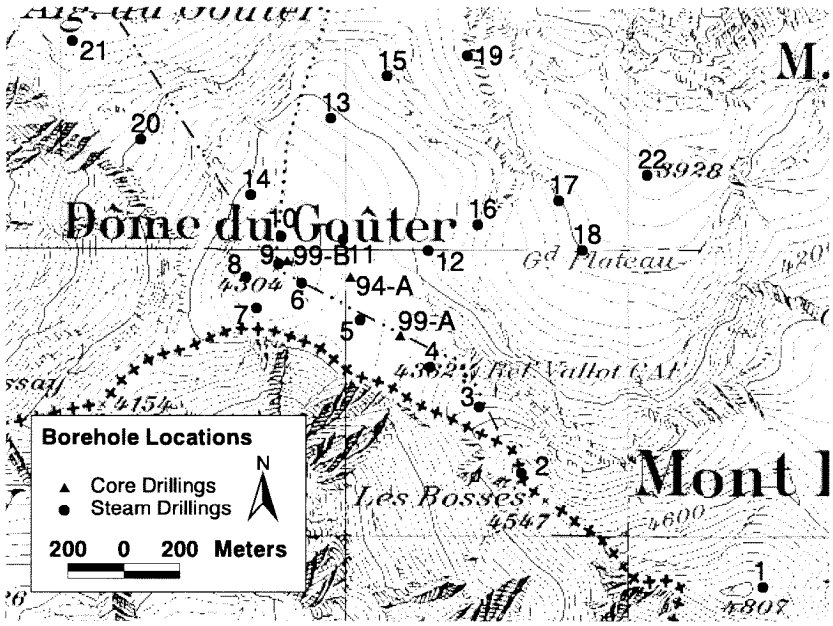

Figure 3.3: Overview of the Mont Blanc study area. The steam drillings from 1998 and the core drillings from 1994 (94-A) and 1999 (99-A and 99-B) are indicated. Map: PM50 ©Swiss Federal Office of Topography.

3.2.2 Previous Studies

The first firn-temperature observations in the area were made at the summit of Mont Blanc by Vallot (1893) at the end of the 19th century already (1891/1892) and at Col du Dôme in 1911 (Vallot, 1913). Later observations were made by Lliboutry et al. (1976), who measured firn temperatures at 15 m depth. Further extended investigations such as accumulation, velocity-field, bed-topography and single firn- and ice-temperature measurements were made in the 1990s, when the core-drilling activities in the saddle area of Col du Dôme started (Suter, 1993; unpublished data from the *Laboratoires de Glaciologie et Géophysique de l'Environnement (LGGE), Grenoble*, 1995; Gagliardini and Meyssonnier, 1997; Vincent et al., 1997). The locations of the various core drillings from the 1990s are given in Figure 3.3.
Meteorological and climatological studies in the area were carried out by eg Vallot, (1893 and 1913) and La Casinière (1974). More recently, a few air-temperature (September 1999 to August 2000) and wind (winter 1997/98) observations were carried out at Observatoire Vallot (personal communication from S. Preunkert, 2001).

3.2.3 Field Observations

All the visits to the field site were made by helicopter and a big advantage and help in the field work was the (private) hut of *Observatoire Vallot*, 4350 m a.s.l., which gave a comfortable and safe shelter during all the field campaigns in the area. The hut is located right beneath *Refuge Vallot CAF*, 4362 m a.s.l. (Figure 3.3).
The first and longest field campaign in connection with this study was made from June 15 to June 29, 1998. During this time, a total of 22 boreholes ranging between 8 and 22 m depth were drilled and firn temperatures measured (Figure 3.3; Section

5). Almost all the boreholes were surveyed using a portable GPS-device (Section 5.3.1). Unfortunately, very bad weather in the following autumn made a second visit to the site impossible so that no accumulation measurements could be made at the location of the boreholes nor some temperature measurements be repeated.
From June 16 to June 18, 1999, radar measurements were made between Observatoire Vallot and Dôme du Goûter to complete existing measurements (Suter, 1993) and to find suitable locations for new core drillings, which were subsequently carried out beneath Observatoire Vallot (99-A) and on top of Dôme du Goûter (99-B) in the following autumn (personal communication from S. Preunkert, 2001; Figure 3.3).
On January 27, 2000, borehole temperatures to 40 m depth could be measured in the electro-mechanically drilled borehole to bedrock 99-B on the summit of Dôme du Goûter (Section 6.4.1).

3.3 Monte Rosa Area

3.3.1 Site Description

The *Monte Rosa* area at the boundary between Italy and Switzerland is geologically formed by the Monte Rosa nappe, which is part of the Penninic nappes, and mainly consists of metamorphic crystalline and sedimentary rocks. The word 'Rosa' or 'Rosae' in the pronunciation of the local people is derived from a dialect expression of Valle d'Aosta which means 'Glacier' (Monterin, 1941). The Monte Rosa area harbours some of the highest peaks of the Alps such as Dufourspitze, 4634 m a.s.l., Signalkuppe, 4554 m a.s.l. (location of *Capanna Regina Margherita*, highest mountain hut of the Alps) and Liskamm, 4527 m a.s.l. and is about 22 km long and 18 km wide. It is bordered by the Italian Val d'Ayas, Val di Gressoney, Val Sesia and Valle Anzasca to the south and east and by the Swiss Mattertal to the north. Its appearance is quite gentle to the west, north and south with heavily glacierized slopes and numerous valley glaciers, whereas it shows a steep and rugged icy and rocky face at its eastern margin. The difference in height between the highest summit, Dufourspitze, and the deepest valley site, Alagna-Valsesia, is 3500 m. The most important valley glaciers are Ghiacciaio del Lys and Ghiacciaio del Belvedere in Italy and Gornergletscher, Grenzgletscher and Findelengletscher in Switzerland (Figure 3.4).
The study area (45° 55' 20" N, 7° 52' 00" E) has a size of about 4 km^2 and covers the accumulation areas of the eastern part of Ghiacciaio del Lys and of Grenzgletscher above approximately 3900 m a.s.l. (Figure 3.5). Ghiacciaio del Lys is divided in an eastern and western branch. Grenzgletscher is part of the Gornergletscher system which forms the second largest coherent glacier system of Switzerland with a length of about 14 km and an area of roughly 70 km^2. The tongue of Grenzgletscher is characterized by very light and air-bubble rich ice, which is a sign of cold firn metamorphosis in the accumulation area. Negative ice temperatures (-2 – -3°C) could still be observed at the glacier snout due to the advection of cold ice from the accumulation area (Haeberli, 1976).
The climate in the study area is characterized by high-altitude conditions, ie practically persistent sub-zero air temperatures all over the year, relatively high precipitation rates and high wind speeds. The snow accumulation is strongly variable ranging between 0.3 m w.e./a at wind-exposed saddles and ridges and 2–3 m w.e./a

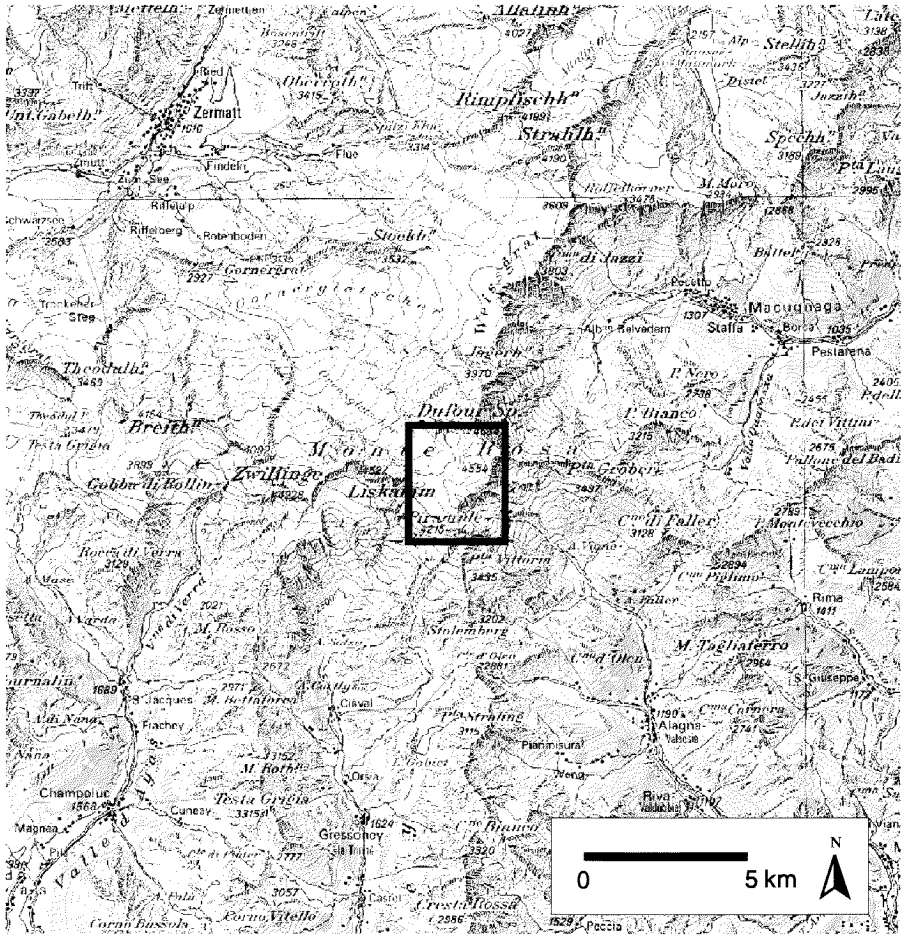

Figure 3.4: Overview of the Monte Rosa region. The study area is marked with a rectangle. Map: PM200 ©Swiss Federal Office of Topography.

at wind-protected sites (Gäggeler et al., 1983; Haeberli et al., 1983; Alean et al., 1983; Eichler et al., 2000). The observed ice depths in the study area range from 40–120 m at wind-exposed crests and saddles, and from 80 to more than 200 m in the central part of firn basins (Haeberli et al., 1988; Vonder Mühll and Funk, 1995; personal communication from G. Rossi, 2001).

3.3.2 Previous Studies

Firn- and ice temperatures in the Monte Rosa area were first investigated by Fisher (1953; 1954; 1955 and 1963). He observed MAFTs of about -3 °C at 4000 m a.s.l. in the south flank of Breithorn (4164 m a.s.l.) and of about -8 and -10 °C at 4260 and 4200 m a.s.l. below Dufourspitze (4634 m a.s.l.), respectively. The measurements were carried out in hand-dug (!) tunnels. Subsequent firn- and ice-temperature measurements in the area were especially made at Colle Gnifetti, 4452 m a.s.l., in deep core-drilled or shallow mechanically-drilled boreholes from about 1977 to 1983 (eg Oeschger et al., 1977; Alean et al., 1983; Haeberli and Funk, 1991). A series of predominantly shallow firn- and ice-temperature measurements was carried out on Grenzgletscher between 4000 and 4470 m a.s.l. in 1991, 1992 and 1994. Dur-

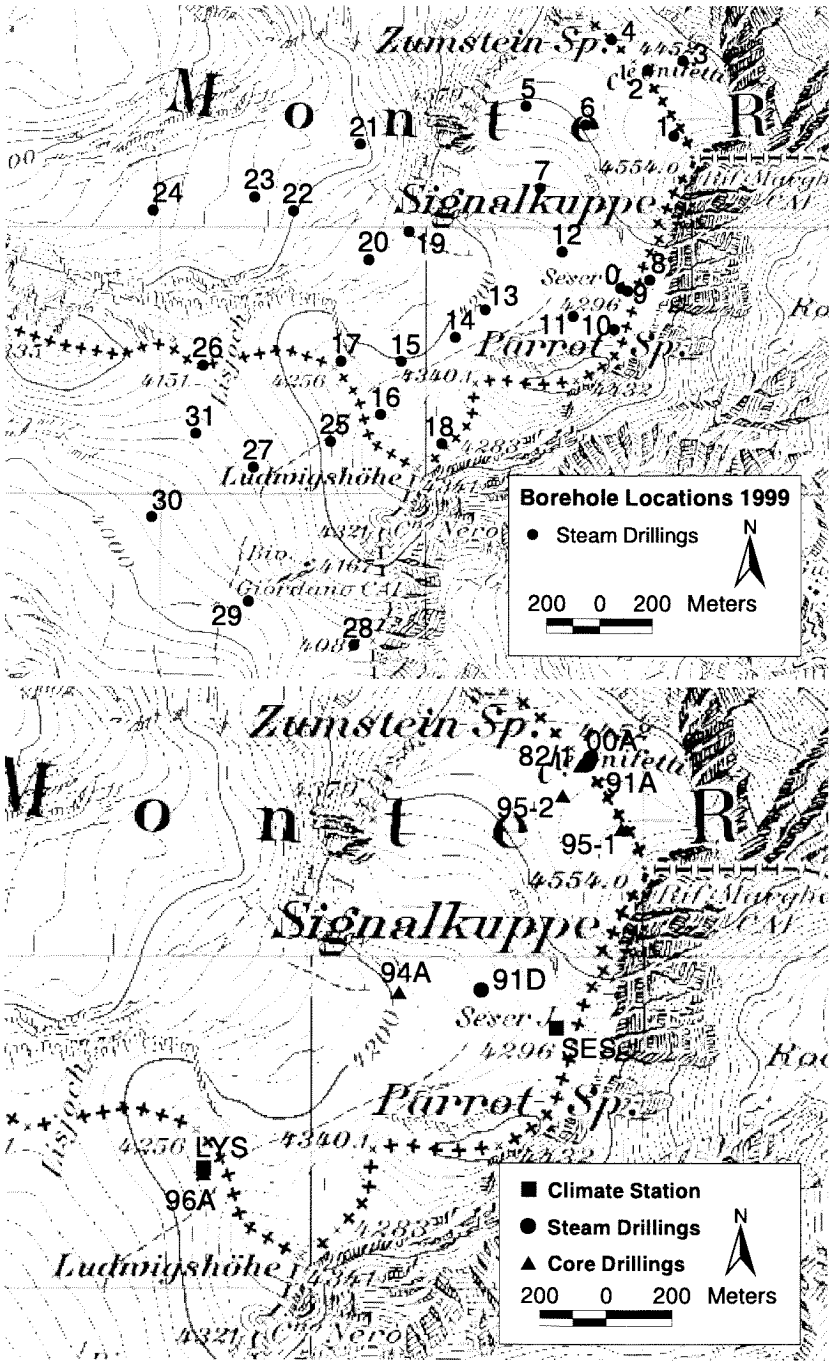

Figure 3.5: Overview of the Monte Rosa study area. The location of the steam drillings from 1999 is given in the upper panel. The lower panel shows the location of the climate stations, earlier steam-drilled boreholes and core drillings of relevance for this study. Maps: PM50 ©Swiss Federal Office of Topography.

ing this time, 10 boreholes ranging between 14 and 120 m depth were sampled (see Figure 3.5 for some borehole locations). These investigations took place in connection with different core-drilling projects by the *Institute of Environmental Physics, University of Heidelberg* and the *Laboratory of Radio and Environmental Chemistry, PSI Villigen and University of Bern* (Suter et al., 2001). In 1995, two deep core

drillings down to bedrock were performed by the Institute of Environmental Physics, Heidelberg and the *Institute of Physics of the University of Bern* in the saddle area of Colle Gnifetti and englacial temperatures measured (Lüthi, 2000). The location of these two boreholes and the observed near-surface firn temperatures are given in Figures 3.5 and 5.5.
The first meteorological investigations in the study area were made in 1894, from 1927 to 1939 and from 1952 to 1958 at Capanna Regina Margherita, 4554 m a.s.l., during summer when the warden was present. Further meteorological observations were only re-initiated at the end of the 1980s with air-temperature and snow-height measurements at Colle Gnifetti from 1986 to 1990 (unpublished data from the Institute of Environmental Physics, Heidelberg), with meteorological observations at the saddle of Colle Vincent, 4087 m a.s.l., from 1991 to 1994 by the *Italian Power Company ENEL* and with the installation of a fully-equipped weather station at Colle del Lys, 4250 m a.s.l., in 1996 by ENEL and the *Università degli Studi di Milano* (Rossi et al., 2000a and 2000b). A further very valuable data set for the area is being recorded at *Gornergrat*, 3135 m a.s.l., at the automated weather station of the SMA and the SFISAR since 1993. The locations cited above are indicated in Figures 3.1 and 3.5.

3.3.3 Field Observations

Due to the remoteness of the area and heavy equipment, access to the study area was only possible by helicopter. Capanna Regina Margherita, 4554 m a.s.l., Bivacco Giordano (Balmenhornhütte), 4167 m a.s.l., or tents at Seserjoch served as a shelter during the various field campaigns.
Firn-temperature measurements were carried out in steam-drilled boreholes to a maximum depth of 22 m from May 24 to June 1, 1999 and from July 15 to July 17, 1999. In May, 1999, a total of 24 boreholes was drilled. In July, 7 additional holes predominantely on Ghiacciaio del Lys could be drilled and logged and some erroneous measurements in the previous boreholes be repeated (Figure 3.5; Section 5). Accumulation could be observed at almost all the boreholes from end of May to mid-July. The stake positions at the boreholes were surveyed with the help of a portable GPS-device or estimated with the help of a map (Section 5.3.2).
During a field campaign from May 3 to May 5, 2000, the drilling of a deeper borehole in the saddle point of Colle Gnifetti could be initiated. The borehole was completed to a depth of about 40 m during a campaign from August 8 to August 10, 2000 and the temperatures logged from August 24 to August 26, 2000 (Section 6.4.2).
The instruments of the energy-balance station and two thermistor chains for measuring firn temperatures (4 and 30 m total length) could be installed at Seserjoch during a field campaign from September 21 to September 24, 1998. Further visits to the station for replacing, adding, repairing and maintaining instruments were made on November 25, 1998; December 17, 1998; January 20, 1999; March 13, 1999; from May 24 to June 1, 1999; from July 15 to July 17, 1999; from November 25 to November 27, 1999; on January 15, 2000 and from May 3 to May 5, 2000. Most of the station was disassembled from August 8 to August 10, 2000 (see Section 4.2 for more details). In the field campaign from August 24 to August 26, 2000, a smaller station was re-installed measuring the firn temperatures and snow height, only. Due to extremely heavy accumulation in autumn 2000, the station was completely buried

and data communication broke down on October 15, 2000. It was finally found under 3 m of snow and disassembled on May 19, 2001.
Density measurements at Seserjoch were carried out on September 22, 1998 (1 m depth), on May 30, 1999 (3.3 m depth) and on May 4–5, 2000 (10 m depth) (Section 6.4.2).
Radar measurements for bedrock detection and mapping of internal layers of the glacier could be performed with the instrument of the *Alfred-Wegener-Institut für Polar- und Meeresforschung (AWI), Bremerhaven* at Colle Gnifetti and at Seserjoch during the field campaign from August 24 to August 26, 2000 (unpublished data from AWI, Bremerhaven).

4 Energy Balance at Seserjoch, Monte Rosa

4.1 Theoretical Background

In the present section, basic thoughts and concepts on energy-exchange processes between the Earth's surface and the atmosphere will be discussed. The energy-conservation law is adapted in form of relevant fluxes with respect to snow and firn surfaces. Signs are taken positive when these fluxes are heat sources for the snow and firn surface.
The energy balance at a (cold) snow/firn surface can be expressed with

$$R + H + LE + S + M = 0 \ , \tag{4.1}$$

where $R =$ net radiation, $H =$ sensible heat flux, $LE =$ latent heat flux (evaporation, condensation and sublimation), $S =$ subsurface heat flux and $M =$ heat flux due to surface melt or re-freezing of water.
In general, the net radiation R (see Section 4.1.1) and the turbulent heat fluxes H and LE (see Section 4.1.2) will be the major contributions to the surface energy balance. The subsurface heat flux is strongly dependent on the near-subsurface temperature gradient, but generally rather small (see Sections 4.1.3 and 4.4.3). At Seserjoch, surface melt only occurs on relatively rare occasions during summer daytime, but can be a rather important short-term energy sink (see Sections 4.1.4 and 4.4.4).
When looking at the energy balance over snow and firn, one has to bear in mind that surface geometry and surface properties are not constant in time. Strictly speaking one has to deal with a free surface, which constantly evolves in time due to mass-accumulation and -erosion processes. If surface accumulation and submerging velocity are in balance, the absolute position of the surface will not change on a longer term. The surface properties, however, (eg albedo, surface roughness etc.) can show a more or less seasonal pattern which influences the corresponding energy fluxes (see Section 4.3 and 4.4).

4.1.1 Radiative Fluxes

Introduction

Solar radiation is the only energy input to the atmosphere/Earth's surface and drives atmospheric and ocean circulation. The radiation in the atmosphere can be subdivided into *shortwave radiation* covering the wavelength range from 0.2–4 μm and into *longwave radiation* from 4–100 μm. The radiation balance or *net radiation* R at the Earth's surface can be written as

$$R = G\,(1 - \alpha) + L\!\downarrow - L\!\uparrow \ , \tag{4.2}$$

where $G =$ global radiation or total shortwave incoming radiation, $\alpha =$ surface albedo, $L\!\downarrow =$ longwave incoming radiation and $L\!\uparrow =$ longwave outgoing radiation.

Shortwave Radiation

The *global radiation* G is the shortwave radiation from the atmosphere which reaches the surface. The global radiation can further be subdivided into *direct* and

diffuse radiation. The direct radiation is the fraction of the top of the atmosphere radiation which directly reaches the surface. Under clear-sky conditions, the direct radiation dominates by far the total shortwave incoming radiation.
An important part of the top of the atmosphere radiation is scattered, reflected and absorbed in the atmosphere. A part of the scattered and reflected radiation reaches the surface as diffuse radiation. There are two different mechanisms for atmospheric scattering:

- *Rayleigh scattering* which is due to scattering by molecules and
- *Mie scattering* which is due to scattering by aerosols.

Rayleigh and Mie scattering typically account for 10–15 % of the diffuse radiation. The main part of the diffuse radiation, however, is due to the reflection of shortwave radiation at clouds (eg water droplets) in all directions and for all wavelengths. Under cloudy conditions, the diffuse radiation can constitute the main part of the global radiation.
The shortwave radiation balance at the surface is strongly dependent on the shortwave outgoing radiation. Over snow surfaces, a large part of the shortwave incoming radiation is reflected. The ratio of the integrated reflected shortwave spectrum to the integrated shortwave incoming spectrum is called *albedo* α (Male, 1980):

$$\alpha = \frac{\int \Re_\lambda I(\lambda)\, d\lambda}{\int I(\lambda)\, d\lambda}\,, \tag{4.3}$$

where $\Re_\lambda$ = reflectance of snow and $I(\lambda)$ = monochromatic irradiance at wavelength λ. The integration limits are taken as the lower and upper boundary of the incident shortwave radiation (0.2–4 μm). The albedo of snow surfaces is a function of grain size and shape of snow crystals, surface impurities, zenith angle, wavelength of the incident spectrum, cloud cover and age of the snow cover (Warren, 1982). An aging of the snow cover is associated with an increase in crystal size and in concentration of impurities. At the Seserjoch site, short-term changes of grain size and shape of snow crystals and a temporary input of impurities (eg Saharan dust fall) can occur. On larger time-scales, however, these effects can be neglected as regular snow fall even during summertime and snowdrift guarantee a steadily high surface albedo above 70 %. At wind-exposed saddles and crests, the albedo can be reduced due to bare firn- and ice exposure during autumn and winter. When looking at a daily mean albedo, effects such as grain size and shape of snow crystals and zenith angle can be neglected. The visible spectrum of the shortwave radiation shows a maximum albedo and a decreasing albedo can be observed for the near infrared. Thus, cloud cover has also an influence on the albedo as the diffuse radiation shows a spectrum which is shifted to the blue (filtering of near infrared). In complex topography, reflections from side walls can also contribute to the total shortwave incoming radiation. Typical results of measured albedos are given in Section 4.3.6.

Longwave Radiation

The longwave radiation which is emitted by the Earth's atmosphere is termed *longwave incoming radiation* $L\downarrow$. It comprises wavelengths above 4 μm and shows a peak intensity at about 10 μm. Typical atmospheric emitters are water vapour,

carbon dioxide and other trace gases. The atmospheric longwave radiation is responsible for the greenhouse effect. The emission of longwave radiation by the atmosphere can be simplified as

$$L\downarrow = \epsilon_a \sigma T_a^4 \,, \tag{4.4}$$

where ϵ_a = longwave atmospheric emissivity, σ = Stefan-Boltzmann constant, T_a = air temperature [K]. Under clear-sky conditions, the longwave atmospheric radiation is also a function of the zenith angle. The influence of the zenith angle is small, however, so that it can be neglected (Plüss, 1997). In complex terrain, steep side walls can also contribute to the total longwave incoming radiation due to longwave emission of snow surfaces. The reflection of longwave radiation over snow surfaces can be neglected as snow perfectly absorbs the longwave spectrum.
The longwave radiation which is emitted and reflected is called *longwave outgoing radiation* $L\uparrow$ and can be written as follows:

$$L\uparrow = -\sigma T_s^4 \,, \tag{4.5}$$

where T_s = surface temperature [K]. The longwave emissivity ϵ_s of snow is very high and in the range between 0.985 and 0.990 (Dozier and Warren, 1982). Thus, snow can be considered a more or less perfect black-body radiator. As snow surface temperatures do never exceed 0 °C, the maximum longwave outgoing radiation is 315.7 W/m^2. Very low temperatures (down to -40 °C) can be observed over snow surfaces in such a way that a longwave outgoing radiation on the order of only 167.6 W/m^2 can occur. Observed longwave fluxes and corresponding surface temperatures from the Seserjoch site are discussed in Section 4.3.

4.1.2 Turbulent Fluxes

Introduction

The physical state of the atmosphere can be described in space (x, y, z) and time (t) by the variables *wind velocity* $\vec{v}$, *air density* ρ_a, *air temperature* T_a and *specific humidity* q. When the energy exchange between the atmosphere and the surface is of interest, it is sufficient to look only at the lowest part of the atmosphere, which is directly influenced by the presence of the Earth's surface. This atmospheric layer is called *atmospheric boundary layer ABL*. The ABL reacts on surface changes within a time-scale of an hour to a day and fluxes of momentum, heat and matter are carried by *turbulent motions*. The extent of the ABL varies from a few hundred meters up to a few kilometers.
The lowest part of the ABL is called *surface layer SL* and is defined as the part of the ABL right above the surface, where the turbulent fluxes and stresses vary less than 10 % of their magnitude at the surface (Stull, 1988). Therefore, this layer is also called *constant flux layer*.
In the lowest few centimeters of the SL, molecular diffusion often dominates turbulent transport and a laminar flow (no convection) and very high temperature gradients can often be observed (Garrat, 1992). This layer is termed *interfacial layer* or *laminar boundary layer*. Within this layer, molecular flux and turbulent flux have about the same order of magnitude. Above it, turbulent transport is by far dominating molecular diffusion. The turbulent fluxes measured in the SL give a

good approximation of the effective flux over the surface and the molecular contribution can be neglected. The description of the atmosphere within the SL can be simplified by the following assumptions:

- **Stationarity**
  The statistical properties of turbulence do not change in time. As turbulence is able to respond quickly to changing flow conditions, and when looking at short time intervals only, the SL can be considered 'quasi steady'.

- **Homogeneity**
  The statistical properties are independent of the position in space. Whereas the vertical fluxes are never homogeneous within the ABL, the horizontal fluxes are homogeneous to a good approximation. For imhomogeneous surfaces and in complex topography, however, the horizontal scale becomes important. As a rule of thumb, the surface should be uniform for an upwind distance larger than 100 times the height of the uppermost measurement level for profile measurements. This distance is also called *fetch area* (Schmid, 1997).

In the SL, two turbulent heat fluxes can be distinguished:

- **the sensible heat flux** H which results from the difference in enthalpy content between the air and the surface and turbulent vertical air exchange and

- **the latent heat flux** LE which results from the difference in water-vapour concentration between the air and the surface and turbulent vertical air exchange.

Based on the assumption of constant fluxes with height and horizontally homogeneous conditions, the sensible heat flux H and the latent heat flux LE can be described as a gradient-flux relationship:

$$H = \rho_a c_a K_H \frac{\partial \overline{\theta}}{\partial z} , \tag{4.6}$$

$$LE = \rho_a L_v K_{LE} \frac{\partial \overline{q}}{\partial z} , \tag{4.7}$$

where $\rho_a =$ air density, $c_a =$ specific heat capacity of air at constant pressure, $K_H =$ eddy diffusivity for heat, $\overline{\theta} =$ time-averaged potential temperature (the potential temperature is the air-pressure normalized air temperature), $z =$ height above the surface, $L_v =$ latent heat of vaporization, $K_{LE} =$ eddy diffusivity for water-vapour exchange and $\overline{q} =$ time-averaged specific humidity.
The atmosphere tends to reach a steady-state situation, ie to minimize the gradients of potential temperature and specific humidity. These gradients are most effectively reduced by turbulent vertical air exchange and/or buoyant effects. The eddy diffusivities K_H and K_{LE} specify the effectiveness of the transfer process and are functions of wind velocity, surface roughness and atmospheric stability. They are experimentally difficult to determine so that other concepts are chosen to measure turbulent fluxes (see below).
At snow and firn surfaces, the latent heat exchange is either due to a phase change from the liquid phase of water to the gaseous phase (evaporation) or vice versa

(condensation) or due to a change from the solid to the liquid phase (melt) or vice versa (re-freezing) (see below) or due to a change from the solid phase to the gaseous phase or vice versa (sublimation). If the snow surface is below freezing point, the heat of vaporization L_v has to be replaced by the heat of sublimation L_s, which is the total of L_v and the latent heat of fusion L_f. The calculation of the latent heat flux at the Seserjoch site is discussed in detail in Section 4.4.2.

Another important concept in boundary layer climatology is *atmospheric stability*. Basically, one has to distinguish between a *static* and a *dynamic* stability. The static stability is a measure of the capability for buoyant convection, whereas the dynamic stability also accounts for wind-shear effects (Stull, 1988). The air is statically stable when the air density decreases or potential temperature increases at height. This is typically the case when the surface is colder than the overlying air. A measure for atmospheric stability is the *gradient Richardson number Ri*, which compares the buoyant production- or consumption term with the wind-shear production term:

$$Ri = \frac{\frac{g}{\overline{\theta}} \frac{\partial \overline{\theta}}{\partial z}}{\left(\frac{\partial \overline{u}}{\partial z}\right)^2} , \tag{4.8}$$

where g = acceleration due to gravity, $\overline{\theta}$ = mean potential temperature, $\frac{\partial \overline{\theta}}{\partial z}$ = vertical gradient of mean potential temperature and $\frac{\partial \overline{u}}{\partial z}$ = vertical gradient of horizontal wind velocity. Under stable conditions, Ri becomes positive and under unstable conditions negative. There is a critical Richardson number in the range between 0.21 and 0.25. Below this range, turbulence is maintained whereas above it, the flow undergoes a transition from turbulent flow to laminar flow.

Another widely used stability parameter is the *Obukhov length L* defined as (Monin and Obukhov, 1956):

$$L = -\frac{u_*^3 \overline{\theta}}{gk\overline{w'\theta'}} , \tag{4.9}$$

where u_* = scaling parameter for wind velocity or friction velocity, k = von Kármán constant, w' = fluctuating vertical wind velocity and θ' = fluctuating potential temperature. Again, L is positive when the atmosphere is stably stratified and negative for an unstable stratification. L is the height above the surface where the energy production due to wind shear is balanced by the energy consumption due to buoyancy forces (Obukhov, 1946).

Using *similarity theory* for expressing relationships between different quantities and to reveal underlying scaling laws, Monin and Obukhov (1956) proposed that the structure of turbulence within the SL can be expressed with a few key parameters. If the coordinate system is aligned with the mean wind, they can be written as follows:

$$u_* = \sqrt{-\left(\overline{u'w'}\right)} = \sqrt{\frac{\tau}{\rho_a}} , \tag{4.10}$$

$$\theta_* = \frac{-\left(\overline{w'\theta'}\right)}{u_*} , \tag{4.11}$$

$$q_* = \frac{-\left(\overline{w'q'}\right)}{u_*} , \tag{4.12}$$

where $u_* =$ scaling parameter for wind velocity or friction velocity, $u' =$ fluctuating horizontal wind velocity, $w' =$ fluctuating vertical wind velocity, $\tau =$ shear stress, $\rho_a =$ air density, $\theta_* =$ scaling parameter for potential temperature, $\theta' =$ fluctuating potential temperature, $q_* =$ scaling parameter for humidity and $q' =$ fluctuating specific humidity. Two additional scaling parameters are the height z above ground and the buoyancy parameter $\frac{g}{\theta}$. The Obukhov length scale is the only length scale which can be derived from these parameters using dimensional analysis. According to Monin and Obukhov (1956), various atmospheric parameters such as gradients, variances and covariances become universal functions of the non-dimensional height $\frac{z}{L}$, if normalized by appropriate powers of the scaling variables. Thus, with the help of the above defined scaling variables, the gradient form of the wind profile and the non-dimensional gradients of temperature and humidity can be written as

$$\frac{d\bar{u}}{dz}\frac{kz}{u_*} = \phi_m\left(\frac{z}{L}\right) , \tag{4.13}$$

$$\frac{d\bar{\theta}}{dz}\frac{kz}{\theta_*} = \phi_h\left(\frac{z}{L}\right) , \tag{4.14}$$

$$\frac{d\bar{q}}{dz}\frac{kz}{q_*} = \phi_q\left(\frac{z}{L}\right) , \tag{4.15}$$

where ϕ_m, ϕ_h and ϕ_q denote non-dimensional stability functions of $\frac{z}{L}$. For neutral conditions, $\frac{z}{L}$ is 0 and $\phi_m\left(\frac{z}{L}\right)$is 1. Under stable conditions, $\phi_m\left(\frac{z}{L}\right)$ is > 1.
The stability parameters Ri and L are related in the following way:

$$Ri = \frac{z}{L}\frac{\phi_h}{\phi_m^2} . \tag{4.16}$$

The stability functions ϕ_m, ϕ_h and ϕ_q have to be determined experimentally, eg Högström (1988):

$$\phi_m = 1 + 6\frac{z}{L} , \tag{4.17}$$

$$\phi_h = \phi_q = 0.95 + 7.8\frac{z}{L} . \tag{4.18}$$

These are the functions for stable stratification. A linear form of the functions seems to be valid up to a $\frac{z}{L}$ value of about 0.5.

Bowen Ratio

A common way to calculate turbulent fluxes, without applying atmospheric stability criteria, is a method first presented by Bowen (1926). The *Bowen ratio* is defined as

$$\beta = \frac{H}{LE} = \frac{K_H}{K_{LE}}\frac{c_a \Delta T}{L_v \Delta q} , \tag{4.19}$$

where $\beta =$ Bowen ratio, $H =$ sensible heat flux, $LE =$ latent heat flux, $K_H =$ eddy diffusivity for heat exchange, $K_{LE} =$ eddy diffusivity for water-vapour exchange, $c_a =$ specific heat capacity of air at constant pressure, $\Delta T =$ temperature gradient, $\Delta q =$ humidity gradient and $L_v =$ latent heat of vaporization.
The turbulent fluxes are then calculated using the following equations:

$$H = \frac{-\beta\,(R+S)}{1+\beta} , \tag{4.20}$$

$$LE = \frac{-(R+S)}{1+\beta} \ , \tag{4.21}$$

where R = net radiation and S = subsurface heat flux. The Bowen-ratio method requires two levels of temperature and humidity measurements and accurate measurements of net radiation and subsurface heat flux. Ohmura (1982) proposed the following criteria to evaluate the usefulness of the turbulent fluxes calculated by the Bowen-ratio method, ie to exclude data from analysis due to physical inconsistencies in the flux-/gradient definition and resolution limits of the instruments:

- As the errors of the net-radiation and subsurface heat measurement are accumulated in the calculation of the turbulent fluxes, the radiation-, subsurface heat, temperature- and humidity measurements require a certain standard of accuracy.
- Wrong signs in calculating the turbulent fluxes must be avoided in that the following two conditions must be valid:
  if $R+S>0$ then $L_v\Delta q + (K_H/K_{LE})c_a\Delta T < 0$ and
  if $R+S<0$ then $L_v\Delta q + (K_H/K_{LE})c_a\Delta T > 0$.
- Although the signs are correct, the magnitude of the turbulent fluxes can become extremely high when the Bowen ratio approaches -1. Such data have to be excluded from evaluation.

Eddy-Correlation Method

The *eddy-correlation method* is based on an isolation of the large-scale variations from the (short-term) turbulent fluctuations in a time series of a variable b. Therefore, the variable b is split into a mean ($\overline{b}$) and a deviation from the mean (b') (*Reynolds decomposition*):

$$b = \overline{b} + b' \ . \tag{4.22}$$

The sensible and latent heat fluxes can directly be calculated from the eddy flux relationships (eg Stull, 1988):

$$H = -\rho_a c_a \overline{w'T'} \ , \tag{4.23}$$

$$LE = -L_v \rho_a \overline{w'q'} \ , \tag{4.24}$$

where ρ_a = air density, w' = fluctuating part of vertical wind velocity ($w' = w - \overline{w}$), T' = fluctuating part of air temperature ($T' = T - \overline{T}$) and q' = fluctuating part of humidity ($q' = q - \overline{q}$). These calculations require high-frequency and high-quality measurements of air temperature, wind velocity and humidity. Studies over snow and ice using eddy correlation measurements have been carried out by eg Ohmura et al. (1994) and Forrer (1999) over the Greenland Ice Sheet and by Plüss (1997) over an Alpine snow cover.

Profile Method

As direct measurements of turbulent fluxes are quite a difficult task, they are often derived from measurements of wind velocity, temperature and humidity at different levels above the surface. The *profile method* or *gradient-flux relationship*

assumes that the gradients of mean wind velocity, mean (potential) air temperature and mean humidity are proportional to the corresponding shear stress, sensible and latent heat flux. The profile method is only valid in the atmospheric surface layer and over homogeneous surfaces. Based on the formulations of the non-dimensional gradients of wind, temperature and humidity (Equations 4.13–4.15) and the stability functions (Equations 4.17 and 4.18), the fluxes are calculated with

$$H = \rho_a c_a u_* \theta_* \ , \tag{4.25}$$

$$LE = \rho_a L_v u_* q_* \ , \tag{4.26}$$

where u_* = scaling parameter for wind velocity (friction velocity), θ_* = scaling parameter for (potential) temperature and q_* = scaling parameter for humidity.

Bulk Method

The *bulk method* is an approximation for the turbulent heat fluxes from only one level of wind-velocity, temperature- and humidity measurements. A constant gradient of these quantities is assumed between the measurement level and the surface. Thus, the surface values have to be assumed or measured. The surface temperature and humidity are well known for a snow surface at melting conditions. The surface temperature is 0 °C and the vapour density is at saturation. For non-melting conditions, these quantities have to be measured or parameterized.
When using the bulk approach, the local gradients of wind velocity, air temperature and humidity are replaced by the corresponding finite differences between the measurement level and the surface. Based on these assumptions, a *Bulk Richardson Number* can be defined:

$$Ri_b = \frac{g \frac{\Delta \overline{T}}{\Delta z}}{\overline{T} \left(\frac{\Delta \overline{u}}{\Delta z} \right)^2} \ . \tag{4.27}$$

The Bulk Richardson Number can be related to the stability functions for momentum (ϕ_m), heat (ϕ_h) and water vapour (ϕ_q) in the following way (Oke, 1987):

$$Ri_b \text{ positive (stable conditions):} \quad (\phi_m \phi_{h,q})^{-1} = (1 - 5Ri_b)^2 \tag{4.28}$$

$$Ri_b \text{ negative (unstable conditions):} \quad (\phi_m \phi_{h,q})^{-1} = (1 - 16Ri_b)^{0.75} \ . \tag{4.29}$$

The turbulent fluxes for heat and water vapour can then be calculated as follows (Oke, 1987):

$$H = \rho_a c_a k^2 z_u z_t \left(\frac{\Delta \overline{u} \Delta \overline{T}}{z^2} \right) (\phi_m \phi_h)^{-1} \ , \tag{4.30}$$

$$LE = \rho_a L_v k^2 z_u z_q \left(\frac{\Delta \overline{u} \Delta \overline{q}}{z^2} \right) (\phi_m \phi_q)^{-1} \ , \tag{4.31}$$

where $z_{u,t,q}$ are the log mean heights defined as

$$z_{u,t,q} = \frac{z - z_{0u,t,q}}{ln \left(\frac{z}{z_{0u,t,q}} \right)} \ . \tag{4.32}$$

The $z_{0u,t,q}$ denote the surface roughness lengths for wind, temperature and humidity. The roughness length is the height above the surface, where these quantities assume the surface value and is related to the general roughness of the surface.

4.1.3 Subsurface- or Ground Heat Flux

The energy- and mass exchange within the snow and firn cover is discussed in detail in Section 6. The different mass- and energy-exchange processes lead to a characteristic englacial temperature profile. As long as the snow and firn cover is not at uniform temperature, a temperature gradient occurs and the subsurface- or ground heat flux S can be written as

$$S = K_i \frac{\partial T}{\partial z} \tag{4.33}$$

where K_i = thermal conductivity of snow or firn, $\frac{\partial T}{\partial z}$ = observed temperature gradient in snow and firn, T = snow or firn temperature and z = depth below the surface. A positive temperature gradient at depth (increasing temperature at depth) leads to a positive subsurface heat flux and vice versa as heat fluxes towards the surface shall be positive. The thermal conductivity is strongly dependent on snow and firn density. It is found between 0.04 for very light snow and 2.21 W/(m·K) for ice at 0 °C. Although the near-subsurface temperature gradient can be quite high due to radiative cooling at night, it will seldom exceed 20 °C/m. This would lead to a subsurface heat flux of approximately 20 W/m^2 for firn. The observed subsurface heat fluxes were generally much smaller (see Section 4.4.3) as a near-surface temperature gradient of more than 20 °C/m could never be observed.
Snow and ice both allow some transmittance of radiation, which means that the incident radiation at the surface can be transmitted, reflected or absorbed in the snow cover. Reflection and absorption of radiation are largest in the uppermost centimeters of the snow cover. Absorption can lead to an important warming in the immediate surface layer. This warming is normally compensated by the longwave outgoing radiation at the surface (Gubler, 1996). Ohmura (1984) investigated the transmission of net radiation on the lower side of a dry seasonal snow cover. As the net radiation within a snow cover could only be measured with an array of buried instruments, it is normally determined indirectly using

$$R_s\downarrow - R_s\uparrow = \rho_s \cdot c_i \int_0^h \frac{dT}{dt} \cdot dz + S_h - S_0 \ , \tag{4.34}$$

where $R_s\downarrow$ = downward radiation flux on the lower side of the snow surface, $R_s\uparrow$ = upward radiation flux on the lower side of the snow surface, ρ_s = snow density, c_i = specific heat capacity of ice, h = depth range considered, T = snow temperature, t = time, z = depth, S_h = conductive heat flux at the bottom of the depth range considered and S_0 = conductive heat flux at the top of the snow cover. Ohmura (1984) found the transmission of net radiation on the lower side of the snow cover to be on the order of the conductive heat flux at the bottom of the snow cover, and to be one order of magnitude larger than the conductive heat flux at the top of the snow cover for the period from May, 3 to June, 6. The conditions for the Seserjoch site are discussed in Section 4.4.3.

4.1.4 Melt and Re-freezing

At the surface, the energy consumed by surface melt and released by re-freezing of liquid water, respectively can be written as

$$M = L_f \vec{m}_w \ , \tag{4.35}$$

where L_f = latent heat of fusion and $\dot{m}_w$ = mass flux of water to be melted or re-frozen per unit area. The mass flux is negative during a melt event (mass loss at the surface due to percolation of melt water) and positive during a re-freezing event. Thus, M becomes negative for a melt event (energy is consumed at the surface for melting) and positive for a re-freezing event (energy is released to the surface).
As already stated, surface melt at the Seserjoch site is restricted to a few events during summer, when the surface temperature reaches 0 °C during the day. A single event can turn over quite an important amount of energy on a daily time-scale (see Section 4.4.4). On a larger time-scale, the absolute energy input to the snow- and firn cover due to frequent melt events with corresponding re-freezing of meltwater in deeper snow- and firn layers can be important and have a major influence on the prevailing mean firn temperature (see Sections 4.4.4 and 6.1). Especially at sites with a high radiation income and/or generally low wind velocities, melt-layer formation becomes frequent and can change the temperature regime of the snow and firn, considerably (Beck et al., 1988).
Re-freezing of liquid water at the surface can occur by re-freezing of melt water or by ad-freezing of undercooled water droplets in clouds or fog (*hoar frost* or *rime accretion*) (see Section 4.4.4 for observed fluxes).

4.2 Energy-Balance Station

4.2.1 General Setting

From September 21 to September 24, 1998, a complete energy-balance station was installed at Seserjoch using two masts of 8 and 4 m height. The position of the small mast was surveyed with the help of digital photogrammetry using aerial photographs from August, 2000 and determined as $x = 633727$, $y = 85785$ and $z = 4292$ in Swiss Coordinates (personal communication from H. Bösch, 2001). Although no earlier (precise) survey exists, it is assumed that the change in position of the masts is less than 1 m over the whole observation period.
3 levels of air-temperature (T), humidity- (H) and wind-speed (WS) measurements were installed at initial heights of 0.9, 2.7 and 6 m above the surface. Additionally, shortwave radiation, net radiation, surface temperature, wind direction and snow height were registered by an albedometer (AM), a net radiometer (NR), an infrared thermometer (IR), a potentiometer (WD) and a sonic ranging sensor (SH), respectively. Two thermistor chains (TS) were lowered into the glacier to measure firn- and ice temperatures. A 4 m chain with 15 sensors at an interval of 0.25 m measured the near-surface short-term temperature variations, whereas a 30 m chain including 30 sensors at a 1 m interval recorded the deep long-term temperature evolution. The data were stored on two seperate data loggers: one for the firn-temperature and one for the climate data. The climate data logger was intended to have a direct mobile phone communication for downloading data and for remote control of the instruments. The data-logging system, additional electronics and cabling were housed in a massive metallic box (CD).
On November 25, 1998, the mobile phone communication was replaced by a radio system due to communication problems. Since then, the climate data could directly be retrieved from Zurich (Figure 4.1). The climate data were recorded every 10 minutes, whereas the resistances from the firn-temperature measurements were stored

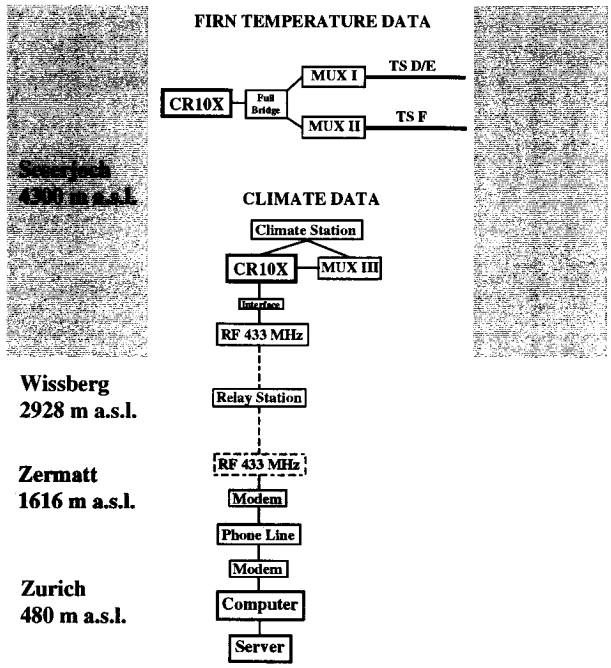

Figure 4.1: Scheme of the data-communication system for the energy-balance and firn-temperature measurements at Seserjoch (Monte Rosa). CR10X denotes a data logger, MUX a multiplexer and TS a thermistor chain.

every 30 minutes (4 m chain) or every two hours (30 m chain). On December 17, 1998, the energy-balance station was checked again. Due to regular battery (BAT) failures during night-time in January, 1999, measurements could only be made during the day when the battery was powered by the 50 W solar panel (SP). At the end of the month, the power supply was completely interrupted because of a blocked fan at the lowest air-temperature sensor. As a consequence of extremly bad weather conditions in February, the power supply could only be re-established on March 13, 1999. Due to a non-logarithmic wind profile (decreasing wind velocity at the 6 m level), the 3 levels for measuring turbulent fluxes were rearranged and set at 4, 2 and 1 m height. No wind velocities could be measured between March and May, 1999 as problems with a pulse-extension device occurred.
A fourth level of air-temperature, humidity- and wind-speed measurements was installed between May 24 and June 1, 1999 and a sonic anemometer run for some days for a direct measurement of the sensible heat flux. Additionally, two *precision infrared radiometers (PIRs)* for measuring longwave incoming and outgoing radiation were installed to replace the rather unprecise net-radiation instrument, which was difficult to handle. Self-heating problems of net radiometers under conditions of high global radiation, with a corresponding underestimation of the measured net radiation, are reported by eg Konzelmann and Ohmura (1995). Figure 4.2 shows the setup of the station after the revisions in May, 1999. Retrieving data by the radio-communication system was very reliable and made the revisions of the station most effective. Further revisions were made from July 15 to July 17, 1999; from November 25 to November 27, 1999; on January 15, 2000 and from May 3 to May 5, 2000. The main problems were caused by an occasional failure of the wind-velocity

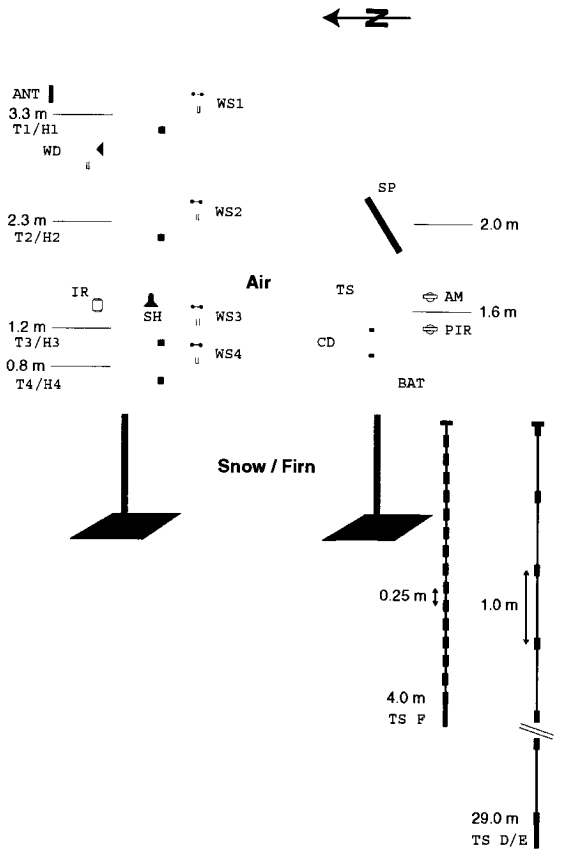

Figure 4.2: Instrumentation of the energy-balance station at Seserjoch (Monte Rosa) after the revisions in May, 1999. For abbreviations, see text. In the following, 'level 1' is referred to the uppermost, 'level 4' to the lowermost observing level.

sensors. The other instruments mostly worked in a reliable way. Heavy accumulation in April, 2000 made the maintenance of the station increasingly difficult, so that most of it was disassembled from August 8 to August 10, 2000. In a field campaign from August 24 to August 26, 2000, a smaller station was re-installed measuring the firn temperatures and snow height only. Due to extremely heavy accumulation in autumn 2000, the station was completely buried and data communication broke down on October 15, 2000. The station was finally found under 3 m of snow and disassembled on May 19, 2001.

4.2.2 Instruments and Calibration

Radiation Measurements

For the radiation measurements, a net radiometer, an albedometer (one up- and one down-facing pyranometer), two precision infrared radiometers or pyrgeometers (up- and down-facing) and an infrared thermometer were used. The characteristics of the sensors are summarized in Table 4.1. The measurement range and accuracy of the instruments are given according to the technical specifications of the manu-

Table 4.1: Characteristics of the radiation instruments. The range and accuracy are referred to the technical specifications of the manufacturer.

Instrument	Type	Quantity	Range	Resolution	Accuracy
Net Radiometer	Swissteco S1	Net Radiation	>0.3 μm	0.06 W/m^2	better than $\pm$10%
Albedometer (Pyranometer)	Kipp & Zonen CM 7B	Shortwave Radiation	0.3-2.8 μm	0.25 W/m^2	$\pm$26 W/m^2 at 500 W/m^2
Precision Infrared Radiometer	Eppley PIR	Longwave Radiation	3.5-50 μm	0.09 W/m^2	$\pm$6 W/m^2 at 200 W/m^2
Infrared Thermometer	IRt/c.5	Surface Temperature	-35 - 10 °C	0.017 °C	$\pm$1.5 °C at -10 °C

facturer. Principally, one has to distinguish between the accuracy and the resolution of the sensor. The *resolution* of the sensor is given by the sensitivity of the device under calibration conditions as calibrated by the manufacturer and by the measurement range and resolution of the data logger.
The *accuracy* depends on the one hand on pure instrumental characteristics (eg resolution of the instrument, linearity of the signal, stability in time, azimuth dependency, temperature dependency etc.), and on the other hand on ambient influences which are not directly linked with the instrument itself (eg atmospheric conditions, formation of surface dew or hoar on the instrument etc.). In the above table, ambient effects are not comprised in the given accuracies.
No extra calibration was performed for the net radiometer and the initial sensitivities were taken to transform the measured voltages into irradiances. The albedometer and the infrared thermometer were re-calibrated at the *World Radiation Center (WRC), Davos* in September, 2000 by comparing them to a corresponding reference instrument (albedometer) or by a calibration in a black-body radiator (infrared thermometer). The initial sensitivities determined by *Kipp & Zonen* and the WRC-sensitivities agreed well. For the transformation of the measured voltages into irradiances, the WRC-calibration was used. Due to technical problems during the calibration procedure, the calibration of the infrared thermometer performed by the WRC could not be applied. Instead, the initial calibration of the instrument performed by *ALPUG (Alpine Umwelt und Gefahren)* was taken. The voltages measured by the two Precision Infrared Radiometers were transformed into irradiances using the *Eppley Laboratory* calibration in a black-body radiator. Further corrections had to be applied to compensate for the self-emissivity of the body and the dome of the instrument (see Section 4.3.7).

Measurements of Turbulent Fluxes

Table 4.2 gives a compilation of the instruments which were used for the measurements of the turbulent fluxes. Again, the measurement range and the accuracy are based on the technical specifications of the manufacturer. The resolution depends

Table 4.2: Characteristics of the instruments for turbulent fluxes. The range and accuracy are referred to the technical specifications of the manufacturer.

Instrument	Type	Quantity	Range	Resolution	Accuracy
Temperature Sensor	Vaisala HMP45DSP	Air Temperature	-40 - 60 °C	0.01 °C	±0.2 °C at 20 °C
Humidity Sensor	Vaisala HMP45DSP	Relative Humidity	0.8 - 100 %	0.1 %	±2 % at 0 - 90 % ±3 % at 90 - 100 %
Cup Anemometer	Aanderaa 2740	Wind Velocity	0 - 79 m/s	0.04 m/s	±2 %
Wind Direction Sensor	Aanderaa 3590	Wind Direction	0 - 360 °	1.3 °	better than ±5 °
Sonic Anemometer	Gill Solent 1012R2A	Wind Speed Components u, v, w	0 - 60 m/s	0.01 m/s	±1 % at 0 - 30 m/s
		Speed of Sound		0.01 m/s	±0.5 % at 0 - 30 m/s of wind speed

on the sensitivity of the sensor, the selected measurement range of the data logger and – in case of the cup anemometers – on the averaging interval.
The *Vaisala* temperature sensors were calibrated in a cold bath (circulation chiller) of the type *Huber CC245* with a 22 l (internal) bath and a warranted bath stability of ±0.02 °C. The bath temperature was controlled by four calibrated temperature sensors of the type *Therm 2284-8*. The system was calibrated at the *Swiss Federal Office of Metrology* in 1996. The absolute accuracy was certificated to ±0.03 °C in the range between 0 and -10 °C and to ±0.04 °C between -12.5 and -20 °C (see Section 5.2.2 for more details). The Vaisala sensors (Pt-100 probes) were calibrated with exactly the same instrumental setting as in the field at (chiller) temperatures of -30, -25, -20, -15, -10, -5, 0, +5 and +10 °C. The calibration measurements were made for time periods of typically half an hour after perfect thermal adjustment of the sensors to the bath temperature. For data analysis, appropriate time windows with high thermal stability were chosen. The sensors showed a good linear behaviour with (bath) temperature. The bath stability was in the range of ±0.02–0.1 °C, but normally at about ±0.05 °C. The relative accuracy of one and the same sensor can be denoted with ±0.01 °C (see Table 4.2), whereas the absolute accuracy can be denoted with ±0.05 °C. The measured (air) temperatures of a sensor were converted into calibrated temperatures using a linear interpolation between the calibration points of the individual sensor. The fourth temperature sensor, which was mounted in May, 1999, never operated possibly due to a cabling problem.
No absolute calibration was performed for the Vaisala humidity sensors. A relative comparison between the sensors during a measuring campaign on the roof of the Institute showed a good accordance (mean differences of only 0.02–0.12 % were observed). The observed differences were considered when converting the measured values into processed ones.
No calibration was performed for the cup anemometers, the wind direction sensor

and the sonic anemometer (see Section 4.4.2). A pulse-extension device (*Campbell SDM-INT8 8-Channel Interval Timer*) was used to measure wind speeds higher than 24 m/s. For unknown reasons, the pulse extension sometimes failed for certain channels or even completely and only restarted after a short power interruption.

Other Measurements

The specifications of the other instruments used at the energy-balance site are summarized in Table 4.3. The sonic ranging sensor was very reliable and the given

Table 4.3: Characteristics of the snow-height and the snow-temperature instruments. The range, resolution and accuracy are referred to the technical specifications of the manufacturer.

Instrument	Type	Quantity	Range	Resolution	Accuracy
Sonic Ranging Sensor	Campbell SR50	Snow Height	0.5 - 10 m	0.1 mm	±1 cm or 0.4 % of distance to target
4 m Thermistor Chain	YSI 44006	Snow and Firn Temperature	-80 - 250 °C	1370 Ω/°C at 0 °C	±0.2 °C at 0 °C
Miniature Temperature Logger	UTL-1	Snow and Firn Temperature	-29 - 39 °C	0.27 °C	±0.1 °C

accuracy of the manufacturer sufficient for the purpose of snow-height measurements. A temperature-compensation formula was used to correct for the temperature effect on the speed of sound.
The technical specifications and the calibration procedure of the thermistor chains used for the snow- and firn-temperature measurements are described in Section 5.2.2. The 4 m thermistor chain was equipped with a set of 15 single thermistors at a 25 cm interval each. The chain was set in September, 1998 with the uppermost thermistor at 25 cm depth. It was intended to accurately measure the subsurface heat fluxes. With time, it was increasingly covered by snow and another way had to be found to measure the near-surface temperatures. Therefore, a rod with 5 miniature temperature loggers of the type *UTL-1* at a 50 cm interval each was installed in November, 1999. The uppermost logger was initially at a depth of 10 cm. The temperature loggers were removed in August, 2000. No additional calibration in a cold bath could be made for the loggers, but the results turned out to be sufficiently accurate.

4.3 Data Analysis and Results

Within this section, data processing and some selected results from the instrumental measurements at the energy-balance station are presented. All the data (high-resolution 10 minute values, daily mean values, monthly mean values or yearly means) are taken from the period between May, 1999 and April, 2000 where the best data were obtained.

4.3.1 Wind Direction

The wind direction at the Seserjoch saddle was strongly influenced by the saddle axis (WNW to ESE) and showed a very constant pattern over the observation period

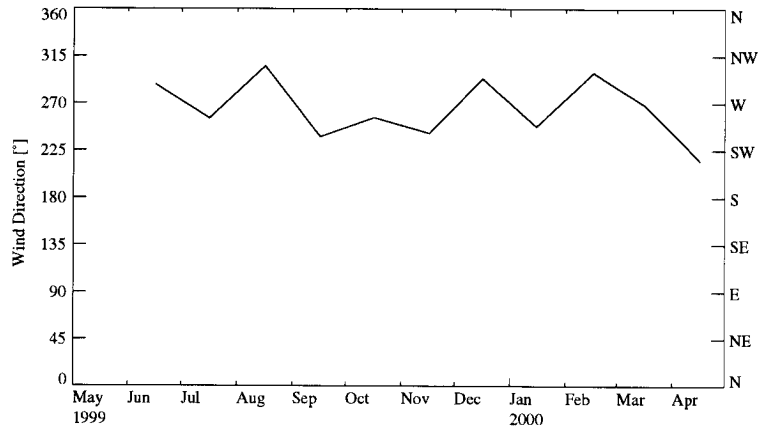

Figure 4.3: Wind direction (monthly mean values) at Seserjoch (Monte Rosa) from May, 1999 to April, 2000.

from May, 1999 to April, 2000 (see Figure 4.3) with a mean wind direction of 264° or approximately W.

4.3.2 Wind Velocity

The wind-velocity measurements turned out to be quite a delicate business due to mechanical (rotating cups) and electronical problems (see Section 4.2.2) so that frequent data gaps occurred. The mechanical problems were mainly due to hoar-frost

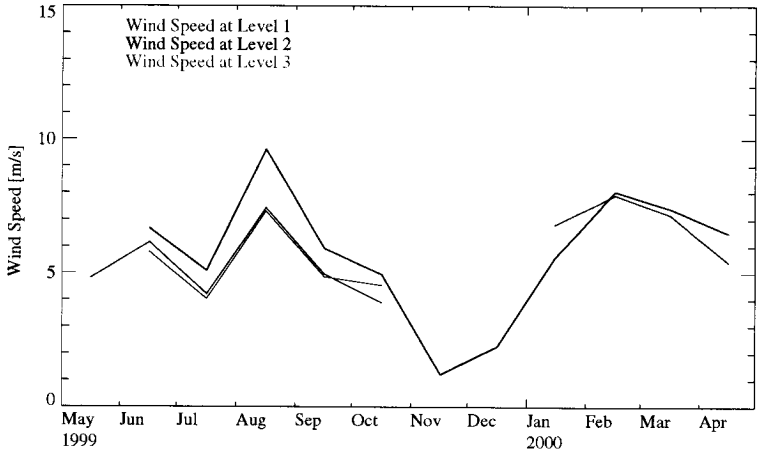

Figure 4.4: Wind speed (monthly mean values) at Seserjoch (Monte Rosa) from May, 1999 to April, 2000.

formation at the rotating cups which diminished or even stopped rotation completely. At times, single cups even broke off the instrument as a consequence of high mechanical stress. The electronical problems arose from a temporary breakdown of

the pulse-extension device which could only be restarted after power interruption. A look at the monthly mean wind speeds from May, 1999 to April, 2000 shows generally higher wind speeds from spring to summer and autumn (Figure 4.4). The monthly mean wind speeds are high and can be found between 1.2 and 9.6 m/s.

4.3.3 Air Temperature

The air-temperature measurement worked in a very reliable way. During the observation period, an uninterrupted ventilation could be maintained. For the calibration and instrumental problems, see Section 4.2.2. Figure 4.5 gives the monthly

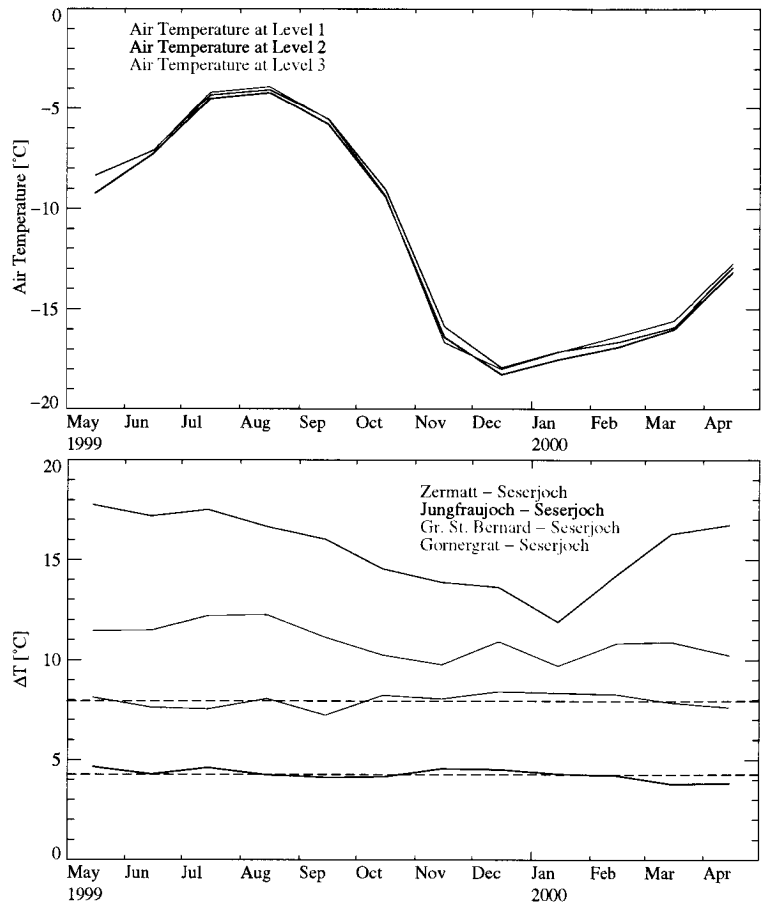

Figure 4.5: Air temperature (monthly mean values) at Seserjoch (Monte Rosa) from May, 1999 to April, 2000 (upper panel) and offset to surrounding meteorological stations (lower panel). The mean offsets (May, 1999 to April, 2000) to the Jungfraujoch and Gornergrat air temperatures are given with dashed lines. See Figure 3.1 for the locations of the weather stations.

mean air temperatures for the period from May, 1999 to April, 2000. The mean air temperature for the observation period (or mean annual air temperature) is -11.2 °C as measured at the uppermost and most undisturbed level. A comparison with air-temperature records (monthly mean values) from surrounding meteorological stations (see Figure 3.1 for locations) shows that the high-elevation sites of Jungfraujoch (3580 m a.s.l.) and Gornergrat (3135 m a.s.l.) have a very constant offset (Figure

4.5) resulting in an air-temperature gradient of -0.59 °C/100 m (Jungfraujoch) and of -0.68 °C/100 m (Gornergrat), respectively. The higher gradient in case of Gornergrat might point at drier and more continental conditions in the Monte Rosa area compared to the Jungfrau area. The offsets from the lower-situated stations of Grand St.-Bernard (2478 m a.s.l.) and Zermatt (1638 m a.s.l.) are not as constant. In case of the valley station of Zermatt, this is probably due to more frequent temperature inversions in the winter half-year; in case of Grand St. Bernard, there might be synoptic reasons as well.

4.3.4 Relative Humidity

The lowest level of relative humidity measurements overestimated the true relative humidity quite frequently as a consequence of a snow-filled entrance of the ventilation tube during snowfall- or snowdrift events. The uppermost two humidity

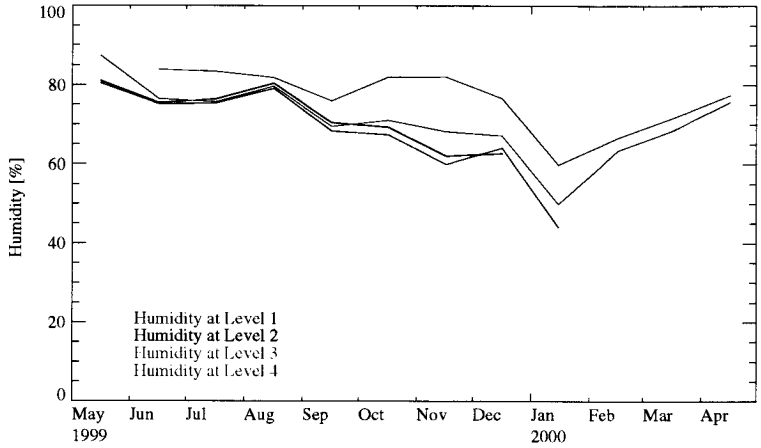

Figure 4.6: Relative humidity (monthly mean values) at Seserjoch (Monte Rosa) from May, 1999 to April, 2000.

sensors completely failed after December, 1999 for unknown reasons. The monthly mean humidities are presented in Figure 4.6. Higher humidities can generally be observed during the warm season.

4.3.5 Shortwave Radiation

The albedometer mostly measured in a reliable way. The instrument was checked for its horizontal position at each visit at the station (see Section 4.2.1) and never found in an oblique position. During the months with high radiation income, a very good agreement of both the shortwave incoming and outgoing radiation was found with an Italian meteorological station at Colle del Lys, 4250 m a.s.l. (see Section 3.3). Data inconsistencies occurred in November, 1999 and from January to April, 2000. At the end of November, the outgoing radiation was too small due to a strong surface, and hence, albedo change in the vicinity of the instrument as a consequence of maintenance work at the station. A typical clear-sky albedo of the Colle del Lys station for November was taken and the outgoing radiation recalculated. In January and February, both the shortwave incoming and outgoing

radiation showed some problems under clear-sky conditions for unknown reasons. Unplausible data were consequently replaced by the Colle del Lys data for time periods without topographic shade effects at Seserjoch. In March and April, the incoming radiation of Seserjoch and Colle del Lys showed a very good agreement again, whereas the observed outgoing radiation at Seserjoch was too small under clear-sky conditions. The downfacing pyranometer was very close to the surface at that time and errors may have occurred due to shade effects of the instrument within its own field of view. The outgoing radiation at Seserjoch was recalculated

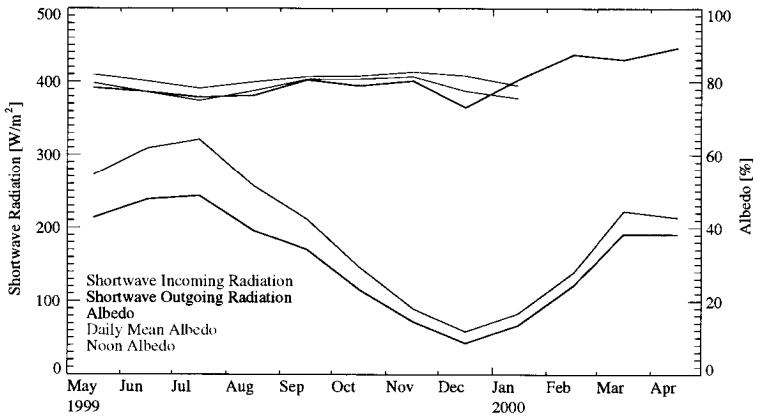

Figure 4.7: Shortwave radiation and albedo (monthly mean values) at Seserjoch (Monte Rosa) from May, 1999 to April, 2000.

for critical days using typical albedo values from the Colle del Lys station for the period in question. After April 29, 2000, the albedometer was snowed in and the last two daily values for the month were taken from Colle del Lys. In Figure 4.7, the monthly mean values of shortwave radiation are presented together with monthly mean albedos (see below).

4.3.6 Albedo

The albedo α was determined using the ratio of the total shortwave outgoing ($K\uparrow$) to total shortwave incoming ($K\downarrow$) radiation as measured by the albedometer:

$$\alpha = \frac{K\uparrow}{K\downarrow} \,. \tag{4.36}$$

Albedo measurements are a very delicate business, but crucial for the radiation and energy balance as the shortwave radiation often constitutes the major energy input (see Section 4.1.1). A diurnal variation of the albedo is presented in Figure 4.8 together with the shortwave incoming and outgoing radiation over an undisturbed surface for a clear-sky (upper panel) and a foggy situation (lower panel). In case of the clear-sky situation, an albedo increase can be observed during the day due to a slightly oblique terrain (5° inclination of the surface towards WNW). The noon albedo is 76.5 % and the daily mean albedo 78.1 %. In case of the cloudy conditions, a generally higher albedo can be observed (see Section 4.1.1 for explanation) with no marked diurnal variation and a noon albedo (87.1 %), which is very close to the

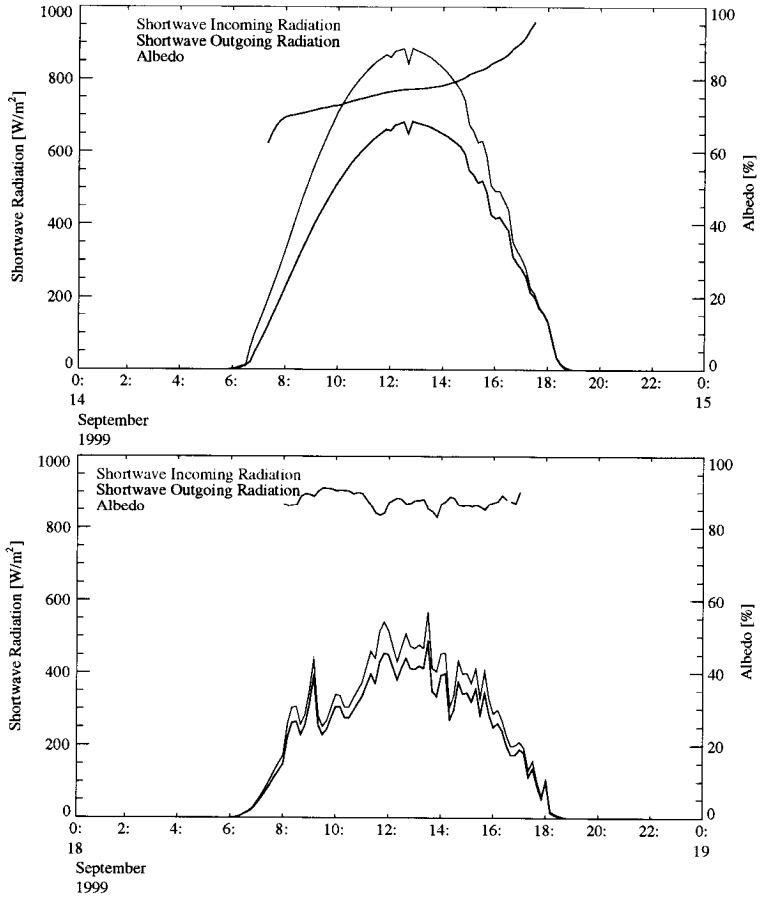

Figure 4.8: Shortwave radiation and diurnal albedo at Seserjoch (Monte Rosa) on September 14, 1999 (clear-sky day; upper panel) and September 18, 1999 (foggy day; lower panel).

daily mean albedo (87.9 %). In Figure 4.7, the monthly mean albedos are depicted. The monthly mean albedos were calculated using the daily mean values (daily mean albedo), noon values (noon albedo) or monthly mean values of the shortwave incoming and outgoing radiation (albedo). No obvious trend from May, 1999 to January, 2000 is visible due to a more or less regular fresh snow accumulation. The albedo values of December and from January to April have to be interpreted with caution due to difficult measuring conditions (flat sun angle at the saddle and shade effects) and data reconstructions (see above). The higher values in March and April are due to fresh snow accumulation. The yearly mean values are very similar: 80.3 % for the albedo, 80.7 % for the daily mean albedo and 78.3 % for the noon albedo. For further analysis, the daily mean values were chosen.

4.3.7 Longwave Radiation

A large effort was necessary to analyse the longwave radiation data measured by the precision infrared radiometers (PIRs) (see Section 4.2.2). The following formula was used to convert the measured data into a corrected longwave radiation (Albrecht

et al., 1974 and Philipona et al., 1995):

$$L\downarrow = \frac{U_{tp}}{C_{PIR}} + \epsilon_{body}\sigma T_{body}^4 - \frac{\epsilon_{dome}}{\tau_{dome}}\sigma\left(T_{dome}^4 - T_{body}^4\right) , \tag{4.37}$$

where U_{tp} = measured voltage over the thermopile, C_{PIR} = sensitivity factor of the pyrgeometer, ϵ_{body} = emissivity of the instrument body, σ = Stefan-Boltzmann constant, T_{body} = temperature of the instrument body, ϵ_{dome} = emissivity of the dome of the instrument, τ_{dome} = transmissivity of the dome of the instrument and T_{dome} = temperature of the dome of the instrument. A major problem in data analysis were the unmeasured dome temperatures. The possible error due to self-heating and corresponding self-emission of longwave radiation of the dome under clear-sky conditions can amount to more than 20 W/m^2 if the instrument is not shaded (Philipona et al., 1995). Therefore, a correction was applied using high-resolution radiation data from the Gornergrat station of the *Baseline Surface Radiation Network of the WMO/WRC* under clear-sky conditions. A very good linear relationship could be found between the shortwave incoming radiation and the temperatures of the silicon dome of the PIR. This relation was used to derive a mean dome temperature for the Seserjoch PIRs using the measured shortwave radiation. The emissivity of the instrument body ϵ_{body} was assumed to be 1 and the body temperatures were measured using the built-in thermistors. The relation between ϵ_{dome} and τ_{dome} was assumed to be 3.5 (Philipona et al., 1995). Due to a cable failure in the course of a revision of the station at the end of November, no longwave incoming radiation could be measured from November 26, 1999 to January 15, 2000. This data gap was filled with data of the Gornergrat station, but only for clear-sky conditions when the measured relative humidity at Seserjoch was below 70 %. A constant shift in

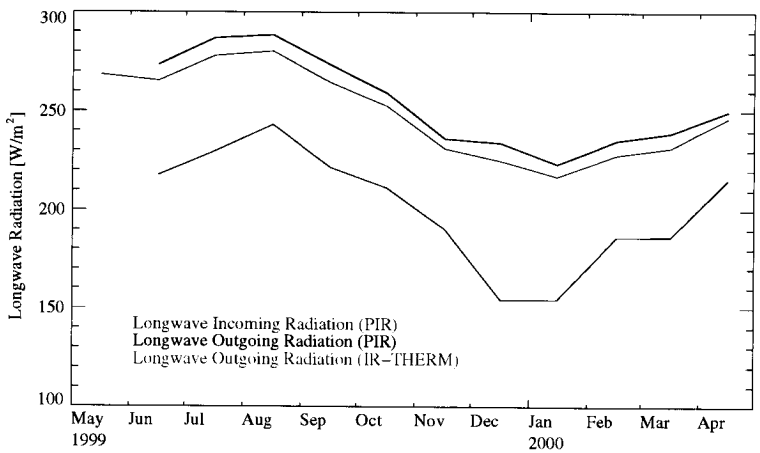

Figure 4.9: Longwave radiation (monthly mean values) at Seserjoch (Monte Rosa) from May, 1999 to April, 2000 measured with the PIRs and derived from the surface temperatures measured by the IR-Thermometer.

longwave radiation of approximately 26 W/m^2 could be found for November 1999 and January 2000 for these cases. This shift was subtracted from the Gornergrat data to obtain the values for Seserjoch. The monthly mean values of longwave radiation are presented in Figure 4.9 together with the longwave outgoing radiation

calculated from the surface temperatures measured by the infrared thermometer (IR-Thermometer) using Equation 4.5 (see below).

4.3.8 Surface Temperature

The *IR-Thermometer* mostly worked in a very reliable way and data gaps were sparse. Problems occurred after the revision of the station in May, 1999. Due to an electrical problem in the cabling at the data logger, the instrument temperature, which is used to correct the effective surface temperature, showed a constant shift to the observed air temperature. Thus, measured air temperatures had to be used as instrument temperature from there on. After this correction, a good accordance could be found to the calculated surface temperatures using the longwave outgoing radiation measured by the PIR and Equation 4.5 (Figure 4.10). Typical offsets be-

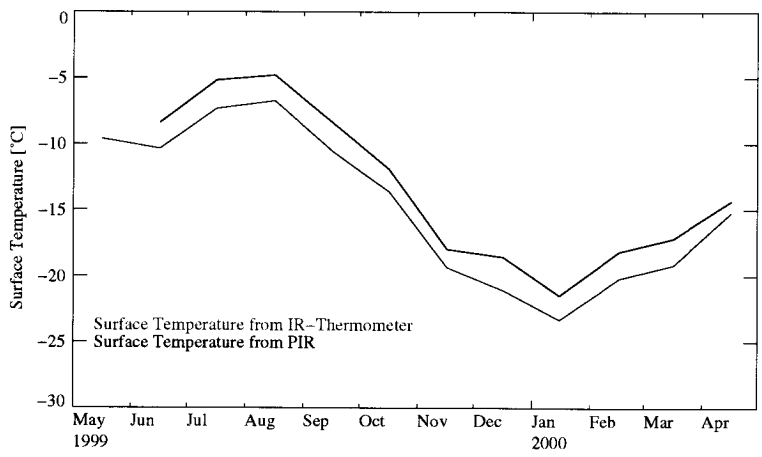

Figure 4.10: Surface Temperatures (monthly mean values) at Seserjoch (Monte Rosa) from May, 1999 to April, 2000 measured with the IR-Thermometer and derived from the longwave radiation measured by the PIR.

tween the two instruments of 2–4 °C occurred on a daily scale, whereas the surface temperatures measured by the IR-Thermometer were on the order of 2 °C deeper on the monthly scale (Figure 4.10). The generally deeper values for the surface temperatures observed with the IR-Thermometer can be explained with the use of too deep an instrument temperature (the instrument temperature of the (unventilated) IR-Thermometer had to be replaced by the (ventilated) air temperature) and with a smaller absolute accuracy of the IR-Thermometer in general.

4.3.9 Snow Accumulation and Ablation

The *Campbell SR50 sonic ranging sensor* was without any exaggeration the most reliable instrument of all. The very sparse outliers could easily be identified and eliminated. As the speed of sound is mainly dependent on the ambient air temperature, the following compensation formula was used:

$$r_{cor} = r_{uncor}\sqrt{\frac{T_a}{273.15}}\ , \tag{4.38}$$

where r_{cor} = corrected distance, r_{uncor} = uncorrected distance and T_a = air temperature [K]. Figure 4.11 shows the evolution of the daily accumulation and ablation at

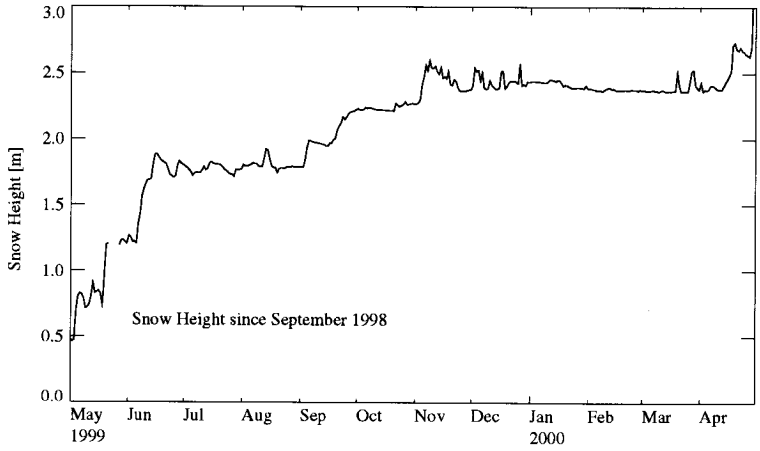

Figure 4.11: Accumulation and ablation (daily mean values) at Seserjoch (Monte Rosa) from May, 1999 to April, 2000. The measurements are referred to the beginning of the series in September, 1998.

Seserjoch from May, 1999 to April, 2000 referred to the start of the measurements in September, 1998. The pattern shows that the main accumulation occurs from late spring to early autumn, whereas practically no accumulation is observed in high winter due to the very deep temperatures, prevailing dry conditions and wind erosion.

4.4 Energy Balance

4.4.1 Net Radiation

The net radiation was calculated using the following measured quantities (cf. Equation 4.2):

$$R = K\downarrow - K\uparrow + L\downarrow - L\uparrow \ , \tag{4.39}$$

where $K\downarrow$ = shortwave incoming radiation, $K\uparrow$ = shortwave outgoing radiation, $L\downarrow$ = longwave incoming radiation and $L\uparrow$ = longwave outgoing radiation. For the calibrations and corrections applied, see Section 4.3. For the longwave outgoing radiation, both the PIR and the IR-Thermometer data were used. The monthly mean values are presented in Figure 4.12. The deviations in the calculated net radiation using the PIR-instrument or the IR-Thermometer are small and typically on the order of 3–9 W/m^2. The calculated net radiation using the outgoing radiation of the IR-Thermometer gives a higher value due to a smaller outgoing radiation by the IR-Thermometer. The value in May was obtained directly from the net radiometer as the PIR-instrument was not yet installed (see Section 4.2.2). As expected, the net radiation is positive during the months with high shortwave incoming radiation (from May to August) and negative during the winter months (from September to April).

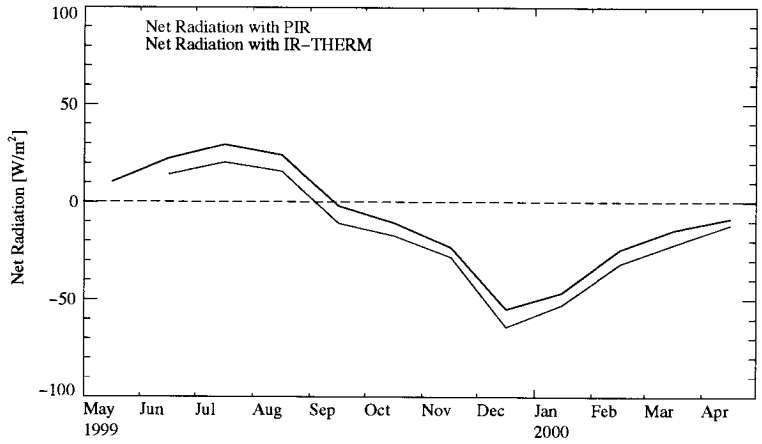

Figure 4.12: Net radiation (monthly mean values) at Seserjoch (Monte Rosa) from May, 1999 to April, 2000. For May, 1999, the net radiation measured by the net radiometer is shown.

4.4.2 Turbulent Fluxes

Although it is usually common to use a 30 minute averaging period for the calculation of the turbulent fluxes, in this study a time window of 10 minutes was taken for three main reasons:

- The exposed firn saddle of Seserjoch is subjected to large and quick changes in the state of the atmosphere. Thus, the character of turbulence should be fully assessed by the time window selected as a compromise between a statistically stationary state of the atmosphere (which limits the averaging period) and the assessment of all high-frequency changes (which requires a certain minimum time window). The analysis of the sonic data (see below) showed that a 10 minute time window was appropriate.

- As the sonic data (see below) are quite sparse and have data gaps, only the use of 10 minute values allowed a reasonable analysis and comparison with other methods (see below).

- A 30 minute resolution would have been too coarse for detecting all high-frequency melt events during the day (see below).

Within this section, the data from May 27 to May 31, 1999 are presented. During this time, controlled measurements could be made at the station and different methods of turbulent flux calculation be compared with sonic anemometer measurements.

Eddy-Correlation Method

During the field campaign in spring 1999, eddy-correlation measurements where carried out at Seserjoch between May 26 and May 29, using a 3-dimensional sonic anemometer of the type *Gill Solent 1012R2A* at a sample frequency of 21 Hz (see Table 4.2). The instrument was mounted 2.1 m above the surface and connected to a portable computer. The data were registered within the *fastcom* software package using mode 1 for calibrated u-,v- and w-components of wind velocity. The sonic

anemometer and the computer were powered by a generator which had to be refueled regularly and which made it impossible to measure during night time. Occasionally, the computer system crashed down for unknown reasons and had to be restarted. The weather conditions during the observation period showed a typical convective pattern with frequent fog formation in the afternoon and evening. On one occasion, the formation of hoar frost could be observed. The mean wind velocity was about 4 m/s and the mean air temperature about -5 °C.
The data processing showed that there were quite frequent error measurements which had to be eliminated by interpolation. Some data sequences had to be rejected as they showed too many errors. Finally, a total of about 20 hours of data could be used for analysis.
The data processing was done using a FORTRAN program which could be used by courtesy of Mathias Rotach (*Institute for Atmospheric and Climate Science, ETHZ*). The program calculated 10 minute values of the geometrically corrected wind-speed components u, v, w and the corresponding covariances $\overline{u'T'}$, $\overline{v'T'}$ and $\overline{w'T'}$. For the calculation of the temperature fluctuations using the measured speeds of sound, the measured relative humidities at the Seserjoch station and the measured air pressures at the Colle del Lys station were taken (Figure 3.5). A run-test (formally a t-test) was applied to check the averaging period and each component for stationarity (eg Forrer, 1999). The run-test turned out to be fulfilled for almost all cases. No additional corrections were applied to the data as the accuracy of the sonic anemometer improved only slightly after applying the result of a wind tunnel calibration (Forrer, 1999) and as effects due to the sampling frequency and the sensor line averaging normally account for 5–10 % of the flux loss only (Moore, 1986).
Figure 4.13 shows an example of the measured sensible heat flux H at Seserjoch of

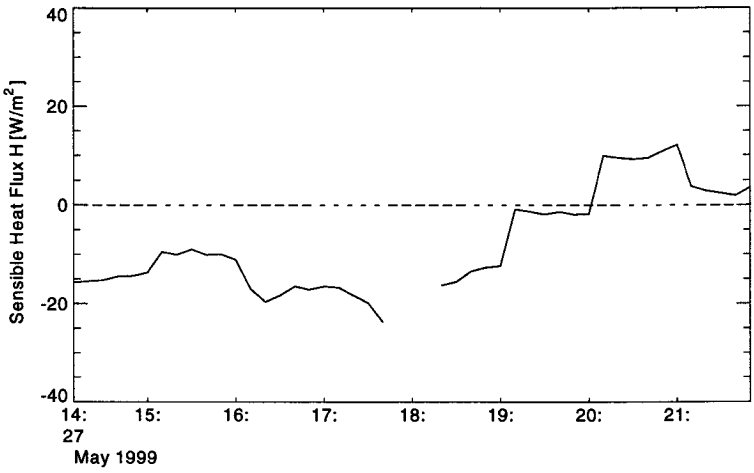

Figure 4.13: Sensible heat flux measured with the sonic anemometer at Seserjoch (Monte Rosa) on May 27, 1999.

May 27, 1999. The flux was calculated using Equation 4.23. The air density ρ_a was calculated using the air-pressure data from the Colle del Lys station with

$$\rho_a = \frac{1}{R_g \cdot T_a} \cdot \left(p \cdot mol_a - e \cdot \left(\frac{mol_a - mol_w}{mol_w} \right) \right) , \tag{4.40}$$

where R_g = universal gas constant, T_a = air temperature, p = air pressure, mol_a = molar mass of (dry) air, e = water-vapour pressure and mol_w = molar mass of water. The pressure data from the Colle del Lys station were corrected for the altitude shift to Seserjoch (50 m) using a constant pressure reduction of 391 Pa. The water-vapour pressure e was calculated using the measured relative humidity at the Seserjoch station and a formula by Lowe (1976) which calculates the saturation water-vapour pressure e_s as a function of the observed air temperature.
If no pressure data from the Colle del Lys station were available, ρ_a was calculated for a polytrope atmosphere taking

$$\rho_a = \rho_0 \left(1 - \frac{\gamma h}{T_0}\right)^{\frac{\rho_0 g T_0 - p_0 \gamma}{p_0 \gamma}} , \tag{4.41}$$

where $\rho_0 = 1.225\,\mathrm{kg/m^3}$ (air density at 15 °C and at 1 atm after Stull 1988), $\gamma = 0.0065\,\mathrm{K/m}$ (mean air-temperature lapse rate), h = altitude above sea level, $T_0 = 288.15\,\mathrm{K}$ (mean air temperature at sea level) and $p_0 = 101325\,\mathrm{Pa}$ (standard air pressure at sea level). ρ_a then becomes $0.79\,\mathrm{kg/m^3}$ at 4300 m a.s.l. The specific heat capacity of dry air at constant pressure c_a was taken as 1004.67 J/(kg·K). As the specific humidity content of the air was generally low even under humid conditions – it did normally not exceed 5 g per kg – no correction was applied to the c_a-value to account for increasing humidity concentration. Using the above specific humidity of 5 g per kg, the c_a-value only changes by 0.4 %.
The sensible heat flux in Figure 4.13 shows a typical pattern for the observation period with negative values during day-time and positive values after sunset, when the negative radiation balance had to be compensated. The magnitude of the flux was rather small and did never exceed $30\,\mathrm{W/m^2}$. A closer look at the measured (uncorrected) vertical velocities w showed that the geometric correction applied (turning of the sonic anemometer into the mean wind direction) strongly reduced the (positive) vertical component w. This indicates a marked glacier up-wind following the (north-west) direction of the glacier beneath the saddle. Although the *footprint* of the sonic anemometer (distance which is sensed by the instrument) was on the order of 5–10 m only, the instrument height of 2.1 m was presumably still too high. Strong horizontal air advection in this layer made it probably impossible to see the small-scale eddies below the instrument. Further investigations using an array of sonic anemometers at different levels above the surface and in space would be necessary to make a statement on the character of turbulence at the site.

Profile Method

As already stated in Section 4.1.2, the profile method is based on the assumption of a relation between mean observed gradients and corresponding heat fluxes within the atmospheric surface layer over a homogeneous surface and under neutral conditions. For the calculation of wind- and temperature profiles, the following relations were used (according to the number of useful levels):

$$x(z) = a\ln z + bz^2 + cz + d \text{ or} \tag{4.42}$$

$$x(z) = a + bz + c\ln z , \tag{4.43}$$

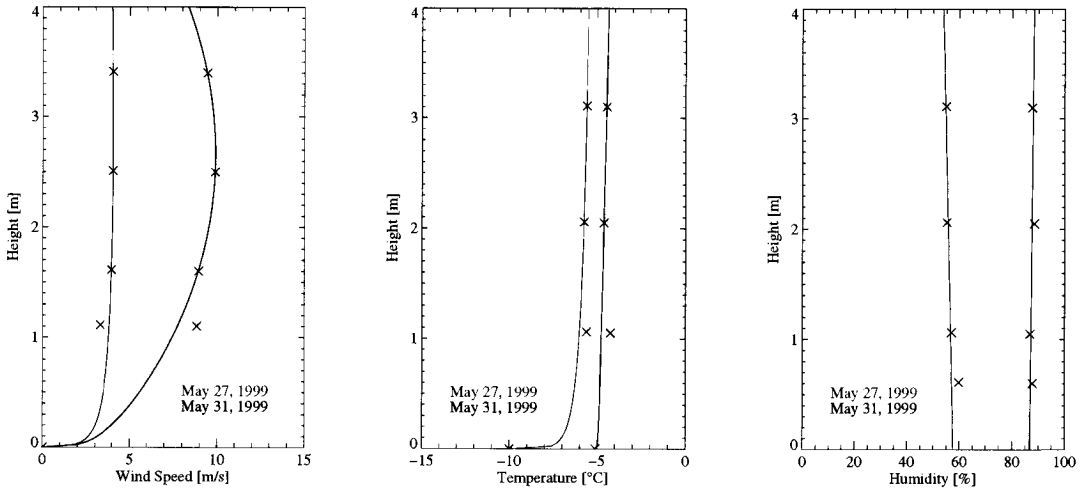

Figure 4.14: Mean wind-speed (left panel), temperature- (middle panel) and humidity (right panel) profiles at Seserjoch (Monte Rosa) on May 27, 1999 (clear-sky day) and May 31, 1999 (foggy day). The curves through the data were calculated using the upper 3 observing levels only.

where $x = \overline{u}$, $\overline{\theta}$, $z =$ height above the surface and a, b, c, $d =$ coefficients. For the specific humidity profiles, the linear relation

$$\overline{q}(z) = az + b \tag{4.44}$$

was taken (Forrer, 1999). At high wind speeds, the wind profile frequently showed a maximum wind speed at about 2.5 m height and a decreasing wind speed further above possibly due to a jet effect at the Seserjoch firn saddle. At low wind speeds, almost identical wind speeds at height could often be observed. The wind velocity at the ground (at roughness length) was assumed to be zero. The lowermost level of temperature measurements had to be omitted often, as it did only badly fit into the logarithmic profile form. At the height of the roughness length, the measured surface temperature was taken. The same can be stated for the lowermost measurement level of humidity, which was also left apart in almost all cases. The other 3 levels often followed a good linear relation. Figure 4.14 shows mean profiles on May 27, 1999 (clear-sky day with low wind speeds) and on May 31, 1999 (foggy day with high wind speeds).

The gradients of wind speed, potential temperature and specific humidity for a certain height above the surface were obtained as the derivative of Equations 4.42, 4.43 and 4.44. The measured relative humidities were transformed into specific humidities using the relation

$$\overline{q} = 0.622 \cdot \frac{RHe_s}{p} \ , \tag{4.45}$$

where $\overline{q} =$ specific humidity, $RH =$ measured relative humidity, $e_s =$ saturation water-vapour pressure at a given air temperature and $p =$ air pressure. The saturation water-vapour pressure was calculated using a formula by Lowe (1976). The stability

functions $\phi_m\left(\frac{z}{L}\right)$, $\phi_h\left(\frac{z}{L}\right)$ and $\phi_q\left(\frac{z}{L}\right)$ were determined iteratively using the following relations for $Ri > 0$ (see Equation 4.8) after Högström (1988):

$$\phi_m = 1 + 6\frac{z}{L} \text{ and} \tag{4.46}$$

$$\phi_h = \phi_q = 0.95 + 7.8\frac{z}{L} \,. \tag{4.47}$$

For an unstable stratification ($Ri < 0$), the following equations were used (Dyer, 1974):

$$\phi_m = \left(1 - 16\frac{z}{L}\right)^{-0.25} \text{ and} \tag{4.48}$$

$$\phi_h = \phi_q = 0.74\left(1 - 16\frac{z}{L}\right)^{-0.5} \,. \tag{4.49}$$

Cases under near-neutral conditions were excluded by applying the following two selection criteria for excluding critical data from analysis (Högström, 1988):

- $u_* < 0.1\,\mathrm{m/s}$
- $|\mathrm{H}| < 10\,\mathrm{W/m^2}$

The scaling parameters for wind velocity (u_*), potential temperature (θ_*) and specific humidity (q_*) were calculated using Equations 4.13, 4.14 and 4.15. Finally, Equations 4.25 and 4.26 were taken for the calculation of the sensible and latent heat flux at a given height above the surface.
Figure 4.15 shows the calculated fluxes at the height of the sonic anemometer (2.1 m

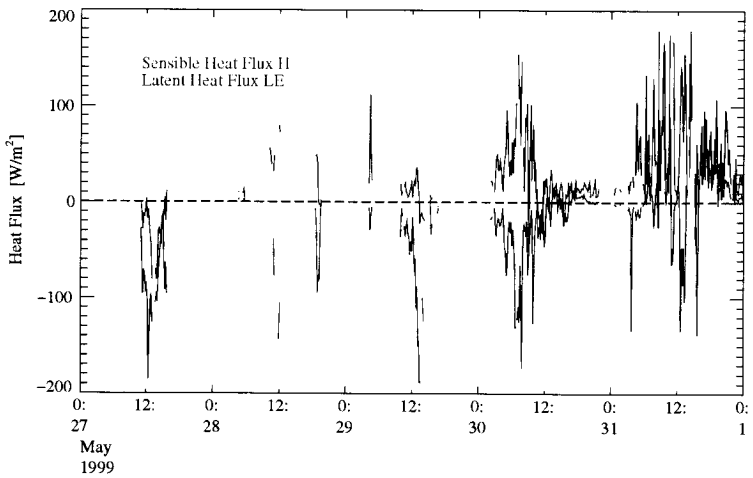

Figure 4.15: Sensible and latent heat flux derived from the profile method at 2.1 m above ground from May 27 to May 31, 1999.

above ground) from May 27 to May 31, 1999. A lot of data had to be rejected for the first three days due to very small or negative values of u_*. The last two days showed very high fluxes due to high wind speeds.
For the application of a simplified turbulent heat-flux calculation it is useful to know the surface roughness length (see Section 4.1.2). This is the height where $u(z) = 0$.

The roughness length is a function of surface geometry and wind speed (drifting snow). The surface roughness length for wind z_{0u} can be determined when plotting mean observed wind speeds at two or more levels against logarithmic heights. A mean surface roughness length of about 0.001 m could be found for wind, which is in good agreement with studies from eg Morris (1989) or Plüss (1997). The roughness length for temperature and humidity was assumed to be one order of magnitude smaller than z_{0u} (Morris, 1989).

Bulk Method

The theoretical background of the bulk method is explained in Section 4.1.2. The wind gradients were calculated using one or the mean of two wind-speed levels in the air and the (assumed) zero wind speed at the surface roughness length for wind (see above). For the sensible heat flux, the temperature gradient between one or the mean

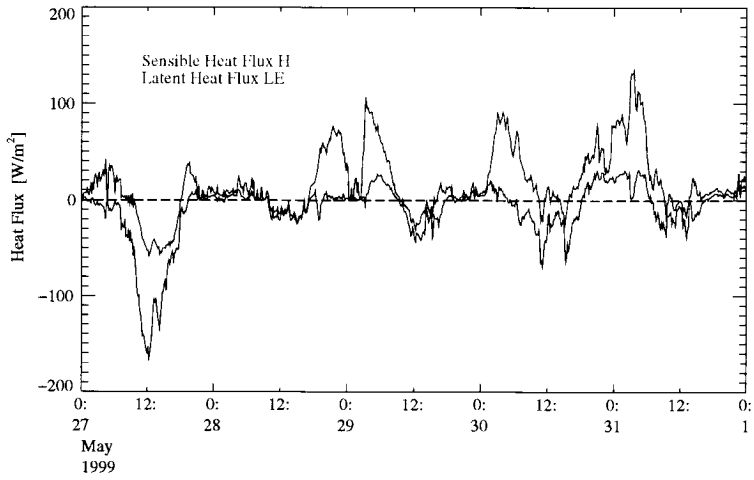

Figure 4.16: Sensible and latent heat flux using the bulk method and levels at about 2 m above ground from May 27 to May 31, 1999.

of two air-temperature levels and the measured surface temperature (taken from the PIR-Instrument or the IR-Thermometer) was used. Consequently, one or the mean of two levels of measured relative humidity and an assumed surface humidity at saturation were taken to calculate the humidity gradient. The relative humidities were converted into specific humidities using Equation 4.45. The specific humidity at the surface was calculated using the saturation water-vapour pressure for the observed surface temperature based on a formula by Lowe (1976). A temperature-dependent latent heat coefficient was used to better consider the different thermal conditions of the surface. Below a surface temperature of -10 °C, the latent heat of sublimation (L_s) and between a surface temperature of -10 – 0 °C a fractioned value of the latent heat of vaporization (L_v) and of L_s was taken according to the observed surface temperature. At 0 °C, the latent heat of vaporization L_v was taken. The evolution of the sensible and latent heat flux from May 27 to May 31, 1999 is shown in Figure 4.16. The wind speeds, temperatures and humidities at the 2 m level and the surface temperature measured by the IR-Thermometer were taken.

Bowen Ratio

The Bowen-ratio calculation was made according to the equations and rejection criteria defined in Section 4.1.2. The net radiation was determined using the PIR-Instruments for longwave incoming and outgoing radiation and a daily mean albedo for the calculation of the shortwave outgoing radiation. For the calculation of the subsurface heat flux, see below. The gradients of temperature and humidity were

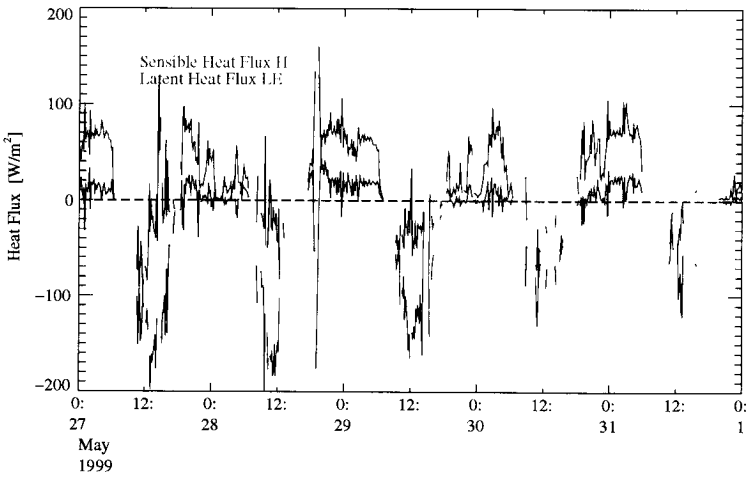

Figure 4.17: Sensible and latent heat flux using the Bowen-ratio method and levels at 3.1 and 2.05 m above ground from May 27 to May 31, 1999.

obtained by taking the measurement levels at 3.1 and 2.05 m above ground. The sign of the temperature gradients could change within the surface layer (see Figure 4.14) which made it sometimes difficult to select two representative levels. Except for May 27, 1999 (where the measured values are a little unsure), the surface temperatures were always below 0 °C, so that melt events are supposed to be absent for the observation period in question. The calculated fluxes are given in Figure 4.17. The methodological problems are further discussed in Sections 4.4.5 and 4.5.

Comparison

A comparison between the sensible heat flux determined by the eddy-correlation method and the sensible heat flux determined by the other methods (profile, bulk and Bowen ratio) from May 27 to May 29, 1999 is presented in Figure 4.18. All the values are referred to the height of the sonic anemometer 2.1 m above ground. Although the sign of the fluxes is mostly correct, all three methods seem to overestimate the fluxes measured by the sonic anemometer. This means that either the sensible heat flux measured by the sonic anemometer is only representative for the height in question, but not for the effective turbulent exchange between the atmosphere and the surface, or the profile, bulk and Bowen-ratio methods all overestimate the fluxes, considerably. Due to the stratification of the surface boundary layer at the time of observation, however, the first may be valid (see above). Thus, a comparison between the sonic anemometer and the other methods applied is difficult. Nevertheless, a certain confidence in the flux calculations is generated by the fact that – in absence of melt – the turbulent fluxes have to adopt a certain magnitude to compensate the radiative flux on a daily time-scale (see Section 4.4.5), and by the fact that the signs

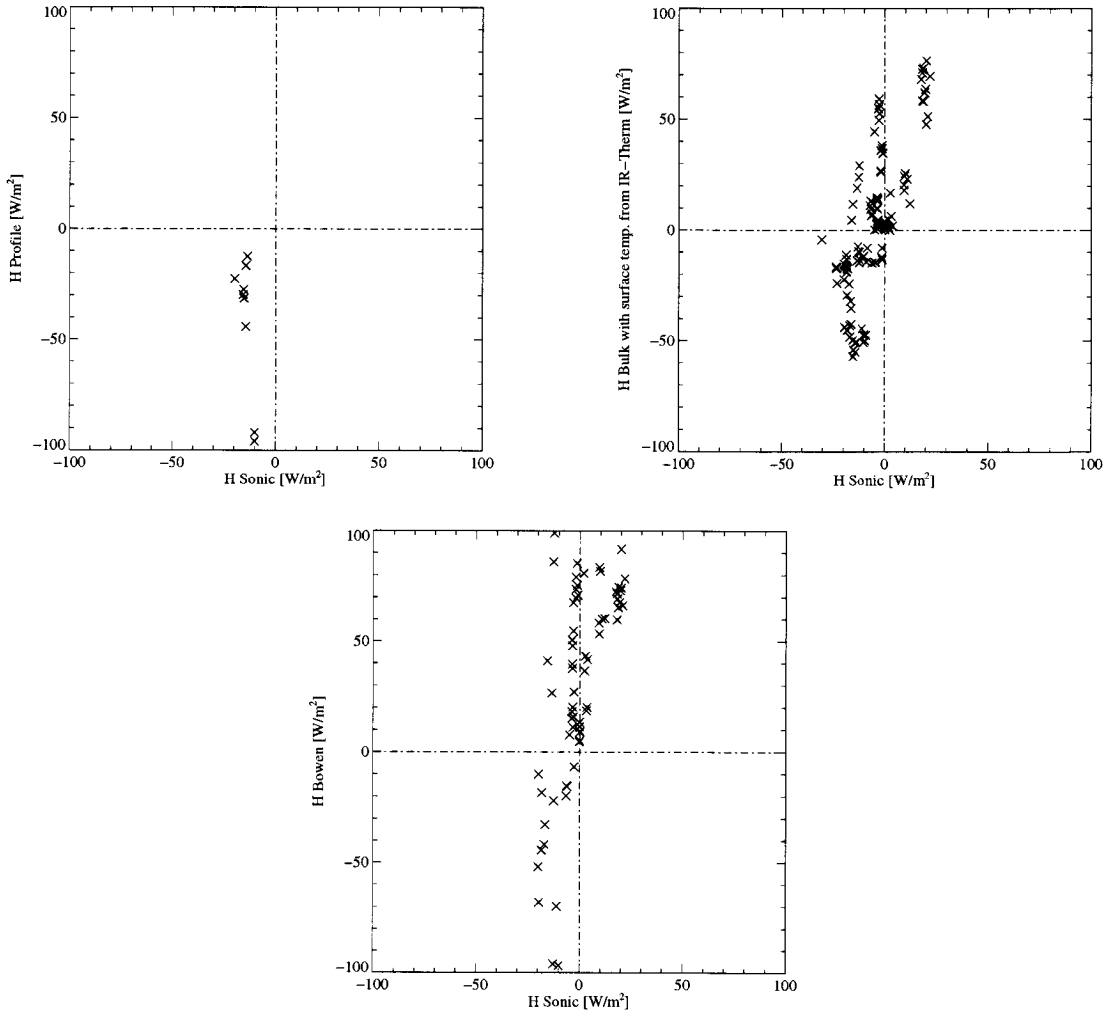

Figure 4.18: Comparison between the sonic-derived sensible heat flux and the sensible heat flux determined by the profile method (upper left panel), the bulk method (upper right panel) and the Bowen-ratio method (lower panel) for the period from May 27 to May 29, 1999.

of the fluxes coincide in the majority of the cases. In Figure 4.19, the daily mean values of sensible and latent heat flux from May, 1999 to April, 2000 are compared using the profile, bulk and Bowen-ratio methods. The flux directions are mostly correct, but the scattering between single observations can still be large.

4.4.3 Subsurface- or Ground Heat Flux

The subsurface heat flux was calculated using Equation 4.33 (see Section 4.1.3). The temperature gradient was determined between the measured surface temperature and the temperature measured by the uppermost thermistor of the 4 m thermistor chain (see Sections 4.2.2 and 5.2.2 for technical and methodological details). In order to get an idea of the effect of the submerging thermistor on the change of the temperature gradient with time, the second derivative of temperature versus depth

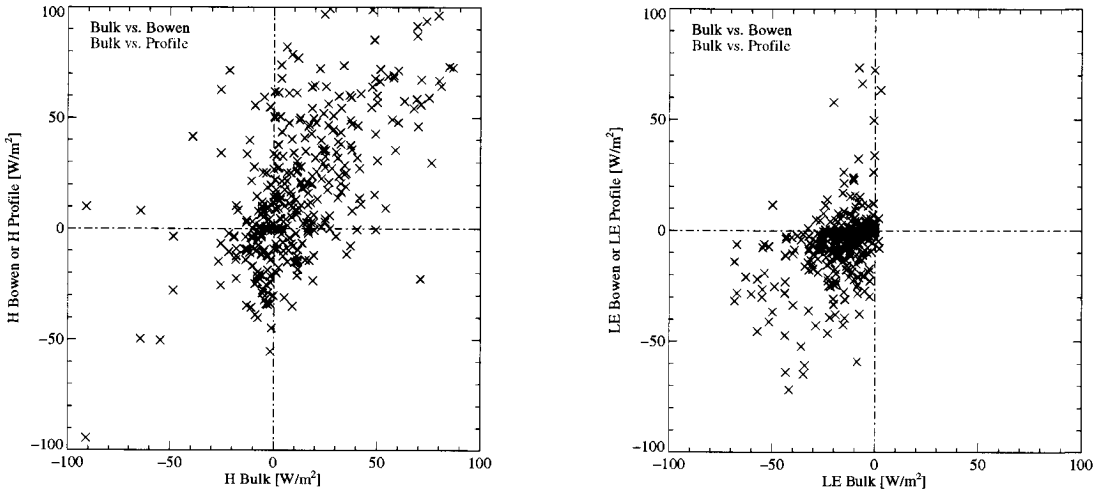

Figure 4.19: Comparison of the daily mean values of sensible (left panel) and latent (right panel) heat flux using the bulk, profile and Bowen-ratio methods from May, 1999 to April, 2000.

was plotted against the evolution of the snow height (Figure 4.20). The thermistor was initially (end of September, 1998) 0.25 m below the surface. The snow accumulation seems to dampen the temperature-gradient change until mid-June due to an important accumulation event. Later on, no trend is visible so that the timely evolution of the temperature gradient might not be too much affected by snow accumulation.
The thermal conductivity K_i was calculated as a mean between

1. the Schwerdtfeger formula (Paterson, 1994)

$$K_i = 2.1 \cdot 10^{-2} + 4.2 \cdot 10^{-4}\rho + 2.2 \cdot 10^{-9}\rho^3 \text{ and} \tag{4.50}$$

2. the van Dusen formula (Paterson, 1994)

$$K_i = \frac{2K_{ice}\rho}{3\rho_{ice} - \rho}\,, \tag{4.51}$$

where $\rho =$ observed density, $K_{ice} =$ thermal conductivity of ice (2.1 W/m·K) and $\rho_{ice} =$ density of ice (900 kg/m^3). The Schwerdtfeger formula represents an upper, the van Dusen formula a lower limit. The density was assumed as a mean between a typical fresh snow value (250 kg/m^3) and a higher value (500 kg/m^3) which is typical for wind-packed or long-exposed snow. A thermal conductivity of 0.5 W/m·K results. This value is not very sensitive; varying the density from 200 to 500 kg/m^3 changes K_i from 0.2–0.7 W/m·K, only.
As already stated in Section 4.1.3, the subsurface heat flux over snow or firn is normally low due to the fact that the surface temperature cannot rise above 0 °C as can be seen in Figure 4.20. The maximum daily value found is about 5 W/m^2. As the temperature gradient is mainly negative from May to September (lower snow

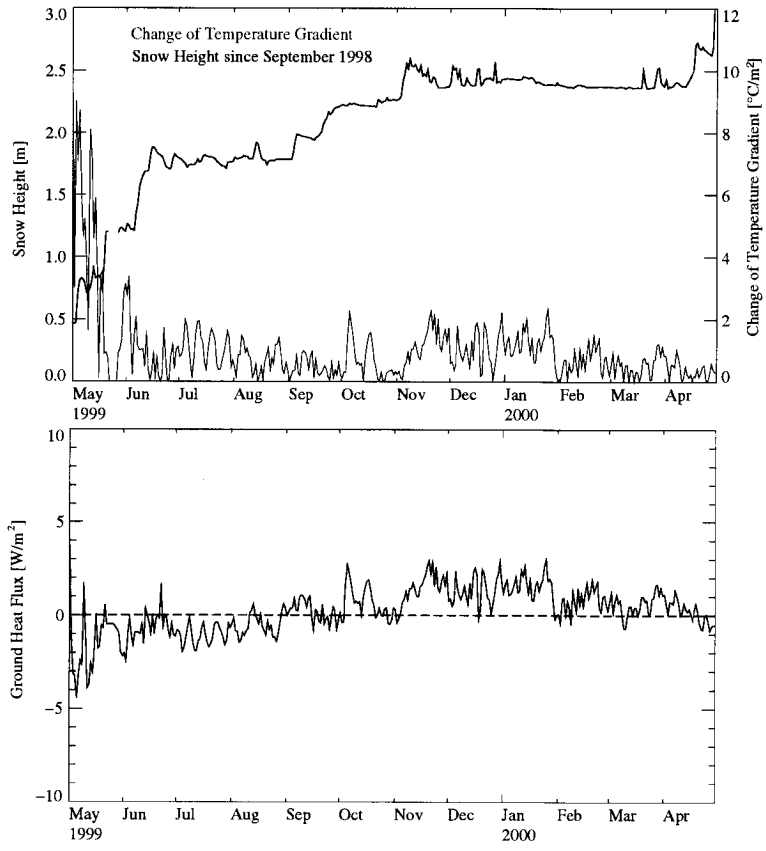

Figure 4.20: Accumulation and absolute change (second derivative of temperature versus depth) of the subsurface temperature gradient (upper panel) and ground heat flux (lower panel) at Seserjoch from May, 1999 to April, 2000.

temperature than surface temperature), predominately negative fluxes can be observed in this period. From October to mid-April, the opposite is the case. Even if one assumes that short-term temperature gradients of 20 °C/m can occur, the subsurface heat flux would not exceed 10 W/m^2.

The effect of transmission of net radiation in the uppermost snow layer on the heat budget of the snow cover was assessed for a few days at the end of March, 1999. At this time, the uppermost thermistor of the 4 m chain was 0.25 m below the surface (no surface accumulation since September, 1998) and the transmission was calculated using Equation 4.34 and daily mean values for the conductive heat fluxes. The heat content of the snow cover for a specific day was calculated between the observed snow-temperature profiles from the surface to the depth of daily variation (0.5–0.7 m). The heat flux due to transmitted net radiation was found to be on the order of the conductive heat flux at the top of the snow cover. Since the uppermost thermistor of the 4 m chain was increasingly buried under snow later on, the heat flux due to transmission of net radiation was not considered for the energy-balance series from May, 1999 to April, 2000.

4.4.4 Melt and Re-freezing

The practical problem in calculating the heat flux due to melt or re-freezing according to Equation 4.35 (Section 4.1.4) lies in the determination of the mass flux which is melted or re-frozen. Although techniques exist to eg determine the free water content in a snow cover, which makes it possible to calculate the mass of liquid water in the uppermost surface layer as a measure for the melted volume of snow, a continuous measurement is extremely difficult and delicate as part of the meltwater from the surface re-freezes within very short vertical distance. The application of a simplified approach using eg a degree-day factor as a measure for surface melt according to the air-temperature degree-day sum (eg Braithwaite, 1992) is not suitable for the Seserjoch site either, as the observed daily mean air temperatures did never and maximum daily values only on rare occations (about 12 events from July to September) exceeded the melting point! Theoretical considerations (Kuhn, 1987) and laboratory experiments (Beck et al., 1988) showed that surface melt events for cold snow and firn can also occur under negative air temperatures. Other factors influencing surface melt are radiative flux, wind speed and air humidity. Higher net radiation and air temperatures favour ice-layer formation, whereas high wind speeds and low air humidities have an inhibitory influence.
Melt events at the Seserjoch site could clearly be identified by the measured surface temperatures which quite frequently showed 0 °C during the day in July and August

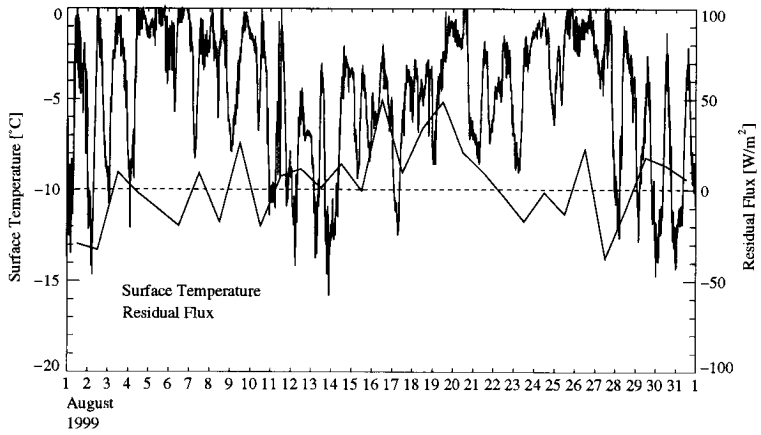

Figure 4.21: Surface temperatures and daily residual heat flux from August, 1999 showing melt events at Seserjoch.

(Figure 4.21) and on few occasions in September. No evidence for melt could be found when looking at the measured snow temperatures. The uppermost thermistor of the 4 m thermistor chain was too much buried under snow (see Section 4.4.3) and the miniature temperature loggers (see Section 4.2.2) installed in November, 1999 unfortunately stopped sampling in early May before the melt period.
That a single melt event can, indeed, turn over a high amount of energy on a short time-scale can be shown by a calculation using Equation 4.35: If a melt rate of 2 mm of snow per hour is assumed (which is a very small rate), an energy of 70 W/m^2 is consumed for a snow density of 375 kg/m^3!
Although the occurrence and timely duration of melt events can clearly be identified (see Table 4.4; Figure 4.21), the mass turnover cannot be determined nor the

heat flux due to melt (or re-freezing) be calculated directly. The determination of the energy balance, however, allows an estimate of these fluxes when looking at the residual fluxes which – besides the inherent errors – contain the energy flux due to melt and re-freezing (see Section 4.4.5). A good correlation between the measured surface temperatures and the calculated daily mean residual fluxes can be found eg for August, 1999 (Figure 4.21). During the melt events, the residual flux is predominately negative indicating an energy surplus which is compensated by melt. During the phases with no melt, re-freezing processes (eg rime accretion) can occur. Ad-freezing of undercooled water droplets could be measured with a high-precision lysimeter. However, the precise mass flux due to rime accretion is extremely difficult to determine, since snowdrift is very frequent at the exposed saddle of Seserjoch and a permanent maintenance of the instrument would be required. Rime accretion could frequently be observed, especially during fog situations in summer and during bad-weather situations in winter. Its contribution to the energy balance cannot be neglected: 2 cm of rime accretion per day (which is a plausible value) induces a daily mean heat flux of 15.5 W/m^2 for a typical rime density of 200 kg/m^3.
Figure 4.22 shows two examples for melt and re-freezing from August, 4 and August 16. Although the air temperature is below freezing point in both cases, melt does occur in the first case due to a high net radiation and relatively low wind speeds. In the latter case, the net radiation is much smaller and wind speeds are high which inhibits melt. Both air humidities are high. The quite large residual energy flux during night might be due to re-freezing processes (either re-freezing meltwater or rime accretion due to fog).
As surface melt events are crucial for the thermal regime of the firn (see Section 6), Table 4.4 summarizes the results from the 1999-melt season at Seserjoch giving the

Table 4.4: Summary of the monthly and yearly sum of melt days, monthly mean and yearly total melt duration and monthly mean and yearly total melt-energy input at Seserjoch. Melt was assumed for surface temperatures T_s greater than -1.0 or -0.5 °C or equal 0 °C.

Time	Number of Melt Days			Mean Daily Melt Duration [h]			Mean Daily Melt Energy Input [J/m²]		
	0 °C	-0.5 °C	-1.0 °C	0 °C	-0.5 °C	-1.0 °C	0 °C	-0.5 °C	-1.0 °C
May 1999	4	4	5	0.47	0.58	0.70	0.00	0.02	0.05
Jun 1999	0	1	4	0.00	0.01	0.06	0.00	0.01	0.05
Jul 1999	18	21	22	0.99	1.83	2.95	3.91	6.11	8.60
Aug 1999	11	17	18	0.57	1.60	3.34	1.09	2.44	4.03
Sep 1999	3	4	5	0.06	0.12	0.21	0.19	0.31	0.50
Yearly Total	**36**	**47**	**53**	**65**	**128**	**225**	**$13.88 \cdot 10^6$**	**$23.78 \cdot 10^6$**	**$35.39 \cdot 10^6$**

number of melt days, the duration of melt and the melt-energy input as monthly (mean) values or yearly totals.
The values were calculated using the 10 minute values of IR-Thermometer or PIR surface temperatures and the negative residual fluxes derived from the energy-balance calculation (see Section 4.4.5). The calculations were made for melting

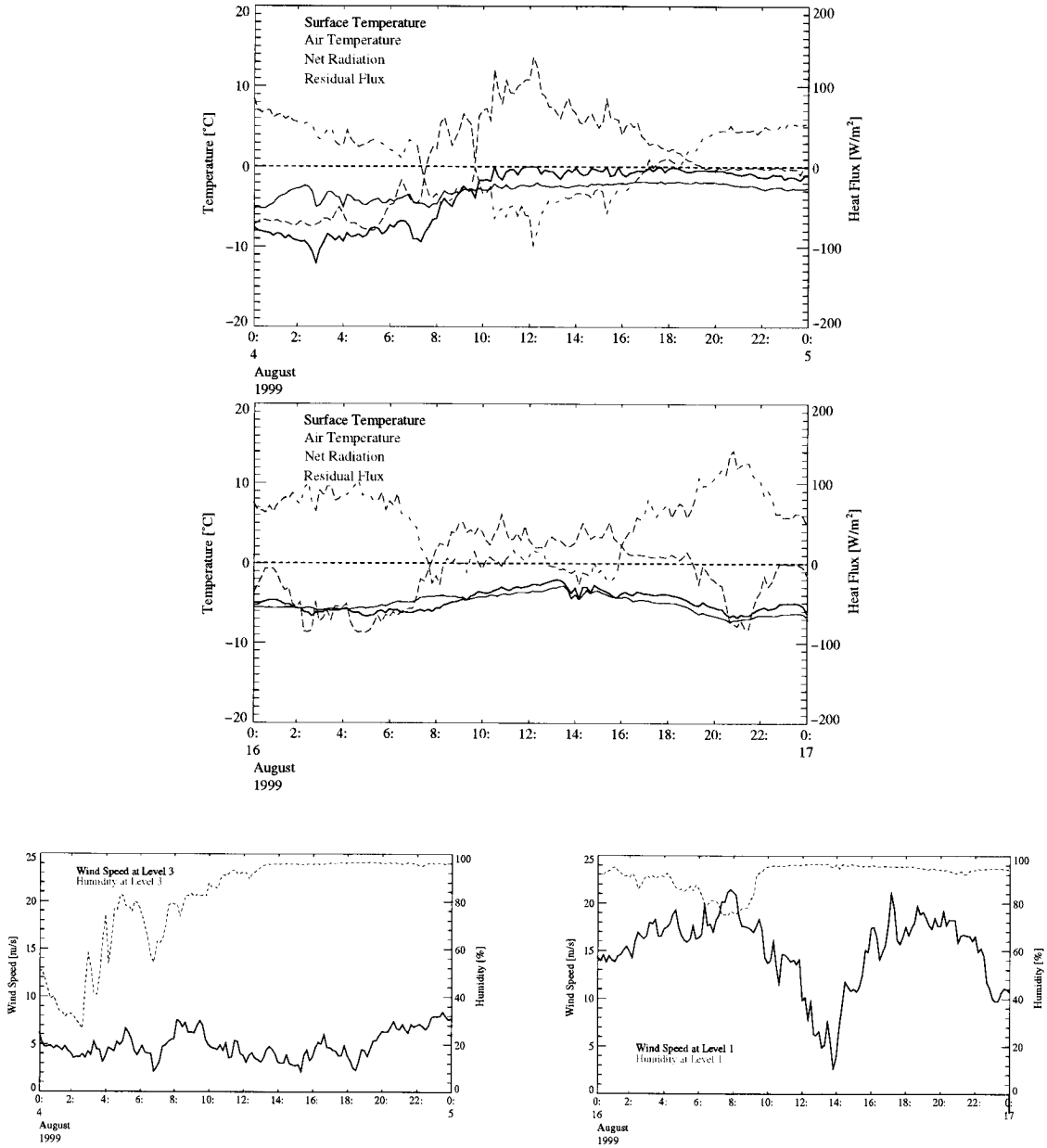

Figure 4.22: Surface and air temperatures, net radiation and residual heat flux from August 4 (upper panel) and August 16, 1999 (middle panel). The lower panels give the observed wind speeds and relative humidities for August 4 (lower left panel) and August 16 (lower right panel).

conditions assumed at surface temperatures T_s greater than -1.0 or -0.5 °C or equal 0 °C to account for the accuracy of the IR-Thermometer with ±0.5 °C at 0 °C and of the Precision Infrared Radiometer with (estimated) ±5 W/m^2 or ±1.1 °C at 0 °C.

4.4.5 Energy Balance and Residual Heat Flux

Within this section, the results of the energy balance are presented using two typical time windows with high-resolution data for summer- and winter conditions and the monthly mean values from May, 1999 to April, 2000.

The *residual heat flux* comprises the melt and re-freezing heat flux M (Sections 4.1.4 and 4.4.4) and the instrumental and methodological errors of the net radiation, sensible, latent and ground heat flux.

High-Resolution Data

The energy balance of June 26, 1999 is presented in Figure 4.23 showing the calculations for the Bowen-ratio, bulk and profile methods. Melt was absent during the day and fog formation could be observed from noon on.
The latent heat flux is generally small and the negative net radiation during night compensated by the positive sensible heat flux. The opposite is the case during day-time, whereas the latent and sensible heat fluxes of the profile method are not able to compensate the positive radiative flux during the day.
The energy balance from November 1 to November 2, 1999 is given in Figure 4.24. Naturally, no surface melt occurs. The first day is a clear sky day, the second shows clouds or fog from noon on. The air temperatures are quite high for November (about -5 °C on average). No useful result could be found when applying the profile method. The Bowen-ratio and bulk methods agree quite well. In order to show the influence of the assumption of a saturated surface, the middle panel shows the latent heat flux calculated with a surface water-vapour pressure at saturation. The lower panel gives the calculation with 55 % of the saturation water-vapour pressure which leads to a smaller residual flux. Under cloudy conditions, a positive net radiation can occur during the day even in high winter. The strange peaks in the Bowen-ratio curves are supposed to be measuring errors of the instruments.

Monthly and Yearly Mean Data

The monthly mean values of the energy balance using the Bowen-ratio, bulk and profile methods are shown in Figure 4.25. Due to missing daily mean values, data gaps occur for the Bowen-ratio and especially for the profile method.
A positive net radiation can only be observed from May to August. A quite large negative radiation balance occurs in December and January due to shading from the adjacent Parrotspitze (see Section 3.3) and due to a small longwave incoming radiation (Figure 4.9). The monthly means of the ground heat flux are very small and do not contribute to the energy balance in an important way.
When looking at the turbulent fluxes calculated with the Bowen-ratio method, the net radiation is mainly compensated by the sensible heat flux and the latent heat flux is very small. The summer values have to be regarded with care as the method does not consider the energy flux due to melt. The turbulent fluxes given by the bulk method show steady positive values for the sensible heat flux and negative values for the latent heat flux. Thus, the positive net radiation during the summer months is mainly compensated by the latent heat flux; the negative net radiation in the winter months by the sensible heat flux. The negative residual flux during summer might be due to melt events. The residual flux from November to January is very high and must be explained by an underestimation of the sensible heat flux, possibly due to an underestimation of the wind speeds caused by hoar frost at the instruments. Another part of the residual flux can be attributed to rime accretion at the surface. The generally rather high latent heat fluxes could be due to the assumption of water-vapour saturation at the surface (see Figure 4.24).

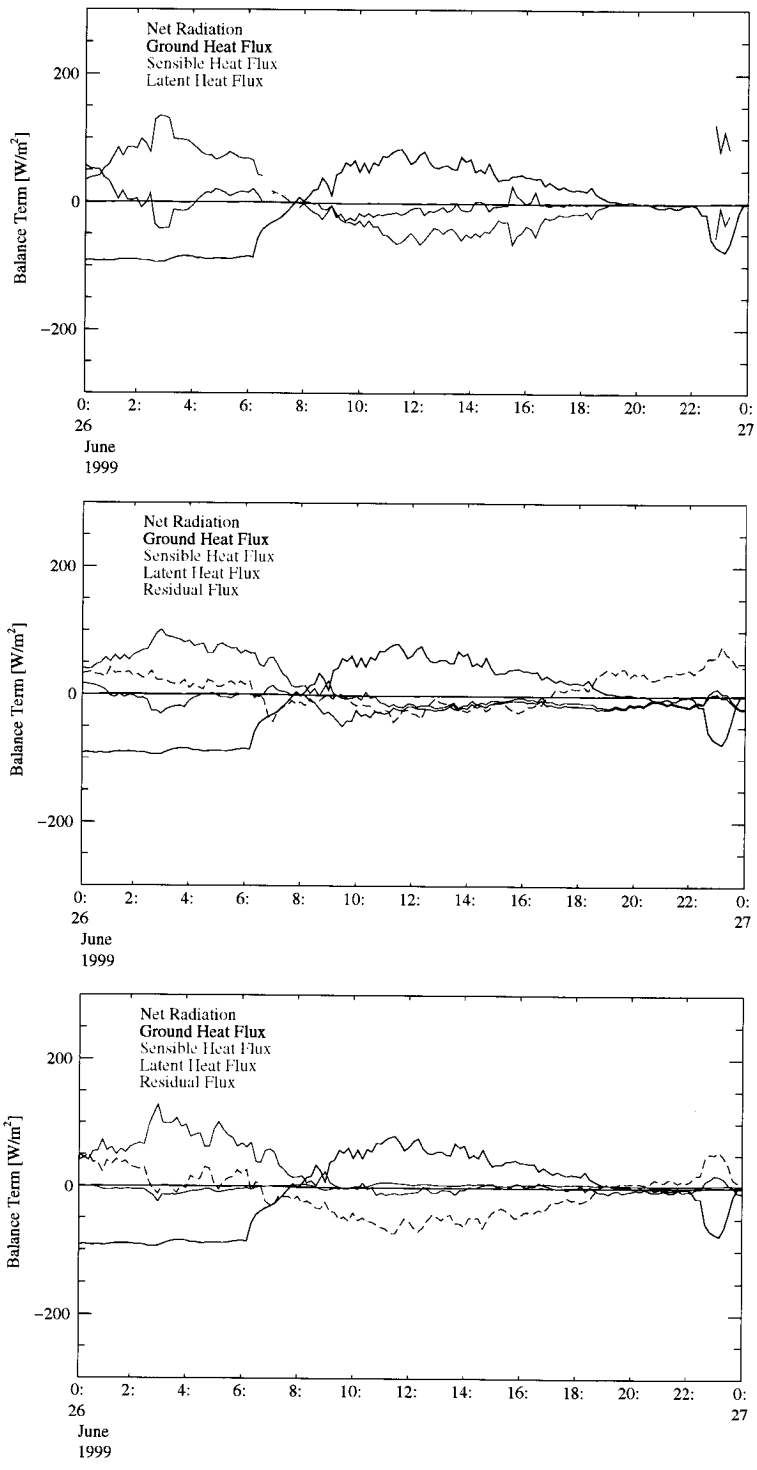

Figure 4.23: Energy balance at Seserjoch on June 26, 1999 using the Bowen-ratio (upper panel), bulk (middle panel) and profile (lower panel) methods.

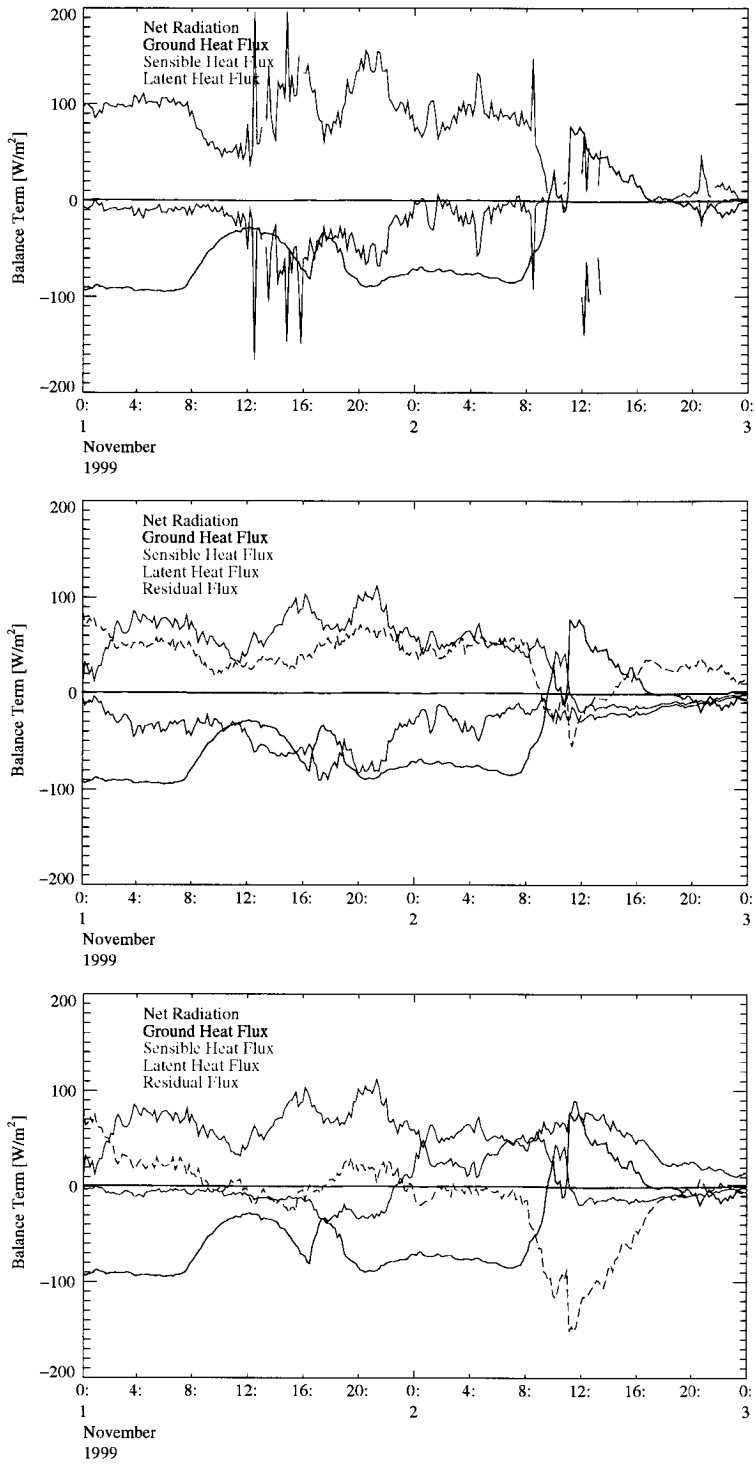

Figure 4.24: Energy balance at Seserjoch from November 1 to November 2, 1999 using the Bowen-ratio (upper panel) and bulk (middle and lower panel) methods. The latent heat flux of the middle panel was calculated using the saturation water-vapour pressure for the surface; the one of the lower panel using only 55 % of the saturation water-vapour pressure.

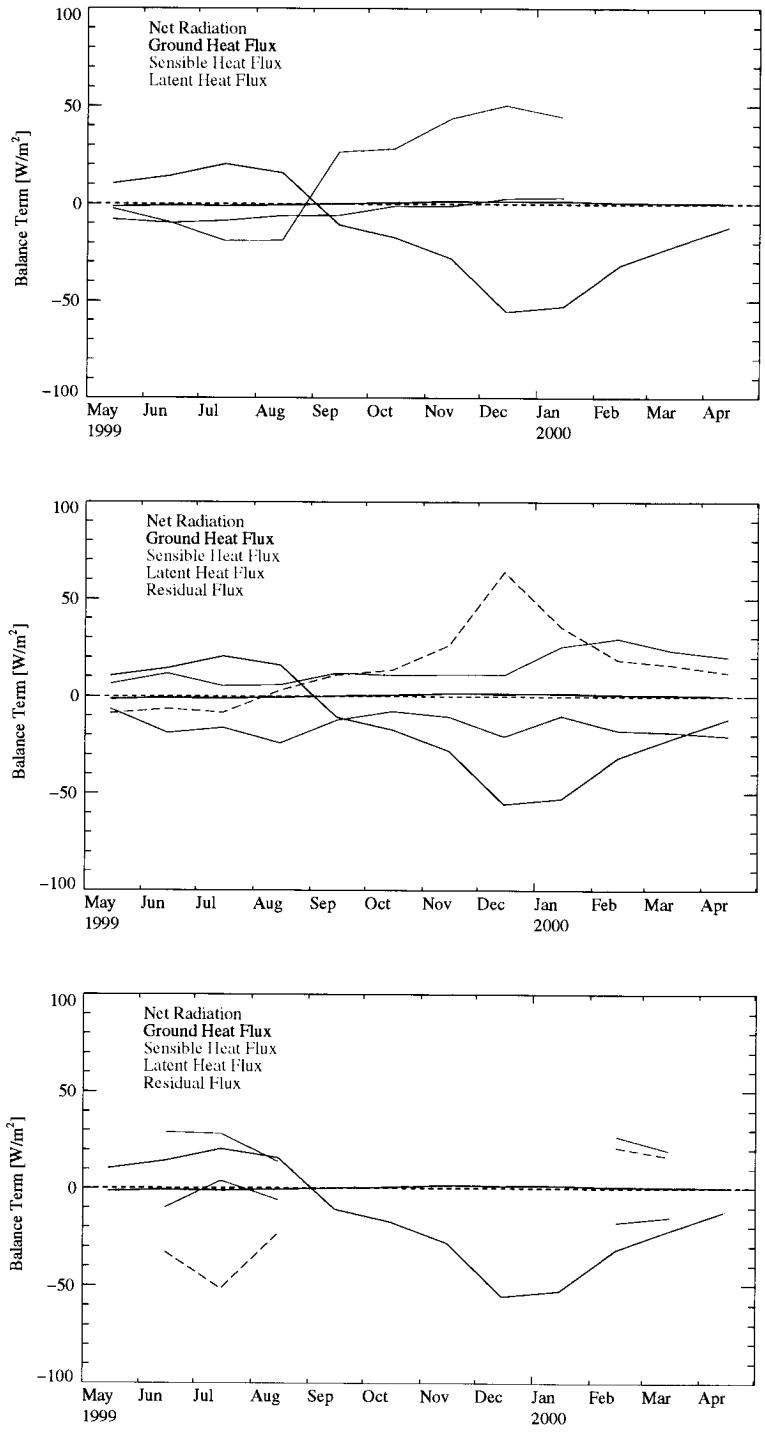

Figure 4.25: Monthly mean energy balance from May, 1999 to April, 2000 at Seserjoch using the Bowen-ratio (upper panel), bulk (middle panel) and profile (lower panel) methods. Data gaps are due to missing daily mean values which made it impossible to calculate a monthly mean.

The useful data calculated with the profile method are sparse. In the direction of the flux, they adequately depict the conditions as calculated with the bulk method, but the magnitude of the fluxes is higher in summer.
As a summary it can be stated that the cold firn saddle of Seserjoch shows predominantly negative fluxes of net radiation and latent heat and positive fluxes of

Table 4.5: Summary of the monthly and yearly mean energy-balance fluxes at Seserjoch showing the net radiation (NR), sensible heat flux (SHF), latent heat flux (LHF), ground heat flux (GHF) and residual heat flux (RES). The turbulent fluxes are derived from the Bowen-ratio, bulk and profile methods. The fluxes are given in W/m^2

Time	NR	SHF Bowen	SHF Bulk	SHF Profile	LHF Bowen	LHF Bulk	LHF Profile	GHF	RES Bowen	RES Bulk	RES Profile
May 1999	10.4	-2.4	6.3		-8.0	-6.5		-1.4		-8.8	
Jun 1999	14.3	-9.5	11.6	29.0	-9.8	-18.8	-9.9	-0.7		-6.4	-32.8
Jul 1999	20.4	-19.0	5.2	28.3	-8.7	-16.2	3.9	-1.1		-8.4	-51.6
Aug 1999	15.9	-18.7	5.7	13.8	-6.1	-24.1	-6.0	-0.5		3.0	-23.2
Sep 1999	-10.8	26.7	11.8		-5.8	-12.2		0.2		10.9	
Oct 1999	-17.2	28.3	10.8		-1.1	-7.7		0.7		13.4	
Nov 1999	-28.1	43.8	11.0		-1.1	-10.6		1.5		26.2	
Dec 1999	-55.6	50.5	10.9		2.8	-20.7		1.3		64.0	
Jan 2000	-52.7	44.7	25.6		3.3	-10.0		1.5		35.6	
Feb 2000	-31.5		29.7	27.0		-17.6	-17.5	0.8		18.6	21.2
Mar 2000	-21.7		23.4	19.5		-18.5	-14.9	0.6		16.1	16.5
Apr 2000	-11.7		20.0			-20.4		0.2		11.2	
Mean	**-14.0**	**16.0**	**14.3**		**-3.8**	**-15.3**		**0.3**	**1.6**	**14.7**	

sensible heat, whereas the direction of the sensible heat flux is not so clear during the summer months depending on the presence or absence of melt. The numerical values (monthly and yearly means) of the fluxes are given in Table 4.5.

4.5 Conclusions

Net Radiation

- Apart from the months of May to August, the net radiation at Seserjoch is negative and constitutes an important energy sink mainly due to a high year-over albedo and a low longwave incoming radiation.

Turbulent Fluxes

- Although the comparability in magnitude of the sonic-derived sensible heat flux with the Bowen-ratio, bulk and profile methods is difficult – maybe as a consequence of a non-homogeneous vertical structure of the surface layer – the direction of the flux does agree.

- The comparability of the turbulent fluxes, determined with the three methods mentioned above, is sometimes difficult on a 10-minute time-scale. However, a much better agreement is found for daily mean values.

- The turbulent fluxes using the Bowen-ratio method have to be interpreted carefully during surface-melt or re-freezing events and during time windows with inaccurate radiation measurements.

- Due to the complex structure of the surface layer with non-ideal profiles of wind, temperature and humidity, the profile method is difficult to handle.

- Due to its instrumental and methodological simplicity, the bulk method meets the difficult conditions at Seserjoch best. Difficulties occur for the latent heat flux due to the assumption of a saturated surface layer which might not always be the case. Several levels of wind, temperature and humidity measurements are crucial, so that at least one level is operating and can be used for the flux calculation. In such difficult conditions as they occur at the Seserjoch site, only the bulk method was able to supply continuous flux calculations.

Subsurface- or Ground Heat Flux

- The subsurface heat flux over cold firn is a small quantity on a larger time-scale. As the yearly mean is positive (Table 4.5), the near-surface snow and firn is cooling down for the period of observation from May, 1999 to April, 2000 (cf. Section 6.4.2).

Melt and Re-freezing

- Melt and re-freezing processes are a very important energy-balance contribution on a daily time-scale, especially during melt or re-freezing events in summer or during hoar-frost events in winter, and cannot be neglected on the monthly time-scale, either.

- The problem in the quantification of the melt or re-freezing heat flux arises from the fact, that it could not be determined directly from measurements. As it is derived indirectly from the residual heat flux of the energy balance, it is rather insecure as all the errors of the energy-balance calculation are comprised in the residual flux.

Energy Balance

- The observed energy fluxes at Seserjoch are large on a daily time-scale, when the high net radiation around noon and during night has to be compensated by turbulent fluxes or melt- and re-freezing-energy fluxes. However, on the monthly or yearly time-scale, the energy fluxes of the single components did not exceed $60\,\mathrm{W/m^2}$.

- On the monthly or yearly time-scale, the major contribution to the energy balance comes from the net radiation, sensible and latent heat flux.

5 Spatial Occurrence of Cold Firn

5.1 Objectives and General Proceeding

One goal of the present study was to systematically investigate the occurrence of cold firn in space and its dependence on climatic and topographic variables. Therefore, the englacial temperature measurements were made

1. to measure a mean annual firn temperature (see Sections 1.2 and 6.1.3);
2. to cover an altitude band as large as possible;
3. to choose sites with varying climatic and topographic conditions;
4. to detect an altitude-dependent boundary between cold and temperate firn and
5. to compare the present-day firn temperatures and cold firn occurrence with earlier observations and models.

The measurements were carried out to a depth of about 22 m to ensure the detection of a mean annual firn temperature and within a wide variety of different aspects, slope angles, topographic geometries and within an altitude band as large as possible. Additionally, the accumulation was observed at the stakes of the firn-temperature measurements where possible.

5.2 Data Acquisition and Analysis

5.2.1 Steam Drilling

Steam drilling is a very efficient and easy way of drilling into firn down to depths of about 30 m. A light-weight system (*Heucke ice drill*) was used in the Mont Blanc and Monte Rosa areas due to the high altitude. The steam drill itself weighs less than 7 kg and was used together with 22 m of insulated drill hose (12 m and 10 m parts) and 15 kg gas cylinders. The drill has a capacity of 4 liters of water which was mostly sufficient for a 22 m drill. The operating pressure was around 0.8 bar with a maximum pressure of 1.8 bar. A jet of 34 mm diameter was used which resulted in a borehole diameter of about 40 mm. The drilling hose was steadily prolonged in the course of the drilling to speed up the drilling procedure. The typical drill time for a 22 m hole was between 40 minutes and 2 hours depending on the firn density and the weather conditions (wind), but typically in the range of 60 to 90 minutes. The maximum depth drilled was about 30 m. Below that depth, an insulated 40 m hose had to be used and the drill system turned out to be too much affected by pressure drop and heat loss along the hose so that a depth of about 30 m seems to be a limit to this drill system in cold firn. Figure 5.1 shows the steam-drill equipment at the 4807 m high Mont Blanc summit. The envisaged depths of 22 m could not always be reached, especially when drilling into massive firn or ice on exposed ridges or saddles. At these sites, the meltwater could not diffuse into the porous snow or firn any more and a water column was formed in the borehole. During the drilling process, the hot steam melts or sublimates the firn in its immediate vicinity and the liquid

Figure 5.1: Steam drilling at the 4807 m high Mont Blanc summit in June, 1998. Photo taken by S. Suter.

or gaseous water diffuses into the surrounding porous firn, where it re-freezes within the nearest centimeters or at the borehole side-walls due to subzero temperatures.

5.2.2 Methodology

Instrumental Setting

A common way to measure temperatures in an industrial and scientific context is the use of *thermistors*. Thermistors are mixed metal-oxide semiconductors. The name is derived from 'thermally sensitive resistor'. In this study, NTC-thermistors were used which have a *n*egative *t*emperature *c*oefficient of resistance, ie a steep drop in resistance for an increasing temperature providing a high sensitivity to small temperature changes. The measured resistances are converted into temperatures using an empirical mathematical expression for the resistance-temperature relationship (see Section 5.2.3).

The instrumental setting of the firn-temperature measurements comprised six different thermistor chains (A–F) and 4 data-logging units ('stations'). The chains A, B and C and their corresponding stations were designed for a mobile use, ie they were used for open-borehole measurements and removed after measuring, whereas the chains D, E and F were permanently installed at the Seserjoch energy-balance site (see Section 4.2).

The thermistor chains were manufactured at *Stump Bohr AG, CH-Nänikon*, a geotechnical instrumentation and drilling specialist. The chains A–C each have 15 thermistors soldered onto a 16-wire cable with an effective length of 30 m and a sensor interval of 2 m. The accuracy in sensor position was specified to ± 0.5 cm by the manufacturer. The shield of the PVC-cable was used as a common ground for all thermistors. A silicon mass, glue and heat-shrink tubing were used to seal the thermistors and to protect them against external mechanical damages and water

infiltration. The thermistors were of the type *YSI 44006* with a 0 °C resistance of 29490 Ω, a resolution of 1370 Ω/°C at 0 °C and an accuracy of ±0.2 °C at 0 °C (according to the manufacturer's specifications).
The thermistor chains *D–F* were assembled in a similar way with the exception of using a 30-wire cable for the 15 sensors to assure an individual ground for each sensor. The chains *D* and *E* had an effective length of 30 and 15 m, respectively and a sensor interval of 1 m. They were installed within the same borehole to have a 30 m deep measurement at a 1 m resolution. The chain *F* had an effective length of 4 m and was equipped with 15 sensors at an interval of 0.25 m (see Section 4.2).
The three stations *A*, *B* and *C* provided the measuring circuit and the data storage for the thermistor chains *A*, *B* and *C* using each a *Campbell CR10X data logger* and a *Campbell AM416 multiplexer* to make full-bridge measurements on the thermistors. The three stations were designed to cover the temperature ranges of approximately 0 – -6.7 °C (station *A*), -6.7 – -13.3 °C (station *B*) and -13.3 – -20 °C (station *C*) using a measurement range of ±25 mV with bridge resistors of 33000, 47000 and 68000 Ω, respectively. The small measurement range guaranteed a high resolution over a small signal range and, thus, the highest possible accuracy over the given temperature range. To make the different stations and their corresponding chains universally applicable (ie over the whole temperature range of 0 – -20 °C), an additional measurement in the range of ±250 mV was made at each run and the data stored on the data logger. The stations were powered with a 12 V battery.
Due to the number of 45 sensors at the energy-balance site of Seserjoch, a data logger with two multiplexers was used for the temperature measurement of the chains *D*, *E* and *F*. Again, a full bridge was applied using the 25 mV range and the same bridge resistors as above with an amplifier on an extra board. Data-logger control ports selected the three different bridges at each run and the values of the three ranges were stored on the data logger.

Thermistor Calibration and Accuracy

The accuracies of the thermistors given by the manufacturer can considerably be improved by a calibration in a cold bath. Therefore, each instrumental set (thermistor chain and station) was individually calibrated before or after use in the field. The cold bath was installed in a cooling chamber and the air temperature kept more or less at the bath temperature to avoid large temperature gradients.

Calibration

The 0 °C calibration was made in an ice-water mixture for all the chains. In the subzero temperature range, the chains *A–C* were calibrated in a mixture of water and anti-freeze using a *Julabo circulation chiller* of the type *VC/3f. F18* and a temperature measuring device of the type *Therm 2284-8* with four external sensors. The circulation chiller had a warranted temperature stability of ±0.02 °C. The four sensors of the temperature measuring device were calibrated at the *Swiss Federal Office of Metrology* in 1996. Their accuracy was certificated to ±0.03 °C in the range 0 – -10 °C and to ±0.04 °C in the range -12.5 – -20 °C. The four external sensors were used to control the bath and air temperature. They were taken as a reference for the absolute bath (thermistor) temperature. Apart from the calibration at 0 °C, the chains *A–C* were calibrated at (chiller) temperatures of -5 and -9 °C. Readings

were taken after perfect thermal adjustment of the sensors for a typical time span of 15 minutes (at a 1 minute sampling rate) and mean values calculated for the bath temperature and the measured resistances.
The chains *D–F* were calibrated in a mixture of methanol and water using a *Lauda circulation chiller* of the type *RC 6 CP* with a force-/suction pump for the use of an external bath so that the whole chain could be immersed into the liquid. A *Pt-100 temperature sensor* was used to regulate the external bath temperature. The warranted temperature stability of the circulation chiller was ±0.01 °C. The same temperature measuring device was used as above. The chains *D–F* were calibrated at (chiller) temperatures of -3.5, -6.7, -13.3 and -17.9 °C. Again, readings were only taken after perfect thermal adjustment of the sensors for typically half an hour (at a 1 minute sampling rate) and mean values of bath temperature and resistances taken for further analysis.
The chains *B* and *C* were subsequently calibrated at approximate temperatures of -7, -10.1, -13.1, -15.1 and -17.1 °C. A circulation chiller of the type *Huber CC245* with a 22 l (internal) bath and a warranted bath stability of ±0.02 °C was used this time. Ethanol of 97 % purity was taken as bath liquid. Otherwise the proceeding was the same as above. This calibration was used for the purpose of borehole-thermometry measurements (see Section 6.3).

Accuracy
The accuracy of the calibration is determined by the following criteria:

- the stability of the cold bath
- the resolution and accuracy of the station (data logger)
- the characteristics of the thermistors and the cable
- the absolute accuracy of the temperature measuring device

The *stability of the cold bath* is a function of the thermal stability of the circulation chiller (see above), the effectiveness of liquid circulation within the cold bath, the thermal properties of the calibration liquid (thermal conductivity and specific heat capacity) and ambient factors (eg temperature gradient between bath liquid and surrounding air). The effectiveness of liquid circulation and exchange in the external box is a function of the power of the force-/suction pump. Although the circulation chiller used had a very effective pumping system of 16–20 l/minute, a loss in bath stability has to be expected, so that it might be somewhat worse than ±0.01 °C. No stability problems should occur within a water-ice mixture and, therefore, no forced circulation is necessary. The thermal conductivity and heat capacity of methanol are 67 and 40 % smaller than the corresponding values for pure water so that a somewhat worse bath stability must be assumed. The effect is weakened by the fact that a mixture between methanol and water was used where the methanol fraction may not have exceeded 30 %. Ambient factors were suppressed by using a coverable insulated box as external bath and by keeping the surrounding air temperature as close to the bath temperature as possible (maximum deviation of 5 °C, but generally less than 1-2 °C). The thermal stability within the cold bath can be checked when looking at the timely evolution of the measured bath temperatures during the calibration procedure. In case of the chains *A–C* it was well within ±0.01 °C, whereas

it was somewhat worse for the chains *D–F*, apparently due to the use of an external bath (±0.01 °C at a bath temperature of -3.5 °C and up to ±0.025 °C at -17.9 °C).

The *resolution and accuracy* of the station is a function of the range and accuracy of the data-logger voltage measurement and the selected fixed resistors within the 4 wire full bridge (see above). The mean resolution of the measurements varies between 0.4 and 0.7 mK (-25 – +25 mV range) and between 3 and 10 mK (-250 – +250 mV range). The accuracy of the station is given by the accuracy of the excitation voltage used (500 ±2 mV), the range of the voltage measurement (±25 or ±250 mV) and the accuracy of the fixed bridge resistors (±0.1 %) and their temperature stability (3 ppm). The data-logger voltage measurement within a radiometric bridge measurement has an accuracy of ±0.02 % of the full scale range and over the entire temperature range, so that the error within the ±25 mV range is less than a thousandth of a degree and a few thousandth of a degree in the ±250 mV range. The fixed bridge resistors used have a very high temperature stability in a way that this effect can be neglected over the temperature range (20 – -20 °C) observed. Despite of the relatively large tolerance of the fixed bridge resistors (±0.1 %), the possible shift in the transformation of the measured voltages into resistances due to an unequilibrated bridge is systematic and considered within the calibration so that no additional errors occur. Nevertheless, the bridges were tested against high-precision fixed resistors to check the absolute accuracy of the measuring circuit. The precision of the fixed resistors (±0.01 % tolerance) lies within ±2 mK. It turned out that the bridges of the stations *A–C* were generally very well equilibrated and the measured values of the high-precision fixed resistors were all lying within the tolerance range, apart from the high resistances of the station *A*.

The *thermistors* used have a tolerance of ±0.2 °C at 0 °C as given by the manufacturer. As the thermistors are subjected to a calibration, this issue is of minor importance. If thermistors are intended for a long-term use (several years), and if they cannot be re-calibrated, aging can be important. The YSI-44006 thermistors are chemically very stable and the thermometric drift is less than 0.01 °C over 100 months so that aging can be neglected. The current over the measurement bridge is small, so that self-heating effects exerted on the thermistors are on the order of a few thousandths of a degree at worst and can be neglected as well. The *cable* between the data logger and the thermistor can act as an additional resistor and alter the measured resistance. As only short cables (maximum length of 40 m) and thermistors with high resistances (about 29000 to 80000 Ω in the temperature range observed) were used, the cable resistance is about 2 Ω in the worst case which leads to a maximum error of 1.5 mK at 0 °C.

Taking into account the above mentioned limitations and errors, the *absolute accuracy* of a thermistor measurement is given by the accuracy of the temperature measuring device as the uncertainty range of the other effects is smaller and can, therefore, be denoted with ±0.03 °C (0 – -10 °C) to ±0.04 °C (-12.5 – -20 °C).
The *relative accuracy* between the thermistors or of one and the same thermistor using the same measuring bridge is much higher, however. The relative accuracy between the thermistors of the same chain can be denoted with ±0.02 °C

(-250 – +250 mV-range) and ±0.012 °C (-25 – +25 mV-range). This accuracy comprises effects such as bath stability, resolution and accuracy of the data logger and cable resistance. The accuracy of one and the same thermistor is only limited by the resolution and accuracy of the data logger and can be denoted with ±0.01 °C (-250 – +250 mV-range) and ±0.001 °C (-25 – +25 mV-range).

Borehole-Temperature Measurements in the Field

After the drilling procedure, each borehole was equipped with a coverable plastic tube of 0.5–1 m length at the surface as a protection against mechanical instabilities or snow drift.

During a measurement in the open borehole, an insulating rubber foam was inserted between the thermistor chain and the plastic tube and sealed with adhesive tape at the surface to guarantee an optimum closing against snowdrift or immediate near-surface air circulation in the borehole, due to air-pressure fluctuations at high wind speeds. This procedure could not completely avoid in-borehole temperature fluctuations due to pressure-induced air circulation commonly referred to *wind pumping*. The effect of *convection* within an air-filled borehole can be estimated with (Zotikov, 1986):

$$\left(\frac{dT}{dz}\right)_{\mathrm{cr}} = -\Gamma + 216\frac{\nu\kappa}{glr^4}\ , \tag{5.1}$$

where $\left(\frac{dT}{dz}\right)_{\mathrm{cr}}$ = critical temperature gradient for air circulation with an axis-symmetrical flow, Γ = dry-adiabatic lapse rate (0.01 °C/m), ν = kinematic viscosity, κ = thermal diffusivity, g = acceleration due to gravity, l = coefficient of thermal expansion and r = borehole radius. As the diameter of a steam-drilled borehole did not exceed 6 cm and when taking typical values for ν, a and l in an air-filled borehole (Zotikov, 1986), a critical temperature gradient of about 1 °C/m results. Such a high gradient was never observed below the depth of annual temperature variations and extremely seldom within the layer of annual variations. Thus, it can be concluded that convection within an air-filled steam-drilled borehole does not occur.

The measurements in the steam-drilled open boreholes were typically made for 12 to 24 hours at a 10- to 15 minute sampling rate. Thermal adjustment of the thermistors to the ambient temperature conditions was normally found after 4 to 5 hours. The relatively large thermal inertia of the sensors is due to their wrapping in thermally insulating material and the low thermal conductivity of 0.025 W/(m·K) of the surrounding (still) air.

A steady installation of the thermistor chains was made in case of the temperature measurement at the energy-balance site of Seserjoch. With time, the original reference surface was increasingly covered with snow and firn and a perfect sealing against surface influences was obtained within the borehole.

The chains were lowered into the boreholes in a way to have the uppermost thermistor aligned with the surface. The accuracy in the surface position of the uppermost sensor was estimated to be better than ±4 cm. A weight was attached at the bottom of the chain to have it ideally stretched. At the surface, the chain was tied around a stake to fix it.

5.2.3 Data Analysis

Converting Resistances into Temperatures

Measured resistances are converted into temperatures using the Steinhart-Hart equation

$$\frac{1}{T} = a + b \cdot \ln R_T + c \cdot \ln^3 R_T \ , \tag{5.2}$$

where T = temperature [K], R_T = resistance [Ω] and a, b, c = calibration coefficients. The Steinhart-Hart equation is the best mathematical representation of the resistance-temperature relationship of NTC-thermistors. When a resistance is measured at 3 reference temperatures at least, the 3 coefficients can be determined from the above equation for each thermistor individually. Thus, each thermistor has its own calibration curve and a most precise representation of its resistance-temperature relationship. The calibration temperatures should be more or less evenly spaced and cover the desired measurement range. The closer the measured temperature is to the reference temperature, the better the absolute accuracy (see Section 5.2.2). In case of the chains *A–C*, the reference temperatures of approximately 0, -5 and -9 °C were taken, whereas three individual calibration curves were considered for each single thermistor of the chains *D–F* using the three temperature sets of 0, -3.5 and -6.7 °C; 0, -6.7 and -13.3 °C and 0, -13.3 and -17.9 °C according to the measured temperature. For the thermometric application of the chains *B* and *C*, the calibration temperatures of approximately -7, -10.1 and -13.1 °C (chain *B*) and of approximately -13.1, -15.1 and -17.1 °C (chain *C*) were taken to calculate the calibration coefficients a, b and c (see Section 6.3).

Effect of the Different Voltage Ranges

During the calibration procedure of the chains *A–C*, the effect of using different measurement ranges (±25 or ±250 mV) turned out to be quite small (2.5–6.8 mK on average). As only a 3-point calibration was made for the chains *A–C* covering a rather large temperature range and as the differences between the two voltage ranges were very small, only the values measured within the ±250 mV-range were taken for the temperature measurements in space. For the chains *D–F* and for the thermometric application of the chains *B* and *C* (see Section 6.3), the small voltage range was taken to have best resolution and accuracy.

Extrapolation Procedure

Steam drilling into cold firn or ice disturbs the temperature distribution in the close surroundings of the borehole. Therefore, a certain time must elapse until the temperatures have adjusted to the previously undisturbed conditions. The time for complete adjustment within a measuring accuracy of 0.1 °C can be on the order of a few days up to about two weeks (Laternser, 1992). Thus, extrapolation of continuous readings right after drilling is an easier and quicker way to obtain the final (undisturbed) temperatures. This procedure was applied to all the temperature measurements in steam-drilled boreholes with no permanent installation of a thermistor chain.

The drilling procedure into cold firn or ice can be considered as an immediate perturbation (energy input) along a linear line (the borehole). The model concept of an *instantaneous line source* seems to be a good approach in case of steam drilling.

The drilling time is assumed to be infinitely small and the energy input at a certain depth occurs at once. In case of steam drilling, it is the energy input by the drill tip, whereas the additional energy input caused by the insulated drill hose in the course of the drilling is rather small. In a homogeneous infinitely expanded medium, the temperature field around a line source can be written as (Carslaw and Jaeger, 1959)

$$\Delta T(r,t) = \frac{Q}{4\pi Kt} \cdot e^{\left(\frac{-\rho_f c_i r^2}{4Kt}\right)} , \tag{5.3}$$

where $\Delta T(r,t)$ = temperature difference between disturbed and undisturbed ambient temperature, r = distance (radius) from line source, t = time since energy input, Q = energy input per unit length, K = thermal conductivity of firn, ρ_f = firn density and c_i = specific heat capacity of ice. As only the temperature along a central line of the borehole is of interest, r equals 0 and if $\Delta T(r,t)$ is written as $T(t) - T_f$, the temperature at time t after drilling is (Lachenbruch and Brewer, 1959)

$$T(t) = \frac{Q}{4\pi K} \cdot \frac{1}{t} + T_f , \tag{5.4}$$

where T_f = undisturbed temperature or final temperature. Thus, $T(t)$ is proportional to $\frac{1}{t}$ and the final temperature T_f is the shift on the temperature axis and can be found at $\frac{1}{t} = 0$ for $t \rightarrow \infty$. In theory, each depth would have a specific t defining the time, which elapsed since the drill tip reached the corresponding depth. As the drilling time was rather short (typically 60 to 90 minutes) as compared to the sampling duration of 12 to 24 hours and as the measurement was only made several hours or even a day or more after drilling in most cases, the same t was taken for the whole depth range and defined as the time which elapsed, since the end of the drilling and the measurement.
After the insertion of the thermistor chain into the borehole, two effects of adjustment can be observed:

1. the thermal inertia of the thermistor in adjusting to the ambient temperature;
2. the actual recording of the decreasing thermal perturbation caused by the steam drilling.

At the beginning, these two effects cannot be separated. The thermal inertia of the thermistor in adjusting to the ambient temperature can be expressed with the following exponential relation

$$T(t) = T_f + (T_b - T_f) \cdot e^{-\frac{t}{\tau}} , \tag{5.5}$$

where $T(t)$ = temperature at time t, T_f = final temperature, T_b = starting temperature and τ = time constant. The *time constant* τ is a measure for the thermal inertia of a sensor and defined as the time until the sensor has adjusted to the final temperature to within 1/e of the total temperature change. In case of thermistors, τ is mainly a function of the thermal insulation of the thermistor and the medium where the temperature is measured in. As can be seen in the above equation, the starting temperature T_b is also of importance. The larger the difference between starting temperature and final temperature, the longer the time until $T(t)$ equals the final

temperature T_f. The time constant τ could be determined experimentally in the field when measuring in a thermally undisturbed borehole. Such measurements under perfect conditions (practically no wind) showed that the thermal adjustment to the ambient conditions was reached 4 to 5 hours after inserting the thermistor chain. Thus, for the linear extrapolation, the first 5 hours of data were generally omitted to avoid any effect of thermal inertia. As in extreme cases a perfect thermal adjustment

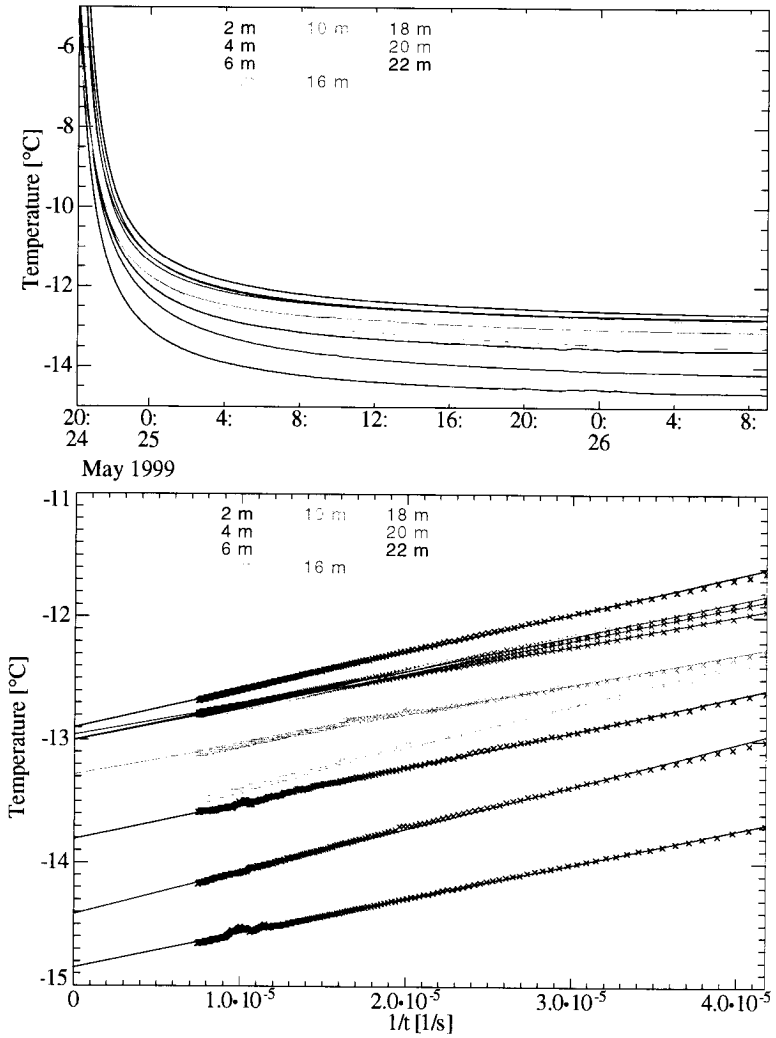

Figure 5.2: Linear extrapolation of the borehole temperatures at borehole 10 *(4330 m a.s.l.) in the Monte Rosa area. The upper panel shows the adjustment of the borehole temperatures versus time. Note the steep curves at the beginning which are due to the thermal inertia of the thermistors. Later on, the adjustment is smoother and reflects the thermal disturbance, alone. The lower panel shows the temperatures versus 1/t. A good linear relation results and correlation coefficients are all higher than 0.99.*

of the thermistors was only reached after 9 hours, the extrapolation was made using 5 data sets where the first 5, 6, 7, 8 and 9 hours were omitted, respectively. The final temperature with the best linearization (highest correlation coefficient) out of these 5 runs was finally taken. Below 10 m depth, the differences between the 5 runs were generally small and typically below 0.01 °C. Under strong wind-pumping con-

ditions, variations were larger and on the order of a few hundredth up to a tenth of a degree at worst. However, values below 10 m depth were practically never affected by wind pumping (see Section 6.1.1). Sometimes further data had to be omitted when strong wind pumping occurred.
A typical extrapolation result from a borehole in the Monte Rosa area is presented in Figure 5.2. The steep adjustment of the thermistors at the beginning – mainly due to thermal inertia – can be clearly distinguished from the smoother adjustment to the thermal disturbance alone.
When temperatures were measured in thermally undisturbed boreholes, the first 3 to 5 hours of data were omitted until thermal stability was given, and a mean value was finally taken. Repeated measurements could be made under disturbed conditions using the linear extrapolation method and under undisturbed conditions after perfect thermal adjustment for one borehole in the Mont Blanc area (borehole 6) and for two ones in the Monte Rosa area (boreholes 21 and 24). The measurements were repeated after 1.5 and 6 weeks, respectively. Below 10 m depth (where a short-term variation due to seasonal temperature changes can be excluded for the period considered), the maximum differences between the extrapolated and undisturbed values were 0.12 (Monte Rosa) to 0.15 °C (Mont Blanc). As quite a strong wind pumping occurred during the 'undisturbed' measurement in the Mont Blanc area, the extrapolated temperatures may generally represent the undisturbed conditions with an accuracy better than ±0.1 °C.
In case of boreholes 1 and 2 from the Mont Blanc area, a few (hand) measurements were made right after inserting the chain into the borehole and an exponential extrapolation procedure was applied to find the undisturbed temperatures (see Section 5.3.1). Care must be taken when the duration of the thermal disturbance is largely prolonged by liquid water that remains in the borehole after the drilling process. In four cases, the drilling procedure was substantially slowed down when a water column was formed in the borehole on exposed ice ridges and steep flanks with more or less bare ice. The water column re-froze quickly after drilling and temperatures could only be measured at shallow depths (see Sections 5.3.1 and 5.3.2).

5.3 Results

A compilation of the field results from the Mont Blanc and Monte Rosa areas is given in the Appendices A.1 and A.2. In the following, firn temperatures at 18 m depth will be taken as MAFTs and be used for statistical analysis (Section 5.4). The theoretical reasoning for taking a firn temperature at 18 m depth (*18-m temperature*) is given in Section 6.1.3. The interpolation of the firn-temperature and accumulation data was made using the TOPOGRID command within ARC/INFO. This command is based on an interpolation method specifically designed for the creation of hydrologically correct digital elevation models (Hutchinson, 1989). The interpolation algorithm uses an iterative finite difference spline interpolation technique (Wahba, 1990).

5.3.1 Mont Blanc Area

Borehole Locations

The locations of the borehole-temperature measurements were surveyed in June,

1998 using a *TOPCON Turbo-G1* portable GPS-device and post-processed with correction data from the reference station of Zimmerwald (CH). The so-received horizontal positions were subsequently checked with the Swiss topographic map 1:50'000. The GPS-elevations were verfied with measured elevations in the field using an altimeter and with the Swiss topographic map 1:50'000. The precision of the horizontal borehole locations can be denoted with a few meters and the precision of the elevations with ±5 m. No GPS-survey could be made for boreholes 20 and 21. Their location was estimated from the map. No repeated measurements were possible as the stakes could not be revisited later in the year.

Firn Temperatures

The result of the observed 18-m temperatures is given in Figures 5.3 and 5.4. The temperatures were obtained using a linear extrapolation (boreholes 4–22), an exponential extrapolation (boreholes 1 and 2) or no extrapolation at all (borehole 3). The temperature measurements from boreholes 2 and 3 represent temperatures

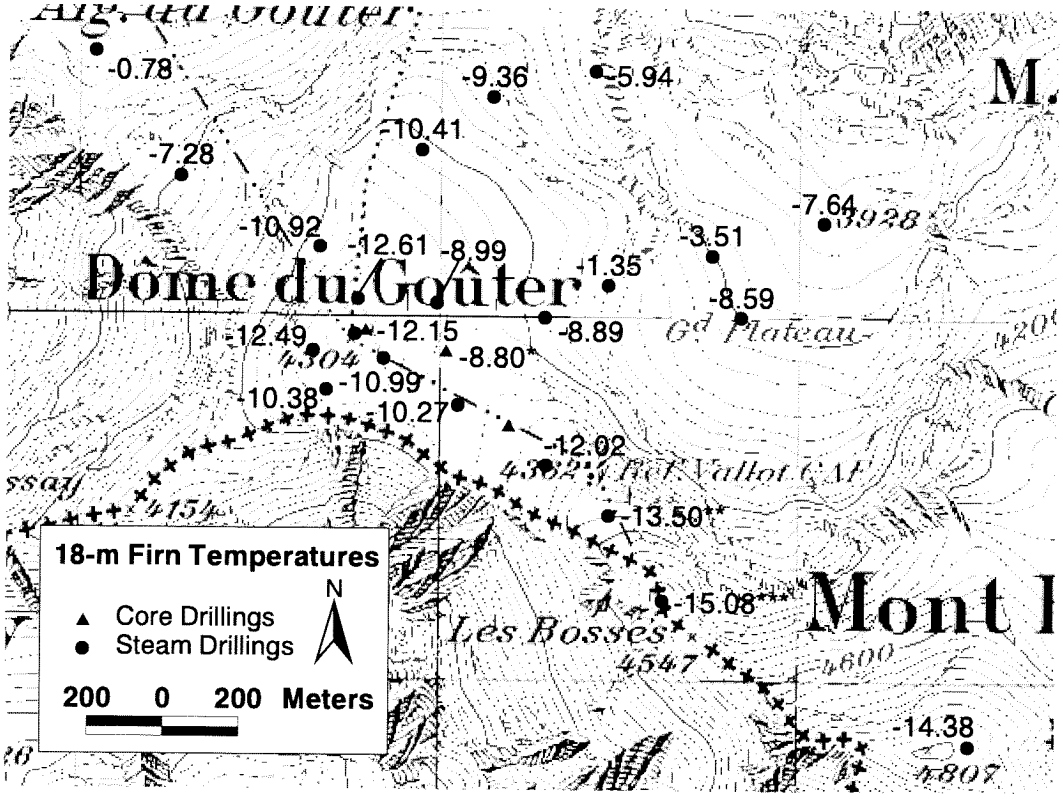

*Figure 5.3: Measured 18-m temperatures in the Mont Blanc area from 1998 showing single values. * denotes a value at 15 m depth (borehole* 94-A*) measured in 1994 (personal communication from C. Vincent, 1994): ** a value measured at 8 (borehole* 3*) and *** a value measured at 12 m depth (borehole* 2*) in 1998. Boreholes* 9 *and* 99-B *showed the same value of -12.15 °C at 18 m depth (see Figure 3.3 for locations). Map: PM50 ©Swiss Federal Office of Topography.*

at 12 and 8 m depth, respectively. Due to re-frozen meltwater in the boreholes after drilling into more or less massive ice, no temperature measurement below these depths was possible. Although the temperatures were not measured at 18 m depth

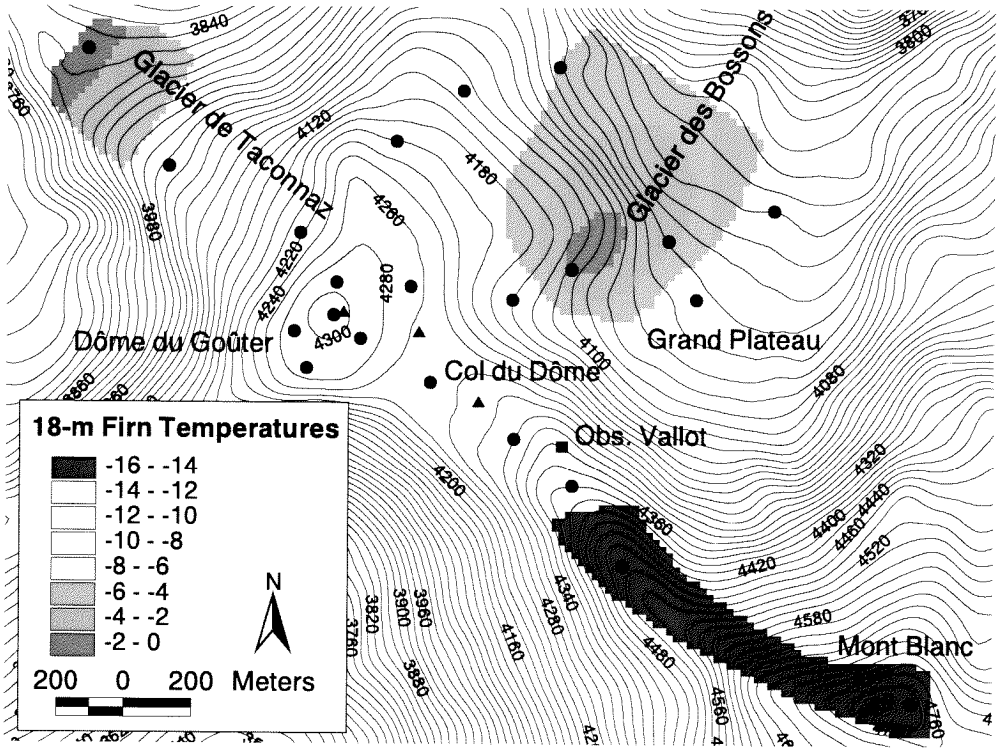

Figure 5.4: Measured 18-m temperatures in the Mont Blanc area from 1998 showing grid-interpolated values using a spline interpolation. The value from 1994 was not considered for the interpolation. See Figure 3.3 for borehole locations (black dots and triangles).

in these two boreholes, they were considered for further analysis as the observed temperature profiles in June were very close to equitemperature below 8 m depth. The 18-m temperature from borehole 6 is the mean between an extrapolated and a thermally undisturbed value (Section 5.2.3).

The measurements show a general trend to higher values with decreasing altitude. The 'hot' spot found at 4100 m a.s.l. on Glacier des Bossons is the result of a high value (-1.35 °C) observed at borehole 16. No errors could be detected during the measurement and data analysis so that the value is considered to be valid. The influence of a crevasse cannot be completely excluded, however. The relatively high value at the Mont Blanc summit of -14.4 °C is remarkable as compared to the observed firn temperatures at lower elevations and to earlier observations of -16.5 °C by Vallot (1893) and of -20.2 °C by Lliboutry et al. (1976), although the latter measurement is very likely to be influenced by a crevasse. Compared to earlier measurements, a warming could be observed at Col du Dôme (-12.8 °C in 1911 (Vallot, 1913); -10.3 °C in 1998), whereas a similar value was measured at Grand Plateau (-8.6 °C in 1998) as in 1974 (-7.3 °C; Lliboutry et al., 1976). The deep values at the foot of Mont Blanc could be due to cold snow deposition by avalanche activity. Temperate firn was found below 3800 m a.s.l. on Glacier de Taconnaz whereas the firn was still cold on the upper reaches of Glacier des Bossons at 3920 m a.s.l.

Accumulation

Due to the very bad weather conditions during the remainder of 1998, the stakes set in June, 1998 could not be revisited and, thus, no direct accumulation measurements be made. That's why an accumulation index was used for the following statistical analysis (see Section 5.4) distinguishing between weak (1), medium (2), heavy (3) and very heavy (4) accumulation as estimated from the topography and (supposed) mean wind velocities.

5.3.2 Monte Rosa Area

Borehole Locations

The locations of the borehole-temperature measurements from May and July, 1999 were surveyed using a *Leica GPS-device* with a reference station at Gornergrat in December 1998 (boreholes 1, 8 and 9) or a *TOPCON Turbo-G1* portable GPS-

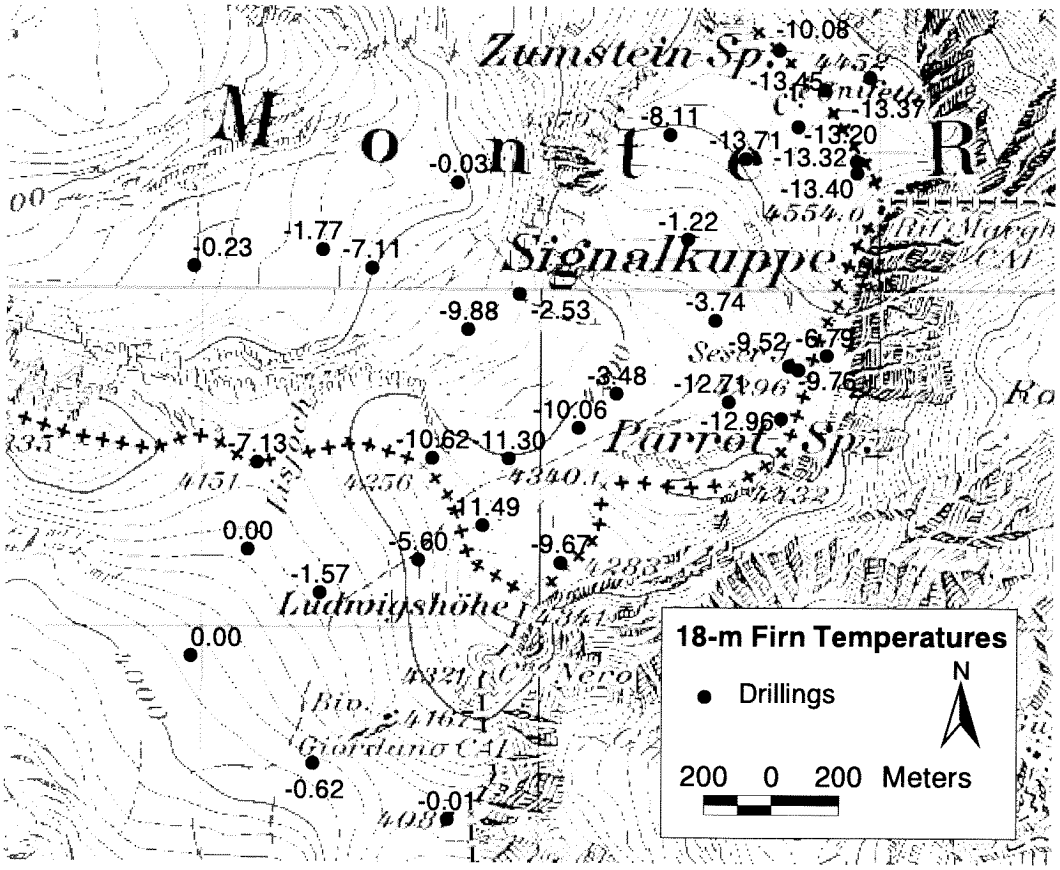

Figure 5.5: Measured 18-m temperatures in the Monte Rosa area from 1996 and 1999 showing single values. The two values from 1996 (boreholes 95-1 *and* 95-2*) are taken from Lüthi (2000). The values of boreholes* 2 *and* 00A *at Colle Gnifetti are identical (see Figure 3.5 for locations). Map: PM50 ©Swiss Federal Office of Topography.*

device (May and July, 1999) using correction data from the reference station of Zimmerwald (CH). The horizontal positions and the GPS-elevations were verfied with the Swiss land registry plan 1:10'000 or the Swiss topographic maps 1:25'000

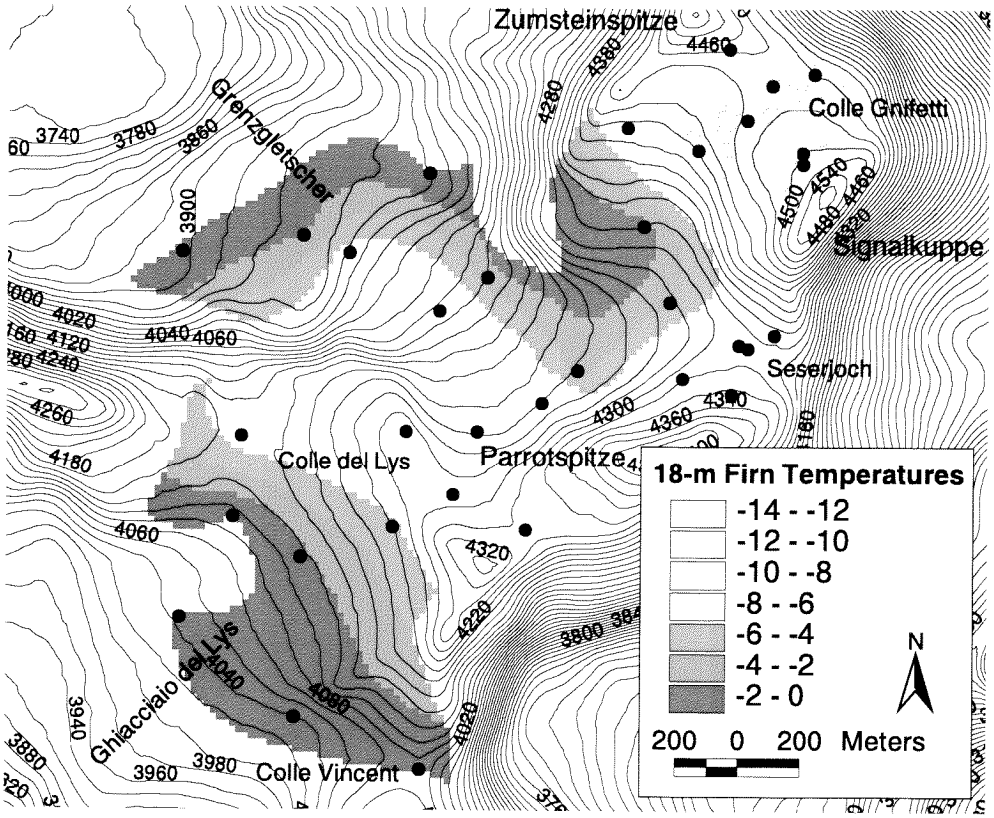

Figure 5.6: Measured 18-m temperatures in the Monte Rosa area from 1996 and 1999 showing grid-interpolated values using a spline interpolation. See Figure 3.5 for borehole locations (black dots).

and 1:50'000 and the elevations with additional altimeter measurements in the field. The precision of the Leica-survey can be denoted with ± 2 cm for the horizontal position and with ± 5 cm for the elevations. For the precision of the TOPCON-survey, the same can be stated as in Section 5.3.1. No GPS-survey could be made for boreholes 3, 4, 6, 7, 10, 11, 14, 17, 19 and 26. Their location was estimated from the maps. The location of borehole 0 (location of the energy-balance station) was determined photogrammetrically (Section 4.2.1). Most of the stakes set in May and July, 1999 disappeared by autumn 1999 and could not be re-surveyed.

Firn Temperatures

The 18-m temperatures were generally obtained using a linear extrapolation (Section 5.2.3). No extrapolation was made for the boreholes where a re-logging was made in July, 1999 due to no or erroneous measurements or where practically undisturbed conditions could be found in May, 1999 due to a long delay between drilling and logging (boreholes 13, 16, 18, 19, 20, 21, 22, 23 and 24). At borehole 8, only a value at 16 m depth could be measured due to re-frozen meltwater in the borehole. The value at the energy-balance station (borehole 0) is a mean value from May

31, 1999 and accumulation-corrected. The observed firn temperatures are given in Figures 5.5 and 5.6. On Grenzgletscher, the 18-m temperatures are strongly influenced by topography with deep values on shady slopes and at exposed firn saddles and crests. A surprisingly high value of almost -1 °C could be found on the steep south slope beneath Colle Gnifetti leading to extreme firn-temperature gradients within short distance. A more altitude-dependent firn-temperature distribution occurs on the gentle south slope of Ghiacciaio del Lys. The transition between cold and temperate firn can be found between approximately 3950 (Grenzgletscher) and 4050 m a.s.l. (Ghiacciaio del Lys). Compared to the observations in the early 1990s (Suter et al., 2001), strongly increased MAFTs could be observed on the steep south slope below Colle Gnifetti at 4250 m a.s.l. (+1.7 °C) and at 4300 m a.s.l. (+4.9 °C), whereas similar MAFTs were detected on Grenzgletscher below 4250 m a.s.l. in 1999.

Accumulation

The accumulation at boreholes 1–24 was estimated using the stake observations from May, 1999 to July, 1999 and the snow-height measurement at the Seserjoch energy-balance station (Section 4.3.9). For the extrapolation to a yearly accumulation rate, it was assumed that the accumulation follows a regular spatial pattern

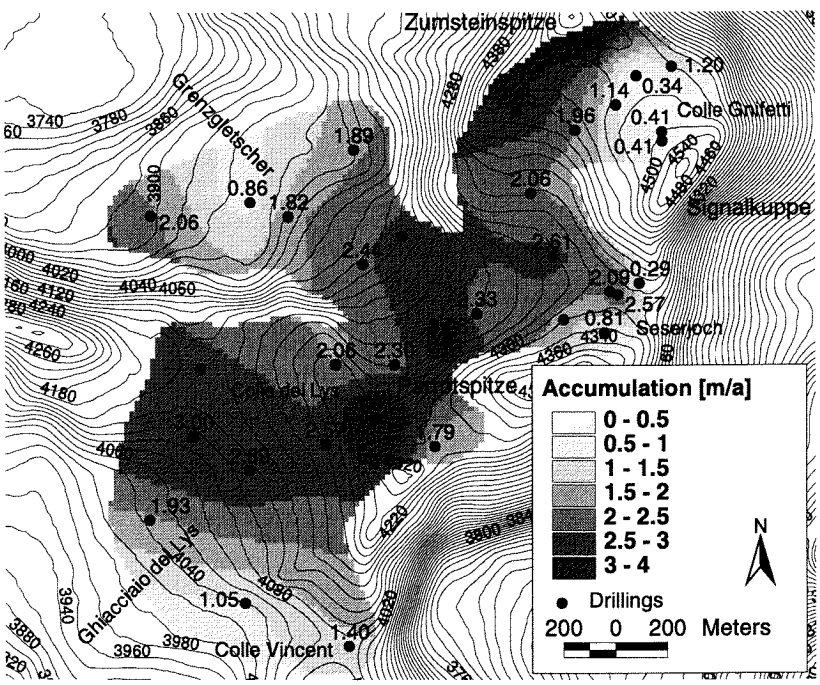

Figure 5.7: Extrapolated accumulation in the Monte Rosa area from June, 1999 to May, 2000 showing the yearly values at the stake points and grid-interpolated values using a spline interpolation.

over the year. Thus, the values observed between May, 1999 and July, 1999 at the above mentioned sites were extrapolated taking a conversion factor derived as the ratio of the Seserjoch accumulation between June 1, 1999 and May 31, 2000 (2.1 m

total accumulation) to the Seserjoch accumulation between June 1, 1999 and July 15, 1999. No stake observations could be made for boreholes 11 and 19. The values for boreholes 4 and 95-2 were taken from Lüthi (2000); the one for borehole 17 from the Colle del Lys meteorological station (personal communication from G. Rossi, 2000). No stake observations could be made for boreholes 25–31 on the Ghiacciaio del Lys in 1999. Instead, yearly accumulation rates from nearest stake points based on observations from September, 1997 to August, 1998 were considered (personal communication from G. Rossi, 2001) under the assumption of similar precipitating conditions during this period as from June, 1999 to May, 2000. The extrapolated yearly accumulation rates are shown in Figure 5.7. As in case of the Mont Blanc area (Section 5.3.1), an accumulation index was derived.

5.4 Statistical Analysis and Models

5.4.1 Theoretical Background

The following regression calculations are based on the assumption of independent observations and normally distributed residuals with uniform variances. Several statistical methods and tests were used to quantify the quality of the statistical validity:

- the *correlation coefficient* r ($-1 \leq r \leq 1$) describing the extent and direction of the correlative coherence;
- the *coefficient of determination* r^2 ($0 \leq r^2 \leq 1$) indicating the part of the variability which can be explained by the regression equation;
- the *F-Test* which carries out a variance analysis giving a relation between dependent variable and independent parameters within a certain error probability (normally 5 %) and
- the *p-value* being a measure for the significance:
  $p > 0.05$: non-significant;
  $0.05 \geq p \geq 0.01$: slightly significant;
  $0.01 \geq p \geq 0.001$: strongly significant;
  $0.001 \geq p$: very strongly significant.

A *simple linear regression* is based on a correlative relation between two quantities only and can be written as

$$y = a + b \cdot x + \epsilon \,, \tag{5.6}$$

where y is the dependent variable, x the independent variable, a and b denote coefficients and ϵ is the residual.
A *multiple linear regression* is used to combine various independent parameters and to analyse their joint effect on the dependent variable. A causal coherence between three or more parameters is presumed and can be written as

$$y = a + b \cdot x_1 + c \cdot x_2 + \ \ldots \ + \epsilon \,, \tag{5.7}$$

where y is the dependent variable, x_1, x_2, ... are independent variables, a, b, c, ... denote coefficients and ϵ is the residual.

A causal relation between dependent variable and independent variables was presumed. The statistical models are considered to be valid in the parameter space of the observations. They have a restricted validity for aspects in the range WSW-S-ESE and potential direct solar radiation exceeding 350 W/m^2 in the Mont Blanc study area due to a limited number of measurements in these aspects.

5.4.2 Further Input Data

Digital Elevation Models

A *digital elevation model (DEM)* is a cell-based representation of the elevation of the Earth's surface. It is used to extract topographic information such as aspect and slope and to calculate the potential direct solar radiation in the study area (see below).

The DEM for the Mont Blanc study area is based on aerial photographs of the Mont Blanc region from 1993 by the *Institut Géographique National (IGN)* in France. After orientating the images with the help of known base points, a digital photogrammetry software calculated a *triangular irregular network (TIN)* of surface points. Additional surface points were added manually to improve the model. Nevertheless, irregularities occurred in the vicinity of the relatively flat Dôme du Goûter, which made a manual correction based on the Swiss topographic map 1:50'000 inevitable. The DEM of the Monte Rosa study area was compiled using digitized contour lines from the 1977 land registry plan 1:10'000 for the Swiss part and merged with a DEM of the Italian Ghiacciaio del Lys based on aerial photographs from 1994 (personal communication from G. Rossi, 1999). The whole DEM was checked with a digitally derived model, based on aerial photographs by the *Swiss Federal Directorate for Cadastral Surveying* from 1999 and 2000 (for the interpretation of the aerial photographs see above). Again, problems occurred at flat topography (eg at Colle Gnifetti) and in the boundary region of the images. The coincidence was very good on the glaciers with steeper topography, in a way, that it can be assumed that no major changes in surface geometry occurred between 1977 and 2000.

The DEM-data were converted into grid data sets with a 20 m mesh resolution and into maps with 20 m contour lines within the *Geographic Information Systems (GIS) ARC/INFO* and *ArcView.*

Aspect and Slope

Topographic aspect and slope can be considered a good proxy-parameter for incoming solar radiation. The aspect- and slope information were derived from the corresponding DEMs for each borehole within ArcView or estimated from the map (aspect). The map-derived and GIS-derived aspects agreed very well. For the aspect, a coding system was used where north receives the smallest (1) and south the highest value (9). The aspects NW and NE (value 3) , W and E (value 5) and SW and SE (value 7) were considered symmetrical. No aspect was attributed to sites with a slope $\leq 4°$.

Potential Direct Solar Radiation

The potential direct solar radiation is an excellent approximation of the shortwave incoming radiation – major contribution to the surface energy balance and its spatial and temporal variation (eg Funk, 1985; Section 4). The potential direct solar

radiation was calculated for each borehole site using the grid-based computer program *SRAD* (Moore et al., 1993a and 1993b) within ARC/INFO and the DEM-data. The program calculates the radiation total on a daily basis and considers – besides aspect and slope angle – topographic shading. Additionally, atmospheric scattering, reflection and absorbtion are taken into account. For the following regression calculations, a daily mean value averaged over one year was calculated. Values normally ranged between 50 and 400 W/m^2 in the study areas.

5.4.3 Simple Linear Regression

The regression of the observed 18-m temperatures or MAFTs against elevation ($ELEV$) can be written as

$$MAFT = a + b \cdot ELEV \ , \tag{5.8}$$

where a denotes the intercept and b the slope. The statistical result is given in Table 5.1. Figure 5.8 gives the observed MAFTs plotted against elevation. In case

Table 5.1: Statistical results of the simple linear regression of the MAFTs against elevation (ELEV) for the Mont Blanc (MB) and Monte Rosa (MR) areas.

Area	r	r^2	F-Test	p-value	Equation
MB	-0.80	0.64	35.9	< 0.001	$MAFT = 52.7 - 0.0148 \cdot ELEV$
MR	-0.77	0.60	47.6	< 0.001	$MAFT = 92.4 - 0.0236 \cdot ELEV$

of the Mont Blanc area, 64 % of the variation of the MAFTs can be explained by the elevation alone; 60 % in case of the Monte Rosa area. An altitude-dependent

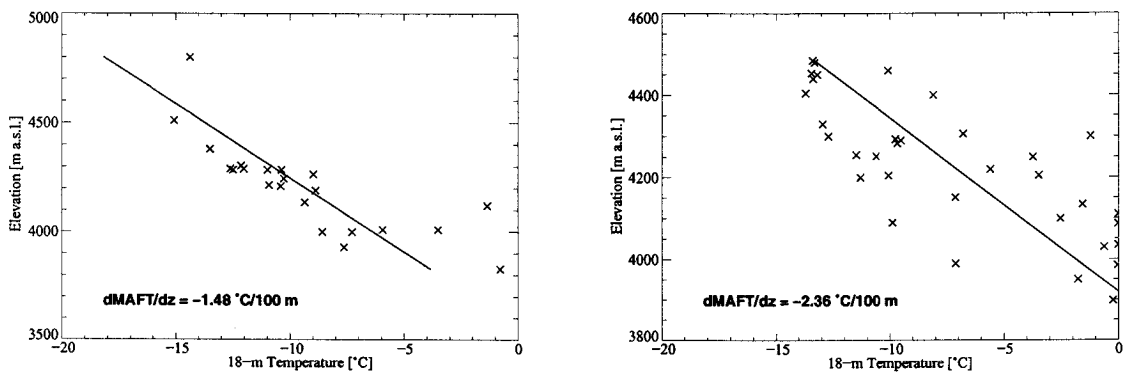

Figure 5.8: Observed MAFTs from the Mont Blanc (left panel) and Monte Rosa (right panel) areas as a function of elevation and calculated regression lines.

firn-temperature gradient of -1.48 °C/100 m and of -2.36 °C/100 m is found for the Mont Blanc and Monte Rosa areas, respectively. The boundary between cold and temperate firn lies at 3570 m a.s.l. in the Mont Blanc area and at 3920 m a.s.l. in the

Monte Rosa area. The large discrepancy in the gradients and in the lower boundary of cold firn occurrence is due to the underrepresentation of southerly aspects in the Mont Blanc sample and the relatively high 18-m temperature at the Mont Blanc summit and should not be interpreted climatologically (see Appendix A.1). If the high MAFT at the Mont Blanc summit is omitted and only values in 'cold' aspects (WNW-N-ENE) are regressed in both samples, the gradients are -1.90 °C/100 m in the Mont Blanc area and -2.14 °C/100 m in the Monte Rosa area. Compared to an earlier investigation (Suter et al., 2001), the altitude-dependent firn temperature gradients are higher in the current datasets.

5.4.4 Multiple Linear Regression

The relation between the dependent variable $MAFT$ and the independent variables elevation ($ELEV$), aspect (ASP), slope (SL), potential direct solar radiation (RAD), accumulation index ($ACCI$) and accumulation (ACC) is given as

$$MAFT = a + b \cdot ELEV + c \cdot ASP + d \cdot SL + \ \ldots \ , \tag{5.9}$$

where a denotes the intercept and b, c, d, ... respective slopes for the individual independent parameters. The statistical results for several parameter combinations are summarized in Table 5.2. All the multiple linear regression models show high correlation coefficients, coefficients of determination and F-Test-values and are very strongly significant. Care must be taken for the Mont Blanc area as southerly aspects are underrepresented which is critical when looking at aspect and radiation. This fact leads to generally better statistical results for the Monte Rosa area.
The easy to determine parameters elevation and aspect are able to explain 73–81 % of the variation of the MAFTs in the Mont Blanc and Monte Rosa areas, respectively (Figure 5.9). For the Monte Rosa area, an even better result is obtained when the

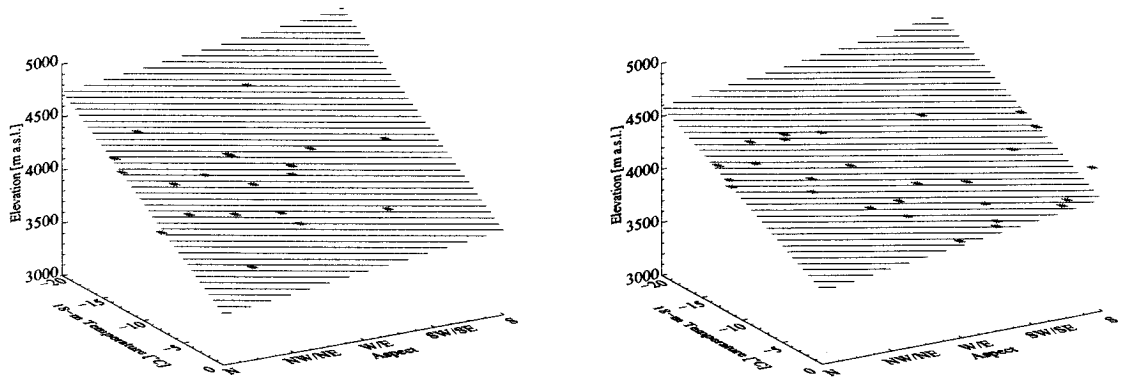

Figure 5.9: Observed MAFTs from the Mont Blanc (left panel) and the Monte Rosa (right panel) areas as a function of elevation and aspect and calculated regression planes through the point observations.

aspect is replaced by the potential direct solar radiation ($r^2 = 0.82$) which is not the case for the Mont Blanc area due to the radiation-exposed location of some very cold sites (Figure 5.10; cf. Figures 5.3 and 5.4). An equally good (Mont Blanc) or much better (Monte Rosa) result is found when the regression is made against elevation,

Table 5.2: Statistical results of the multiple linear regression of the MAFTs against the parameter set of elevation (ELEV), aspect (ASP), slope (SL), potential direct solar radiation (RAD), accumulation index (ACCI) and accumulation (ACC) for the Mont Blanc (MB) and Monte Rosa (MR) areas.

Area	r	r^2	F-Test	p-value	Equation
MAFT vs ELEV and ASP					
MB	0.85	0.73	22.5	< 0.001	$MAFT = 54.8 - 0.0158 \cdot ELEV + 0.6337 \cdot ASP$
MR	0.90	0.81	50.7	< 0.001	$MAFT = 80.1 - 0.0218 \cdot ELEV + 1.0081 \cdot ASP$
MAFT vs ELEV and RAD					
MB	0.81	0.65	17.6	< 0.001	$MAFT = 53.8 - 0.0155 \cdot ELEV + 0.0080 \cdot RAD$
MR	0.90	0.82	47.6	< 0.001	$MAFT = 94.8 - 0.0269 \cdot ELEV + 0.0419 \cdot RAD$
MAFT vs ELEV and ACCI					
MB	0.86	0.73	26.3	< 0.001	$MAFT = 17.5 - 0.0074 \cdot ELEV + 1.5822 \cdot ACCI$
MR	0.78	0.61	24.0	< 0.001	$MAFT = 77.6 - 0.0205 \cdot ELEV + 0.6447 \cdot ACCI$
MAFT vs ELEV and ACC					
MR	0.78	0.60	21.1	< 0.001	$MAFT = 81.5 - 0.0212 \cdot ELEV + 0.4067 \cdot ACC$
MAFT vs ELEV, ASP and SL					
MB	0.85	0.73	14.5	< 0.001	$MAFT = 52.3 - 0.0154 \cdot ELEV + 0.6213 \cdot ASP + 0.0488 \cdot SL$
MR	0.94	0.88	57.7	< 0.001	$MAFT = 84.5 - 0.0219 \cdot ELEV + 1.0781 \cdot ASP - 0.2680 \cdot SL$
MAFT vs ELEV, ASP and ACCI					
MB	0.89	0.79	20.3	< 0.001	$MAFT = 23.4 - 0.0091 \cdot ELEV + 0.5480 \cdot ASP + 1.4322 \cdot ACCI$
MR	0.90	0.81	32.4	< 0.001	$MAFT = 82.4 - 0.0223 \cdot ELEV + 1.0148 \cdot ASP - 0.0992 \cdot ACCI$
MAFT vs ELEV, RAD and ACCI					
MB	0.88	0.77	20.6	< 0.001	$MAFT = 12.3 - 0.0074 \cdot ELEV + 0.0187 \cdot RAD + 1.9391 \cdot ACCI$
MR	0.91	0.82	46.8	< 0.001	$MAFT = 81.7 - 0.0242 \cdot ELEV + 0.0418 \cdot RAD + 0.5673 \cdot ACCI$
MAFT vs ELEV, RAD and ACC					
MR	0.91	0.84	45.6	< 0.001	$MAFT = 94.7 - 0.0271 \cdot ELEV + 0.0460 \cdot RAD - 0.0415 \cdot ACC$
MAFT vs ELEV, ASP, SL and ACCI					
MB	0.89	0.79	14.4	< 0.001	$MAFT = 22.8 - 0.0091 \cdot ELEV + 0.5439 \cdot ASP + 0.0230 \cdot SL + 1.4031 \cdot ACCI$
MR	0.94	0.89	43.3	< 0.001	$MAFT = 70.8 - 0.0190 \cdot ELEV + 1.0432 \cdot ASP - 0.2879 \cdot SL + 0.5940 \cdot ACCI$
MAFT vs ELEV, RAD, SL and ACCI					
MB	0.90	0.81	18.0	< 0.001	$MAFT = 9.2 - 0.0079 \cdot ELEV + 0.0320 \cdot RAD + 0.1390 \cdot SL + 1.8093 \cdot ACCI$
MR	0.91	0.82	34.1	< 0.001	$MAFT = 78.4 - 0.0234 \cdot ELEV + 0.0410 \cdot RAD - 0.0291 \cdot SL + 0.7249 \cdot ACCI$
MAFT vs ELEV, RAD, SL and ACC					
MR	0.91	0.84	33.1	< 0.001	$MAFT = 94.8 - 0.0271 \cdot ELEV + 0.0459 \cdot RAD - 0.0181 \cdot SL - 0.0088 \cdot ACC$

aspect and slope. The combination of aspect and slope gives a better proxy for the radiation. The slope can additionally be considered a proxy for the turbulent heat exchange being generally more effective in flatter terrain than on steep slopes. Elevation and accumulation alone are not very good in explaining the 18-m temperature variation, unless for the Mont Blanc area where deep MAFTs coincide with a low accumulation index ($r^2 = 0.73$). However, very satisfying results are yielded when combining the radiative parameters aspect/slope or radiation with accumulation. For the Mont Blanc area, the parameters elevation, aspect and accumulation index or elevation, aspect, slope and accumulation index are able to explain 79 % of the MAFT-variation. In case of the Monte Rosa area, the percentage amounts to 89 % for the parameter set of elevation, aspect, slope and accumulation index. When combining altitude, radiative, heat-exchange (slope) and accumulation information, coefficients of determination of 0.81 (Mont Blanc) and of 0.82–0.84 (Monte Rosa) are found.

It can be concluded that the climatic and topographic proxies of elevation, aspect, slope, potential direct solar radiation and accumulation are useful statistical parameters for explaining the firn-temperature distribution.

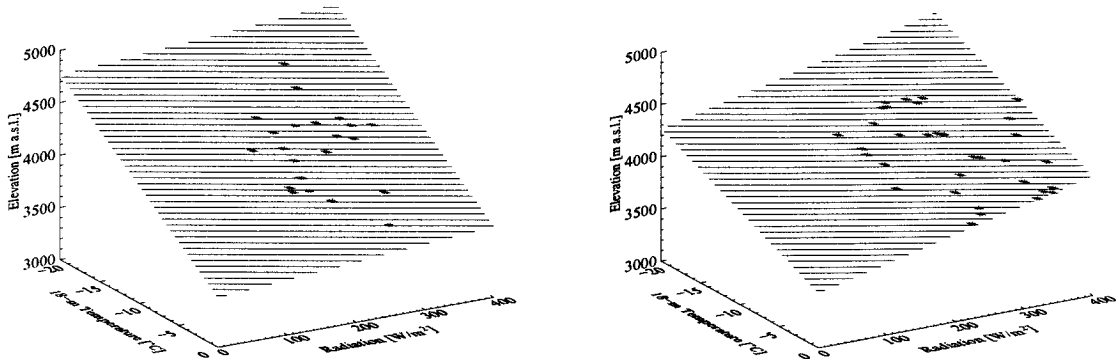

Figure 5.10: Observed MAFTs from the Mont Blanc (left panel) and the Monte Rosa (right panel) areas as a function of elevation and potential direct solar radiation and calculated regression planes through the point observations.

5.4.5 Distribution Models

Lower Boundaries of Cold Firn Occurrence

Using the statistical relationships from Section 5.4.4 it is possible to derive spatial distribution models for cold firn based on the topographic and climatic parameters $ELEV$, ASP, SL, RAD, $ACCI$ and ACC which are relatively easy to measure, estimate or calculate. The lower boundary of cold firn occurrence is found where the MAFT equals 0 °C and can then be written as (cf. equation 5.9)

$$ELEV_{bound} = -(a + c \cdot ASP + d \cdot SL + \ ...)/b \tag{5.10}$$

where $ELEV_{bound}$ is lower boundary of cold firn distribution, a is intercept, c, d, ... are slopes of the variables ASP, SL, ... and b is slope of the parameter elevation (see Table 5.2).

$\mathbf{ELEV_{bound}}$ vs ASP

The aspect-dependent lower boundaries of the two areas (Table 5.3) are quite similar and differ on the order of 230 m. The discrepancy increases towards southerly aspects maybe due to lacking observations on south-exposed slopes in the Mont Blanc area.

Table 5.3: Lower boundaries [m a.s.l.] of cold firn occurrence as a function of aspect (ASP) for the Mont Blanc and Monte Rosa areas.

ASP	Mont Blanc	Monte Rosa
N	3510	3720
NW/NE	3590	3820
W/E	3670	3910
SW/SE	3750	4000
S	3830	4090

$ELEV_{bound}$ vs RAD

The radiation-dependent lower boundaries of the Monte Rosa area show a slightly larger scatter than the aspect-dependent values (Table 5.4). However, ranges are very similar.

Table 5.4: Lower boundaries [m a.s.l.] of cold firn occurrence as a function of potential direct solar radiation (RAD) for the Mont Blanc and Monte Rosa areas.

RAD [W/m^2]	Monte Blanc	Monte Rosa
100	3520	3680
200	3570	3840
300	3630	3990
400	3680	4150

$ELEV_{bound}$ vs ASP and SL

When combining aspect with slope information, the lower boundaries rise for steeper terrain in the Mont Blanc area whereas the contrary is observed for the Monte Rosa area (Table 5.5). This fact can be explained with some relatively deep values on steep and shady slopes in the Monte Rosa area. The ranges found are well on the order of the aspect-dependent lower boundaries showing that the influence of the slope alone is rather weak. The scatter is somewhat larger in the Monte Rosa area than in the Mont Blanc area.

Table 5.5: Lower boundaries [m a.s.l.] of cold firn occurrence as a function of aspect (ASP) and slope (SL) for the Mont Blanc and Monte Rosa areas.

	Mont Blanc			Monte Rosa		
ASP	SL [°]			SL [°]		
	10	20	30	10	20	30
N	3480	3510	3540	3790	3660	3540
NW/NE	3560	3590	3620	3880	3760	3640
W/E	3640	3670	3700	3980	3860	3740
SW/SE	3720	3750	3780	4080	3960	3840
S	3800	3830	3860	4180	4060	3940

$ELEV_{bound}$ vs ASP and ACCI

The incorporation of an accumulation index leads to a strong decrease in the elevation of the 0 °C firn-temperature line in case of the Mont Blanc area whereas practically no influence of the accumulation index can be seen for the Monte Rosa area (Table 5.6).

Table 5.6: Lower boundaries [m a.s.l.] of cold firn occurrence as a function of aspect (ASP) and accumulation index (ACCI) for the Mont Blanc and Monte Rosa areas.

	Mont Blanc				Monte Rosa			
ASP	ACCI				ACCI			
	1	2	3	4	1	2	3	4
N	2770	2930	3090	3250	3740	3740	3730	3730
NW/NE	2890	3050	3210	3360	3830	3830	3830	3820
W/E	3010	3170	3330	3480	3930	3920	3920	3910
SW/SE	3130	3290	3450	3600	4020	4010	4010	4000
S	3250	3410	3570	3720	4110	4100	4100	4090

$ELEV_{bound}$ vs RAD and ACCI

When replacing the aspect by the calculated potential direct solar radiation, an even larger – and maybe unrealistic – decrease of the lower boundaries can be observed for the Mont Blanc area whereas a similar pattern is found for the Monte Rosa area showing increasing lower boundaries with increasing radiation and accumulation index (Table 5.7).

Table 5.7: Lower boundaries [m a.s.l.] of cold firn occurrence as a function of potential direct solar radiation (RAD) and accumulation index (ACCI) for the Mont Blanc and Monte Rosa areas.

	Mont Blanc				Monte Rosa			
RAD [W/m²]	ACCI				ACCI			
	1	2	3	4	1	2	3	4
100	2170	2430	2690	2950	3570	3600	3620	3640
200	2420	2680	2940	3200	3750	3770	3790	3820
300	2670	2930	3190	3450	3920	3940	3970	3990
400	2920	3180	3440	3700	4090	4120	4140	4160

$ELEV_{bound}$ vs ASP, SL and ACCI

A rise of the lower boundaries of cold firn occurrence results for an increase in slope and accumulation index for the Mont Blanc area whereas a decreasing trend is revealed for an increasing slope and a decreasing accumulation index for the Monte Rosa area (Table 5.8).

Table 5.8: Lower boundaries [m a.s.l.] of cold firn occurrence as a function of aspect (ASP), slope (SL) and accumulation index (ACCI) for the Mont Blanc and Monte Rosa areas.

Mont Blanc

ASP	SL [°] 10				20				30			
	ACCI 1	2	3	4	1	2	3	4	1	2	3	4
N	2760	2910	3070	3220	2780	2940	3090	3250	2810	2960	3120	3270
NW/NE	2880	3030	3190	3340	2900	3060	3210	3370	2930	3080	3240	3390
W/E	3000	3150	3300	3460	3020	3180	3330	3480	3050	3200	3360	3510
SW/SE	3120	3270	3420	3580	3140	3300	3450	3600	3170	3320	3480	3630
S	3240	3390	3540	3700	3260	3420	3570	3720	3290	3440	3600	3750

Monte Rosa

ASP	SL [°] 10				20				30			
	ACCI 1	2	3	4	1	2	3	4	1	2	3	4
N	3660	3700	3730	3760	3510	3540	3580	3610	3360	3390	3420	3460
NW/NE	3770	3810	3840	3870	3620	3650	3690	3720	3470	3500	3530	3570
W/E	3880	3920	3950	3980	3730	3760	3800	3830	3580	3610	3640	3680
SW/SE	3990	4030	4060	4090	3840	3870	3910	3940	3690	3720	3750	3780
S	4100	4140	4170	4200	3950	3980	4020	4050	3800	3830	3860	3890

$ELEV_{bound}$ vs Rad, SL and ACCI

An even wider range of lower boundaries is found for the Mont Blanc area if the aspect is replaced by the potential direct solar radiation (Table 5.9). At low radiation values, unrealistic lower boundaries occur. A similar distribution pattern is, however, yielded for the Monte Rosa area.

A relatively wide range of lower boundaries is found for the Mont Blanc area when combining various sets of climatic and topographic parameters. A more robust pattern results for the Monte Rosa area with lower boundaries in the range between 3360 and 4200 m a.s.l.. The representativity of the Mont Blanc data set may be limited due to lacking observations in southerly aspects.

Table 5.9: Lower boundaries [m a.s.l.] of cold firn occurrence as a function of potential direct solar radiation (RAD), slope (SL) and accumulation index (ACCI) for the Mont Blanc and Monte Rosa areas.

Mont Blanc

RAD [W/m²]	SL [°] 10				20				30			
	ACCI 1	2	3	4	1	2	3	4	1	2	3	4
100	1980	2200	2430	2660	2150	2380	2610	2840	2330	2560	2780	3010
200	2380	2610	2840	3070	2560	2790	3010	3240	2730	2960	3190	3420
300	2790	3010	3240	3470	2960	3190	3420	3650	3140	3370	3590	3820
400	3190	3420	3650	3880	3370	3600	3820	4050	3540	3770	4000	4230

Monte Rosa

RAD [W/m²]	SL [°] 10				20				30			
	ACCI 1	2	3	4	1	2	3	4	1	2	3	4
100	3550	3580	3610	3640	3540	3570	3600	3630	3520	3550	3590	3620
200	3720	3750	3790	3820	3710	3740	3770	3800	3700	3730	3760	3790
300	3900	3930	3960	3990	3890	3920	3950	3980	3870	3910	3940	3970
400	4070	4110	4140	4170	4060	4090	4120	4160	4050	4080	4110	4140

Statistically Simulated MAFTs for the Mont Blanc and Monte Rosa Study Areas

The MAFTs for the Mont Blanc and Monte Rosa study areas are simulated in Figure 5.11. The distribution was calculated within *ArcView* using the respective relations between MAFT and elevation/aspect from Table 5.2 for the Mont Blanc and Monte Rosa areas and the corresponding DEMs.

Cold-Firn Distribution in the Zermatt Region

Based on the relation between the observed MAFTs in the Monte Rosa study area and the parameters elevation and aspect, a firn-temperature distribution for a larger area in the Zermatt region was computed. Such a distribution model should be able to explain 81 % of the firn-temperature variation (Table 5.2), if the same relation between MAFT and elevation/aspect is valid for the Zermatt region. The calculation was performed within ARC/INFO and ArcView based on a digital elevation model with a 25-m resolution by the *Swiss Federal Institute of Topography*. The result of the simulation is given in Figure 5.12. Compared to an earlier distribution model for the region (Suter et al., 2001), the present occurrence of cold firn is restricted to high-elevation sites above approximately 3700 m a.s.l.

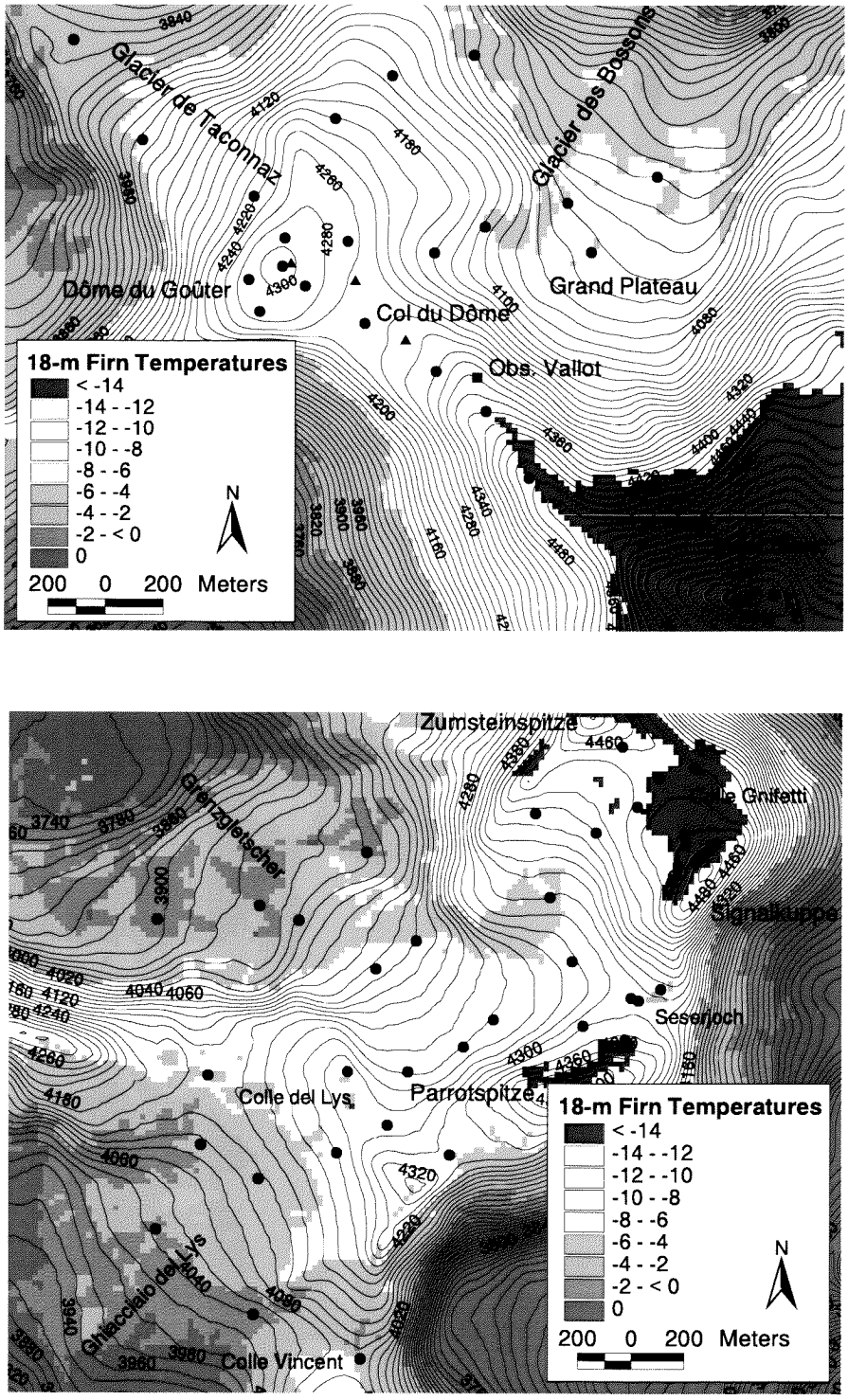

Figure 5.11: Statistically simulated MAFTs for the Mont Blanc (upper panel) and Monte Rosa (lower panel) study areas using the respective relations between MAFT and elevation/aspect (Table 5.2). See Figures 3.3 and 3.5 for borehole locations (black dots and triangles).

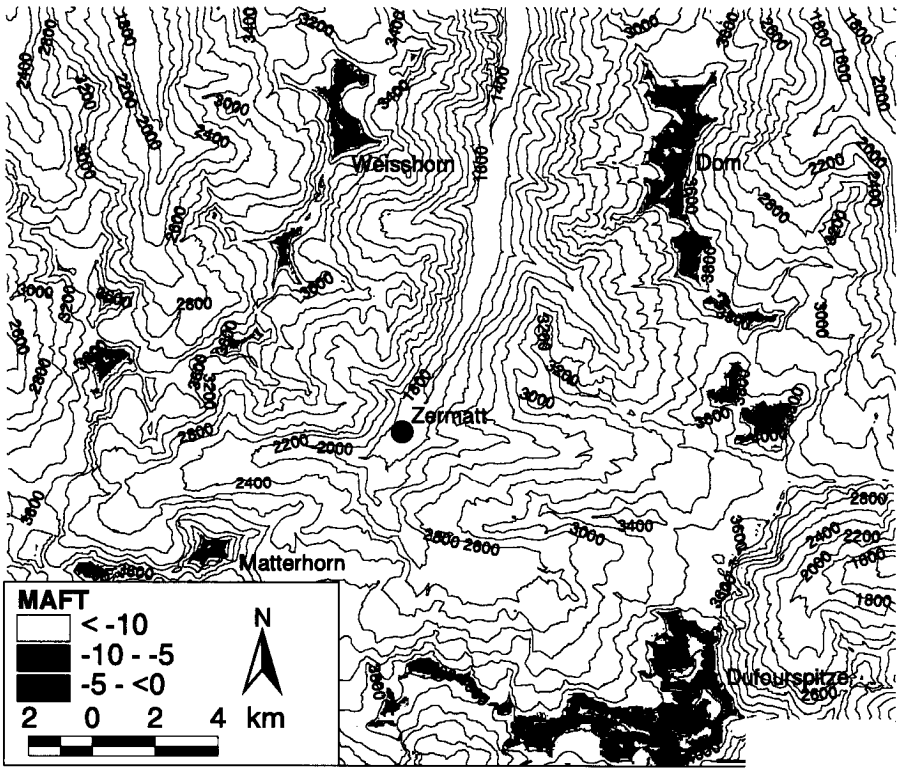

Figure 5.12: Statistically simulated cold-firn distribution in the Zermatt region based on the parameters elevation and aspect. Light grey, white dotted areas represent glacier extent. (Topographic data: DHM25 ©Swiss Federal Office of Topography.)

5.5 Conclusions

Data Acquisition and Analysis

- Steam drilling is a quick and appropriate way for drilling shallow boreholes in cold firn to a depth of approximately 30 m.
- Englacial borehole-temperature measurements need a careful preparation in selecting suitable thermistors, data-storing units and in preparing and performing a calibration in a cold bath, if a certain accuracy shall be obtained.
- The absolute accuracy of the thermistors used is found between ± 0.03 and $\pm 0.04\,^{\circ}\mathrm{C}$; the relative accuracy of one and the same thermistor, however, can be denoted with $\pm 0.001\,^{\circ}\mathrm{C}$.
- Temperature measurements in open air-filled boreholes normally provide a high accuracy if some precautions (surface sealing, no measurements during strong winds, enough adjusting time) are taken into account.

- Borehole temperatures which were measured under thermally disturbed conditions (eg by steam drilling) can easily be extrapolated to receive undisturbed values using a linear relation between observed temperatures and 1/t, where t denotes the time since drilling. The accuracy of the so-extrapolated final temperatures is better than $\pm 0.1\,^{\circ}C$.

Results of the Field Observations

- In the Mont Blanc area as well as in the Monte Rosa area, the 18-m firn temperatures generally decrease with elevation. (Wind-) Exposed saddles and crests show deep temperatures whereas relatively steep slopes in southerly aspects are often close to temperate conditions which results in high firn-temperature variations within very short distance. The observations in the Monte Rosa area show a clearer dependence on aspect and radiation than the ones in the Mont Blanc area.

- The distribution pattern found suggests a strong influence of radiation and turbulent heat exchange (being generally more effective at wind-exposed sites). During the surface-melt period in summer these two energy fluxes mainly determine the melt-energy input into the snow and firn and, herewith, the near-surface temperatures found (cf. Sections 4 and 6).

- The observed and extrapolated accumulation in the Monte Rosa study area shows decreasing values towards exposed saddles and crests and at lower altitude.

Statistical Analysis and Models

- 64 and 60 % of the variation of the MAFTs can be explained by the parameter elevation in the Mont Blanc and Monte Rosa areas, respectively. The resulting high firn-temperature gradients (change of 18-m temperature with elevation) cannot be explained by the air-temperature lapse rate only, but rather show the strong influence of latent heat release for the near-surface thermal regime and, herewith, a high spatial variation in micro-climatic conditions.

- The climatic and topographic parameters elevation, aspect, slope, potential direct solar radiation and accumulation are able to explain up to 81 and 89 % of the MAFT-variation in the Mont Blanc and Monte Rosa study areas, respectively.

- The representativity of the Mont Blanc data set has to be regarded with care as observations from southerly aspects are sparse which leads partly to unrealistic relations for the parameters aspect and radiation.

- Lower boundaries of cold firn occurrence were calculated for the two study areas based on aspect, slope, radiation and accumulation showing a very plausible range for the Monte Rosa area (3360–4200 m a.s.l.) and a more unrealistic pattern for the Mont Blanc area (1980–4230 m a.s.l.), especially if aspect or radiation was combined with accumulation. The representativity of the Mont Blanc data set is questionable for southerly aspects, since measurements in these aspects are sparse.

- The effect of the slope did not clearly come out as steeper slopes showed a cooling effect in the Monte Rosa area and a warming effect in the Mont Blanc area. The representativity of the Mont Blanc data set may play a role again.

- The distribution of cold firn was modeled for the Zermatt region based on the statistical relationship between 18-m temperature, elevation and aspect. Compared to an earlier distribution model, based on elevation and aspect using a data set of the Alps from 1950 to 1994 (Suter et al., 2001), cold firn now occurs at lower elevations on slopes with southerly aspects in the Mont Blanc and at higher elevations on slopes with northerly aspects in the Monte Rosa area. The aspect-dependent range of the lower boundaries is less pronounced in the present study and found between 300 and 400 m compared to 750 m in the earlier investigation.

- Some single sites in the Mont Blanc and Monte Rosa areas show a significant increase in MAFT since earlier investigations. However, the present-day distribution pattern of cold firn lies well within the boundaries of the previous distribution model based on elevation and aspect (Suter et al., 2001). Although the lower boundaries of cold-firn occurrence are higher in northerly aspects and lower in southerly aspects than in the previous model, a major change in cold-firn occurrence cannot be inferred for the Alps over the last 50 years.

Seite Leer /
Blank leaf

6 Borehole Thermometry

6.1 Theoretical Background

Borehole thermometry is a tool for reconstructing surface-temperature and surface-melt information from (measured) englacial temperatures. Analytical and numerical methods are discussed to model the englacial temperature distribution and measured englacial temperature profiles are used to estimate the potential of such records in view of climate-change detection.

6.1.1 Thermal Processes in a Cold Glacier

Within this section, the thermal boundary conditions of and the thermal processes within a cold glacier and their influence on the englacial temperature distribution are discussed. The glacier is assumed to be cold throughout, ie frozen to its

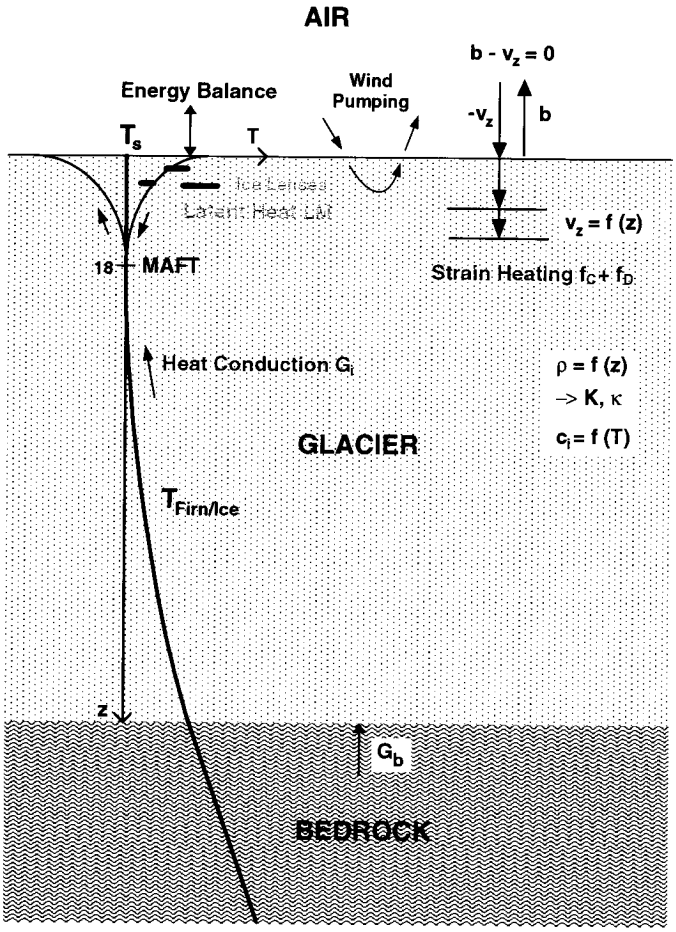

Figure 6.1: Thermal processes at the boundaries of and within a cold glacier for a one-dimensional case. The (steady-state) temperature profile is given in blue. For the thermal properties and their dependence on other parameters and for the explanation of the symbols, see text below.

bed. Figure 6.1 summarizes the thermal processes at the boundaries of and within

a cold glacier and gives the thermal properties of firn and ice and their dependence on other parameters.

Boundary Conditions

Surface Temperature

The *surface temperature* T_s of a firn- and ice body strongly influences the englacial temperature distribution and constitutes the upper boundary condition. For measured surface temperatures over cold snow and firn, see Section 4.3.8. Due to the fact that the temperature of a natural snow- and firn cover cannot rise above 0 °C, the surface temperature has a well defined thermal maximum. As climate-change scenarios often imply a change in air temperature, it has to be shown whether there is a systematic relation between the air temperature and the surface temperature. A parallel evolution of the two quantities can, indeed, be shown with the measurements at the Seserjoch energy-balance station from May, 1999 to April, 2000 (Figure 6.2). A more or less regular shift in the mean annual temperatures of 3.5 °C (shift between

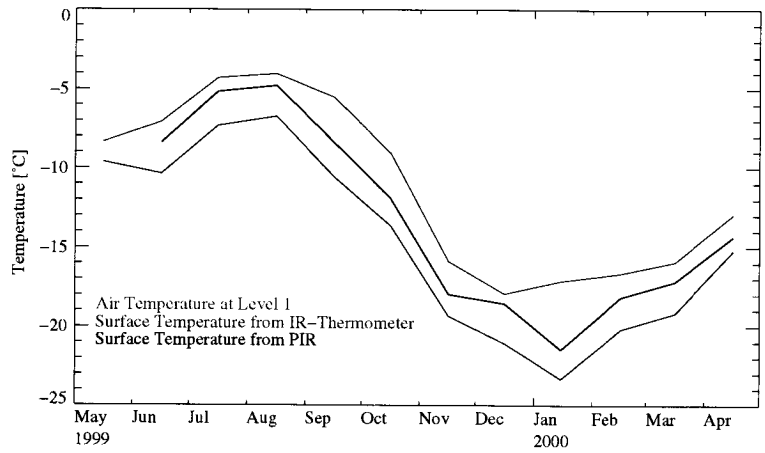

Figure 6.2: Monthly mean values of measured air- and surface temperatures at Seserjoch (Monte Rosa) from May, 1999 to April, 2000.

air temperature and surface temperature measured by the IR-Thermometer) and of 1.8 °C (shift between air temperature and surface temperature measured by the PIR) can be observed. Thus, as long as the (monthly mean) surface temperatures do not rise to 0 °C, it can be expected that a climatic trend in the air temperatures can equally be observed in the surface temperatures. As soon as the surface temperature assumes 0 °C, surface melt can occur and significantly change the near-surface temperature distribution within the snow and firn on a short time-scale (see Section 6.1.3).

Basal Heat Flux

The *basal heat flux* or *geothermal heat flux* G_b is an important heat source at the glacier base and constitutes the lower boundary condition of the glacier. The basal heat flux is triggered by the prevailing temperature gradient and the thermal conductivity of the rock material and can be written as

$$\vec{G_b} = -K_r \nabla T \ , \tag{6.1}$$

where $\vec{G}_b = (G_{b_x}, G_{b_y}, G_{b_z})$, K_r = thermal conductivity of rock and ∇T = vector of temperature gradients $\left(\frac{\partial T}{\partial x}, \frac{\partial T}{\partial y}, \frac{\partial T}{\partial z}\right)$. Although the basal heat flux is well-known in densely populated areas and/or at more or less sea level for central Europe (Medici and Rybach, 1995), high-mountain areas show more complex heat-flow patterns due to their three-dimensional geometry with corresponding lateral effects and due to paleo-temperature effects or additional heat sources or sinks, eg thawing (rock) permafrost (Wegmann, 1998; Lüthi, 2000). A typical geothermal heat flux at the sea level in Switzerland is 70 mW/m^2 (Medici and Rybach, 1995). At the base of high-situated cold glaciers, a strongly reduced heat flux on the order of 20 to 40 mW/m^2 could be observed (Haeberli and Funk, 1991; Lüthi, 2000). The thermal conductivity of rock K_r depends on the rock type, anisotropy and water content and can typically be found between 2.5 and 3.3 W/(m·K) for granite and gneiss (Busslinger, 1998). A mean value of 2.9 W/(m·K) was taken for all the calculations in the Mont Blanc and Monte Rosa areas, where mainly granite-type and metamorphic rocks are found (Section 3).

Heat-Transfer and Heat-Production Processes within the Glacier

Heat Conduction

Heat conduction is by far the most important and rapid energy transfer process within a cold glacier (see Section 6.1.3). The heat flux G_i through the glacier is driven by the thermal conductivity and the prevailing temperature gradient and can be written as

$$\vec{G}_i = -K_i \nabla T \ , \tag{6.2}$$

where $\vec{G}_i = (G_{i_x}, G_{i_y}, G_{i_z})$, K_i = thermal conductivity of snow, firn or ice and ∇T = vector of temperature gradients $\left(\frac{\partial T}{\partial x}, \frac{\partial T}{\partial y}, \frac{\partial T}{\partial z}\right)$. The thermal conductivity of a porous medium such as snow, firn and ice is difficult to determine and the values found in literature show a strong scattering. In this study, the mean value of two parameterizations is taken to express the density dependence of the thermal conductivity, namely

1. the Schwerdtfeger formula (Paterson, 1994)

$$K_i = 2.1 \cdot 10^{-2} + 4.2 \cdot 10^{-4}\rho + 2.2 \cdot 10^{-9}\rho^3 \text{ and} \tag{6.3}$$

2. the van Dusen formula (Paterson, 1994)

$$K_i = \frac{2K_{ice}\rho}{3\rho_{ice} - \rho} \ , \tag{6.4}$$

where ρ = observed density of snow, firn or ice, K_{ice} = thermal conductivity of ice (2.1 W/(m·K)) and ρ_{ice} = density of ice (900 kg/m^3). The Schwerdtfeger formula represents an upper, the van Dusen formula a lower limit. For the density-depth profiles, either a linear interpolation between a measured surface density and a measured or assumed density at the glacier bed (Sections 6.1.2 and 6.1.3) or measured density-depth profiles from ice-core analysis were used (Sections 6.4.1 and 6.4.2).

Firn- and Ice Flow

Within a cold glacier, heat is also transported by the compaction and (downward) movement of the firn and ice. The temperature distribution within a cold glacier due to firn- and ice flow can be described with the following differential equation

$$\frac{\partial T}{\partial t} = -\vec{v} \cdot \nabla T \,, \tag{6.5}$$

where $T =$ firn- or ice temperature, $t =$ time, $\vec{v} =$ velocity vector (v_x, v_y, v_z) and $\nabla T =$ vector of temperature gradients $\left(\frac{\partial T}{\partial x}, \frac{\partial T}{\partial y}, \frac{\partial T}{\partial z}\right)$. In the following, two different velocity-depth models for one-dimensional (vertical) firn- and ice compaction were used. Both models assume a constant surface geometry, ie a steady state between the surface accumulation b and the vertical surface velocity $v_z\,(0)$:

1. a linear compaction model at depth:

$$v_z = \frac{b\,(h - z)}{h} \text{ and} \tag{6.6}$$

2. an exponential parameterization of the vertical velocity (Ling, 1985; Haeberli et al., 1988):

$$v_z = b\frac{\mu}{\mu + s\,(z)}\left(1 - \frac{\Lambda z - s\,(z)}{\Lambda h - 1 + \mu}\right) \,, \tag{6.7}$$

where $v_z =$ vertical velocity in the glacier, $z =$ depth, $h =$ ice thickness, $\mu =$ ratio of surface density to maximum ice density, $s\,(z) = (1 - \mu)\left(1 - \mathrm{e}^{-\Lambda z}\right)$ and $\Lambda =$ scale-depth parameter of density increase. Examples of calculated temperature profiles including the effect of vertical velocities are given in Sections 6.1.2 and 6.1.3.

Latent Heat

In case of surface melt (see Section 4.4.5), meltwater percolates from the surface into the snow or firn until it re-freezes at a certain depth as a consequence of an ambient subzero temperature. At the same time, the snow or firn temperature rises due to the release of latent heat. Due to gravity forces, the direction of the percolating meltwater is always vertical, unless the meltwater spreads out laterally, eg caused by an ice lens. Thus, the release of latent heat LM per unit volume within the snow- and firn cover can be written as

$$LM = L_f \vec{m}_w \,, \tag{6.8}$$

where $L_f =$ latent heat of fusion and $\vec{m}_w =$ vertical mass flux of water to be re-frozen per unit volume. The mass flux shall be positive as the snow- and firn layer considered is gaining mass due to the re-freezing of meltwater. The release of latent heat leads to an increase of the firn temperature per unit time by ΔT:

$$\Delta T = \frac{LM}{\rho_f c_i} \,, \tag{6.9}$$

where $\rho_f =$ snow or firn density and $c_i =$ specific heat capacity of ice. Once the temperature is at 0 °C, meltwater can percolate into and re-freeze within deeper

snow- and firn layers or cause additional melt within the snow- and firn cover at melting point, when further percolation is inhibited eg by an ice lens. In an earlier study of englacial temperatures on the upper Grenzgletscher, temperate conditions could be observed down to a depth of 4 m in September (Suter et al., 2001) indicating a strong firn warming due to re-freezing meltwater.

Heat Production due to Firn Compaction and Ice Deformation (Strain Heating)
About the upper 30–40 m of a cold glacier normally consist of firn where the (vertical) compaction is largest. Below this depth, the glacier consists mainly of ice and the vertical compaction can be neglected. The release of heat per unit volume and time due to firn compaction f_C can be described as (Paterson, 1994)

$$f_C = \frac{v_z g \int_0^z \rho\,(z)\,dz}{\rho} \cdot \frac{d\rho}{dz}\ , \tag{6.10}$$

where v_z = vertical velocity, g = acceleration due to gravity, ρ = density, z = depth and $\frac{d\rho}{dz}$ = density-depth gradient. Let's assume a depth of 1 m, a density of 500 kg/m^3, a surface velocity of 4 m/a and a density-depth gradient of 50 kg/m^4. A heat production of 1962 J/(m$^3 \cdot a$) results which corresponds to a temperature change of $\Delta T = \frac{f_C}{\rho c_i} = 0.002$ °C/a. For larger depths with higher densities and smaller vertical velocities, the heat release and corresponding temperature increase is even smaller so that the effect of firn compaction can be neglected.
Ice deformation is greatest in the vicinity of the glacier bed and can be defined in a simplified way as a simple shear in a xz-plane. The heat production per unit volume and time due to firn- and ice deformation f_D can then be written as (Paterson, 1994)

$$f_D = 2\dot{\epsilon}_{xz}\tau_{xz}\ , \tag{6.11}$$

with

$$\tau_{xz} = \rho g z \sin\alpha \text{ and} \tag{6.12}$$

$$\dot{\epsilon}_{xz} = A_0 \tau_{xz}^n\ , \tag{6.13}$$

where $\dot{\epsilon}_{xz}$ = strain rate in the xz-plane, τ_{xz} = shear stress in the xz-plane, ρ = firn or ice density, g = acceleration due to gravity, z = depth, α = slope, A_0 = parameter of the ice flow law ($4.9{\cdot}10^{-25}$ 1/(Pa$^3\cdot$ s); Paterson, 1994) and n = dimensionless exponent of the ice flow law (between 1 and 3 for cold firn and ice; Wagner, 1996 and Lüthi, 2000). For an ice density of $\rho = 900$ kg/m^3, a depth of $z = 120$ m, a slope of $\alpha = 10°$ and using the above-mentioned parameter A_0 and $n = 3$, a heating of 0.00438 W/m^3 results which corresponds to a temperature change of 0.077 °C/a. At first sight, this value does not seem to be negligible. However, the calculated value marks an upper limit for the boreholes investigated within this Section. If the flow law parameter n is assumed to be smaller than 3, which was suggested for cold firn and ice in some studies (Wagner, 1996), the energy release due to firn- and ice deformation can definitely be neglected.

Englacial Air Convection or Wind Pumping
As snow, firn and ice are porous media, air can be exchanged as long as the pores are not closed-off from each other. *Air convection* could be triggered by temperature gradients in the snow- and firn cover. However, the resistance to gradient-forced air

convection in cold snow and firn is very high (see Section 5.2.2), in a way that such effects can be excluded.
Pressure-induced air circulation or oscillation within the snow- and firn body commonly referred to *wind pumping* can occur under high surface wind speeds. Wind pumping can disturbe the englacial temperature distribution on a short time-scale. An example of a wind-pumping event at Dôme du Goûter, Mont Blanc area, is shown in Figure 6.3. As the penetration depth of wind pumping seems to be restricted to a

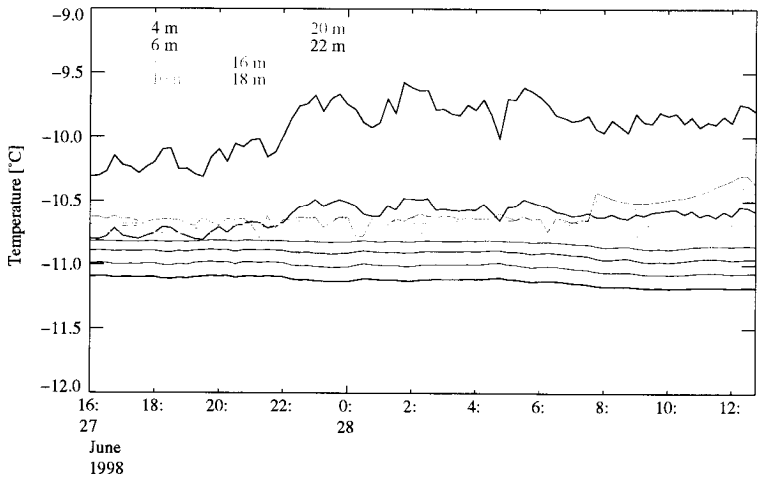

Figure 6.3: Wind pumping event at borehole 6, *Dôme du Goûter, Mont Blanc area. Evolution of the firn temperatures at various depths. The perturbation stops at about 10 m depth.*

few meters and very high wind speeds are needed to create such events (more than 100 km/h were estimated for this event) and as the interstitial air has a low thermal conductivity which inhibits a rapid warming of the ice matrix, wind pumping is an episodic event and can normally be neglected as an energy-exchange process.

The General Heat-Transfer and -Production Equation

As a consequence of the described heat-transfer and heat-production processes, the general heat-transfer and -production equation within a cold glacier can be written as (Carslaw and Jaeger, 1959)

$$\frac{\partial T}{\partial t} = \nabla\left(\kappa \cdot \nabla T\right) - \vec{v} \cdot \nabla T + \frac{LM}{\rho c_i} \text{ with} \tag{6.14}$$

$$\kappa = \frac{K_i}{\rho c_i} \,, \tag{6.15}$$

where $T =$ temperature, $t =$ time, $\kappa =$ thermal diffusivity, $\vec{v} =$ vector of glacier flow velocity, $LM =$ latent heat, $\rho =$ firn or ice density, $c_i =$ specific heat capacity of ice and $K_i =$ thermal conductivity of snow, firn or ice. The specific heat capacity of ice is temperature-dependent. The temperature dependence can be written as (Paterson, 1994)

$$c_i = 152.5 + 7.122 \cdot T \,, \tag{6.16}$$

where T = absolute temperature [K]. The specific heat capacity of the interstitial air in snow, firn and ice can be neglected due to the much smaller density of the air than the ice. Due to the fact that liquid water only occurs in the uppermost meters of the snow and firn during summer and might not exceed a few volume percent of the total volume, the specific heat capacity of water can also be neglected.
Analytical and numerical solutions of Equation 6.14 with corresponding boundary conditions are presented in Sections 6.1.2 and 6.1.3.

6.1.2 Analytical Solutions

Seasonal Temperature Variations

The near-surface thermal regime of a glacier is mainly the result of surface energy- and mass-exchange processes (see Section 1). The influence of lateral firn- and ice advection is normally weak, so that the analytical solutions presented here are restricted to one-dimensional (vertical) cases. If only heat conduction in one dimension and a constant thermal diffusivity κ is taken into account, Equation 6.14 reduces to

$$\frac{\partial T}{\partial t} = \kappa \cdot \frac{\partial^2 T}{\partial z^2} \; . \tag{6.17}$$

For longer time periods, the upper boundary condition can well be approximated with a sinusoidal surface-temperature variation with a period of one year (cf. Section 6.1.1):

$$T(0,t) = T_s + \Delta T_s \sin(\omega t - \phi) \tag{6.18}$$

and the lower boundary condition can be defined by a constant temperature gradient at great depth:

$$T(z,t) = T_s + z\frac{dT}{dz} \; . \tag{6.19}$$

Finally, the solution of the differential equation 6.17 becomes (Carslaw and Jaeger, 1959)

$$T(z,t) = T_s + z\frac{dT}{dz} + \Delta T_s \cdot \mathrm{e}^{-z\sqrt{\frac{\omega}{2\kappa}}} \sin\left(\omega t - z\sqrt{\frac{\omega}{2\kappa}} - \phi\right) \; , \tag{6.20}$$

where $T(z,t)$ = temperature at depth z and time t, T_s = mean annual surface temperature, ω = angular frequency ($\omega = \frac{2\pi}{P}$, where P = period), ϕ = constant phase shift of the sine curve, $\frac{dT}{dz}$ = constant temperature gradient and κ = thermal diffusivity. The phase shift is added to move the sine curve along the time axis to have the deepest temperatures in winter and the highest in summer.
The penetration depth of the annual temperature variation for pure heat conduction depends on the characteristics of the firn such as the density ρ and the thermal conductivity K, and the amplitude of the surface-temperature variation ΔT_s. Figure 6.4 gives the penetration depth of the seasonal temperature variation (annual variation of 0.1 or 0.01 °C) as a function of the amplitude of the surface-temperature variation ΔT_s and the density ρ. The thermal diffusivity was calculated using Equation 6.15 and the thermal conductivity as a mean of Equations 6.3 and 6.4. The specific heat capacity was calculated for -10 °C using Equation 6.16. A typical amplitude of the surface-temperature variation and a typical mean density of the near-surface firn can be given as $\Delta T_s = 8\,°\mathrm{C}$ and $\rho = 585\,\mathrm{kg/m^3}$, respectively, which results in a typical

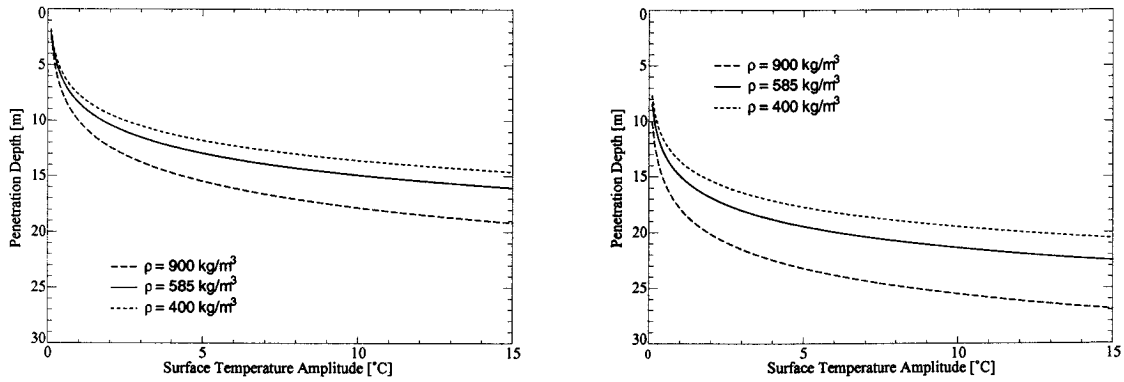

Figure 6.4: Penetration depth of seasonal temperature variations in cold firn for pure heat conduction as a function of the amplitude of the surface-temperature variation ΔT and the density ρ. The left panel shows the depths where the annual variation is 0.1 °C and the right panel the ones where the annual variation is 0.01 °C.

seasonal penetration depth of 14 m for an annual variation of 0.1 °C. The effect on the seasonal penetration depth due to a non-constant density at depth and due to the vertical velocity is shown in Section 6.1.3.

Steady-State Temperatures

For a one-dimensional steady-state situation ($\frac{\partial T}{\partial t} = 0$) assuming a constant thermal diffusivity κ and neglecting the latent heat contribution, Equation 6.14 can be written as

$$\frac{\partial T}{\partial t} = \kappa \cdot \frac{\partial^2 T}{\partial z^2} - v_z \cdot \frac{\partial T}{\partial z} = 0 \,, \tag{6.21}$$

where $v_z =$ vertical velocity. In a thermal steady state, the glacier geometry and the glacier velocity field have also to be in a steady state, which means that the net mass balance at the surface balances the vertical surface velocity and that the velocity-depth distribution does not change in time.
Under the assumption of a constant mean annual surface temperature T_s, a constant temperature gradient $\left(\frac{dT}{dz}\right)_b$ at the glacier bed and a vertical velocity of $v_z = -\frac{bz}{h}$, where $b =$ net mass balance, $z =$ height above the bedrock and $h =$ glacier thickness, the temperature T at height z above the bedrock can be written as (Robin, 1955)

$$T(z) = T_s + \frac{\sqrt{\pi}}{2} l \left(\frac{dT}{dz}\right)_b \left(\operatorname{erf}\frac{z}{l} - \operatorname{erf}\frac{h}{l}\right) \,, \text{ where} \tag{6.22}$$

$$l = \sqrt{\frac{2\kappa h}{b}} \text{ and} \tag{6.23}$$

$$\operatorname{erf}(z) = \frac{2}{\sqrt{\pi}} \int_0^z \mathrm{e}^{-y^2} dy \tag{6.24}$$

is the error function. Typical steady-state temperature profiles for a 100 m deep glacier were calculated using a depth-dependent thermal diffusivity based on a linear density-depth profile, K as a mean of Equations 6.6 and 6.7, c calculated for -10 °C using Equation 6.16 and a surface temperature T_s of -10 °C. The deviations from the

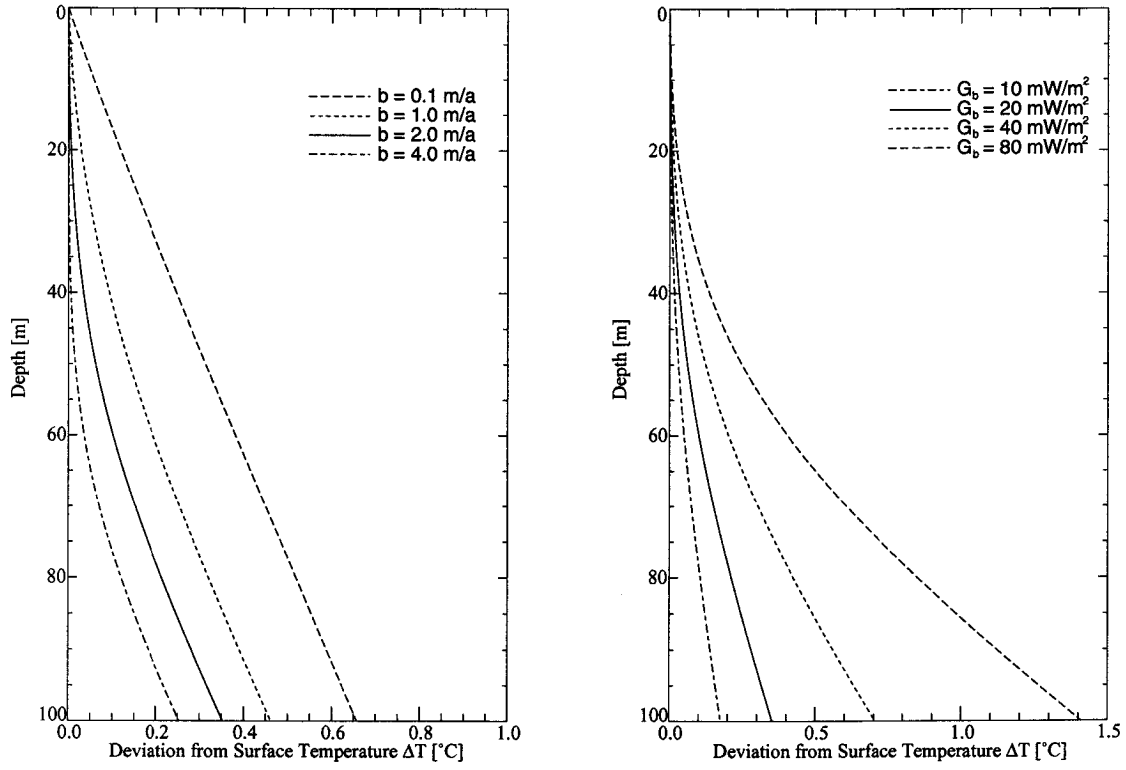

Figure 6.5: Calculated englacial steady-state profiles with different values for the net mass balance b (left panel) and the ground heat flux G_b (right panel) for a 100 m deep glacier showing the temperature deviations ΔT from the surface temperature T_s = -10 °C. The calculations were made for $G_b = 20\,mW/m^2$ (left panel) and $b = 2\,m/a$ (right panel).

constant surface temperature using different values for the net mass balance at the surface b and for the ground heat flux G_b are shown in Figure 6.5. An application of calculated steady-state profiles is given in Sections 6.1.3 and 6.4.

6.1.3 Numerical Solutions

If only one-dimensional (vertical) heat-transfer and -production processes are taken into account, Equation 6.14 can be written as

$$\frac{\partial T}{\partial t} = \kappa(z)\,\frac{\partial^2 T}{\partial z^2} + \frac{\partial \kappa}{\partial z}\cdot\frac{\partial T}{\partial z} - v_z\cdot\frac{\partial T}{\partial z} + \frac{LM}{\rho c_i}\,. \tag{6.25}$$

Equation 6.25 was solved using an explicit finite-difference scheme (see below). For the calculations made within this section, a 100 m deep glacier was assumed (a typical ice thickness of an Alpine firn saddle). A linear density-depth distribution from 500 kg/m^3 at the surface to 900 kg/m^3 at the base was taken for the calculation of the thermal diffusivity using Equation 6.15. The thermal conductivity was determined as a mean of Equations 6.3 and 6.4. The specific heat capacity was calculated for -10 °C using Equation 6.16. The steady-state temperature at the surface was assumed to be -10 or -15 °C and the ground heat flux was set to 20 mW/m^2. A linear velocity-depth model (Equation 6.6) and/or an exponential one (Equation 6.7) were

used for the calculation of the vertical velocities, which means that the surface accumulation b equals the vertical velocity at the surface $v_z(0)$. The parameter Λ in Equation 6.7 was assumed to be 0.06 as inferred from density measurements from a Colle Gnifetti ice core (Haeberli et al., 1988). The depth step was chosen as 0.5 or 1 m and the time step as 6, 12 or 24 h (see below).

The Explicit Finite-Difference Scheme

The following explicit finite-difference scheme with a first-order accuracy was used (Mitchell and Griffiths, 1987):

$$\begin{aligned} T_{z,t+1} = & \underbrace{\left[1 - r\left(\kappa_{z+\frac{1}{2}} + \kappa_{z-\frac{1}{2}}\right)\right] \cdot T_{z,t} + r\left[\kappa_{z+\frac{1}{2}} \cdot T_{z+1,t} + \kappa_{z-\frac{1}{2}} \cdot T_{z-1,t}\right]}_{1)} \\ & \underbrace{- \left[p \cdot v_z \left(T_{z,t} - T_{z-1,t}\right)\right]}_{2)} \\ & \underbrace{+ p \cdot \frac{LM_z}{\rho_z c_{i_z}}}_{3)} , \end{aligned} \tag{6.26}$$

where 1) denotes the scheme for the heat-conduction part, 2) for the velocity part and 3) for the latent heat part. r and p are mesh ratios ($r = \frac{\Delta t}{\Delta^2 z}$ and $p = \frac{\Delta t}{\Delta z}$, where Δt = time step and Δz = depth step). Here, LM is the latent heat flux due to re-freezing meltwater per unit area.
The boundary conditions are as follows:

$$T_{z=0,t} = T_{s_t} \text{ and} \tag{6.27}$$

$$T_{z=h-1,t} = T_{z=h,t} - \left[\frac{dT}{dz}\right]_t \cdot \Delta z , \tag{6.28}$$

which means that the uppermost temperature at time t ($T_{z=0,t}$) is equal to the surface temperature at time t (T_{s_t}) and the second lowest temperature at time t ($T_{z=h-1,t}$) is given as the difference between the lowermost temperature ($T_{z=h,t}$) and a constant temperature gradient at great depth ($\frac{dT}{dz}$). Here, h denotes the maximum depth considered for the calculation.
The time steps have to be chosen in a way to meet the stability criterion (Morton, 1980)

$$\Delta t < \frac{1}{2} \cdot \frac{\Delta^2 z}{\kappa} . \tag{6.29}$$

Seasonal Temperature Variations

The knowledge of the penetration depth of a seasonal surface-temperature variation is crucial for measuring and comparing mean annual firn temperatures (cf. Section 5). Figure 6.6 shows typical seasonal penetration depths as a function of the surface-temperature amplitude and the surface accumulation rate for both velocity-depth models. The calculations were made for T_s = -15 °C, a sinusoidal surface-temperature variation with a period of one year, Δt = 1 d and Δz = 0.5 m. Starting from an analytical steady-state temperature profile, first, a 30-year period was calculated to make sure to have reached a numerical steady-state situation.

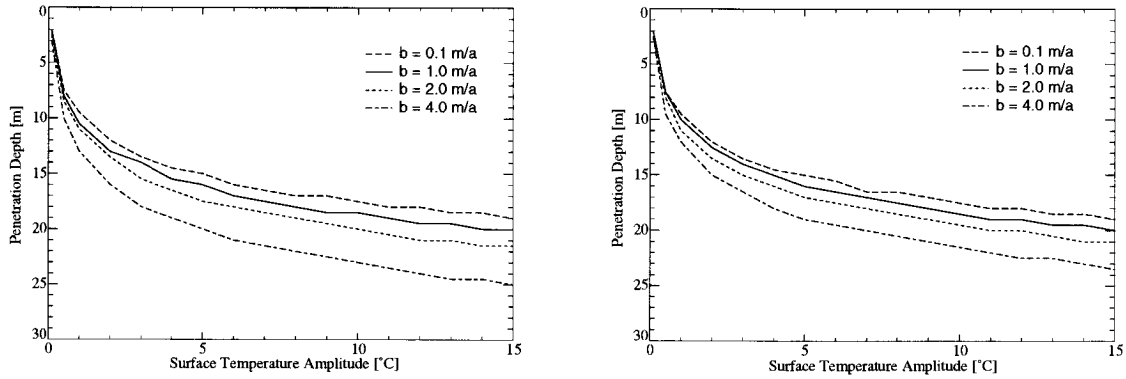

Figure 6.6: Numerically calculated penetration depth of seasonal temperature-variations in cold firn as a function of the amplitude of the surface-temperature variation ΔT and the surface accumulation b. The depths are shown where the annual variation amounts to 0.1 °C. The left panel uses the linear and the right panel the exponential velocity-depth model.

Then, the depths were recorded where the seasonal temperature variation amounts to 0.1 °C. As compared to the analytically calculated penetration depths, the enhanced penetration due to the effect of the vertical velocity comes out clearly. The linear velocity-depth model gives somewhat larger penetration depths than the exponential one and a larger range between the different accumulation rates. When looking at the (more realistic) exponential velocity-depth model, it can be concluded that for a typical annual surface-temperature amplitude of about 8 °C (cf. Section 4), the penetration depth of the 0.1 °C signal can be found between 16 and 20 m for an accumulation rate of 0.1–4 m of snow per year. Thus, to be sure to exclude annual temperature variations in firn-temperature measurements, an appropriate depth for looking at a mean annual firn temperature is 18 m.

Steady-State Temperatures

An important test for the numerical code is the calculation of a steady-state situation and a corresponding comparison with an analytical solution. This was made using Equation 6.22 to calculate an analytical steady state. The analytically calculated profile showed no deviation from the numerical one using the same boundary conditions, firn- and ice properties and linear velocity-depth model (cf. Equation 6.6).

Due to the two different velocity-depth models, differences occur in the calculated steady-state profiles. Typical maximum deviations of 0.01 °C ($b = 0.1$ m/a) to 0.06 °C ($b = 4.0$ m/a) were found in the calculated steady-state temperature profiles, which means that the effect of the different velocity formulations is fairly weak.

Time-Dependent Calculation without Latent Heat

Some calculation examples are given neglecting the effect of latent heat, ie LM is assumed to be zero in Equation 6.26. The sensitivity of englacial temperatures to changes in the surface temperature is shown as well as an estimate of the time information made, which can be resolved in a cold glacier.

In order to get an idea of the time horizon which can be resolved in cold firn and ice, the velocity-depth distribution and – inferred from this – the age-depth distribution for the linear and exponential velocity-depth models are shown in Figure 6.7.

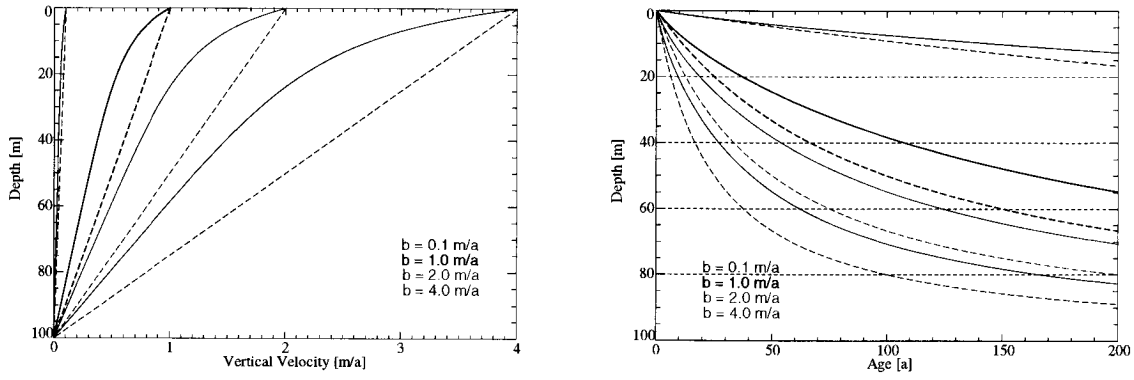

Figure 6.7: Velocity-depth (left panel) and age-depth (right panel) distribution in a 100 m deep glacier for different accumulation rates b. The velocities and ages were calculated using Equations 6.6 and 6.7. Solid lines represent the exponential and dashed lines the linear vertical velocity model.

The lower third of the calculated age-depth distribution has to be considered very carefully as such simple relations normally fail at greater depths (Haeberli et al., 1988). A more realistic velocity- and age-depth modeling was made in two and three

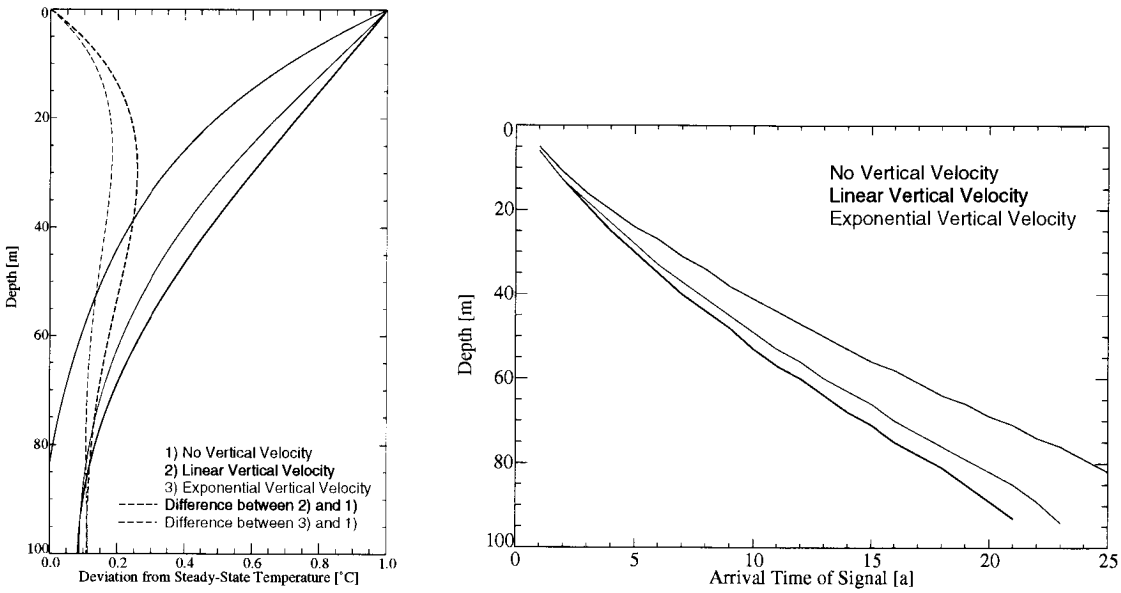

Figure 6.8: Deviations from steady-state temperatures for the two vertical velocity models and for no vertical velocity and differences between the vertical velocity models and the profile calculated with no vertical advection (left panel) and arrival time at depth of 1 % of the surface perturbation (right panel) for a 1 °C linear surface-temperature increase in 30 years.

dimensions for cold firn saddles (Wagner, 1996; Lüthi, 2000). For a rough estimate,

however, simple approaches can give a basic idea of the time-scales involved. As can be seen, the surface accumulation determines the age structure of the ice in an important way. High accumulation rates limit the time horizon of ice-core information, drastically.
The age-depth distribution of the ice gives a maximum time horizon of an integrated surface-temperature information. It is clear that the time information of a surface-temperature history, registered in an englacial temperature profile, cannot

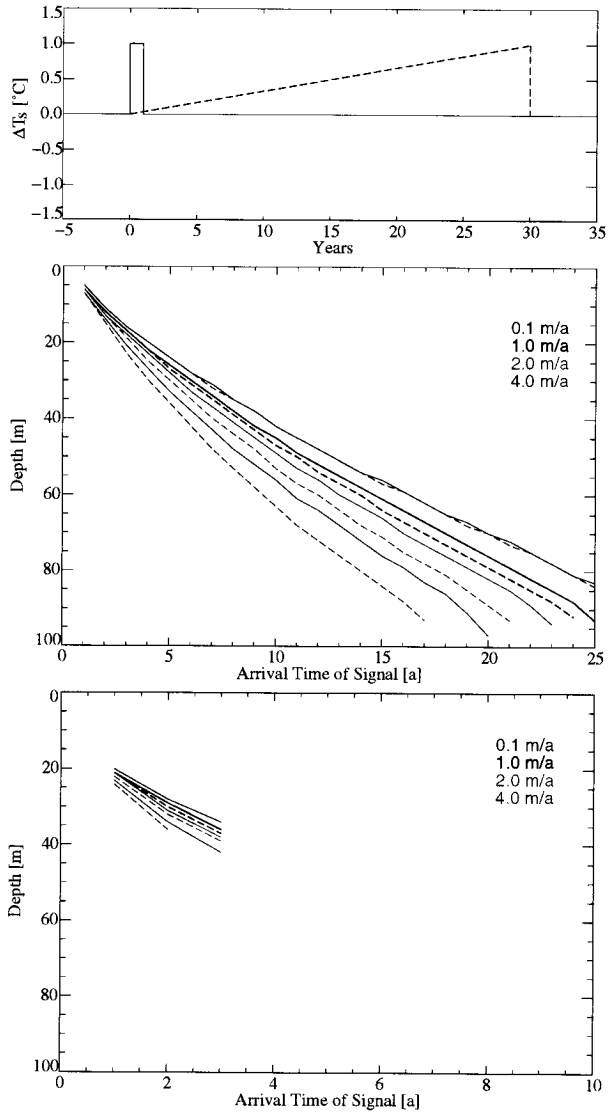

Figure 6.9: Arrival time at depth of 1 % of a 1 °C surface perturbation exerted for 30 years (middle panel) or for 1 year (lower panel) for different surface accumulations and the two vertical velocity models. Solid lines represent the exponential and dashed lines the linear vertical velocity model. The input signal is shown in the upper panel, where the dashed line represents the input signal for the middle panel and the solid line the input signal for the lower panel, respectively.

go beyond the age of the ice. However, the age-depth distribution does not tell about how fast a surface-temperature signal propagates into the firn and ice. Figure

6.8 shows the effect on a steady-state temperature profile due to a linear surface-temperature increase by 1 °C within 30 years for the two velocity models where the surface velocity is 2 m/a and for no vertical movement at all. The propagation of 1 % of the surface perturbation with time is shown in the same Figure. The penetration of the surface-temperature signal is very quick as compared to the age of the ice. Due to the vertical movement, the time horizon which can be resolved becomes even smaller. The temperature differences between the profile with no vertical advection and the two profiles calculated with the two velocity models are on the order of 10–20 % of the surface perturbation for the time horizon of 30 years.
Figure 6.9 shows the arrival time at depth of 1 % of a 1 °C surface-temperature increase in 30 years and in 1 year, respectively, for different surface accumulations and the two vertical velocity models. After these time periods, the previous surface temperature is prescribed again. In the first case, the 1 % signal arrives at 60 m depth after 9 to 17 years, already. Due to a surface-temperature increase within shorter time, the second case shows a much quicker penetration, which even stops between 35 and 40 m depth after 2 to 3 years.
When looking at 18-m temperatures (see Section 5), the question has to be answered, whether these temperatures integrate about the same time horizon of surface-temperature history for various values of surface accumulation. Therefore, a calculation using the exponential vertical-velocity model was made for a typical maximum surface-temperature perturbation of +1.5 °C (cf. Figure 6.28) and the effect on the 18-m temperature calculated for surface accumulations of 0.1, 1, 2 and 4 m/a. Before and after the perturbation, a (seasonal) steady-state situation was assumed. The

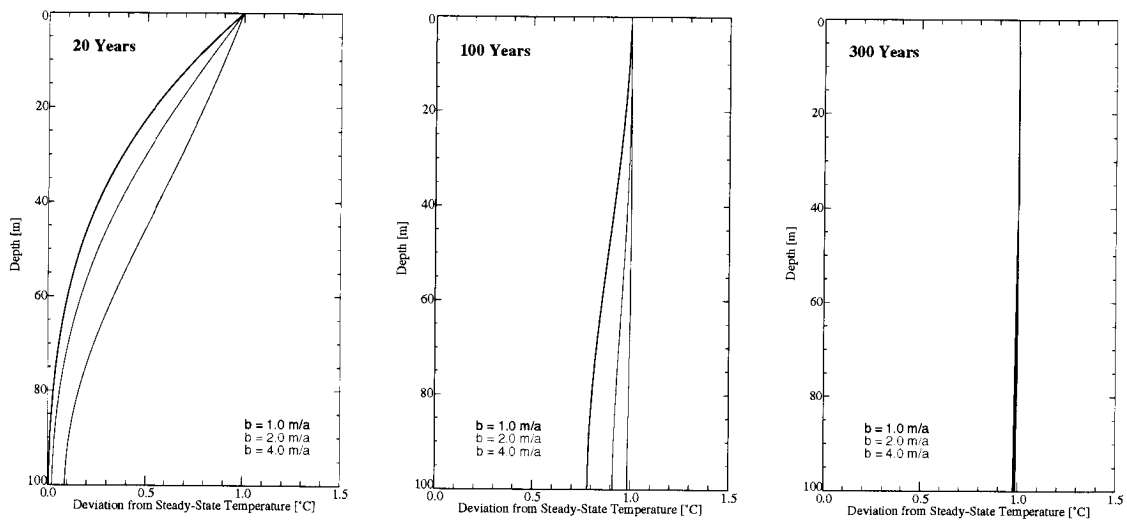

Figure 6.10: Thermal evolution (temperature shift from steady state) caused by a linear surface-temperature increase by 1 °C within 20 years and for different accumulation rates b, until steady state is reached again. The situations after 20 (left panel), 100 (middle panel) and 300 years (right panel) are shown.

maximum of the perturbation arrived at 18 m depth after 845 ($b = 4$ m/a) to 859 days ($b = 0.1$ m/a). Thus, the time horizon of surface-temperature history resolved is comparable for different accumulation rates as heat diffusion dominates. On the

other hand, larger differences are found when comparing the time horizons, until the previous (steady-state) 18-m temperature was reached again. This time horizon varied between 16.3 ($b = 4$ m/a) and 24.4 years ($b = 0.1$ m/a), indicating a maximum back-in-time resolution of a 18-m temperature under ideal conditions which, however, cannot go beyond the age of the firn at 18 m depth (Figure 6.7).
The thermal response time of a glacier can be defined as the time which elapses from one steady-state situation to the next one. A typical thermal response time of a 100 m deep glacier to a linear 1 °C surface-temperature increase within 20 years and for different accumulation rates is presented in Figure 6.10. After 20 years, the new steady-state surface temperature is reached. After 300 years, the new steady state is practically reached for all values of surface accumulation. The higher the accumulation rate, the quicker the new steady state is reached.

Time-Dependent Calculation Simulating the Effect of Latent Heat

The effect of latent heat on the englacial temperature distribution can be simulated when the near-surface temperatures of the snow and firn are set to 0 °C

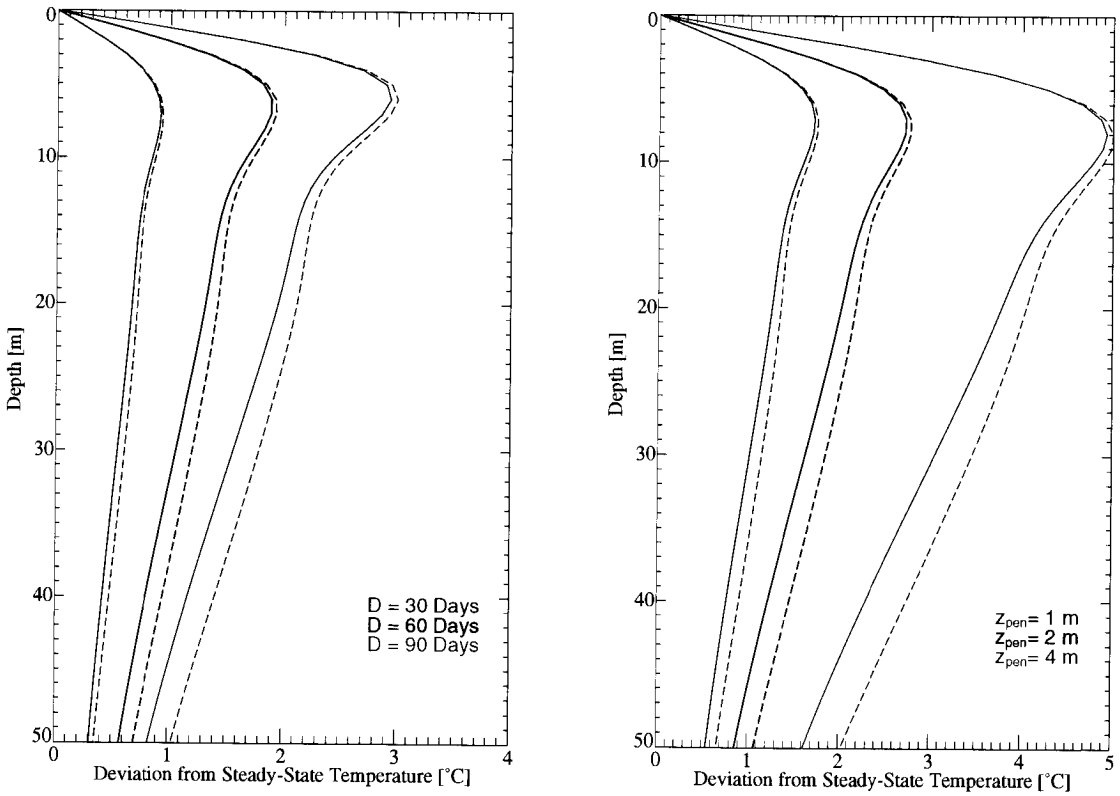

Figure 6.11: Effect of simulated latent heat on a steady-state temperature profile for different durations D of surface melt (left panel) and penetration depths z_{pen} of the 0 °C front (right panel). Solid lines represent the exponential, dashed lines the linear velocity-depth model. The deviations from the steady-state temperature profile after 20 years are shown.

during a certain time of the year. Based on earlier observations on the upper Grenzgletscher, 0 °C surface temperatures could typically be observed for 30 to 90 days

during summer and the maximum penetration depth of the 0 °C front was found at about 4 m depth (Suter et al., 2001).
To evaluate the effect of the duration D of the melt events and the penetration depths z_{pen} of the 0 °C front on the temperature distribution, these two effects were treated separately in Figure 6.11. The calculation was made for $b = 2$ m/a, for both velocity-depth models and for a period of 20 years. In case of the left panel of Figure 6.11, only the duration of the 0 °C surface temperature was varied, but no penetration of the 0 °C front allowed. In the right panel, the duration of the 0 °C event was set constant to 30 days and the penetration depth of the 0 °C front varied, accordingly. The penetration depth of the 0 °C front seems to have a larger effect on the temperature profile than the duration of a 0 °C event at the surface. This is a very important finding in terms of melt-layer formation. If melt layers are formed within the snow cover near the surface in an early stage of the year, they can inhibit a further penetration of the meltwater and, thus, substantially change the near-surface thermal regime when the 0 °C front is stopped at shallow depth.

Time-Dependent Calculation Including Latent Heat

Finally, some calculations are made including the effect of re-freezing meltwater within the snow- and firn cover. The model was designed as follows using the explicite finite-difference scheme (Equation 6.26):
Once the surface temperature is at 0 °C, surface melt occurs. A certain amount of energy is prescribed at the surface (eg as an output of the energy-balance calculation) and taken to melt the snow. The meltwater percolates into the first model layer and is entirely re-frozen. If the amount of energy released is smaller than the amount of energy needed to warm the snow and firn to 0 °C, the snow- and firn temperature is increased by the temperature change caused by re-freezing (cf. Equation 6.9) and the percolation stops. If the temperature in the corresponding layer exceeds 0 °C, the temperature of the layer is set to 0 °C and the excess energy calculated from the temperature excess (amount of temperature above 0 °C). This energy is taken and released in the next model layer and the process is repeated. Once the temperature of a certain layer reaches 0 °C, the meltwater is allowed to percolate through this layer.
The model layer depth for the following calculations was taken as 0.5 m. As the temperature change within a model layer is scaled with the thickness of the layer, the choice of the vertical grid space does not have an influence on the temperature distribution on a larger time-scale. The effects on the temperature distribution due to a variable duration D of the melt events and a variable amount of surface energy available for melt M are shown in Figure 6.12. The calculations were made for $b = 2$ m/a, for both velocity-depth models and for a period of 10 years. In case of the left panel of Figure 6.12, only the duration of the surface melt was varied and the amount of melt energy kept constant (10 W/m^2). In the right panel, the duration of the melt event was set constant to 30 days and the amount of melt energy varied. The effects on the temperature profiles (deviation from steady-state profile) from varying both the duration and melt-energy input are on the same order of magnitude and drastically change the near-surface thermal regime. Typical maximum penetration depths of the 0 °C signal were 2, 4.5 and 9 m for the three cases in the left panel and 1.5, 4.5 and 11.5 m for the ones in the right panel (Figure 6.12).

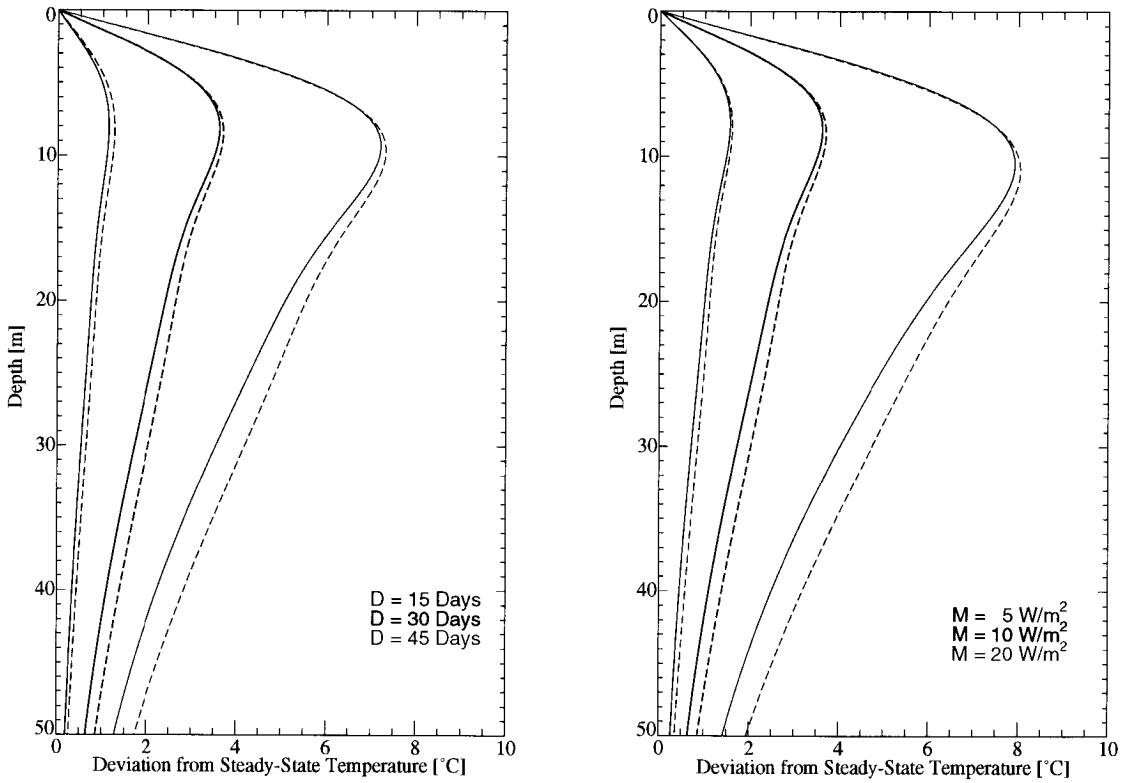

Figure 6.12: Effect of latent heat release on a steady-state temperature profile for different durations D (left panel) and melt-energy inputs M (right panel). Solid lines represent the exponential, dashed lines the linear velocity-depth model. The deviations from the steady-state temperature profile after 10 years are shown.

In nature, steady 0 °C surface temperatures over cold firn can seldom be observed for several days or even weeks. In order to get an idea of the effect on the temperature distribution resulting from the assumption of a 0 °C surface temperature for several days or weeks, a calculation over 10 years was made for a 30 day melt period (August) and a mean daily melt-energy flux of 2, 5 and 10 W/m^2 (5.18, 12.96 and 25.92 MJ/m^2 total yearly melt-energy input) using a sinusoidal surface-temperature variation with an amplitude of 8 °C. In the first case, a steady 0 °C surface temperature was assumed over the melting period of 30 days. In the second case, the 0 °C surface temperature and melt-energy input were restricted to 12 hours of the day over the melting period of 30 days releasing the same daily melt-energy during this time. Finally, a third scenario was calculated, where the 0 °C surface temperature and melt-energy input were restricted to 6 hours of the day with 10 events, evenly distributed over the melting period of 30 days, and again releasing the same amount of total melt energy (Figure 6.13). The effect is strongly depending on the total melt-energy input. A relatively small melt-energy input reduces the effect of the duration of the melt signal on the steady-state profile, whereas larger – and non-negligible – effects occur for a higher total melt-energy release. The maximum penetration depth of the 0 °C signal during the melt season varies between 0 (lowest energy input) and 0.5 to 4.5 m (highest energy input).
It can be concluded that the latent heat release within a cold firn- and ice body is

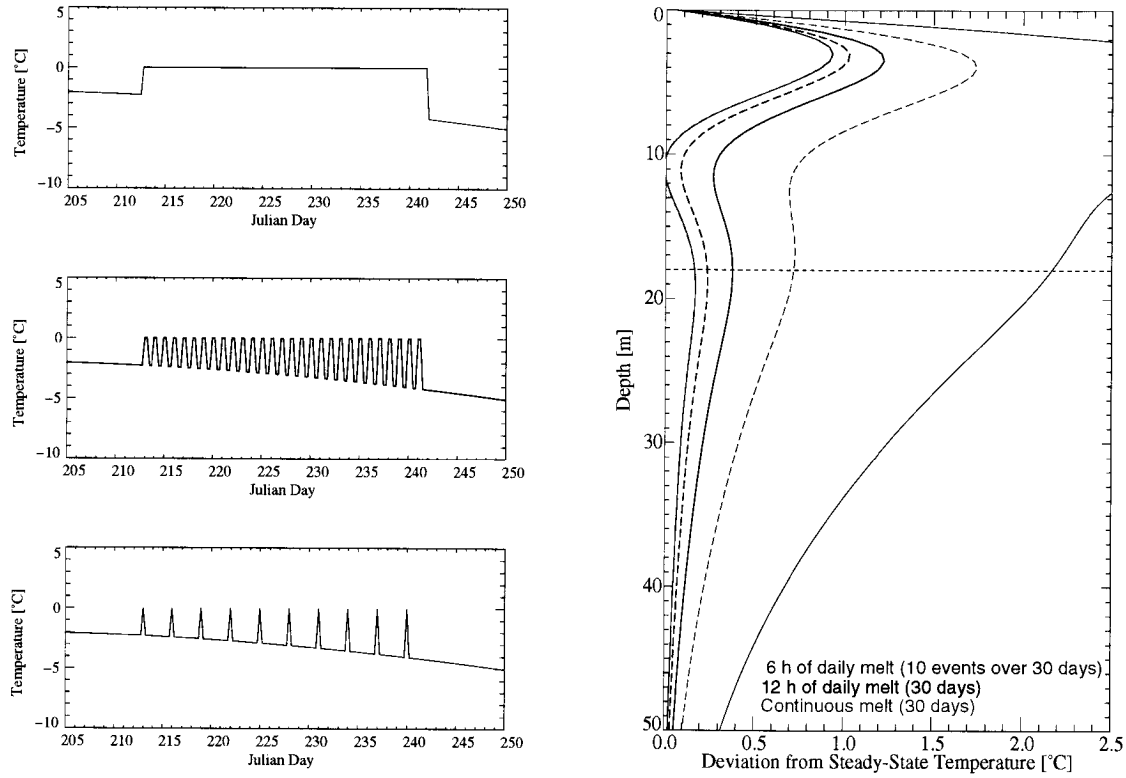

Figure 6.13: Effect of the distribution of the melt signal over the melting period on the temperature profile for daily mean melt-energy inputs of 5 (dashed lines) and 10 W/m^2 (solid lines). The left panels give the input signal over the melting period: a steady 0 °C surface temperature (upper left panel) and an interrupted 0 °C surface temperature, where the (same) melt-energy input is restricted to 12 hours of the day over 30 days (middle left panel) or to 6 hours and to 10 events over 30 days (lower left panel). The temperature deviations from the (January 1) steady-state profile after 10 years are given in the right panel.

of major importance for its thermal structure. Further calculations using observed temperature profiles from the Monte Rosa and Mont Blanc areas are made in Section 6.4.

6.2 Site Selection

Relatively simple glacier geometries are most suitable for a thermometric application of borehole temperatures. Perfect saddle- and dome configurations allow a one-dimensional (vertical) treatment of the heat-flow problem, when the borehole is relatively shallow and situated in the saddle point or on the vertex of a dome. Due to the exposed character of saddle- and dome geometries, frequent snowdrift reduces accumulation and leads to relatively shallow total ice thicknesses of typically 50 (dome geometries) to 100 m (saddle geometries) with a limited time-scale for thermometric reconstructions. On the other hand, persistent and high wind speeds guarantee a high and efficient turbulent heat exchange at these sites leading

to a strongly reduced or even absent percolation of surface meltwater. Care must be taken when a site shows a free and exposed side-wall. In such a case, the 'temperature transport' from the drill site to the side-wall due to heat conduction and ice flow has to be more effective than a possible propagation of a temperature signal from the side-wall to the drill site.
Taking into account the above-mentioned criteria, thermometric borehole-temperature measurements were made at the two Monte Rosa firn saddles of Seserjoch, 4300 m a.s.l. and Colle Gnifetti, 4452 m a.s.l. (see Section 3.3) and at the firn dome of Dôme du Goûter, 4304 m a.s.l. (see Section 3.2).

6.3 Data Acquisition and Analysis

6.3.1 Boreholes

For the thermometric application, the borehole at Seserjoch (borehole 0; Figure 3.5), a steam-drilled borehole at Colle Gnifetti (borehole 00A; Figure 3.5) and an electro-mechanically drilled borehole at Dôme du Goûter (borehole 99-B; Figure 3.3) were considered.
The temperature measurement at the Seserjoch site was made in a steam-drilled 30 m borehole using two permanently installed thermistor chains with a regular data recording (see Sections 4.2 and 5.3.2).
The 40 m borehole at Colle Gnifetti (Section 3.3) was drilled using a powerful steam-drilling system (*Sarbach steam drill*). The drill is heavy (about 30 kg) and not easy to carry, but the operating pressure is between 3–4 bar which made it possible to reach 40 m depth within reasonable time. The borehole was drilled in May/August, 2000 reaching 39 m depth. Due to an effect of in-borehole meltwater, only a depth of 25 m could be reached at the subsequent temperature measurement in the open borehole two weeks later (August 24 to August 26, 2000).
The 40 m borehole at Dôme du Goûter (Section 3.2) was the result of an ice-core extraction made by the *Laboratoires de Glaciologie et Géophysique de l'Environnement (LGGE), Grenoble* in autumn, 1999. The measurement in the open borehole was made on January 27, 2000.
Shallow borehole-temperature measurements with a smaller precision (see Sections 5.3.1 and 5.3.2) were additionally used to illustrate short-term changes.

6.3.2 Methodology of the Temperature Measurements

Instrumental Setting

A thorough description of the thermistor chains used at the Seserjoch site and for the shallow temperature soundings is given in Sections 4.2 and 5.2.2 . At the Colle Gnifetti site, station C and chain C were used for the 25 m borehole to measure within the high-resolution voltage range (-25 – +25 mV) (see Section 5.2.2). Five different measurements were made with the lowermost thermistor at 25, 24.5, 24, 23.5 and 23 m depth. For each depth range, the measurements were continuously registered at a five minute sampling rate over periods of 5 to 16 hours. Only data after perfect thermal adjustment were taken for further analysis.
At the Dôme du Goûter site, the station B and chain B were used together with 3 single thermistors at a 1 m interval. Two thermistors out of these three were of

the same type as the ones from the chains *A–F* (see Section 5.2.2), and one was of the type *Fenwal 197-103LAG-A01* with a 0 °C resistance of approximately 32500 Ω. The 3 single thermistors were first set at 38, 39 and 40 m depth and the lowermost thermistor of the chain *B* at 34 m depth. A continuous reading (five minute sampling rate) was made for 4 hours until perfect thermal adjustment was reached. A second measurement was finally made with the 3 single thermistors at 35, 36 and 37 m depth and the lowermost thermistor of the chain *B* at 33 m depth. A continuous data recording was made for 1.5 hours this time.

Thermistor Calibration and Accuracy

As already stated in Section 5.2.2, the chains *B* and *C* and the 3 additional thermistors mentioned above were calibrated at approximate temperatures of -7, -10.1, -13.1, -15.1 and -17.1 °C. A circulation chiller of the type *Huber CC245* with a 22 l (internal) bath and a warranted bath stability of ±0.02 °C was used. Ethanol of 97 % purity was taken as bath liquid. Otherwise the proceeding was the same as described within Section 5.2.2. Unfortunately, the circulation chiller could not be operated in a cooling chamber this time due to possible humidity problems (condensation). All four sensors of the temperature measuring device were used to control the bath temperature in close vicinity to the thermistors.

A thorough discussion of the accuracy of a thermistor calibration is given in Section 5.2.2. Although the bath stability was referred to ±0.02 °C by the manufacturer, temperature fluctuations of up to ±0.05 °C could be observed by the four temperature sensors during the calibration procedure. But generally, the fluctuation was on the order of ±0.03–0.04 °C. Due to their thermal inertia, the temperature fluctuations of the thermistors were only about half of the above fluctuation. The larger instability as compared to the calibrations in Section 5.2.2 may be due to the relatively large bath volume and due to the heat flux into the bath by the cable, which could not be immersed into the bath liquid, completely. Observations were made at a one minute sampling rate over typical time periods of 30 to 45 minutes to average the bath instability effect.

For the resolution and accuracy of the station, the characteristics of the thermistors and cable and for the absolute accuracy of the temperature measuring device the same can be stated as in Section 5.2.2.

Two single thermistors of the chains *B* and *C* were additionally calibrated in the above-mentioned cold bath using a bath inset with an additional circulation mechanism to guarantee a very high thermal bath stability. The observed bath stability was on the order of ±0.004 (best case at higher temperatures) to ±0.02 °C (worst case at lower temperatures), but normally between ±0.005 and ±0.01 °C. Again, the temperature fluctuations of the thermistors were only about half of the bath fluctuation. A high-precision temperature measuring device of the type *ASL Precision Thermometer F250* was used to control the bath temperature. The precision of the system (measuring device and external *Pt-100* temperature sensors) is denoted with ±0.025 °C between -50 and 250 °C by the manufacturer. The whole system was calibrated together with the two external Pt-100 temperature sensors to an absolute accuracy of ±0.01 °C at the *Swiss Federal Office of Metrology*. The two thermistors of each chain were calibrated at temperatures of approximately -6.9, -9.9, -12.8, -14.7 and -16.8 °C. Observations were made at a one minute sampling rate over

typical time periods of 12 to 20 minutes to average the bath-instability effect and time windows with high stability taken for further analysis.
Thus, the absolute accuracy of a thermistor measurement of the chain B or C can be denoted with $\pm 0.03\,°C$ (0 – -10 °C) to $\pm 0.04\,°C$ (-12.5 – -20 °C) (see Section 5.2.2). The absolute accuracy of the 4 thermistors calibrated with the inset is much better, however, and can be denoted with $\pm 0.01\,°C$. Due to the not so satisfying bath stability, the relative accuracy between the thermistors of one and the same chain is on the order of ± 0.032–$0.042\,°C$ only; the relative accuracy of one and the same thermistor, however, on the order of $\pm 0.001\,°C$.

Borehole Temperature Measurements in the Field

As the time lag between the drilling and the measurement was at least 2 weeks, thermal perturbations due to the drilling operation can be excluded. Again, the open boreholes were protected against snowdrift or air circulation using a plastic tube and an isolating rubber foam to seal the borehole. Although the wind speed was not all the time low during the measurements and wind pumping might have occurred, such an effect would only affect the thermistors within the uppermost 10 m of the borehole (see Section 6.1.1). However, no strong variations could be observed within the uppermost 10 m.
In-borehole convection can also be neglected as the borehole at Seserjoch was sealed at the surface with time and as the one at Colle Gnifetti had the same diameter as the ones for which the calculation of the critical temperature gradient was made within Section 5.2.2. In case of Dôme du Goûter, the initial borehole diameter was 10.5 cm. The critical temperature gradient is $0.12\,°C/m$ using Equation 5.1. Such a high gradient only occurred above 10 m depth (maximum value of $0.13\,°C/m$) and is very close to the critical temperature gradient so that a convection effect can be neglected.
The positioning accuracy of the sensors in the borehole is again estimated to be better than ± 4 cm.
The measurements in the shallow boreholes (22 m depth) are described in Section 5.2.2.

6.3.3 Data Analysis

Converting Resistances into Temperatures

For converting the measured resistances into temperatures, the same procedure was applied as in Section 5.2.3 using Equation 5.2. For the chains B and C and the three additional thermistors, the calibration temperatures of approximately -7, -10.1 and -13.1 °C (chain B and the 3 additional thermistors) and of approximately -13.1, -15.1 and -17.1 °C (chain C) were taken to calculate the calibration coefficients a, b and c. The resistances of the two lowermost thermistors of the chains B and C were converted into temperatures using the high-precision calibration at approximately -6.9, -9.9 and -12.8 °C (chain B) and at -12.8, -14.7 and -16.8 °C (chain C).

Calculation of the Temperature Profiles

As described above, an absolute accuracy of $\pm 0.01\,°C$ can be attributed to the two lowermost thermistors of the chains B and C which were calibrated under special conditions. In order to obtain a high absolute accuracy for the whole temperature

profile, the other temperature measurements were connected to the high-precision ones using the measured temperature gradients between one and the same thermistor with a relative accuracy of $\pm 0.001\,°C$ (see Section 5.2.2).
In case of the thermometric measurement in the 25 m borehole at Colle Gnifetti, the temperatures measured with the two lowermost thermistors (21–25 m depth range) were regarded as fixed values. The above-lying values were then obtained by extrapolating from the 21 m value on, using the measured high-precision temperature gradients.
A similar procedure was applied to the measurement at the Dôme du Goûter site. This time, the temperatures of the second lowest thermistor (at 31 and 32 m depth) were taken to be fixed. The adjacent temperature values were finally obtained using the measured and – between different thermistors – interpolated temperature gradients.

6.4 Results and Comparison with other Climate Records

The borehole-temperature measurements and corresponding calculations are – with one exception – restricted to sites with simple geometries (saddles or domes) which make a one-dimensional treatment possible.

6.4.1 Mont Blanc Area

Extreme differencies in the accumulation rate are characterizing the two sites presented from the Mont Blanc area. Whereas at the saddle of Col du Dôme, 4250 m a.s.l., the yearly accumulation is on the order of 5.8 m (Vincent et al., 1997),

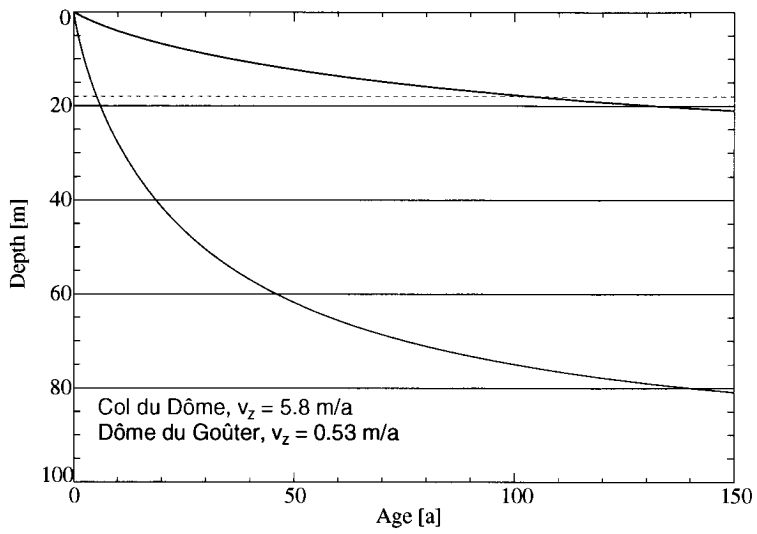

Figure 6.14: Age-depth distribution of the Col du Dôme (98 m ice thickness) and Dôme du Goûter (40 m ice thickness) sites in the Mont Blanc area using measured accumulation rates and the exponential vertical velocity model. The horizontal dashed line indicates 18 m depth.

it is only 0.53 m at the top of Dôme du Goûter (personal communication from S. Preunkert, 2001). Accordingly, the time scales involved differ greatly (Figure

6.14). The temperature at 18 m depth at Col du Dôme is the result of 5 years of accumulation, only.

Col du Dôme

Figure 6.15 gives the measured temperature profile and the corresponding temperature gradients at the flat firn saddle of Col du Dôme from 1998 (borehole 5; Sections 3.2 and 5.3.1). The measured profile is off steady state due to negative temperature gradients at depth in the lower part (Figure 6.15). The saddle is characterized by a very high accumulation rate of 5.8 m/a, which gives an age of the firn at 22 m depth of only about 7 years (see Figure 6.14) for an ice thickness of approximately 98 m (Vincent et al., 1997). For the numerical calculations, a density-depth profile of an

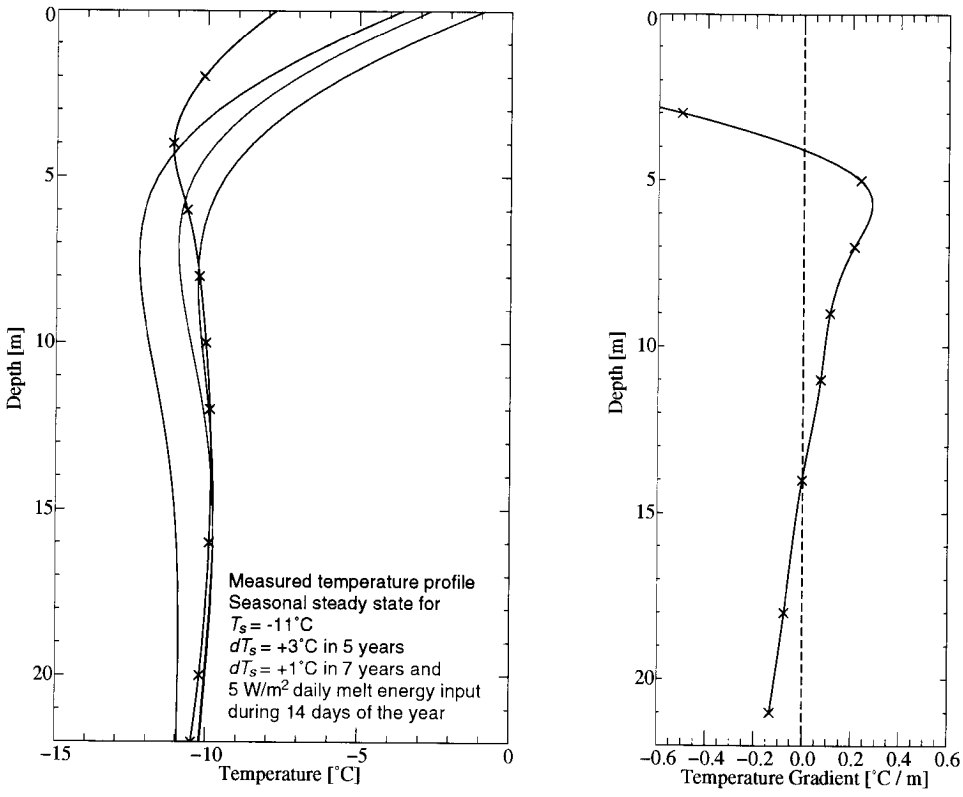

Figure 6.15: Measured and calculated firn temperatures (left panel) and measured temperature gradients (right panel) at Col du Dôme, Mont Blanc area. Starting from a steady-state profile with T_s = -11 °C, the situations for dT_s = +3 °C in 5 years and for dT_s = +1 °C and melt for 14 days per year with a mean daily melt input of 5 W/m² in 7 years are shown.

ice core drilled a little bit further down the saddle from 1994 was taken (borehole 94A; Figure 3.3; Preunkert et al., 2000) and a corresponding velocity-depth distribution derived from b, h and $\rho(z)$ (see Section 6.1.1). Starting from a numerical steady-state profile for T_s = -11 °C, ΔT_s = 8 °C and G_b = 0.03 W/m² for June, 23, a situation for a surface-temperature increase of dT_s = +3 °C in 5 years with no melt and a situation for dT_s = +1 °C and melt for 14 days per year with a mean daily melt input of 5 W/m² during 7 years (6.05 MJ/m² total yearly melt-energy input)

was calculated (Figure 6.15). Both scenarios yield about the same result and fit the lower part of the measured profile well. In the upper part, the offset between the observed and modeled situation is due to the simplified assumption of a sinusoidal surface-temperature variation over the year. The latter scenario is more realistic as an increase in (summer) surface temperature is very likely to be connected to an increase in surface-melt frequency.
The shallow temperature profile, combined with a very high accumulation rate at the site, can only give climatic evidence for a short time period.

Dôme du Goûter

The measured profile at the top of Dôme du Goûter (borehole 99-B; Sections 3.2, 5.3.1 and 6.3) shows again a very strong off steady-state shape (Figures 6.16 and

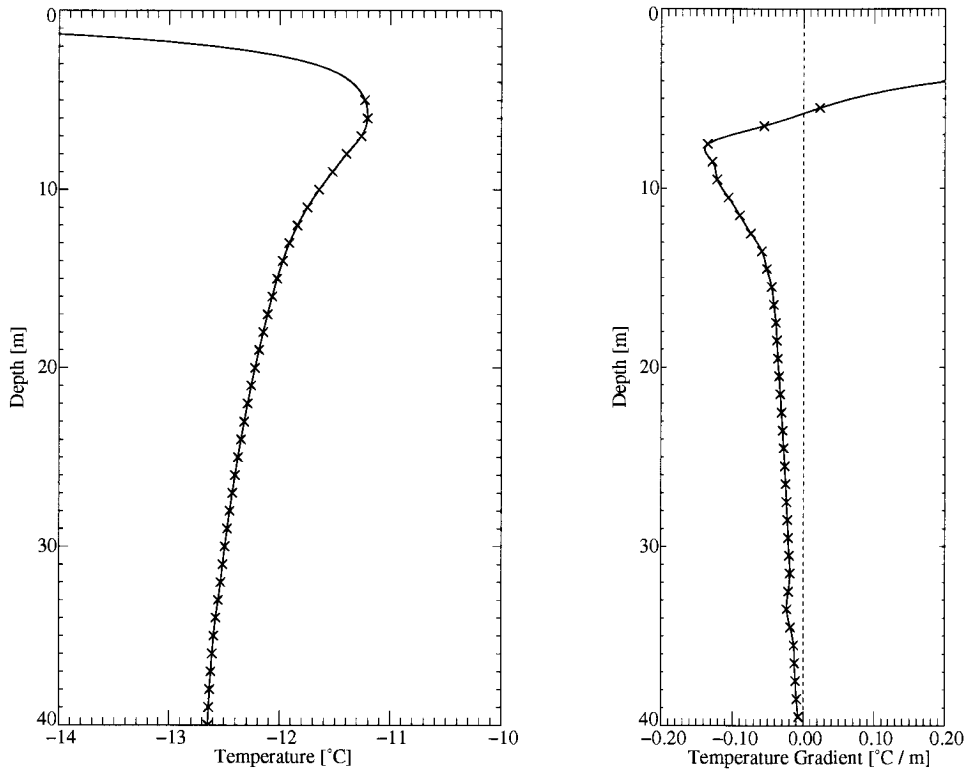

Figure 6.16: Measured englacial temperatures (left panel) and temperature gradients (right panel) at Dôme du Goûter, Mont Blanc area from January, 2000.

6.17). The 18-m temperature measured in January, 2000 and the 18-m temperature measured at the same site two years earlier in June, 1998 (borehole 9; Section 5.3.1) agree very well ($\Delta T_{18} = +0.007\,°C$).
Due to the shape of the measured temperature profile (Figure 6.17), the heat flux anomaly (negative temperature gradient at depth) continues in the bedrock, but might meet the steady-state temperature profile faster than it would in the ice, as a consequence of a higher thermal conductivity of rock ($K_r \approx 2.9$ W/(m·K); Section 6.1.1) than of ice. In order to estimate the surface-temperature increase found in the measured temperature profile as compared to a (presumed) steady-state situation,

the measured temperature profile was extrapolated into the underlying bedrock by assuming a constant second derivative of temperature versus depth ($\frac{\partial^2 T}{\partial z^2} = \text{const}$), until the steady-state temperature gradient in the bedrock given as $\frac{\partial T}{\partial z} = \frac{G_b}{K_r}$ was reached. The second derivative of temperature versus depth was taken as a mean from the lowermost 5 m of the measured temperature profile and enhanced by the factor $\frac{K_r}{K_i}$ to account for the higher thermal conductivity in the bedrock. The effect of the enhancement on the extrapolated temperature profile was, however, small and did only lead to a maximum difference of $\Delta T = 0.05\,°C$. Finally, the steady-state temperature profile was calculated numerically in a way to fit the lowermost part of the measured and extrapolated temperature profile with $h = 40\,m$, $T_s = -13.12\,°C$, $b = 0.53\,m/a$, $G_b = 0.03\,W/m^2$ and using the density-depth profile of the ice core drilled to bedrock from 1999 (personal communication from S. Preunkert, 2001). A

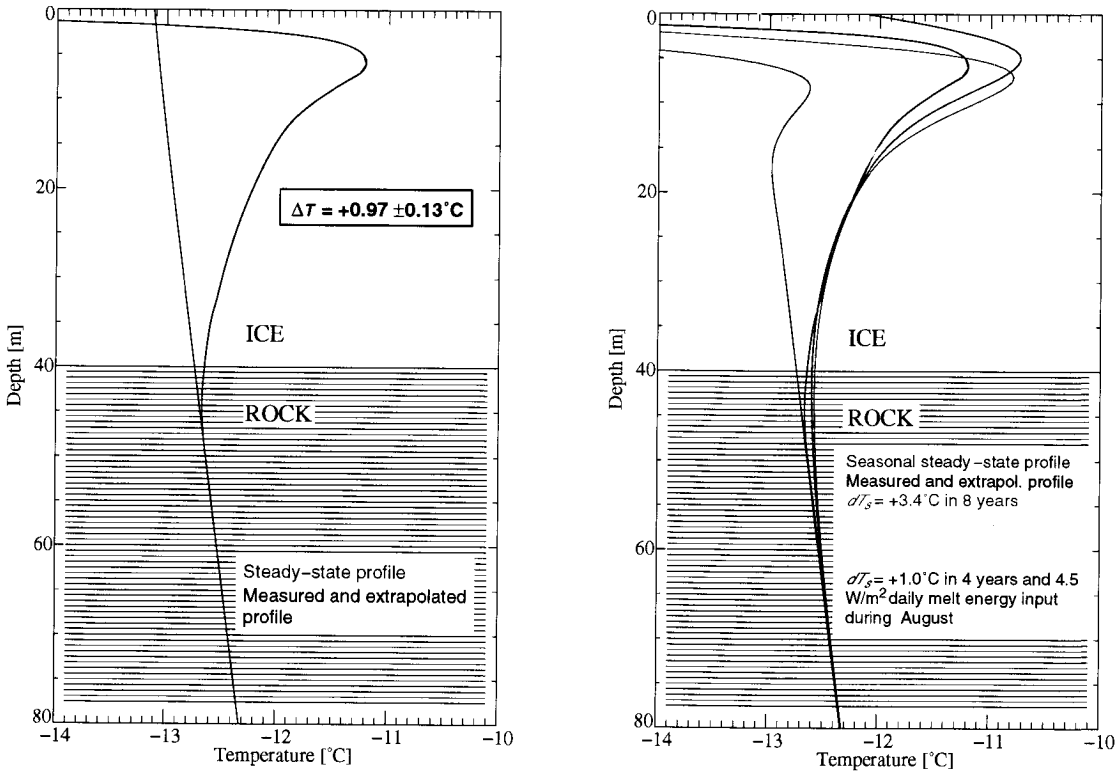

Figure 6.17: Measured and extrapolated temperature profile, calculated steady-state situation and surface-temperature change (left panel) and transient temperature profiles (right panel) at Dôme du Goûter, Mont Blanc area. Three different transient situations starting from a (seasonal) steady-state profile were calculated: $dT_s = +3.4\,°C$ in 8 years with no melt; $dT_s = 0.0\,°C$ and a mean daily melt-energy input of 5.5 W/m^2 during August in 4 years and $dT_s = +1.0\,°C$ and a mean daily melt-energy input of 4.5 W/m^2 during August in 4 years.

deviation between calculated steady-state (surface) temperature and observed 18-m temperature of $\Delta T = +0.97 \pm 0.13\,°C$ results (Figure 6.17). This deviation can only be interpreted in terms of a surface temperature change, if melt is absent and the observed 18-m temperature practically equals the mean annual surface temperature.

The uncertainty range results from varying b from 0.41–0.62 m/a according to different surface densities, G_b from 0.02–0.04 W/m^2 and the mean second derivative of temperature versus depth by considering the lowermost 3–8 m of the measured profile. Due to the small vertical velocities, only a very small discrepancy in surface-temperature change of 0.01 °C was found, when using an analytical steady-state temperature profile (see Section 6.1.2).
A time-dependent calculation is needed to quantify the time horizon of the observed warming. Three different scenarios were calculated starting from a (seasonal) steady-state situation for January 27 using a surface-temperature amplitude of $\Delta T_s = 8$ °C and $h = 40$ m, T_s = -13.12 °C, $b = 0.53$ m/a, $G_b = 0.03$ W/m^2 and the density-depth profile of the ice core drilled to bedrock from 1999 (Figure 6.17):

1. $dT_s = +3.4$ °C in 8 years with no melt;
2. $dT_s = 0.0$ °C and a mean daily melt-energy input of 5.5 W/m^2 during August in 4 years (14.73 MJ/m^2 total yearly melt-energy input);
3. $dT_s = +1.0$ °C and a mean daily melt-energy input of 4.5 W/m^2 during August in 4 years (12.05 MJ/m^2 total yearly melt-energy input).

A large high-frequency energy input is needed to find a reasonable fit with the measured profile. It cannot be stated clearly, whether the energy input needed comes from a surface-temperature increase and/or an increase in melt energy. However, the observed temperature profile at Dôme du Goûter is a clear sign of a very rapid and pronounced change in the thermal boundary condition either in terms of surface temperature or melt energy or a combination of both during the last 5 to 10 years.

Comparison with Air-Temperature Records

Air temperature records from the immediate surroundings of the Mont Blanc area of the last 70 years are presented in Figure 6.18. The deviations from the 68 year MAAT of the Jungfraujoch High-Alpine Research Station (Figure 3.1; Section 4.3.3) and the deviations from the 20th century mean of 16 high-level stations (above 1500 m a.s.l.) of the European Alps, taking the nearest grid point to the Mont Blanc area of the grid-based data set (Böhm et al., 2001), may reflect the air-temperature evolution in the Mont Blanc area best (see Section 4.3.3). The low-pass filtered curves both show an air temperature evolution relatively close to the corresponding means since about 1950, until a distinct warming can be observed starting at 1980. The 1990s are above average on the order of +0.6 (Jungfraujoch) to +1.0 °C (high-level stations).
The air temperature data confirm the warming signal found in the borehole temperatures. The observed firn-temperature anomaly is, thus, mainly the result of the very warm 1990s and – based on the air temperature evolution – it can be assumed that the englacial thermal regime was very close to a steady-state situation before.

Comparison with Observed Melt Layers

No direct evidence for an increase in melt-layer frequency could be found in the upper part of the ice core drilled at the Dôme du Goûter summit in autumn, 1999 (personal communication from S. Preunkert, 2001). However, as the upper 1.4 m of the surface snow and firn were removed when the drill shaft was prepared and,

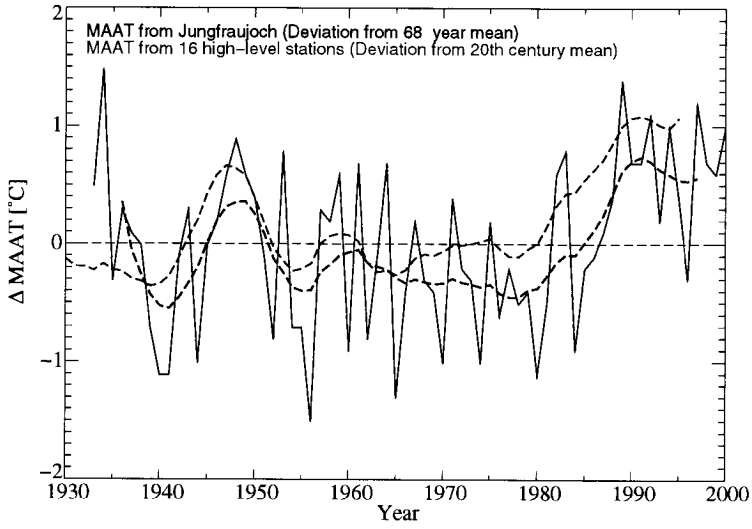

Figure 6.18: MAAT-series from Jungfraujoch and from 16 high-level stations of the Alps (nearest grid point to the Mont Blanc area) showing the deviations from the 68 year mean (Jungfraujoch) or the 20th century mean (16 high-level stations). The dashed lines represent double 5-year low-pass filtered values to give a trend. For better readability, the single MAATs from the 16 high-level stations are not shown.

thus, not analysed, no direct information from the surface layer is available. Strong evidence for an increased melt-layer formation within the surface layer was observed during the dig of the shaft by visual inspection and heavy digging work through massive ice layers (personal communication from S. Preunkert, 2001). The age of the 1.4 m thick surface layer can be denoted with 3 years for the accumulation rate of $b = 0.53$ m/a. This corresponds to the time period of 4 years needed to explain the observed warming in the borehole-temperature profile using a combined scenario of surface-temperature increase and melt-energy input (see above).

6.4.2 Monte Rosa Area

A number of borehole-temperature sites from the Monte Rosa area is presented within this Section. The accumulation rates at the sites and the corresponding time-scales involved are presented in Figure 6.19.

Colle Gnifetti

On Colle Gnifetti, firn-temperature observations could be made since the late 1970s thanks to ongoing core-drilling activities (see Sections 1, 3.3, 5.3.2 and 6.3). 20 years of firn-temperature history are presented in Figure 6.20. The temperature profile from 1983 (borehole 82/1; Figure 3.5) is taken from Haeberli and Funk (1991); the one from August, 1991 (borehole 91A; Figure 3.5) from Suter et al. (2001). Whereas the temperature profiles from 1983 and 1991 are very similar, the ones from May, 1999 (borehole 2; Figure 3.5) and August, 2000 (borehole 00A; Figure 3.5) show an increase in the 18-m temperature of +0.58 °C since 1991.

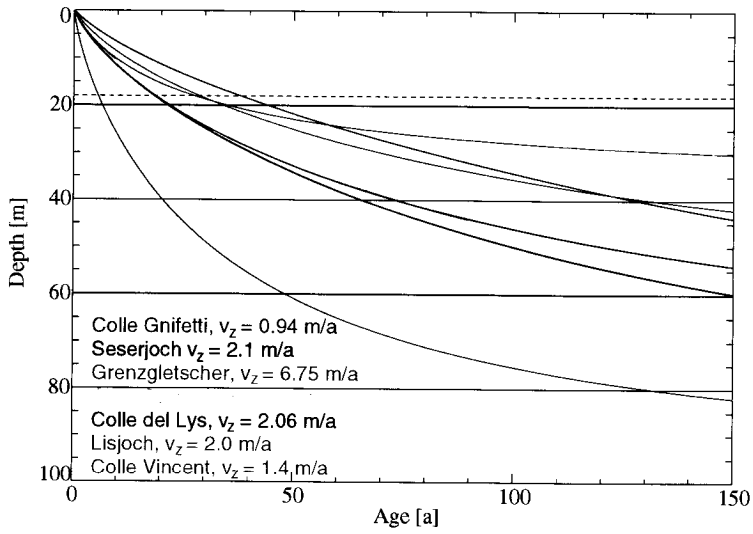

Figure 6.19: Age-depth distribution for various sites in the Monte Rosa area using measured and/or estimated accumulation rates and the exponential vertical velocity model. The horizontal dashed line indicates 18 m depth.

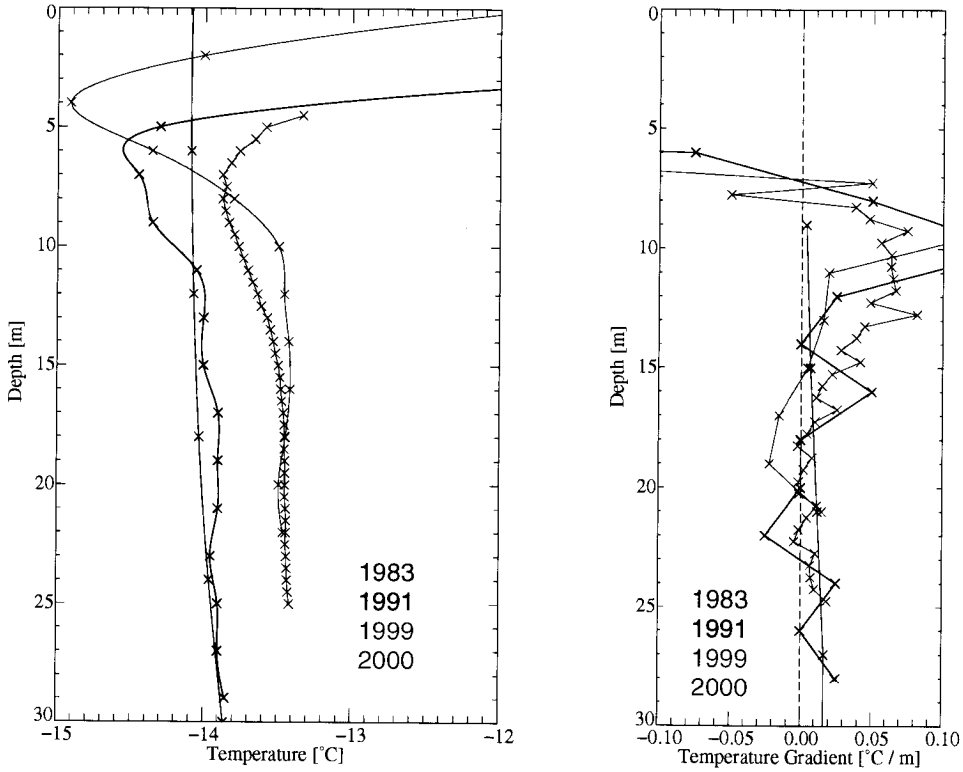

Figure 6.20: Measured englacial temperatures (left panel) and temperature gradients (right panel) at Colle Gnifetti, Monte Rosa area from 1983 to 2000 showing the situations for 1983, 1991, 1999 and 2000.

The measured profile from 1983 is very close to a steady-state profile (Haeberli and Funk, 1991). The steady-state situation for the 1983-profile was recalculated using $h = 124\,\mathrm{m}$, $T_s = -14.1\,^\circ\mathrm{C}$, $b = 0.94\,\mathrm{m/a}$, $G_b = 0.04\,\mathrm{W/m^2}$ and the density-depth profile of the saddle ice core drilled to bedrock in 1982 (personal communication from M. Lüthi, 2001; Figure 6.21). For the profile from the year 2000, a steady

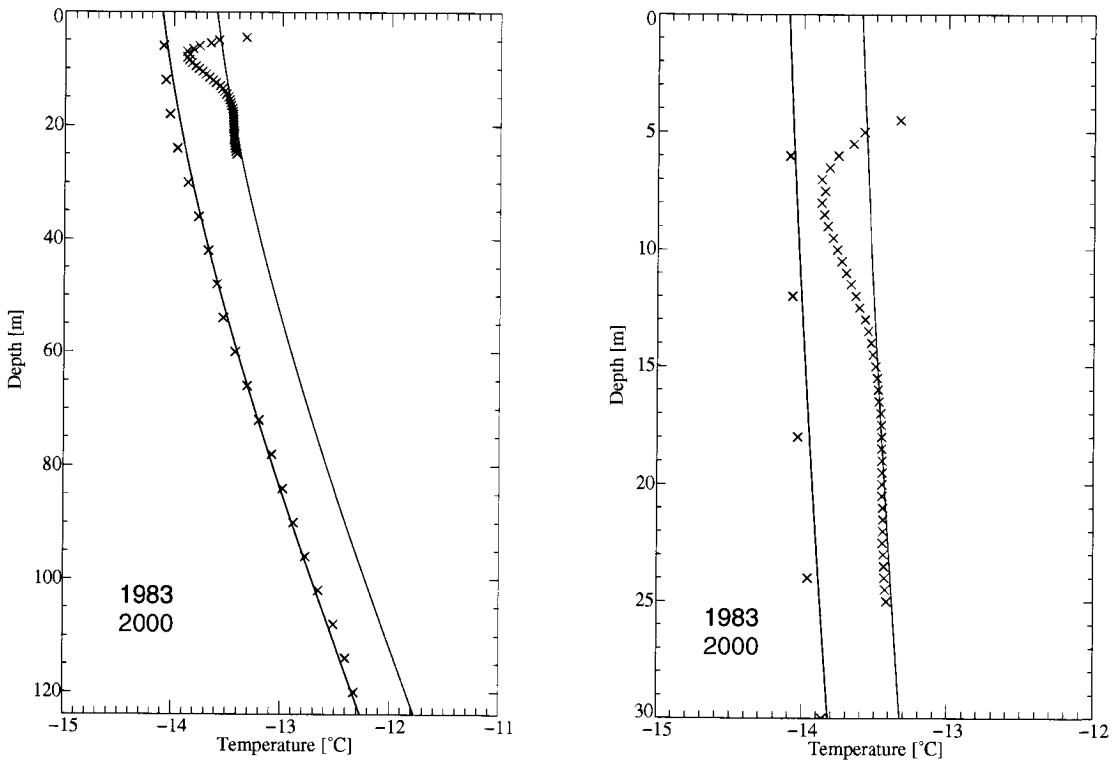

Figure 6.21: Measured and calculated (steady-state) temperature profiles at Colle Gnifetti, Monte Rosa area for the situation in 1983 ($T_s = -14.1\,^\circ C$) and in 2000 ($T_s = -13.6\,^\circ C$). The left panel shows the situation for the whole depth range ($h = 124$ m); the right panel gives an enlarged view on the upper 30 m.

state was calculated with $T_s = -13.6\,^\circ\mathrm{C}$ and the other input parameters being the same as above (Figure 6.21). The lower part of the measured profile from the year 2000 shows a very good fit to the new steady-state profile. This means that the perturbation in the temperature profile due to the recent warming must be found below 25 m depth. The 20 year time series of englacial temperatures at Colle Gnifetti suggests a surface-temperature increase of approximately $+0.6\,^\circ\mathrm{C}$ since about 1990, under the assumption of a stable or negligible surface melt-energy input.

Seserjoch

Although the permanently installed thermistor chain at Seserjoch (borehole 0; Figure 3.5) was observed over almost 2 years, it is very likely that the chain was never in complete contact with the surrounding firn. Borehole closure experiments in cold firn (eg Lüthi, 2000) showed that closure rates are very small in the upper 20–30 m of the firn. It is, however, possible that the lower part of the chain was frozen in after the drilling process due to re-freezing meltwater at the bottom of the

borehole. Additionally, the chain was fixed with the glacier at the surface. In the bottom part of the borehole (where the chain was perhaps frozen in), the relative changes in the thermistor intervals due to changing vertical velocities at depth would be small and can be neglected. Thus, the absolute depths of the thermistors were calculated for a free-hanging chain and corrected according to the observed surface accumulation.

Observed Firn-Temperature Profiles from 1998 to 2000

Figure 6.22 gives the observed firn temperatures and temperature gradients at Seserjoch (see Sections 3.3, 5.3.2 and 6.3) from 1998 to 2000. The time series from October 31, 1998 to October 31, 1999 and October 13, 2000 and the winter-/summer profiles from January 25, 1999, September 1, 1999, January 25, 2000 and September 1, 2000 are shown. Both the observed temperature profiles and the calculated temperature gradients suggest an ongoing cooling since October, 1998 with a decrease of the 18-m temperature by -0.74 °C until October, 2000. If no depth correction is made, the thermistor at 18 m depth gives a cooling of -0.39 °C. However, no long-term trend can be derived from these observations due to the short observation period.

Determination of the Thermal Diffusivity κ

Using the analytical solution of the heat-conduction problem in one dimension (Equation 6.20), it is possible to calculate the thermal diffusivity κ of the snow and firn for a certain depth, if a one year time series of measured temperatures is available. The calculation is based on the assumption of a strictly periodical (sinusoidal) surface temperature, no vertical motion and thermal steady-state conditions:

$$\kappa = \frac{\omega}{2} \cdot \left(\frac{z_1 - z_2}{\ln \frac{\Delta T_2}{\Delta T_1}} \right)^2 , \tag{6.30}$$

where ω = angular frequency for a one year period, z = depth, ΔT = maximum temperature amplitude over a year at depth z. The time period from April, 1999 to March, 2000 was taken. For a certain depth, the mean values were calculated by using two neighbouring thermistors without applying a depth correction (free-hanging chain). The derived thermal diffusivities and calculated thermal conductivities (Equation 6.15) are given in Figure 6.23 together with the parameterized values for κ (Equation 6.15) and K (Equations 6.3 and 6.4). The thermal conductivities were calculated with the measured density profile from the upper 10 m of snow and firn at Seserjoch from May, 2000 (Section 3.3.3) and – for the lower part – with the profile from the Colle Gnifetti ice core from 1995 (borehole 95-2; personal communication from L. Keck, 2000) and with a heat capacity at -10 °C (Equation 6.16). As only the uppermost 20 m of the firn are seasonally influenced, only this depth range is shown. The observed and parameterized values for κ and K agree quite well although single outliers occur. The observed scattering of κ and K can be explained with density irregularities due to ice-layer formation. The determination of κ and K has to be regarded with care since a cooling is observed (see above), the assumption of a strictly periodical (sinusoidal) surface signal might not be valid, the temperatures are not measured at the same depth referred to the actual surface and the density is not strictly constant in time at the position of a certain thermistor.

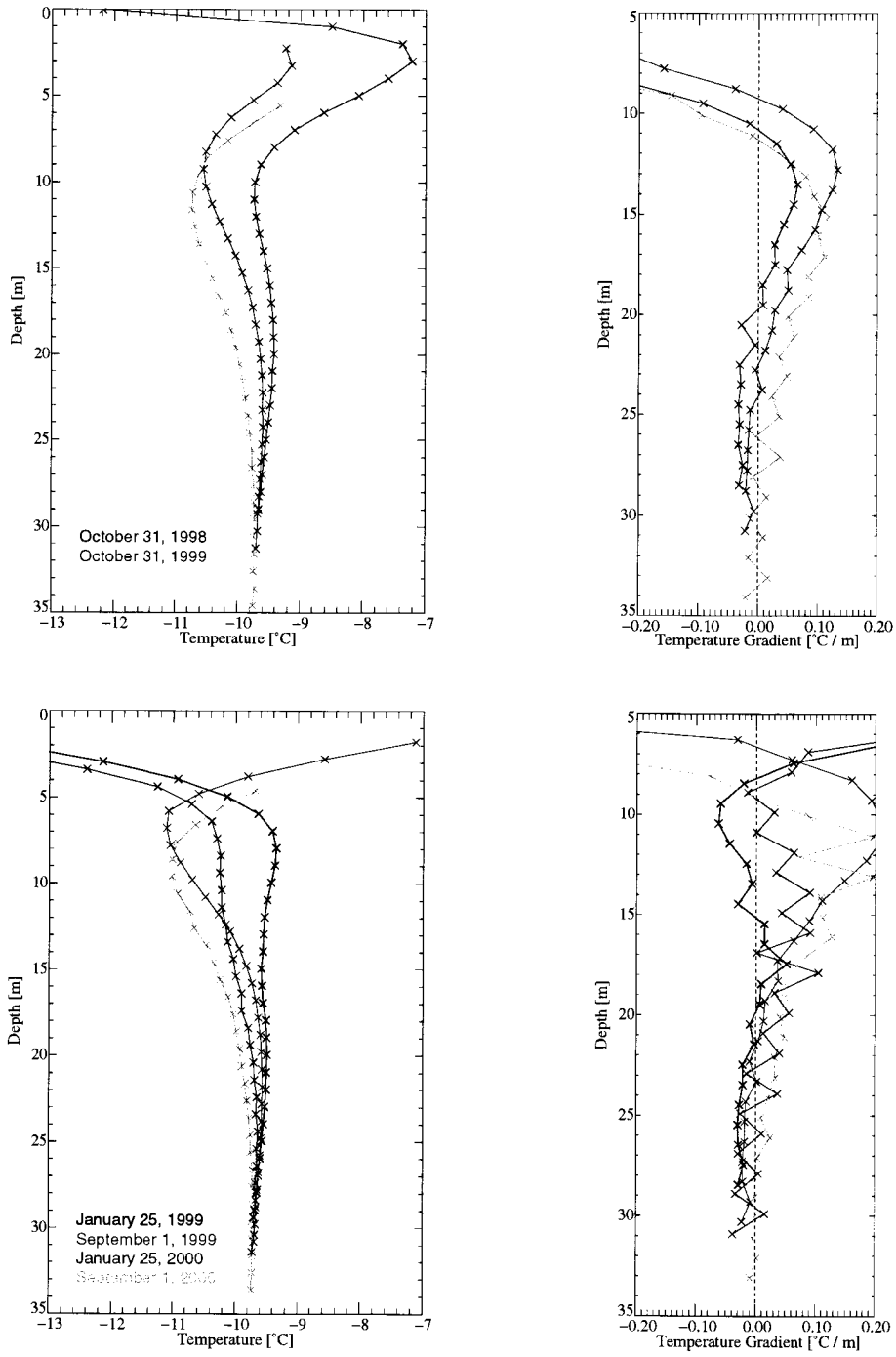

Figure 6.22: Measured englacial temperatures and temperature gradients at Seserjoch, Monte Rosa area from 1998 to 2000. The profiles from October 31, 1998; October 31, 1999 and October 13, 2000 (upper panel) and the winter-/summer profiles from January 25, 1999; September 1, 1999; January 25, 2000 and September 1, 2000 (lower panel) are presented. The depth 0 is referred to the momentary surface.

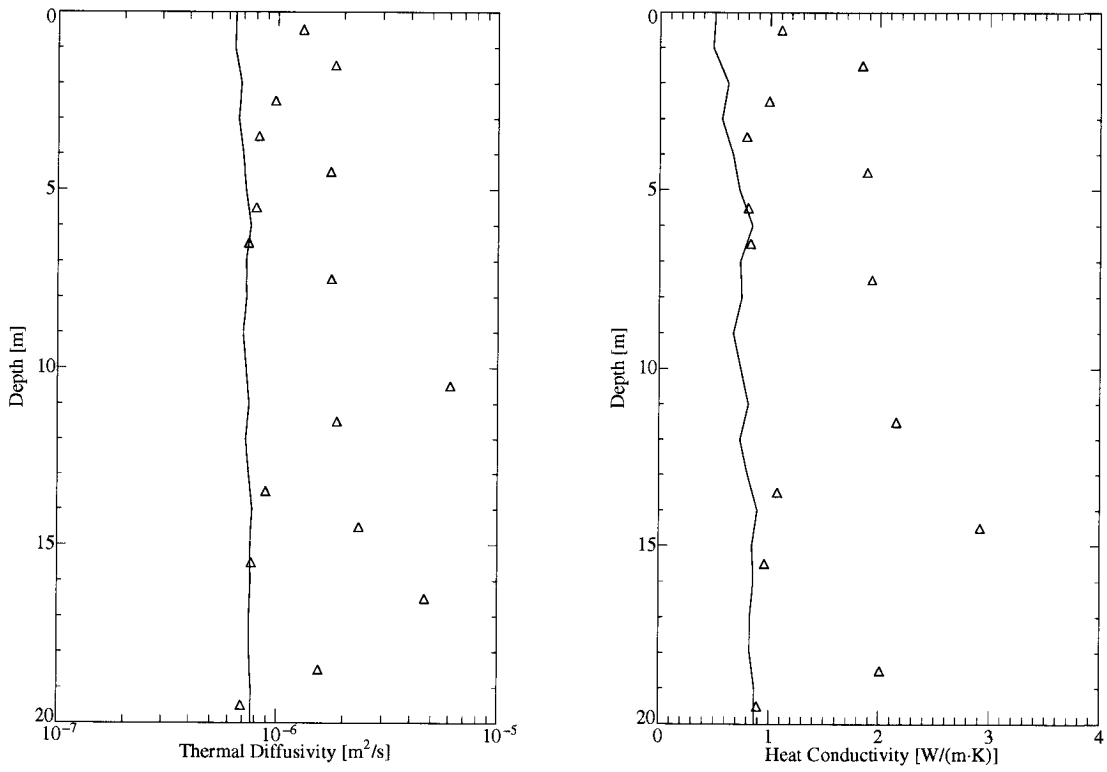

Figure 6.23: Observed (triangles) and parameterized (solid lines) thermal diffusivities κ (left panel) and thermal conductivities K (right panel) at Seserjoch using the observed temperature amplitudes at depth from April, 1999 to March, 2000 (triangles) and a density-dependent parameterization (solid line). 0 m depth is referred to the position of the uppermost thermistor.

Controlled Simulation of Englacial Firn Temperatures

An important test for the plausibility of the thermal model are direct comparisons with observed englacial temperature profiles. The continuous temperature observations at Seserjoch from September, 1998 to October, 2000 offer the possibility for a direct verification. The time period from March 15, 1999 to January 25, 2000 with high-quality (energy-balance and firn-temperature) data was selected to have an optimum upper boundary condition. The measured 10 minute surface temperatures T_s and – in case of a 0 °C surface temperature – the 10 minute residual fluxes of the energy-balance calculation as melt-energy input (see Section 4.4.4) were taken as the upper boundary conditions. To account for the instrumental inaccuracies, calculations were also made for melting conditions starting at measured surface temperatures of -0.5 and -1.0 °C. This accounts for the accuracy of the IR-Thermometer with ±0.5 °C at 0 °C and of the Precision Infrared Radiometer with (estimated) ±5 W/m^2 or ±1.1 °C at 0 °C. The firn temperature measured at 29 m depth from March 15, 1999 was prescribed as the lower boundary condition. The time step Δt was chosen as 10 minutes in order to directly feed in the observed surface values and the depth step Δz as 0.25 m to have a very accurate depth representation during the melt season. The horizontal velocity at the surface was taken as 2.1 m/a (Section

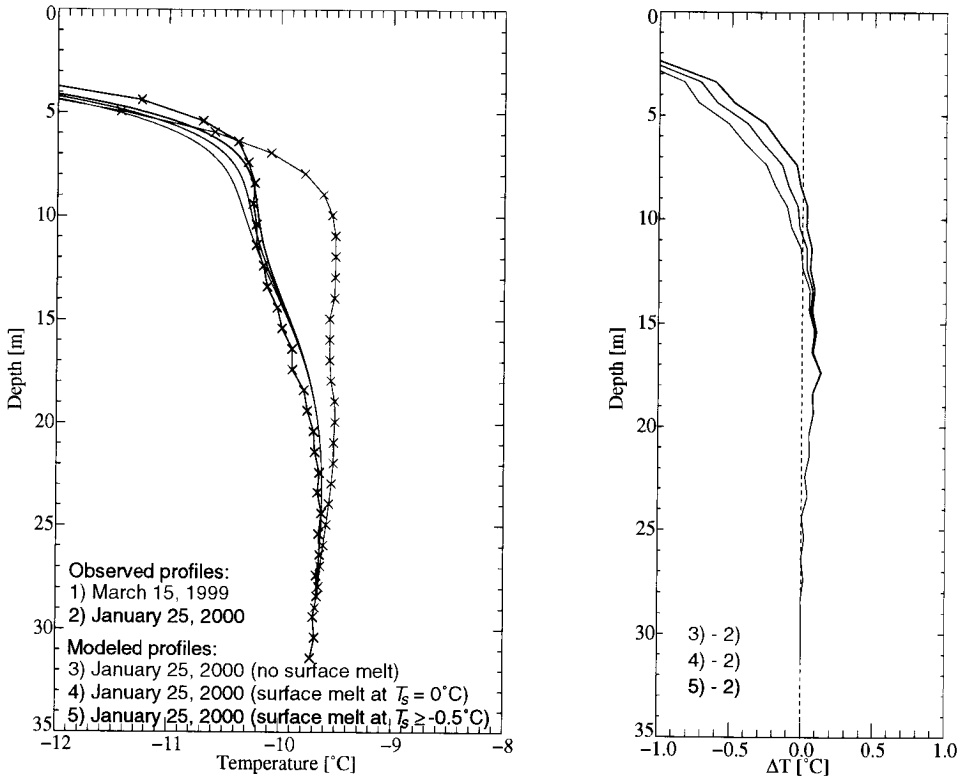

Figure 6.24: Controlled simulation of the englacial firn temperatures at Seserjoch, Monte Rosa. Firn temperatures were calculated from March 15, 1999 (initial condition) to January 25, 2000 using 10 minute values of measured surface temperatures and – in case of a 0°C surface temperature T_s – the residual energy flux of the energy-balance calculation as melt-energy input. Runs are shown for a situation with no melt, surface melt starting at $T_s = 0°C$ and surface melt already starting at $T_s = -0.5°C$. Profiles are given in the left panel; deviations from the measured profile of January 25, 2000 in the right panel using the corresponding colors from the left panel.

4.3.9). Rare data gaps were interpolated to have a complete surface input signal. The initial condition was the measured temperature profile from March 15, 1999. The result from the calculation is presented in Figure 6.24. The measured and calculated profiles for the time period considered agree very well. The best result is obtained by assuming a start of surface melt at a measured surface temperature of -0.5 °C, already.

Borehole Thermometry

An assessment of the surface-temperature increase found in the measured temperature profile as compared to a (presumed) steady-state situation was made by extrapolating the measured temperature profile to the underlying bedrock at 103 m depth (personal communication from O. Eisen, 2000). To do so, a constant second derivative of temperature versus depth ($\frac{\partial^2 T}{\partial z^2} = \text{const}$) was assumed, until the steady-state temperature gradient in the ice given as $\frac{\partial T}{\partial z} = \frac{G_i}{K_i}$ was reached. The second derivative of temperature versus depth was taken as a mean from the low-

ermost 5 m of the measured temperature profile omitting the lowest thermistor due to an irregularity (see Figure 6.22). The relatively high intervals between the single thermistor readings of 1 m and the somewhat worse relative and absolute accuracy between the different thermistors (see Section 5.2.2), made the extrapolation quite sensitive to the choice of the thermistor set, in such a way that only the above constellation gave a useful extrapolated profile. To avoid complications with depth adaption (see above), a profile from January 25, 1999, was chosen with no surface accumulation since the installation of the thermistor chain. As for the measured profile at Dôme du Goûter (Section 6.4.1), the steady-state temperature profile was calculated numerically in a way to fit the lowermost part of the extrapolated temperature profile with $h = 103$ m, $T_s = -9.98$ °C, $b = 2.1$ m/a, $G_i = 0.03$ W/m^2 and using the above-mentioned density-depth profile for calculating the velocity-depth distribution of the Seserjoch site (see Section 6.1.1). A deviation between the calculated steady-state (surface) temperature and the observed 18-m temperature of $\Delta T = +0.48+0.27/-0.11$ °C results (Figure 6.25). The uncertainty range results from varying b from 1.1–3.1 m/a due to an unknown long-term vertical velocity and G_i from 0.02–0.04 W/m^2. When using an analytically calculated steady-state temperature profile (see Section 6.1.2) a surface-temperature change of +0.36 °C results. A time-dependent calculation is needed to quantify the time horizon of the observed warming. Four different scenarios were calculated starting from a (seasonal) steady-state situation for January 25 using a surface-temperature amplitude of $\Delta T_s = 8$ °C and h, T_s, b and G_i from above (Figure 6.25):

1. $dT_s = +2.5$ °C in 8 years with no melt;
2. $dT_s = 0.0$ °C and a mean daily melt-energy input of 5.2 W/m^2 during 26 days in 7 years (11.68 MJ/m^2 total yearly melt-energy input);
3. $dT_s = +1.0$ °C and a mean daily melt-energy input of 2.1 W/m^2 during 48 days in 7 years (8.71 MJ/m^2 total yearly melt-energy input);
4. a combined scenario with $dT_s = +1.0$ °C and a mean daily melt-energy input of 2.1 W/m^2 during 48 days in 5 years (8.71 MJ/m^2 total yearly melt-energy input) and, subsequently, $dT_s = -0.5$ °C and a mean daily melt input of 1.0 W/m^2 during 7 days in 2 years (0.60 MJ/m^2 total yearly melt-energy input).

As in case of the Dôme du Goûter situation, the observed warming can hardly be explained by a surface-temperature increase nor an increase in surface melt alone. A combined scenario gives a very good representation of the observed profile, which can be explained by a surface cooling and corresponding decrease of surface melt during 2 years, after a strong surface warming over 5 years starting from the (assumed) steady-state profile. The mean surface-temperature increase of +0.5 °C over the calculation period of 7 years is in good agreement with the derived warming from the comparison between the observed and extrapolated profile and the numerically calculated steady-state profile (see above).

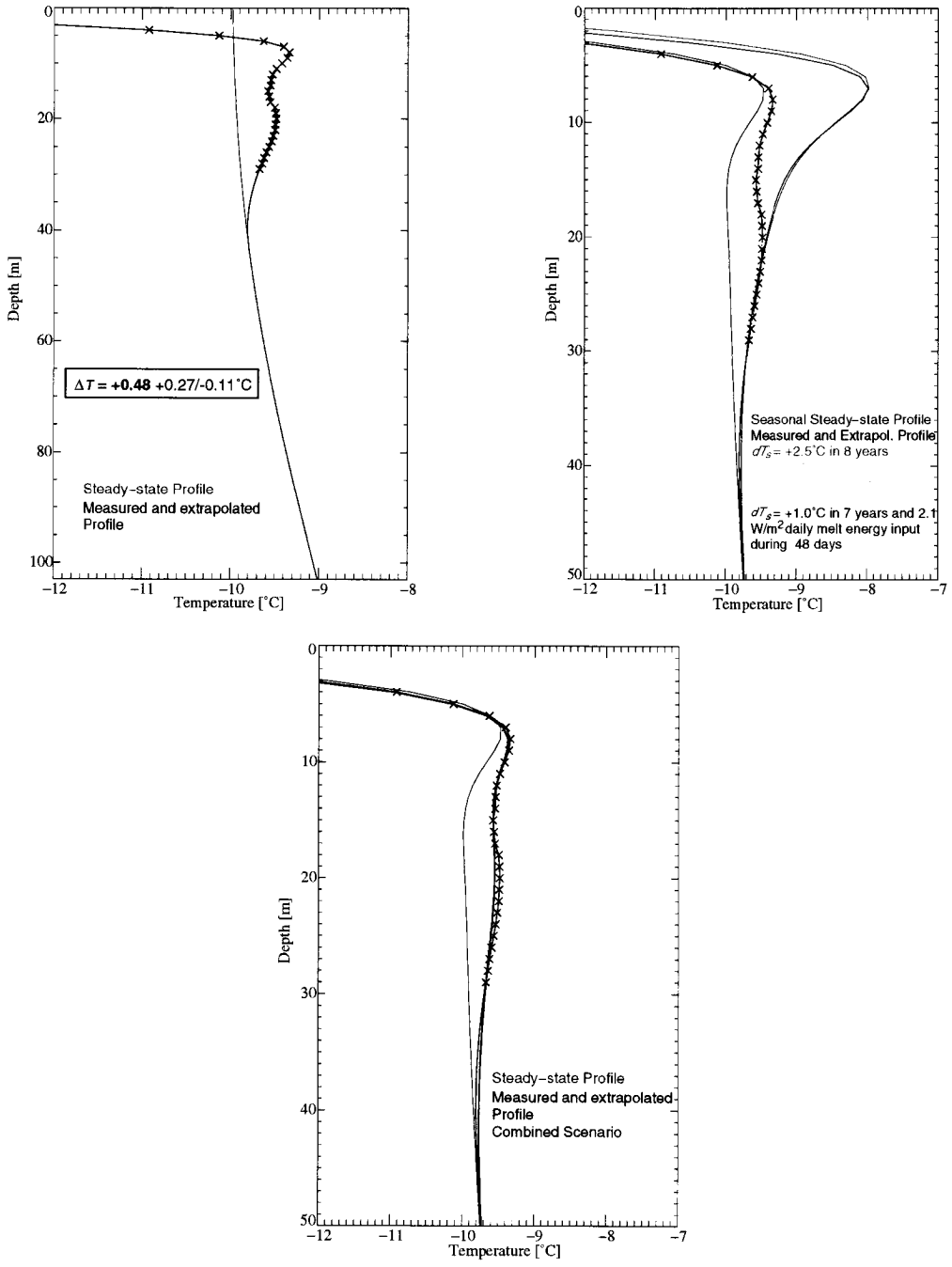

Figure 6.25: Measured and extrapolated temperature profile, calculated steady-state situation and surface-temperature change (upper left panel) and transient temperature profiles (upper right and lower panel) at Seserjoch, Monte Rosa area. The upper right panel shows three different transient situations starting from a (seasonal) steady-state profile: $dT_s = +2.5\,°C$ in 8 years with no melt; $dT_s = 0.0\,°C$ and a mean daily melt-energy input of 5.2 W/m^2 during 26 days in 7 years and $dT_s = +1.0\,°C$ and a mean daily melt-energy input of 2.1 W/m^2 during 48 days in 7 years. The lower panel gives a combined scenario with $dT_s = +1.0\,°C$ and a mean daily melt-energy input of 2.1 W/m^2 during 48 days in 5 years and, subsequently, $dT_s = -0.5\,°C$ and a mean daily melt input of 1.0 W/m^2 during 7 days in 2 years.

In order to assess the steady-state melt-energy input which is needed to meet the present-day steady-state temperature profile (see above), a steady-state profile for the expected mean annual surface temperature with no melt was calculated and a melt-energy input prescribed, until the profile fitted the present-day situation. The mean annual surface temperature to be expected was derived from mean annual air-temperature data from Jungfraujoch from 1965 to 1998, which corresponds to the age of the firn at 29 m depth, and extrapolated to the altitude of the Seserjoch site (see Section 4.3.3), which resulted in T_s = -12.07 °C (taking the air temperature) or in T_s = -13.87 °C (adding the shift between air temperature and surface temperature observed at the Seserjoch energy-balance station; see Section 6.1.1). In the first case, a mean daily melt-energy input of 5.3 W/m^2 during 37 days had to be prescribed (16.94 MJ/m^2 total yearly melt-energy input) and in the latter case of 8.5 W/m^2 during 37 days (27.17 MJ/m^2 total yearly melt-energy input). These total yearly melt-energy inputs agree well with the observed total yearly melt-energy at Seserjoch from 1999 (see Section 4.4.4).
Using the situation at the Seserjoch site, a sensitivity between surface temperature and total yearly melt-energy input can be assessed, which is 8.95 MJ/(m^2·°C). Thus, a yearly melt-energy input of 8.95 MJ/m^2 is equivalent to a 1 °C surface-temperature increase. Care must be taken as not only the total melt-energy input, but also the total duration and the distribution of the melt signal over the melting period is of importance (see Section 6.1.3).

Firn Basin of Grenzgletscher

Rapidly changing thermal conditions in time can be found at a high-accumulation site in a firn basin of Grenzgletscher, 4250 m a.s.l. (Figure 3.5; Sections 3.3 and 5.3.2). The yearly accumulation amounts to 5–8 m of snow (Eichler et al., 2000) which leads to an age of the firn at 18 m depth of approximately 6 years, only (Figure 6.19). The observed firn-temperature profiles and temperature gradients in August, 1991 (borehole 91D; Figure 3.5; Suter et al., 2001) and May, 1999 (borehole 12; Figure 3.5) are presented in Figure 6.26. Due to the high accumulation rate, the upper 18 m of the firn cover were completely replaced since 1991. The increase of the 18-m temperature of ΔT = +5.5 °C is considerable and points out a drastical change in the temperature- and melt regime at the surface. The sensitivity study (Section 6.1.3) shows that a warming of approximately +6 °C requires a total yearly melt-energy input on the order of 40–50 MJ/m^2 (Figure 6.12). This melt-energy input is about a factor of 2–4 higher than the melt-energy input observed at Seserjoch (Table 4.4). Thus, it can be assumed that the observed warming is on the one hand the result of the air-temperature increase starting in the 1980s (Figure 6.28), and on the other hand of a strongly enhanced melt-energy input in the 1990s due to more frequent surface melt in summer.

Other Sites

Within this paragraph, firn-temperature profiles and corresponding temperature gradients from four additional saddle- or dome sites of the Monte Rosa area are presented. All the temperatures were measured in 1999 (see Sections 3.3 and 5.3.2). The observed temperature profiles, temperature gradients and calculated steady-state

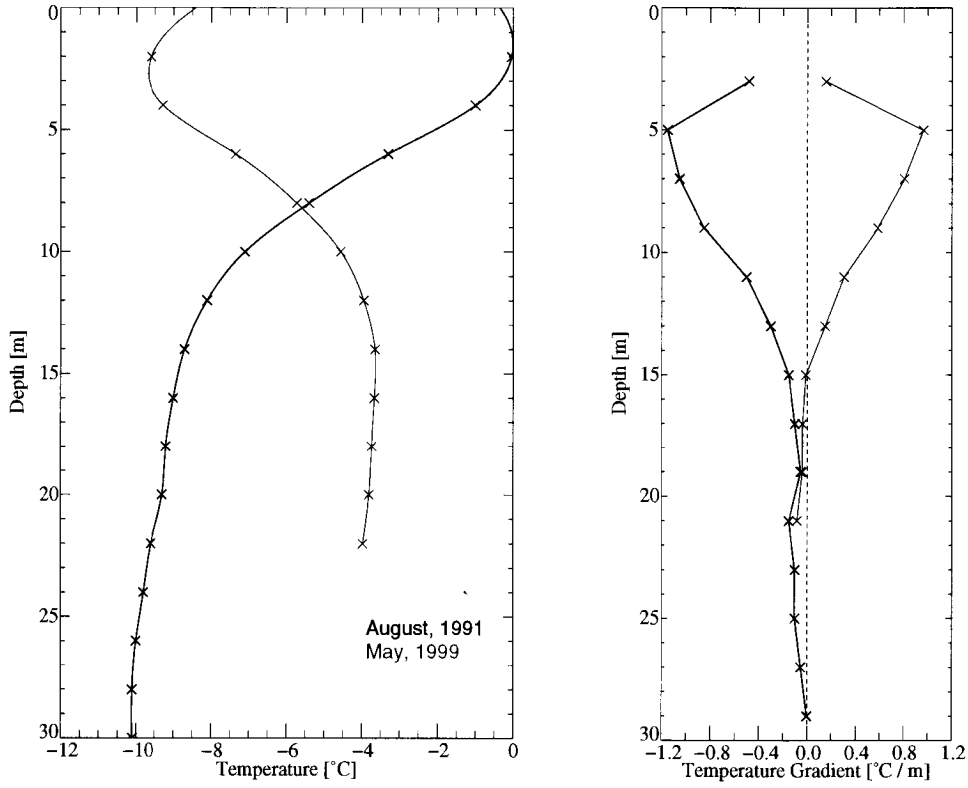

Figure 6.26: Measured firn temperatures (left panel) and temperature gradients (right panel) in a firn basin on Grenzgletscher, 4250 m a.s.l., Monte Rosa area. The situation in August, 1991 and May, 1999 is shown.

situations (see below) are given in Figure 6.27. The steady-state profiles for the individual sites were calculated taking extrapolated MAAT-data from the High-Alpine Research Station of Jungfraujoch (Figure 3.1) as the upper boundary condition and for the time period of the age of the firn at 18 m depth. Additionally, a certain amount of yearly melt-energy input was assumed, in a way to meet the observed temperature profiles or 18-m temperatures.

Saddle between Ludwigshöhe and Parrotspitze (Colle Parrot), 4283 m a.s.l.
The steady-state temperature profile for the saddle between Ludwigshöhe and Parrotspitze (borehole 18; Figure 3.5) was obtained with $h = 100$ m, $T_s = -11.66$ °C (extrapolated mean air temperature over 19 years), $b = 1.8$ m/a, $G_b = 0.03$ W/m^2, $\Delta T_s = 8.0$ °C, the density-depth profile of a 100 m deep ice core from Colle Gnifetti drilled in 1995 (borehole 95-2; personal communication from L. Keck, 2000) and by assuming a mean daily melt-energy input of 6 W/m^2 during 32 days of the year or a total yearly melt-energy input of 16.59 MJ/m^2 (Figure 6.27). The observed temperature profile shows no heat flux anomaly, ie positive temperature gradients at depth and is very close to the calculated steady-state situation. The difference ΔT between the measured 18-m temperature and the steady-state surface temperature T_s amounts to +1.99 °C.

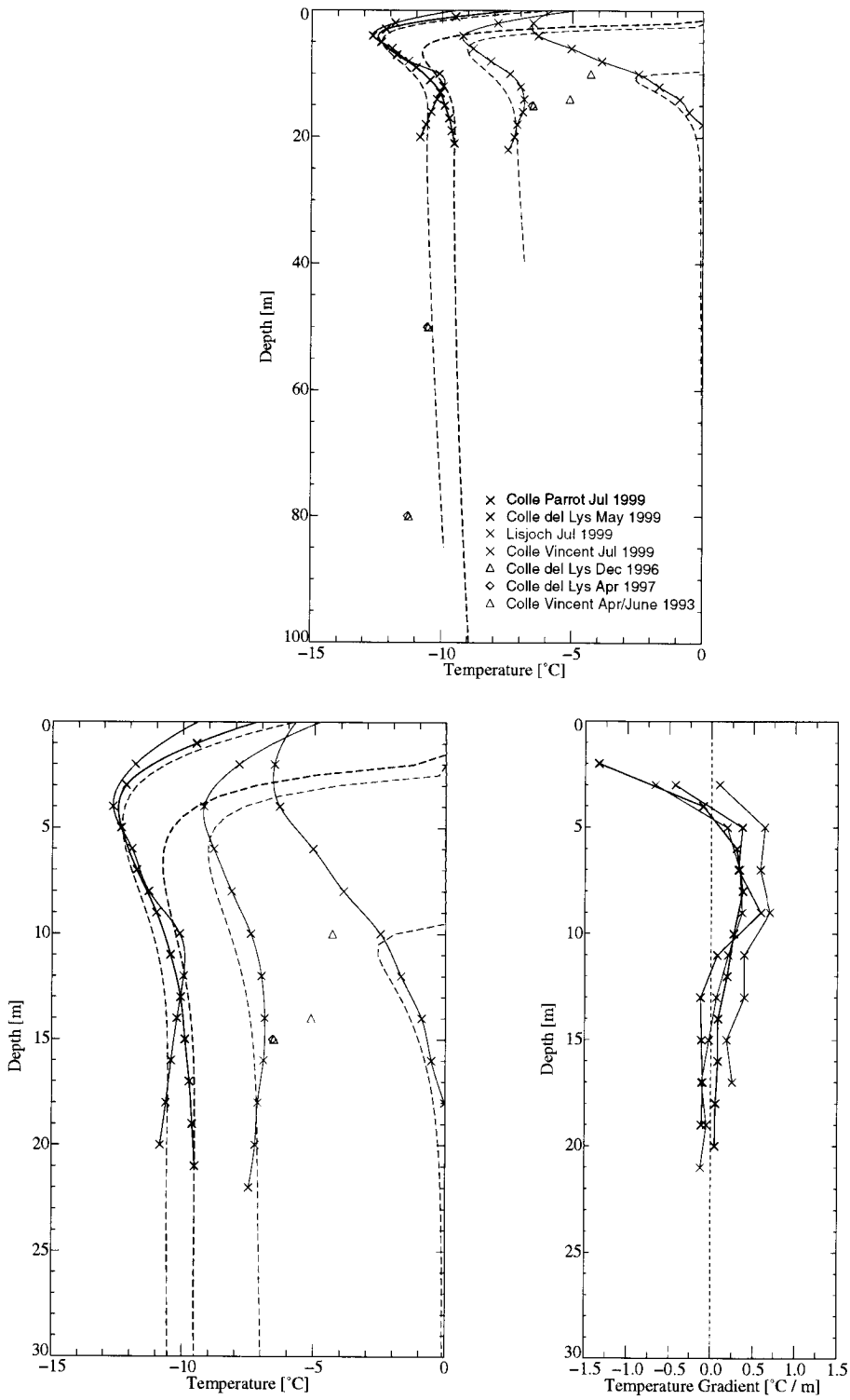

Figure 6.27: Measured firn temperatures (solid lines) and calculated steady-state situations (dashed lines; upper and lower left panel) and temperature gradients (lower right panel) at the saddle between Ludwigshöhe and Parrotspitze (Colle Parrot), Colle del Lys, Lisjoch and Colle Vincent from 1999. The calculated steady-state profiles are based on extrapolated MAAT-data from the High-Alpine Research Station of Jungfraujoch and a certain amount of yearly melt-energy input (see text). The values from earlier observations are given for comparison.

Colle del Lys, 4256 m a.s.l.

The Colle del Lys (borehole 17; Figure 3.5) steady-state profile was calculated using $h = 85$ m (personal communication from G. Rossi, 2001), $T_s = $-11.36 °C (extrapolated mean air temperature over 17 years), $b = 2.1$ m/a, $G_b = 0.03$ W/m^2, $\Delta T_s = 8.0$ °C, the density-depth profile of a 80 m deep ice core drilled at the site in June, 1996 (borehole 96A; Figure 3.5; Rossi et al., 1998; Smiraglia et al., 2000) and with 26 days of melt per year with a mean daily melt input of 3 W/m^2 corresponding to a yearly total of 6.74 MJ/m^2 (Figure 6.27). Again, observed and calculated profiles are quite close and ΔT is found to be +0.74 °C. The actual observed profile is off steady state and shows a warming trend in the bottom part. Compared to englacial temperature observations from December, 1996 and April, 1997 in the deep hole reaching 80 m depth (personal communication from G. Rossi, 2001), a cooling can be observed at 15 m depth since, whereas the deep observations at 50 and 80 m depth give evidence for an off steady-state situation.

Lisjoch, 4151 m a.s.l.

A warming trend in the lower part and a more distinct temperature offset of $\Delta T = +3.60$ °C is found for the situation at Lisjoch (borehole 26; Figure 3.5). The steady-state profile is given by $h = 40$ m (personal communication from G. Rossi, 2001), $T_s = $ -10.73 °C (extrapolated mean air temperature over 25 years), $b = 2.0$ m/a, $G_b = 0.03$ W/m^2, $\Delta T_s = 8.0$ °C, the density-depth profile of the 40 m Dôme du Goûter ice core drilled to bedrock in 1999 (borehole 99-B; Figure 3.3; personal communication from S. Preunkert, 2001) and by 37 days of melt per year with a mean daily melt input of 5.7 W/m^2 or a yearly total of 18.22 MJ/m^2 (Figure 6.27).

Colle Vincent, 4087 m a.s.l.

A very high mean daily melt-energy input of 20 W/m^2 during 45 days of the year (77.76 MJ/m^2 of total yearly melt-energy input) is needed to match the observed (temperate) firn-temperature profile at the Colle Vincent site (borehole 28; Figure 3.5). The other parameters for the steady-state calculation were $h = 70$ m (personal communication from G. Rossi, 2001), $T_s = $-10.67 °C (extrapolated mean air temperature over 26 years), $b = 1.4$ m/a, $G_b = 0.03$ W/m^2, $\Delta T_s = 8.0$ °C and using the density-depth profile from the 80 m deep ice core drilled at the Colle del Lys site in June, 1996 from above (Figure 6.27). A very high ΔT of +10.66 °C results. A strong recent warming is also suggested by shallow temperature observations from April and June, 1993 in the saddle of Colle Vincent (personal communication from G. Rossi, 2001; Figure 6.27).

It is evident that such observed firn-temperature profiles as at Colle Vincent can by no means be explained by a surface- or air-temperature history alone. The duration, frequency and energy release of surface melt events is crucial for understanding the different thermal regimes at the four sites.

Comparison with Air-Temperature Records

The deviations from the 68 year MAAT of the Jungfraujoch High-Alpine Research Station (Figure 3.1; Section 4.3.3) and the deviations from the 20th century mean of 16 high-level stations (above 1500 m a.s.l.) of the European Alps, taking the nearest grid point to the Monte Rosa area of the grid-based data set, (Böhm et al., 2001)

are given in Figure 6.28. As in Section 6.4.1, both low-pass filtered curves show a temperature evolution close to the corresponding means since about 1950, until a distinct warming can be observed starting at 1980. The 1990s are above average on

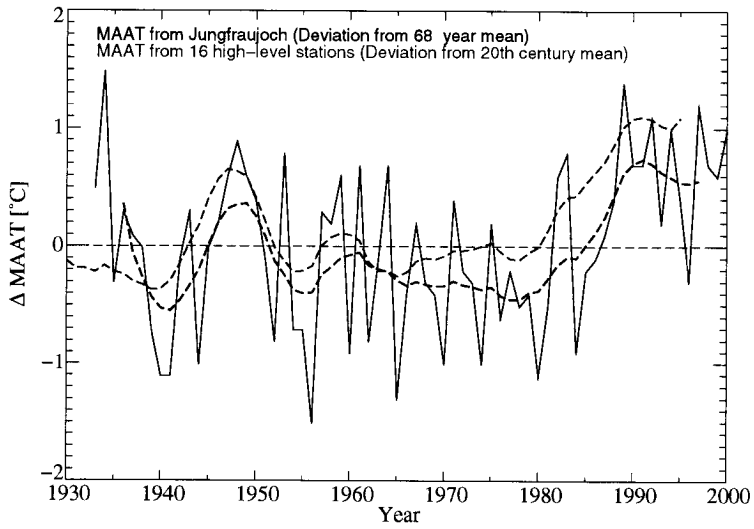

Figure 6.28: MAAT-series from Jungfraujoch and from 16 high-level stations (Monte Rosa grid point) of the Alps showing the deviations from the 68 year mean (Jungfraujoch) or the 20th century mean (16 high-level stations). The dashed lines represent double 5-year low-pass filtered values to give a trend. For better readability, the single MAATs from the 16 high-level stations are not shown.

the order of +0.6 (Jungfraujoch) to +1.0 °C (high-level stations).
The air-temperature data confirm the warming signal found in the borehole temperatures. A very good agreement is found between the air-temperature signal and the firn-temperature increase at Colle Gnifetti (direct observation), and at Seserjoch (calculation) since about 1990. The observed firn-temperature anomalies in the various profiles from the Monte Rosa area are, thus, mainly the result of the very warm 1990s and it can – as for the Mont Blanc area – be assumed that the englacial thermal regime was very close to a steady-state situation before.

Comparison with Observed Melt Layers

The observed melt layers in the ice core from borehole 95-1 at Colle Gnifetti (personal communication from L. Keck, 2001) shows a distinct increase in frequency and thickness of the ice layers in the 1990s (Figure 6.29). Thus, the observed increase of the MAFT at Colle Gnifetti of about +0.6 °C since 1990 could at least be partly the result of a higher latent heat contribution to the snow and firn by stronger surface melt events.

Comparison with Observed $\delta^{18}O$ Records

During the condensation of humid air masses in the atmosphere, the water is subjected to an isotopic disenrichment of the heavier ^{18}O isotopes. According to a simple Rayleigh condensation model, the disenrichment is a function of the remaining fraction of water vapour in the air and, thus, of the difference between

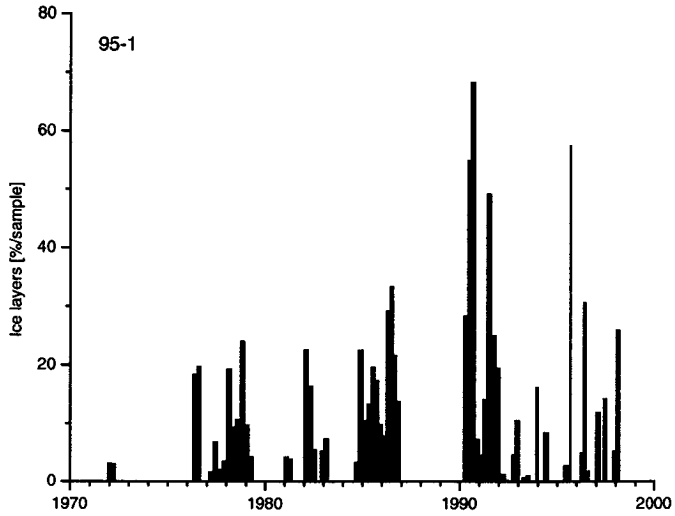

Figure 6.29: Melt-layer frequency of borehole 95-1 *at Colle Gnifetti, Monte Rosa showing a time series from 1970 to 2000. %/sample means thickness of all ice layers in the sample divided by the length of the sample and multiplied by 100.*

the temperature at the beginning of the condensation and the local condensation temperature (Dansgård, 1964). If the source region of water vapour is more or less

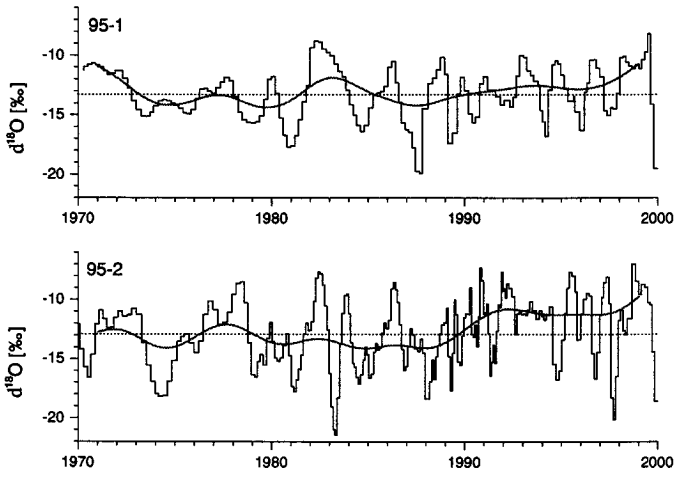

Figure 6.30: $\delta^{18}O$ record of boreholes 95-1 *and* 95-2 *at Colle Gnifetti, Monte Rosa showing a time series from 1970 to 2000 and a cubic spline interpolation (solid lines).*

constant, the magnitude of the disenrichment can be considered a proxy for the condensation or precipitation temperature. In middle and high latitudes, a positive correlation between temperature and ^{18}O value is mostly observed. The $\delta^{18}O$ value

is defined as the difference between the observed ^{18}O concentration and the value for *standard mean ocean water (SMOW)* divided by the SMOW-value and expressed in ‰. Thus, the more negative the $\delta^{18}O$ value, the deeper the (precipitation) temperature.
The $\delta^{18}O$ records of the Colle Gnifetti boreholes **95-1** and **95-2** from 1970 to 2000 are shown in Figure 6.30 (personal communication from L. Keck, 2001). Both cores concurrently indicate $\delta^{18}O$ values above average since about 1990. Care must be taken as $\delta^{18}O$ records only tell about the air-temperature conditions during a precipitation event. Furthermore, snow deposition at Colle Gnifetti is more or less restricted to the period from June to September (Alean et al., 1983), in a way that the isotopic thermometer only reflects summer air temperatures. As summertime is crucial in terms of surface melt, however, the isotopic record can be regarded as an ideal proxy for summer conditions and would then support the observed increase of the MAFT at Colle Gnifetti since 1990.

6.5 Conclusions

Theoretical Calculations

- For a typical high-elevation dome- or saddle site of the Alps with a glacier thickness of 100 m, a thermal surface perturbation of 1 °C in 20 to 30 years penetrates into the glacier rather quickly, leading to a thermal response time on the order of a few 100 years, only.

- Thus, the surface-temperature history can be reconstructed for a few centuries at best. Time-dependent forward calculations can only detect a general long-term trend and are not able to resolve high-frequency changes of the surface-temperature signal. Inverse modeling, however, should have the potential to trace back a surface-temperature history with a higher resolution in time, requiring spatially high-resolved and very accurate borehole-temperature data.

- The release of latent heat due to penetrating and re-freezing meltwater is crucial for the englacial thermal regime. The duration of the surface melt and the mean daily melt-energy input influence the (temporal) penetration depth of the 0 °C front into the snow and firn, which is – besides the mean annual surface temperature – the decisive criterion influencing the (near-surface) thermal conditions of the firn area of a glacier.

- The distribution of the melt signal over the melting period has an important effect on the thermal regime for a high total melt-energy input. Less frequent melt events releasing high amounts of energy favour the formation of cold firn rather than a steady melt-energy release of a small magnitude.

Site Selection

- Cold-firn domes and saddles with a relatively simple geometry and low surface accumulation make a one-dimensional treatment possible and are most suitable for thermometric applications, although the temporal resolution is very limited due to their shallow ice thickness.

Data Acquisition and Analysis

- An absolute accuracy of $\pm 0.01\,^{\circ}C$ can be attributed to the high-precision borehole-temperature measurements at Dôme du Goûter and Colle Gnifetti, whereas it is $\pm 0.03\,^{\circ}C$ for the Seserjoch site.
- The best relative accuracy is obtained when measuring temperature gradients in a borehole and when using one and the same thermistor ($\pm 0.001\,^{\circ}C$). When using a thermistor chain, measured gradients between the thermistors can be connected to a single thermistor with a very accurate absolute temperature.

Results and Comparison with other Climate Records

- Borehole-temperature records from the Mont Blanc and Monte Rosa areas show a surface-temperature increase on the order of $+0.5 - +1\,^{\circ}C$ for the last decade.
- These observations agree well with observed warming trends in air-temperature series and ice-core data (ice layers and $\delta^{18}O$ records) for the 1990s.
- The 2 year time series of firn-temperature measurements at Seserjoch shows a cooling for the 18-m temperature on the order of -0.5 °C from September, 1998 to August, 2000.
- The measured surface energy-balance information (surface temperature and melt energy) is able to reproduce the observed firn temperatures at Seserjoch, using a time-dependent heat-transfer model including latent heat.

Seite Leer /
Blank leaf

7 A Coupled Energy-Balance/Firn-Temperature Model

7.1 Introduction

Coupling the energy-balance information from the surface with the thermal regime of the firn and ice links the atmospheric with the firn-temperature signal and gives evidence for a future development of the cold-firn occurrence under conditions of fast climate change.
The spatial energy-balance model used was developed for complex alpine topography and is based on former works by Funk and Hoelzle, 1992; Konzelmann et al., 1994; Plüss, 1997; Fierz et al., 1997; Hock, 1999 and Hoelzle et al., 2001. A further description is given in Section 7.2. The firn-temperature model is based on the one-dimensional time-dependent thermo-mechanical firn-temperature model from Section 6.1.3 and the application of the firn-temperature model to the calculation of the scenarios described in Section 7.3.
The coupled model was applied to calculate future scenarios of the firn temperature evolution at the firn saddles of Seserjoch and Colle Gnifetti and to model the future cold firn distribution in the Monte Rosa study area. The future evolution was calculated based on the air-temperature scenarios of the Third Assessment Report of Working Group I of the *Intergovernmental Panel on Climate Change (IPCC)* (IPCC, 2001).

7.2 Spatial Energy-Balance Model

The climatological data (daily mean values) for the energy-balance model and the various parameterizations were taken from the meteorological station at Colle del Lys and the energy-balance station at Seserjoch for the time period from May, 1999 to April, 2000 (cf Sections 3.3 and 4).
A comparison was aspired between the model-derived energy-balance components using the meteorological data from the Colle del Lys station and the observed values at the Seserjoch energy-balance station in order to test and verify the model.

7.2.1 Model Description

Shortwave Radiation

The shortwave incoming radiation or global radiation G was directly taken from the Colle del Lys station. The spatial distribution of the global radiation $G_{i,j}$ can be written as

$$G_{i,j} = G_{dir_{i,j}} + G_{dif_{i,j}} \ , \tag{7.1}$$

where $G_{dir_{i,j}}$ = direct shortwave radiation and $G_{dif_{i,j}}$ = diffuse shortwave radiation. $G_{dif_{i,j}}$ was calculated using a parameterization for the ratio of diffuse to global radiation and a fractioning between sky- and terrain contribution (Plüss, 1997):

$$G_{dif_{i,j}} = G_{Lys} \cdot \left(k_d \cdot F_{s_{i,j}} + \alpha \cdot F_{t_{i,j}}\right) / \pi \ , \tag{7.2}$$

with

$$F_{s_{i,j}} = \int_0^{2\pi} \int_{\zeta(\varphi)}^{\pi} \cos\iota \cos\zeta d\zeta d\varphi \text{ and} \tag{7.3}$$

$$F_{t_{i,j}} = \int_0^{2\pi} \int_0^{\zeta(\varphi)} \cos\iota \cos\zeta d\zeta d\varphi \ , \tag{7.4}$$

where G_{Lys} = global radiation at the Colle del Lys station, $k_d = \frac{G_{dif_{Lys}}}{G_{Lys}}$, $F_{s_{i,j}}$ = fraction of the hemisphere which is unobstructed by the terrain (in fractions of π), α = surface albedo, $F_{t_{i,j}}$ = fraction of the hemisphere which is obstructed by the terrain (in fractions of π), ζ = angular height relative to the horizontal plane, φ = azimuth angle and ι = angle between the vector vertical to the terrain and the vector of interest. The fractions F_s and F_t were calculated with a program developed by Funk (1985). In the model, the ratio k_d of diffuse radiation to global radiation was parameterized with (Collares-Pereira and Rabl, 1979)

$$\begin{aligned} k_d &= 0.99 \text{ for } k_t < 0.17 \\ k_d &= 0.17 \text{ for } k_t > 0.8, \text{ otherwise} \\ k_d &= 1.19 - 2.27 \cdot k_t + 9.47 \cdot k_t^2 - 21.86 \cdot k_t^3 + 14.65 \cdot k_t^4 \ , \end{aligned} \tag{7.5}$$

where $k_t = \frac{G_{Lys}}{I_{toa}}$, being the ratio of the global radiation at the Colle del Lys station to the instantaneous solar radiation on a horizontal surface on top of the atmosphere I_{toa}.
$G_{dir_{i,j}}$ was obtained with (Plüss, 1997)

$$G_{dir_{i,j}} = \frac{G_{Lys} \cdot (1 - k_d)}{G_{pot_{Lys}}} \cdot G_{pot_{i,j}} \ , \tag{7.6}$$

where $G_{pot_{Lys}}$ = potential direct solar radiation at Colle del Lys and $G_{pot_{i,j}}$ = potential direct solar radiation at each grid cell calculated with a program especially adapted for the Alps (Funk and Hoelzle, 1992; cf Section 5.4). A comparison between the observed and modeled global radiation $G_{i,j}$ for Seserjoch is shown in Figure 7.1. A good coincidence with some scarce outliers is found.
The shortwave outgoing radiation $K_{i,j}\uparrow$ for each grid cell was obtained with

$$K_{i,j}\uparrow = \alpha_{Ses} \cdot G_{i,j} \ . \tag{7.7}$$

The observed albedo at the Colle del Lys station α_{Lys}, showed some problems probably due to a down-facing pyranometer which was mounted too high above the surface. Therefore, a relatively bad agreement between α_{Lys} and α_{Ses} (albedo at Seserjoch) was found. Thus, no useful parameterization could be found for α_{Lys} using, eg parameters like snowfall events or air temperature (eg Plüss, 1997). Thus, α_{Ses} was taken as the model albedo for the whole area. Although micro-scale albedo variations have to be expected in the study area, this simplification might hold, as the regime and type of precipitation and the air temperatures are very similar for the study area.

Longwave Radiation

The longwave outgoing radiation for each grid cell $L_{i,j}\uparrow$ was obtained using a parameterization of the surface temperature $T_{s_{i,j}}$ based on air temperature and longwave incoming radiation. The coefficients were derived from the observed values at the Seserjoch energy-balance station:

$$T_{s_{i,j}} = -17.2298 + 0.732111 \cdot T_{a_{i,j}} + 0.0605953 \cdot L_{i,j}\downarrow \ , \tag{7.8}$$

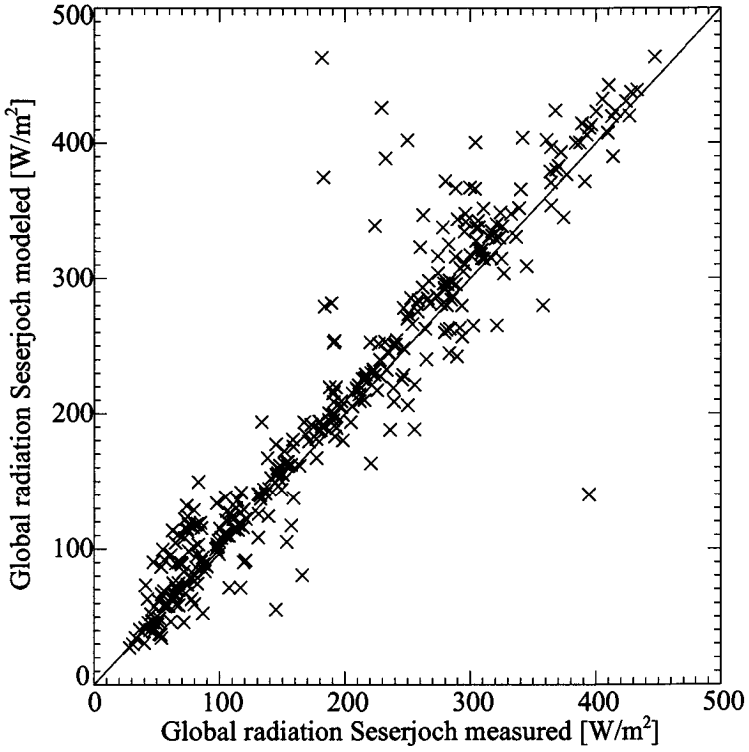

Figure 7.1: Comparison between the observed and modeled global radiation $G_{i,j}$ at Seserjoch for the period from May, 1999 to April, 2000.

where $T_{a_{i,j}}$ = air temperature at each grid cell [°C] and $L_{i,j}\downarrow$ = longwave incoming radiation at each grid cell (see below). The air temperature was distributed over the area by taking the (observed) lapse rate between Gornergrat and Seserjoch of 0.0068 °C/m (Section 4.3.3). The longwave outgoing radiation is finally given by

$$L_{i,j}\uparrow = \sigma \cdot T_{s_{i,j}}^4 \ , \tag{7.9}$$

where σ = Stefan-Boltzmann constant. A parameterization of the surface temperature as proposed by Plüss (1997) based on the parameters air temperature and cloud-cover fraction did not lead to a useful result. Although the surface temperature will actually be the outcome of the energy balance, a parameterization is inevitable for the calculation of the longwave incoming radiation and the turbulent fluxes (see below). A comparison between the observed and parameterized surface temperature at Seserjoch is given in Figure 7.2. A relatively satisfying coincidence is found with a scatter on the order of ±6 °C.
The longwave incoming radiation from the sky $L_{s_{i,j}}\downarrow$ was parameterized with (Konzelmann et al., 1994)

$$L_{s_{i,j}}\downarrow = \left[\left(0.23 + 0.483\left(\frac{e_{i,j}}{T_{a_{i,j}}}\right)^{0.125}\right)\cdot\left(1-cl^3\right) + 0.963cl^3\right]\sigma T_{a_{i,j}}^4 \ , \tag{7.10}$$

where $e_{i,j}$ = water-vapour pressure [Pa], $T_{a_{i,j}}$ = air temperature [K] and cl = cloud-cover fraction [fraction of 1] taken to be uniform over the area. The water-vapour

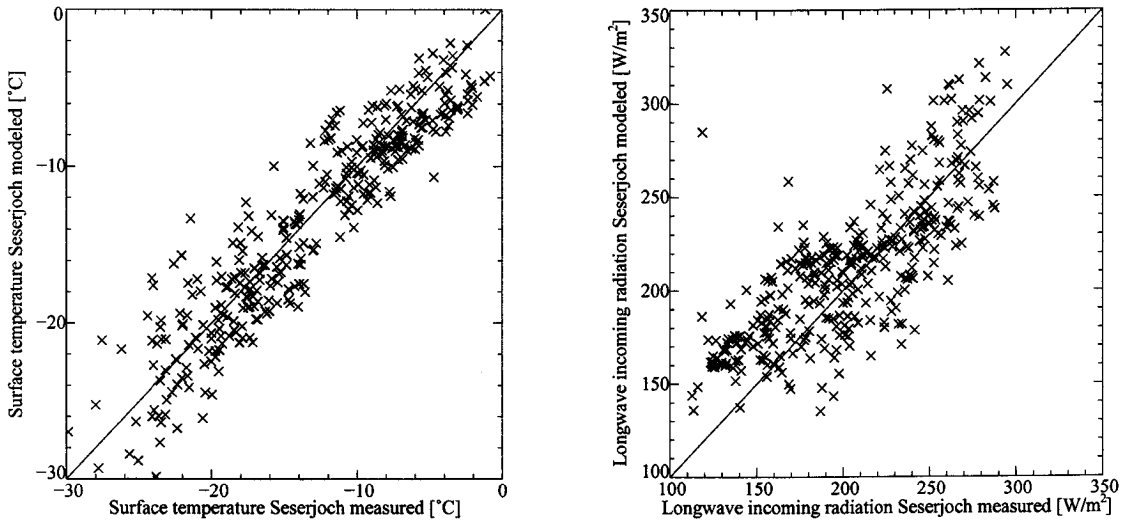

Figure 7.2: Comparison between the observed and parameterized surface temperature T_s (left panel) and longwave incoming radiation $L_{i,j}\downarrow$ (right panel) at Seserjoch for the period from May, 1999 to April, 2000.

pressure was calculated from the measured relative humidity at the Colle del Lys station (Section 4.4.2) and distributed over the area with

$$e_{i,j} = e_{Lys} \cdot e^{-0.00044 \cdot \Delta z} \ , \tag{7.11}$$

whereby e_{Lys} = water-vapour pressure at Colle del Lys and Δz = height difference between each grid cell and the height of the Colle del Lys station. The cloud-cover fraction was parameterized with (Plüss, 1997)

$$cl = \frac{k_d}{0.8627} + 0.046 \ , \tag{7.12}$$

with k_d being the ratio of diffuse to global radiation at Colle del Lys (see above). The contribution to the longwave incoming radiation originating from the terrain $L_{t_{i,j}}\downarrow$ can be written as (Plüss, 1997)

$$L_{t_{i,j}}\downarrow = \left(\frac{L_b}{\pi} + c \cdot \left(2 \cdot T_{a_{i,j}} + T_{s_{i,j}} \right) \right) \cdot F_{t_{i,j}} \ , \tag{7.13}$$

where L_b = emitted radiation of a black body hemisphere at 0 °C and c = constant (0.5 1/°C). Finally, the total longwave incoming radiation for each grid cell $L_{i,j}\downarrow$ is given as

$$L_{i,j}\downarrow = \frac{L_{s_{i,j}}\downarrow \cdot F_{s_{i,j}}}{\pi} + L_{t_{i,j}}\downarrow \ . \tag{7.14}$$

A comparison between the observed and parameterized longwave incoming radiation $L_{i,j}\downarrow$ is shown in Figure 7.2. Although a linear relation can be observed, the scattering is relatively large and on the order of $\pm 40\,\mathrm{W/m^2}$.

Turbulent Fluxes

The turbulent fluxes over the area were calculated using the input data (wind speed, air temperature, humidity, air pressure and sensor heights) from the Colle del Lys station and by applying a bulk approach (Section 4.4.2). The stability was taken into account for each grid cell, individually (Section 4.1.2).
The spatial sensible heat flux $H_{i,j}$ was derived from the distributed air temperature (see above) and the parameterized surface temperature (Equation 7.8). The wind field over the area was calculated using a simplified approach with the wind speed $u_{i,j}$ as

$$u_{i,j} = (u_{Lys} + \Delta z \cdot \Delta u_{SesLys}) \cdot \left(1 - \frac{\alpha}{100}\right) , \tag{7.15}$$

whereby u_{Lys} = wind speed at Colle del Lys, Δz = height difference between each grid cell and the height of the Colle del Lys station and α = slope [°]. Δu_{SesLys} is the mean wind-speed gradient with altitude determined as the difference between the mean Seserjoch and the mean Colle del Lys wind speed from May, 1999 to April, 2000 (0.0058 (m/s)/m). Thus, the higher and the less inclined the grid cell, the higher the wind speed. The assumption is based on the observation of generally lower wind speeds on slopes as compared to exposed saddles and crests. A very good agreement between the observed and parameterized wind speed could be obtained for the Seserjoch site. A comparison between the observed (Bulk method) and

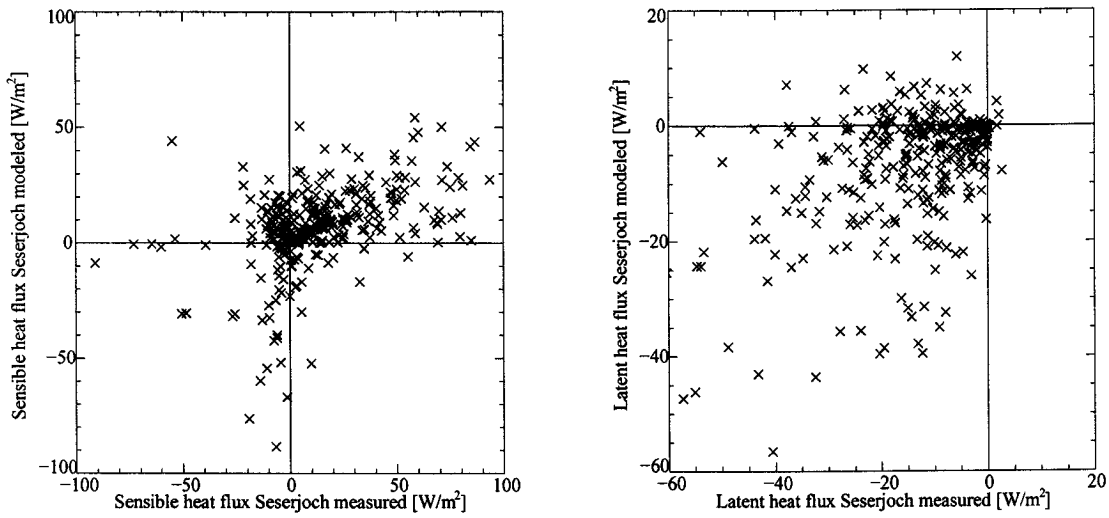

Figure 7.3: Comparison between the observed and parameterized sensible $H_{i,j}$ (left panel) and latent heat flux $LE_{i,j}$ (right panel) at Seserjoch for the period from May, 1999 to April, 2000. The observed heat fluxes were determined with the Bulk method.

modeled sensible heat flux at the Seserjoch site is given in Figure 7.3. Although the flux direction is mostly correct, large absolute errors occur.
The latent heat flux in space $LE_{i,j}$ was obtained by using the above wind field and by assuming a water-vapour saturated surface. For the calculation of the heat of vaporization and sublimation and the specific humidities see Section 4.4.2. The latent heat flux derived for Seserjoch is compared with the observed values (Bulk method) in Figure 7.3. Again, the flux direction is mostly correct, however, the absolute errors are large.

Subsurface- or Ground Heat Flux

Although the daily mean values of the ground heat flux are very small (cf Section 4.4.3), the flux was parameterized and considered in the energy-balance calculation. The subsurface heat flux for each day was calculated using a third-order polynomial fit through the observed data from Seserjoch (Figure 4.20).

Re-freezing Energy

As was shown in Sections 4.4.4 and 4.4.5, the heat flux due to re-freezing of melt-water or rime accretion at the surface can be important under certain atmospheric conditions and, hence, cannot be neglected. The re-freezing energy $M_{i,j}\downarrow$ [W/m^2] was parameterized with

$$M_{i,j}\downarrow = 13.0069 - 0.5683 \cdot T_{s_{i,j}} + 1.3432 \cdot u_{i,j} \ , \tag{7.16}$$

thus, being a function of the surface temperature $T_{s_{i,j}}$ and the wind speed $u_{i,j}$ ($r = 0.44$). The parameterization was derived from the observed daily mean values of re-freezing energy from the Seserjoch energy-balance calculation (Sections 4.4.4 and 4.4.5). Relatively few re-freezing events could be observed for relative humidities below 80 %, so that the re-freezing energy was assumed to be zero for such cases.

Melt Energy

The surface melt was parameterized as a function of daily mean surface temperature using the daily mean melt-energy data from the Seserjoch station from May to September, 1999 (Figure 7.4). The parameterization of the surface melt flux $M_{i,j}\uparrow$

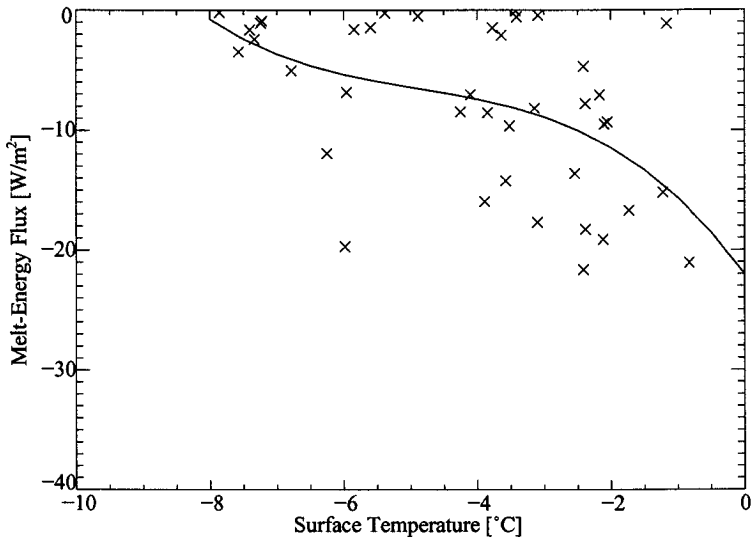

Figure 7.4: Relation between the observed daily mean surface temperatures T_s and the calculated daily mean melt-energy flux $M_{i,j}\uparrow$ at Seserjoch showing the data from May to September, 1999 and the parameterized curve.

[W/m^2] was derived as a third-order polynomial fit through the data:

$$M_{i,j}\uparrow = -0.0946 \cdot T_{s_{i,j}}^3 - 1.3842 \cdot T_{s_{i,j}}^2 - 7.6747 \cdot T_{s_{i,j}} - 22.0288 \ . \tag{7.17}$$

7.2.2 Resulting Energy Balance

After the determination of all the relevant energy-balance components, the energy-balance equation (Equation 4.1) can be solved to yield the surface temperature for each grid cell $T_{s_{i,j}}$ [K] as

$$T_{s_{i,j}} = \left[\frac{1}{\sigma}\left(G_{i,j}\cdot(1-\alpha) + L_{i,j}\downarrow + H_{i,j} + LE_{i,j} + S_{i,j} + M_{i,j}\downarrow + M_{i,j}\uparrow\right)\right]^{\frac{1}{4}}. \quad (7.18)$$

A comparison between the observed and model-derived surface temperatures for Seserjoch from May, 1999 to April, 2000 is presented in Figure 7.5. For August 1,

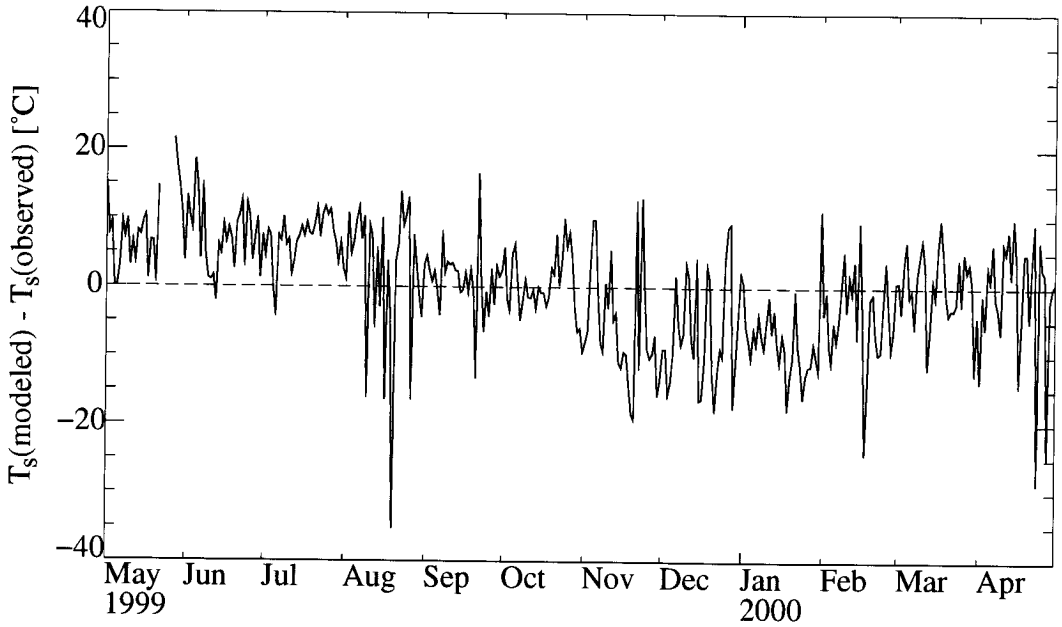

Figure 7.5: Difference between the model-derived and observed surface temperatures T_s at Seserjoch for the period from May, 1999 to April, 2000.

1999 (Figure 7.6) and December 6, 1999 (Figure 7.7), the daily mean values of surface temperatures and – in case of August – of melt energy in space were calculated. Two days were selected when not only the observed and modeled surface temperatures at Seserjoch agreed well (ΔT = -1.1 and -1.7 °C, respectively), but when also the observed and modeled heat fluxes (Equation 7.18) showed a good coincidence with maximum deviations on the order of 20, but typically of 10 %. In the situations with a large ΔT, the observed and modeled fluxes showed a large deviation as well. On August 1, 1999, higher surface temperatures and, herewith, a higher melt-energy input can be observed on steep slopes and in the lower reaches of the glacier as a consequence of a higher net radiation due to backscattered diffuse and longwave radiation on that cloudy and foggy day. The contribution of the turbulent fluxes to the energy balance is negligible on that specific day.
On the clear-sky day of December 6, 1999, the pattern of the modeled surface temperatures is dominated by the shortwave incoming radiation which leads to aspect-related discrepancies. The turbulent fluxes are large on that specific day (H = 71 W/m^2 and LE = -11 W/m^2 as observed at Seserjoch) and compensate the negative net radiation balance.

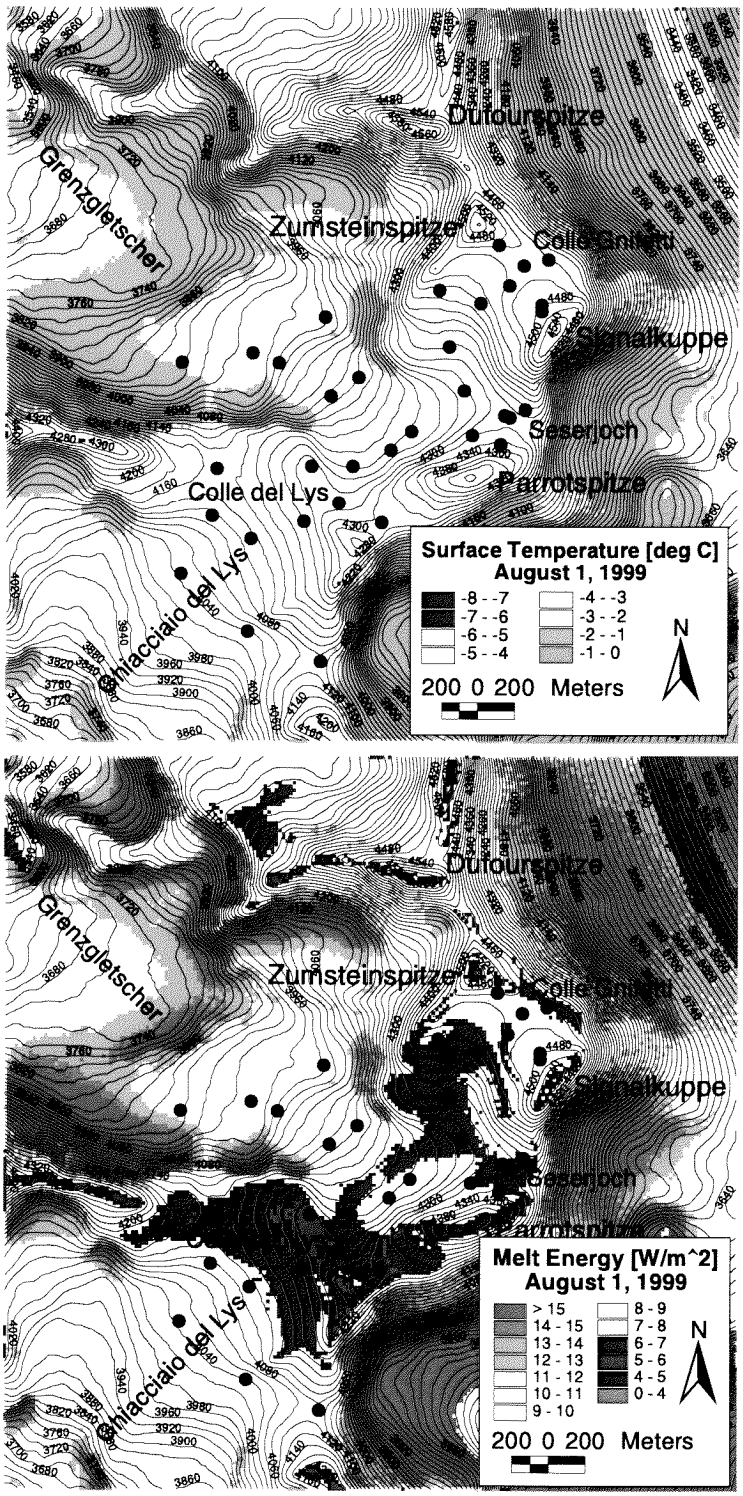

Figure 7.6: Daily mean values of modeled surface temperatures (upper panel) and melt energy (lower panel) on August 1, 1999. Black dots indicate borehole locations.

7.2.3 Discussion

Large discrepancies occur between the observed and model-derived surface temperatures. Omitting the most extreme outliers, the deviations amount to +10/-15 °C

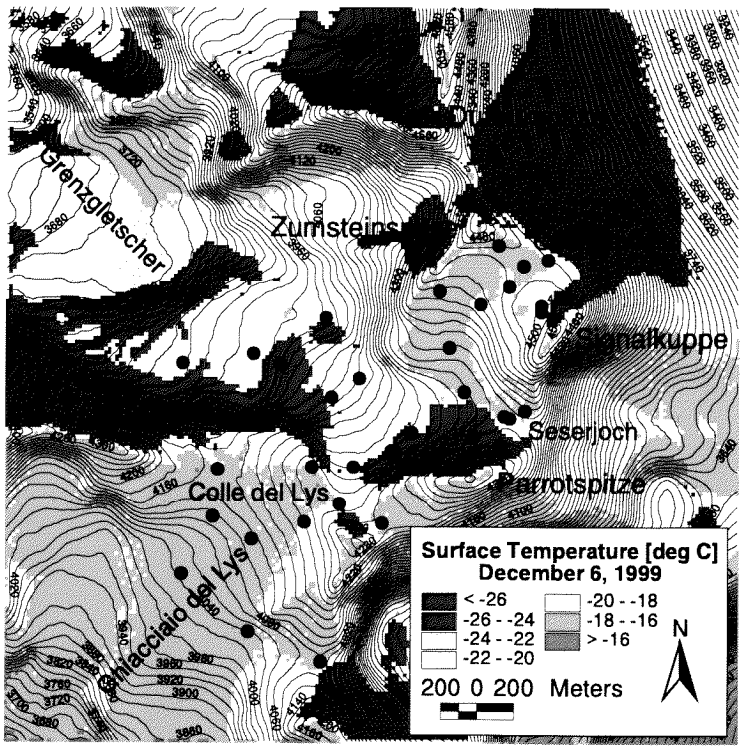

Figure 7.7: Daily mean values of modeled surface temperatures on December 6, 1999. Black dots indicate borehole locations.

or to about $\pm 50\,\mathrm{W/m^2}$ in terms of longwave outgoing radiation (Equation 4.5). The surface temperatures are substantially overestimated during summertime and underestimated during wintertime. The best agreement is found for September and October and for March and April. The large deviations can be explained as follows:

- The parameterization for the longwave incoming radiation (Equation 7.10; Figure 7.2) does not meet the conditions for Seserjoch or the study area very accurately.
- The relatively large errors in the determination of the turbulent fluxes for the Seserjoch site are due to the assumption of a surface temperature, which not only influences the magnitude and direction of the sensible heat flux, but also the saturation water-vapour pressure at the surface for the latent heat flux.
- The parameterizations of the re-freezing- and the melt energy give a general trend which, however, can lead to substantial errors in single cases.

Suggestions, how the model could be further improved, are given in Section 7.5. As the melt-energy flux decisively influences the thermal regime of the firn (Section 6.1.3) and as it shows a high and non-linear sensitivity to the surface temperature (Figure 7.4), modeled surface temperatures require a certain standard of accuracy to reproduce the melt-energy input at a certain location accurately enough. Taking into account the above problems and limitations, a simplification is proposed which, nevertheless, should be able to yield a useful surface boundary condition for an adequate modeling of the future firn-temperature evolution at the firn saddles of

Seserjoch and Colle Gnifetti and of the cold firn occurrence in the Monte Rosa study area.

7.2.4 Simplification

For an adequate modeling of the thermal regime of the firn and ice, the knowledge of the surface boundary condition in terms of surface temperature and melt-energy input is crucial (Section 6.1.3). For the following applications, the energy-balance model is reduced to the parameterization of the surface temperature (Equation 7.8) and of the melt-energy input (Equation 7.17) as derived from the Seserjoch energy-balance station. Thus, the surface temperature becomes mainly a function of air temperature, besides the parameter longwave incoming radiation – which itself is a function of air temperature, water-vapour pressure, cloudiness and contribution from the terrain (Equations 7.10–7.14). The melt-energy flux is only a function of surface temperature (Equation 7.17).
It is evident that such a simplified model may work at sites with similar climatological conditions as Seserjoch (where the parameterizations were derived), but not at sites with rather different micro-climatic conditions such as slopes. Thus, it cannot be expected that the model can reproduce the spatial short-scale firn-temperature variations as observed in the Monte Rosa study area (Figure 5.6), but it might be able to give an idea of the lower boundaries of cold firn occurrence and, herewith, of possible changes of this boundary under conditions of global warming.

7.3 Firn-Temperature Model

The one-dimensional time-dependent firn-temperature model including latent heat is described in detail in Section 6.1.3. The time step was taken as $\Delta t = 1\,\mathrm{d}$ and the depth step as $\Delta z = 1\,\mathrm{m}$. It is assumed that the surface geometry is and will be in a steady state. The vertical velocities were calculated with the exponential velocity-depth model (Equation 6.7) using the observed glacier depths for Seserjoch and Colle Gnifetti and a uniform total depth of 100 m in case of the calculation for the study area (a simplification which seems acceptable in view of the other assumptions made). In the following, the specific input data for the three calculated situations are described.

7.3.1 Seserjoch

The starting profile for the Seserjoch site (initial condition) was obtained by connecting the measured profile from October 13, 2000 (borehole 0; Figure 3.5) with the extrapolated profile to the glacier bed at 103 m depth (cf Section 6.4.2). The upper boundary condition was given by the parameterized values of surface temperature and melt-energy flux; the lower boundary condition at the glacier bed by $G_b = 0.03\,\mathrm{W/m^2}$. The vertical velocity at the surface was taken as $b = 2.1\,\mathrm{m/a}$ and the density-depth distribution was derived from the measured density profile of the upper 10 m of snow and firn at Seserjoch from May, 2000 (Section 3.3.3) and – for the lower part – from the profile of the Colle Gnifetti ice core from 1995 (borehole 95-2; personal communication from L. Keck, 2000).

7.3.2 Colle Gnifetti

The input parameters for the calculation at Colle Gnifetti were $h = 124\,\mathrm{m}$, $b = 0.94\,\mathrm{m/a}$, $G_b = 0.04\,\mathrm{W/m^2}$ and the density-depth profile of the saddle ice core drilled to bedrock in 1982 (personal communication from M. Lüthi, 2001). The initial temperature profile for the saddle point of Colle Gnifetti was composed of the measured profile from August 26, 2000 (borehole 00A; Figure 3.5) and of a time-dependent profile in the lower part – calculated from the steady-state situation in 1983 (Section 6.4.2) in a way to meet the observed 25-m temperature from 2000.

7.3.3 Monte Rosa Study Area

The calculations in space were made to a depth of 22 m. The observed accumulation rates (Figure 5.7) were taken as vertical surface velocities under the assumption of being representative for each grid cell. The lower boundary condition was prescribed as $G_b = 0\,\mathrm{W/m^2}$. The assumption of a temperature gradient assuming zero can be justified by the fact that the local heat-flow conditions are not known and that the firn temperatures at these depths are mainly influenced by the near-surface thermal conditions. The same density-depth profile was adapted for each grid cell (density-depth profiles are only known for a few sites with core drillings) choosing the profile from the Seserjoch site. The observed 18-m temperatures from May/July, 1999 were taken as initial condition (Figure 5.6) and uniformly distributed over the depth range at the beginning. This simplified assumption of the basal boundary condition can also be justified by the fact that a very good agreement (maximum deviation of approximately 1 °C in the calculated scenarios below) could be found for the 18-m firn temperatures at Seserjoch and Colle Gnifetti between the fully-implemented models from above and this simplified model.

7.4 Scenarios

For the calculation of scenarios, the representative present-day climatic conditions for the area (starting conditions) and presumed future climatic conditions have to be known or assumed.

The present-day climatic conditions were derived from mean observed values from the Colle del Lys meteorological station of the period January 1, 1997 to August 17, 2000 (cf Section 3.3.2). Although about 4 years of observations are a relatively short climatological period, the small time horizon can be justified by the fact that the maximum of a surface perturbation arrives at 18 m depth after 2 to 3 years, already (Section 6.1.3). The air temperature series from 1997 to 2000 of the Colle del Lys station is presented in Figure 7.8 together with the mean annual air temperatures from 1997 to 1999. A cooling from -10.65 (1997) to -11.60 °C (1999) can be observed, which agrees with the observed cooling of the firn at Seserjoch between September, 1998 and October, 2000 (Section 6.4.2). The variation of the MAAT at Colle del Lys is in the range of normal year-to-year fluctuations at high-alpine sites (cf Figure 6.28).

Due to the large uncertainties involved, the future evolution of climatic parameters other than air temperature is extremely difficult to predict, so that only air-temperature scenarios are used to assess the future thermal evolution of cold firn.

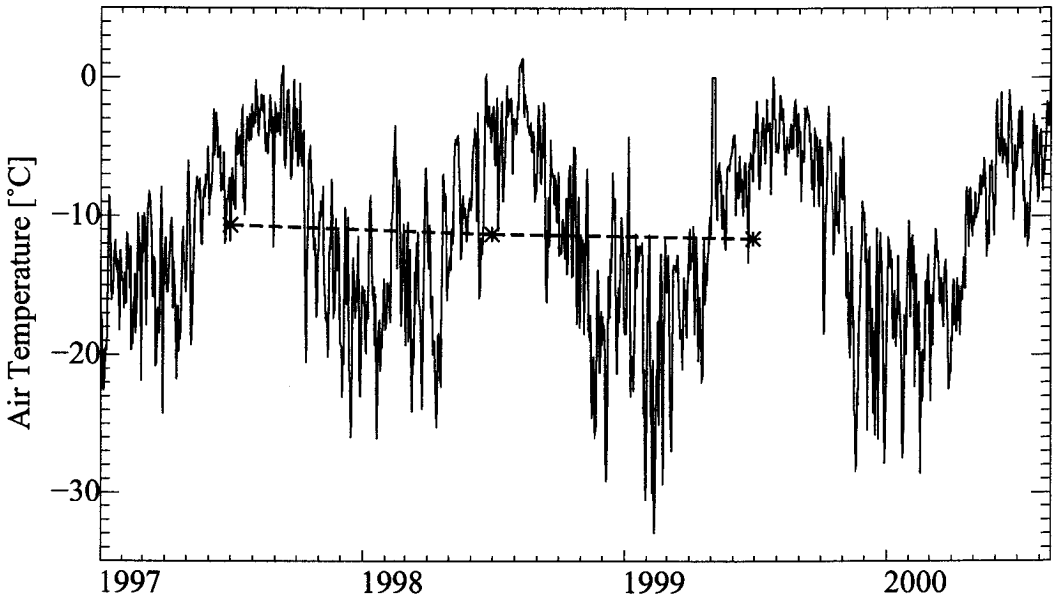

Figure 7.8: Daily mean air temperatures from the Colle del Lys station from 1997 to 2000 and mean annual air temperatures from 1997 to 1999 (dashed line).

Based on the Third Assessment Report of Working Group I of the Intergovernmental Panel on Climate Change (IPCC), three global air-temperature scenarios were applied (IPCC, 2001):

1. +0.45 °C until 2020;
2. +1.48 °C until 2050 and
3. +3.18 °C until 2100.

These scenarios are based on mean values from an envelope of the outcome of different climate models predicting the increase in global temperature based on various emission scenarios by the IPCC (IPCC, 2001). Whether these global scenarios are valid for the Alps and especially for high-elevation sites as well remains an open question. Unfortunately, no updated regional scenarios were yet available from the IPCC at the time of calculation. In the model calculations, a linear increase of the air temperature between the time steps 2000–2020, 2020–2050 and 2050–2100 was assumed and the signal modulated onto the observed daily mean values of the Colle del Lys station from 1997 to 2000.

7.4.1 Seserjoch

Figure 7.9 shows the evolution of the firn- and ice temperatures at Seserjoch until 2100. In order to get an impression of the representativity of the climatic input data from Colle del Lys, a run to 2020 was made without any air-temperature increase. The 18-m temperature rose by about +0.6 °C, either as a consequence of an imbalance between the Colle del Lys climate data and observed 18-m firn temperatures in 2000 or of slight inaccuracies in the formulation of the upper boundary condition (parameterization of surface temperature and melt-energy input). A cooling can be

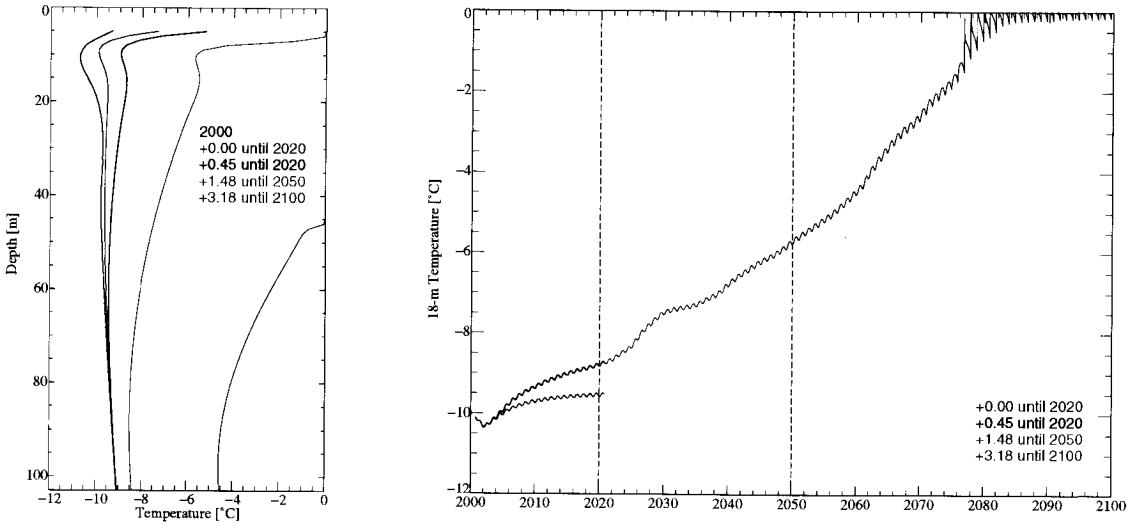

Figure 7.9: Observed (2000) and modeled future firn- and ice temperatures at Seserjoch showing the state in 2020, 2050 and 2100. The left panel shows the evolution of the temperature profiles; the right panel the evolution of the 18-m temperature with time.

observed until about 2002 until a steady-state situation is reached in 2010.
The pattern of the 18-m temperature for the different scenarios shows a strongly non-linear behaviour and an acceleration of the warming with time due to a higher release of melt energy with increasing surface temperature (Figure 7.9). The 18-m firn temperature rises from -10.1 (October, 2000) to -8.7 (2020) to -5.6 °C (2050). In 2100, the firn at 18 m depth can be considered temperate together with the uppermost 45 m of the firn and ice.

7.4.2 Colle Gnifetti

The future englacial temperature profiles and the future pattern of the 18-m firn temperature at Colle Gnifetti are depicted in Figure 7.10. After 20 years, the 18-m temperature at Colle Gnifetti is practically in balance with the present-day climate from 1997 to 2000. The discrepancy between the observed 18-m temperature in 2000 and the 'steady-state temperature' in 2020 is +1.06 °C. The same reasons can be stated for this phenomenon as above.
Again, the future 18-m firn temperature follows a non-linear evolution with time showing values of -12.0 (2020), -9.8 (2050) and -3.5 °C (2100). Thus, the firn and ice at Colle Gnifetti are still cold in 2100, although being very close to temperate conditions.

7.4.3 Monte Rosa Study Area

Due to the simplifications and limitations of the energy-balance model (Section 7.2.4), a precise spatial differentiation in 18-m temperatures within the Monte Rosa study area reproducing the observed short-scale variations cannot be expected. However, the model may give an idea of the changes in cold firn occurrence and its

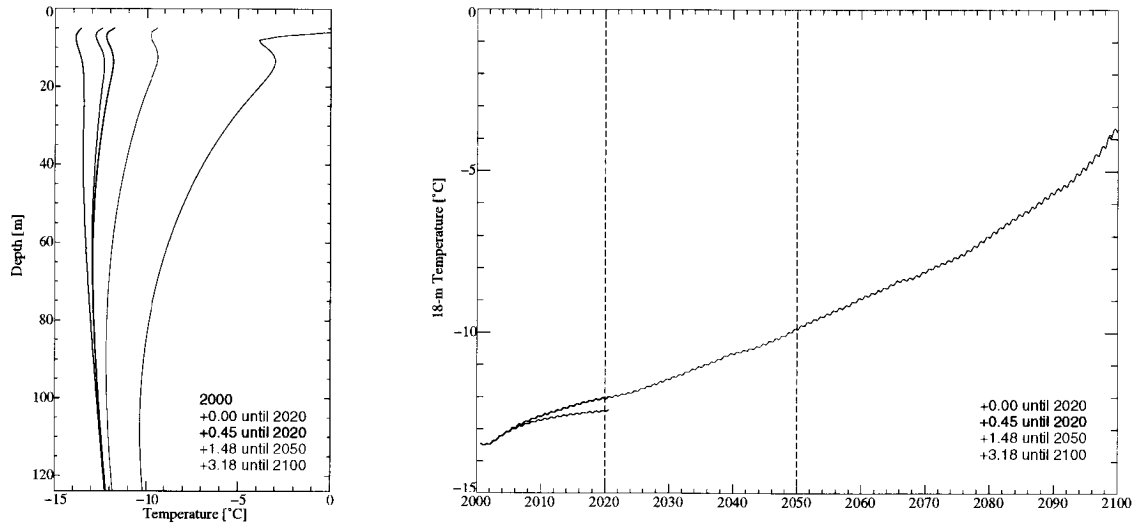

Figure 7.10: Observed (2000) and modeled future firn- and ice temperatures at Colle Gnifetti showing the state in 2020, 2050 and 2100. The left panel shows the evolution of the temperature profiles; the right panel the evolution of the 18-m temperature with time.

sensitivity to a presumed climate change in the study area (Figure 7.11). To account for the accuracy of the temperature measurements (Section 5.2.3), the firn was considered to be temperate for 18-m temperatures above -0.15 °C, already. As a consequence of the model simplifications, the lower boundary of cold firn occurrence rises in case of Grenzgletscher and is more or less stable in case of Ghiacciaio del Lys, if a test run without any air-temperature change is made until 2020 (dashed lines in Figure 7.11). The boundary between temperate and cold firn would be found between 4100 and 4200 m a.s.l. in 2050. However, as some sensitive areas on exposed south-faced slopes were already very close to temperate conditions in 1999 (Figure 5.6), it is very probable that the occurrence of cold firn will be restricted to exposed saddles and crests and to very shady slopes above approximately 4100 m a.s.l. by 2050, already.

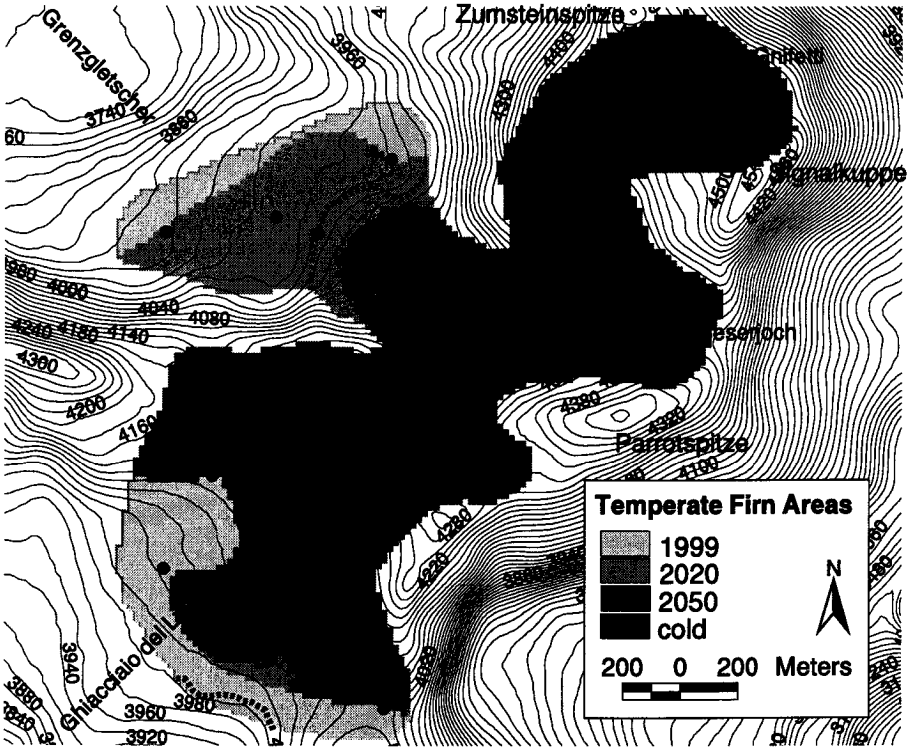

Figure 7.11: Evolution of the cold-firn occurrence (18-m temperatures) in the Monte Rosa study area under conditions of global warming. The state in 1999 (observed), 2020 (+0.45°C) and 2050 (+1.48°C) is shown. The thick, dashed line marks the boundary between temperate and cold firn in 2020, if no air temperature increase is assumed. Black dots indicate borehole locations.

7.5 Conclusions

Spatial Energy-Balance Model

- The spatial energy-balance model presented here takes into account all relevant energy-exchange processes between the cold snow and firn and the atmosphere. Major problems arise from the parameterizations of the longwave incoming radiation and the turbulent fluxes which do not adequately represent the conditions found. Other inaccuracies originate in the formulation of the melt- and re-freezing energy.

- The available input data from the meteorological station (eg lacking observation of longwave incoming radiation) and the accuracy of the turbulent fluxes at the control site of Seserjoch (eg severe underestimation of the turbulent fluxes in winter; Section 4.4.5) make up a further model restriction.

- Although periods with reasonable coincidence between the observed and modeled surface temperatures and, herewith, also between the observed and modeled magnitude of the single energy-balance components can be found, the

day-to-day scatter in the one-year series from May, 1999 to April, 2000 is too large for a direct application in a coupled energy-balance/firn-temperature model.

- An inherent difficulty is the high sensitivity of the surface temperature to small errors in the energy-balance calculation (Equation 7.18). A modest error of $\pm 10\,W/m^2$ in the whole energy balance amounts to an uncertainty in the surface temperature of already $\pm 2\,°C$ at a temperature close to $0\,°C$. As the surface temperature is used to parameterize the melt-energy input and as the two quantities probably show a non-linear relation especially in the vicinity of the melting point, such an error can already have a large effect on the melt-energy input at the surface.

- Although a further improvement of the spatial energy-balance model seems possible in finding more adequate parameterizations of the critical fluxes and in improving eg the spatial wind field using a macro-scale three-dimensional wind model, other critical assumptions (eg initial surface temperature) remain. Thus, it is questionable, in how far the accuracies can ever be obtained which are needed for an adequate formulation of the surface boundary condition.

- The daily time-scale used for the calculations may be another source of (principal) errors and limitations. Whereas surface temperature is a continuous signal which can well be averaged for a day, melt events are extremely episodic. Thus, a functional relation between mean daily surface temperature and mean daily melt energy is not evident and, in fact, critical (Figure 7.4). An improvement of this relation can only be obtained when going beyond the daily time scale. This would, however, make intensive adaptations of the model necessary in terms of input data (hourly values needed at least) and computational resources.

- A simplified formulation of the surface temperature and melt energy adequately depicts the surface boundary condition for Seserjoch and for similar sites (eg Colle Gnifetti). However, it cannot be expected that the model resolves a precise spatial differentiation of the englacial 18-m temperatures as a result of the surface energy balance, since, in particular, the spatial variation of the global radiation and the turbulent fluxes are not considered.

Firn-Temperature Model

- The firn-temperature model used in the calculations proved to be an adequate description of the thermo-mechanical processes in the snow and firn in one dimension and on the depth-scale considered.

Scenarios

- The calculated firn-temperature scenarios for Seserjoch and Colle Gnifetti are considered to be robust enough in order to make a statement on the future evolution of the englacial thermal regime under conditions of global warming, whereas the future lower boundaries of cold-firn occurrence have to be interpreted more in terms of an assessment than in terms of a precise prediction.

- A massive and non-linear warming on the order of +4.5 and +3.7 °C has to be expected for Seserjoch and Colle Gnifetti for the year 2050, respectively, if the warming scenarios are correct. In 2100, the firn at Seserjoch will be temperate and Colle Gnifetti be very close to temperate conditions.
- The lower boundaries of cold-firn occurrence in the Monte Rosa study area will be subjected to a rise on the order of 100–300 m until 2050.

Seite Leer /
Blank leaf

8 Conclusions and Perspectives

The main achievements and results of this study can be summarized as follows:

- Cold firn is a common phenomenon on high-elevation Alpine glaciers and can be found above 3500–3700 m a.s.l. in northerly aspects and above 3800–4100 m a.s.l. in southerly aspects in the Mont Blanc and Monte Rosa areas.

- The highly variable micro-climatic conditions in alpine topography lead to a complex structure of near-surface firn temperatures in space with very high firn-temperature gradients within very short distances.

- Mean annual firn temperatures (MAFTs) show a good statistical relation to topographic and climatic parameters such as elevation, aspect, slope, potential direct solar radiation and accumulation.

- A detailed energy-balance study over cold firn shows that the net radiation and the turbulent heat fluxes are the major contribution to the surface energy balance. The determination of the turbulent fluxes is a difficult task due to instrumental and methodological problems under severe meteorological conditions and in rugged topography.

- Under special meteorological conditions, the contributions from the melt-energy flux (surface melt) and the re-freezing-energy flux (re-freezing of surface meltwater and rime accretion) cannot be neglected and show high (daily) values.

- Besides surface temperature, the quantification of the melt-energy input is crucial for understanding the near-surface thermal regime. The high variability of the mean annual firn temperatures in space is a direct consequence of the varying melt-energy input.

- A parallel evolution of the observed air- and surface temperatures at the energy-balance site suggests that a possible future air-temperature increase under conditions of global warming is equally transfered to an increase in surface temperature as long as other climatic parameters remain constant and mean daily surface temperatures do not assume 0 °C.

- The thermal regime of cold saddle- and dome-type glaciers can adequately be described with a one-dimensional heat diffusion and -advection model including the effect of latent heat. An upper boundary condition (in terms of surface temperature and melt-energy input) and a lower boundary condition (in terms of basal heat flux) have to be known.

- The time horizon for reconstructions of the surface-temperature history at cold Alpine glacier saddles is restricted to a few centuries under ideal conditions. This is a consequence of shallow ice thicknesses on the order of only 100 m, high propagation velocities of thermal surface perturbations due to a very effective heat transfer by heat diffusion, limitations in the thermal and spatial resolution of englacial temperature measurements and the use of a forward model approach.

- At sites with high melt-energy input, warming or cooling signals in measured englacial temperature profiles cannot be transfered into an increase in surface temperature, directly. An increase in surface temperature is normally accompanied with a higher release of surface melt energy. Warming or cooling trends in observed englacial temperature profiles have, thus, to be regarded with care since surface-temperature and melt signal cannot be separated. A plausible assumption of a surface melt-energy input, however, makes a calculation of the surface-temperature increase possible.

- Borehole-temperature records from the Monte Rosa and Mont Blanc areas suggest a warming of $+0.5 - +1\,^{\circ}C$ for the 1990s, which is in good agreement with instrumental air-temperature series and ice-core information (ice-layer frequency and $\delta^{18}O$ records).

- The spatial energy-balance model presented is able to reproduce realistic patterns of surface temperatures and melt energy in cases, where the single energy-balance components are adequately modeled. However, large discrepancies occur between the observed and model-derived surface temperatures at the energy-balance site during the one-year observation period.

- A simplified energy-balance formulation leading to parameterized surface boundary conditions makes a coupling between surface energy balance and cold firn possible. The model yields useful and robust results for the future thermal evolution of the cold firn saddles of Seserjoch and Colle Gnifetti under conditions of global warming.

- A strong and non-linear warming has to be expected for these two sites until 2100, if the warming scenarios are correct. By then, the firn at Seserjoch will be temperate and Colle Gnifetti be very near to temperate conditions.

- Near-surface firn temperatures show a high temporal and spatial sensitivity which makes them a distinct, rapidly-reacting and enhanced climate signal. They offer the possibility to detect short-term climate changes in an area, where no direct observations are normally available. They are particularly sensitive to a change in the surface melt-energy input. Especially under higher air temperatures in summer, cold firn areas will be subjected to a drastic change in the thermal structure within very short time in the future.

- Rising firn temperatures are not only likely to lead to a rapid and irreversible deterioration or even complete destruction of a unique paleo-climatic archive containing environmental and climatic information built up in glaciers over centuries or millenia. Beyond it, firn warming could lead to stability problems of steep hanging glaciers and to an increased runoff of surface meltwater in formerly cold firn areas.

Future investigations and research could address the following topics:

- Monitoring of firn temperatures on regular intervals at suitable sites with a long firn-temperature history should globally be established for detecting

on-going – and possibly accelerated – climate changes in very sensitive high-mountain areas besides existing observing programs for the cryosphere like glacier fluctuations, mass balances and permafrost temperatures.

- Emphasis should be given to a better determination of the upper boundary condition as an output of the surface energy balance. This could be done with high-quality and high-resolution measurements of the surface temperature and melt-energy flux in space, especially at sites with very different micro-climatic conditions. The quantification of the melt-energy flux could be improved by the determination of the free water content in the snow using time-domain reflectometry.

- The spatial energy-balance model could be refined with the help of an improved physical basis (eg by implementing three-dimensional wind fields), better and more adequate parameterizations of relevant fluxes (eg melt- and re-freezing energy) and by adapting a higher temporal resolution of the flux calculations going beyond the daily time-scale.

- The spatial energy-balance model could be completed with the integration of other surface types such as rock, in order to yield an improved thermal boundary condition for modeling three-dimensional thermo-mechanical problems in complex alpine topography (eg glacier-flow models for exposed hanging glaciers).

- More realistic climate scenarios could be applied taking into account other climate variables besides air temperature, if sophisticated regional climate models are down-scaled and coupled with local area models for complex topography.

- Inverse modeling could have the potential to trace back a surface-temperature history with a higher resolution in time, requiring spatially high-resolved and very accurate borehole temperatures, however.

Seite Leer /
Blank leaf

A Field Data

A.1 Mont Blanc Area

Borehole	x-Coord. [m]	y-Coord. [m]	18-m Temp. [°C]	Elevation [m]	Aspect	Aspect Code	Slope [°]	Radiation [W/m^2· day]	Acc. Index
1	555462	75813	-14.38	4800	E	5	9	260.3	1
2	554609	76214	-15.08	4510	NNE	2	10	286.2	1
3	554460	76448	-13.50	4380	N	1	21	210.3	1
4	554286	76587	-12.02	4290	WNW	4	19	217.7	2
5	554041	76753	-10.27	4245	-	-	3	290.6	2
6	553835	76881	-10.99	4285	ESE	6	11	317.7	2
7	553677	76794	-10.38	4285	SSW	8	11	342.2	1
8	553639	76903	-12.49	4285	WNW	4	14	284.0	1
9	553755	76949	-12.15	4304	-	-	3	316.2	1
10	553763	77045	-12.61	4290	N	1	9	254.5	2
11	553981	77034	-8.99	4265	E	5	9	299.1	3
12	554281	76996	-8.89	4190	E	5	17	258.7	4
13	553938	77459	-10.41	4210	NNE	2	19	214.4	2
14	553657	77189	-10.92	4215	NW	3	27	175.1	3
15	554136	77607	-9.36	4135	ENE	4	19	217.2	3
16	554455	77085	-1.35	4120	ESE	6	29	257.2	4
17	554741	77169	-3.51	4010	ENE	4	17	204.7	4
18	554823	76998	-8.59	4000	NNE	2	10	218.7	4
19	554417	77679	-5.94	4010	ENE	4	23	199.0	4
20	553270	77385	-7.28	4000	NW	3	22	186.8	3
21	553030	77730	-0.78	3830	NNE	2	10	257.9	4
22	555052	77260	-7.64	3930	N	1	16	195.8	4

Borehole	x-Coord. [m]	y-Coord. [m]	18-m Temp. [°C]	Elevation [m]	Aspect	Aspect Code	Slope [°]	Radiation [W/m^2· day]	Acc. Index	Accumulation [m/a]
0	633722	85776	-9.52	4290	WNW	4	5	289.7	2	2.09
1	633924	86347	-13.40	4485	NW	3	12	249.8	1	0.41
2	633826	86595	-13.45	4454	-	-	2	306.8	1	0.34
3	633960	86630	-13.37	4440	NE	3	13	254.4	1	1.20
4	633690	86710	-10.08	4460	S	9	21	405.8	3	3.14
5	633367	86460	-8.11	4400	S	9	16	372.1	3	2.95
6	633590	86390	-13.71	4405	SW	7	25	301.0	3	1.96
7	633420	86150	-1.22	4300	S	9	14	347.0	3	2.06
8	633834	85808	-6.79	4306	SSW	8	19	366.0	2	0.29
9	633750	85765	-9.76	4293	-	-	2	285.6	2	2.57
10	633700	85620	-12.96	4330	N	1	15	228.8	3	0.81
11	633545	85670	-12.71	4300	NNW	2	27	174.2	2	-
12	633502	85911	-3.74	4250	WSW	6	15	313.8	4	2.61
13	633213	85692	-3.48	4205	WNW	4	8	247.2	4	2.33
14	633100	85590	-10.06	4205	NW	3	21	185.9	4	3.26
15	632895	85499	-11.30	4200	N	1	20	193.7	4	2.30
16	632819	85300	-11.49	4255	N	1	12	250.3	3	3.81
17	632670	85500	-10.62	4252	-	-	4	281.4	2	2.06
18	633049	85190	-9.67	4283	-	-	3	293.6	2	1.79
19	632925	85985	-2.53	4100	WNW	4	17	228.4	4	-
20	632774	85881	-9.88	4090	NW	3	18	209.6	4	2.44
21	632741	86315	-0.03	3985	WSW	6	17	236.5	4	1.89
22	632489	86062	-7.11	3990	WNW	4	22	195.4	4	1.82
23	632344	86116	-1.77	3951	-	-	4	253.2	4	0.86
24	631961	86065	-0.23	3898	W	5	11	226.5	4	2.06
25	632629	85197	-5.60	4220	W	5	16	300.0	3	2.57
26	632150	85485	-7.13	4151	-	-	4	308.4	2	-
27	632339	85100	-1.57	4134	WSW	6	17	317.4	4	2.89
28	632721	84430	-0.01	4087	-	-	6	328.8	2	1.40
29	632321	84595	-0.62	4030	SSW	8	18	347.9	4	1.05
30	631956	84911	0.00	4035	WSW	6	11	318.7	4	1.93
31	632124	85227	0.00	4110	SSW	8	14	341.2	4	3.00
95-1	633922	86383	-13.32	4480	NNW	2	6	281.4	1	0.41
95-2	633746	86484	-13.20	4450	WNW	4	19	244.2	2	1.14

References

Albrecht, B., Peollet, M., and Cox, S. (1974). Pyrgeometer measurements from aircraft. *Review of Scientific Instruments*, 45:33–38.

Alean, J. (1985). Ice avalanches: some empirical information about their formation and reach. *Journal of Glaciology*, 31(109):324–333.

Alean, J., Haeberli, W., and Schädler, B. (1983). Snow accumulation, firn temperature and solar radiation in the area of the Colle Gnifetti core drilling site (Monte Rosa, Swiss Alps): distribution patterns and interrelationships. *Zeitschrift für Gletscherkunde und Glazialgeologie*, 19(2):131–147.

Arnold, N. S., Willis, I. C., Sharp, M. J., Richards, K. S., and Lawson, W. J. (1996). A distributed surface energy–balance model for a small valley glacier. I. development and testing for Haut Glacier d'Arolla, Valais, Switzerland. *Journal of Glaciology*, 42(140):77–89.

Bamber, J. (1989). Ice/bed interface and englacial properties of Svalbard ice masses deduced from airborne radio echo-sounding data. *Journal of Glaciology*, 35(119):30–37.

Beck, N., Wagenbach, D., and Münnich, K. (1988). Laboratory experiments on the formation of solar radiation induced melt layers in dry snow. *Zeitschrift für Gletscherkunde und Glazialgeologie*, 24(1):31–40.

Bjørnsson, H., Gjessing, Y., Hamran, S.-E., Hagen, J., Liestøl, O., Pálsson, F., and Erlingsson, B. (1996). The thermal regime of sub-polar glaciers mapped by multi-frequency radio-echo sounding. *Journal of Glaciology*, 42(140):23–32.

Blatter, H. (1987). On the thermal regime of an Artic valley glacier: a study of White Glacier, Axel Heiberg Island, N.W.T., Canda. *Journal of Glaciology*, 33(114):200–211.

Böhm, R., Auer, I., Brunetti, M., Maugeri, M., Nanni, T., and Schöner, W. (2001). Regional temperature variability in the European Alps 1760-1998. *International Journal of Climatology*. In Press.

Bowen, I. (1926). The ratio of heat losses by conduction and by evaporation from any water surface. *Physical Review*, 27:779–787.

Braithwaite, R. (1992). Degree-day factor, energy balance, and the increased melting of the Greenland ice sheet under a warmer climate. *Rapp. Grønlands geol. Unders.*, 155:79–83.

Brock, B., Willis, I., Sharp, M., and Arnold, N. (2000). Modelling seasonal and spatial variations in the surface energy balance of Haut Glacier d'Arolla, Switzerland. *Annals of Glaciology*, 31:53–62.

Brun, E., Martin, E., Simon, V., Gendre, C., and Coleou, C. (1989). An energy and mass model of snow cover suitable for operational avalanche forecasting. *Journal of Glaciology*, 35(121):333–342.

Busslinger, A. (1998). *Geothermische Prognosen für tiefliegende Tunnel.* PhD thesis, ETH Zürich. Diss. ETH Nr. 12715.

Carslaw, H. S. and Jaeger, J. C. (1959). *Conduction of heat in solids.* Clarendon Press, Oxford, second edition.

Cihlar, J., Ortega, E., Haeberli, W., Kuma, K., Landwehr, J., Norse, D., Running, S., Scholes, R., Solomon, A., and Zhao, S. (1997). GCOS/GTOS plan for terrestrial climate-related observation. *GCOS*, 32. WMO/TD - No. 796, UNEP/DEIA/TR. 97-7.

Collares-Pereira, M. and Rabl, A. (1979). The average distribution of solar radiation correlations between diffuse and hemispherical and between daily and hourly insolation values. *Solar Energy*, 22:155–164.

Dahl-Jensen, D. and Johnsen, S. (1986). Paleotemperatures still exist in the Greenland ice sheet. *Nature*, 320(6059):250–252.

Dahl-Jensen, D., Morgan, V. I., and Elcheikh, A. (1999). Monte Carlo inverse modelling of the Law Dome (Antarctica) temperature profile. *Annals of Glaciology*, 29:145–150.

Dansgård, W. (1964). Stable isotopes in precipitation. *Tellus*, 16:436–468.

Dozier, J. and Warren, S. (1982). Effect of viewing angle on the infrared brightness temperature of snow. *Water Resources Research*, 18:1424–1434.

Dyer, A. (1974). A review of flux-profile relationships. *Boundary-Layer Meteorology*, 7:363–372.

Eichler, A., Schwikowski, M., Gäggeler, H., Furrer, V., Synal, H., Beer, J., Saurer, M., and Funk, M. (2000). Glaciochemical dating of an ice core from the upper Grenzgletscher (4200 m a.s.l.). *Journal of Glaciology*, 46(154):507–515.

Escher-Vetter, H. (1985a). Energy balance calculations for the ablation period 1982 at Vernagtferner, Oetztal Alps. *Annals of Glaciology*, 6:158–160.

Escher-Vetter, H. (1985b). Energy balance calculations from five years meteorological records at Vernagtferner/ Oetztal Alps. *Zeitschrift für Gletscherkunde und Glazialgeologie*, 21:397–402.

Fierz, C., Plüss, C., and Martin, E. (1997). Modelling the snow cover in a complex alpine topography. *Annals of Glaciology*, 25:312–316.

Fischer, H., Wagenbach, D., Laternser, M., and Haeberli, W. (1995). Glacio-meteorological and isotopic studies along the EGIG line, Central Greenland. *Journal of Glaciology*, 41(139):515–527.

Fisher, J. E. (1953). The cold ice tunnel on the Silbersattel, Monte Rosa. *Journal of Glaciology*, 2(13):195–196.

Fisher, J. E. (1954). The cold ice tunnel on the Silbersattel, Monte Rosa (progress 1953). *Journal of Glaciology*, 2(15):341.

Fisher, J. E. (1955). Internal temperatures of a cold glacier and conclusions therefrom. *Journal of Glaciology*, 2(18):583–591.

Fisher, J. E. (1963). Two tunnels in cold ice at 4000 m on the Breithorn. *Journal of Glaciology*, 4(35):513–520.

Föhn, P. (1973). Short-term snow melt and ablation derived from heat- and mass-balance measurements. *Journal of Glaciology*, 12(65):275–289.

Forrer, J. (1999). The structure and turbulence characteristics of the stable boundary layer over the Greenland ice sheet. Zürcher Geographische Schriften 75, ETH Zürich. pp. 120.

Funk, M. (1985). Räumliche Verteilung der Massenbilanz auf dem Rhonegletscher und ihre Beziehung zu Klimaelementen. Zürcher Geographische Schriften 24, ETH Zürich. pp. 183.

Funk, M. and Hoelzle, M. (1992). A model of potential direct solar radiation for investigating occurrences of mountain permafrost. *Permafrost and Periglacial Processes*, 3(2):139–142.

Gäggeler, H., von Gunten, H. R., Rössler, E., Oeschger, H., and Schotterer, U. (1983). ^{210}Pb–dating of cold alpine firn/ice cores from Colle Gnifetti, Switzerland. *Journal of Glaciology*, 29(101):165–177.

Gagliardini, O. and Meyssonnier, J. (1997). Flow simulation of a firn-covered cold glacier. *Annals of Glaciology*, 24:242–248.

Garrat, J. (1992). *The atmospheric boundary layer.* Cambridge University Press.

Greuell, W. and Oerlemans, J. (1986). Sensitivity studies with a mass balance model including temperature profile calculations inside the glacier. *Zeitschrift für Gletscherkunde und Glazialgeologie*, 22(2):101–124.

Gubler, H. (1996). Physik von Schnee. Vorlesungsskript ETH Zürich, Sommersemester 1996 (unveröffentlicht).

Haeberli, W. (1976). Eistemperaturen in den Alpen. *Zeitschrift für Gletscherkunde und Glazialgeologie*, 11(2):203–220.

Haeberli, W. (1990). Glacier and permafrost signals of 20th-century warming. *Annals of Glaciology*, 14:99–101.

Haeberli, W. and Alean, J. (1985). Temperature and accumulation of high altitude firn in the Alps. *Annals of Glaciology*, 6:161–163.

Haeberli, W., Alean, J. C., Müller, P., and Funk, M. (1989). Assessing risks form glacier hazards in high mountain regions: some experiences in the Swiss Alps. *Annals of Glaciology*, 13:96–102.

Haeberli, W. and Funk, M. (1991). Borehole temperatures at the Colle Gnifetti core drilling site (Monte Rosa, Swiss Alps). *Journal of Glaciology*, 37(125):37–46.

Haeberli, W., Iken, A., and Siegenthaler, H. (1979). Glaziologische Aspekte beim Bau der Fernmelde-Mehrzweckanlage der PTT auf dem Chli Titlis. In *Mitteilung 41.* Versuchsanstalt für Wasserbau, Hydrologie und Glaziologie der ETH Zürich. 59–75.

Haeberli, W., Schmid, W., and Wagenbach, D. (1988). On the geometry, flow and age of firn and ice at the Colle Gnifetti core drilling site (Monte Rosa, Swiss Alps). *Zeitschrift für Gletscherkunde und Glazialgeologie*, 24(1):1–19.

Haeberli, W., Schotterer, H. U., Wagenbach, D., Haeberli-Schwitter, H., and Bortenschlager, S. (1983). Accumulation characteristics on a cold, high-alpine firn saddle from a snow–pit study on Colle Gnifetti, Monte Rosa, Swiss Alps. *Journal of Glaciology*, 29(102):260–271.

Haeberli, W. and Stauffer, B., editors (1994). *Glaciological basis of ice core drilling on mid-latitude glaciers: Greenhouse gases, isotopes and trace elements in glaciers as climatic evidence of the Holocene.*, VAW-Arbeitsheft, VAW-ETHZ. Report on a ESF/EPL Workshop.

Haefeli, R. and Brentani, F. (1955). Observations in a cold ice cap. *Journal of Glaciology*, 2(18):571–581.

Hock, R. (1999). A distributed temperature-index ice- and snowmelt model including potential direct solar radiation. *Journal of Glaciology*, 45(149):101–111.

Hock, R. and Noetzli, C. (1997). Areal melt and discharge modelling of Storglaciären, Sweden. *Annals of Glaciology*, 24:211–217.

Hoelzle, M., Mittaz, C., Etzelmüller, B., and Haeberli, W. (2001). Surface energy fluxes and distribution models of permafrost in European mountain areas: an overview of current developments. *Permafrost and Periglacial Processes*, 12:53–68.

Högström, U. (1988). Non-dimensional wind and temperature profiles in the atmospheric surface layer: a re-evaluation. *Boundary-Layer Meteorology*, 42:55–78.

Hooke, R. L., Gould, J., and Brzozowski, J. (1983). Near-surface temperatures near and below the equilibrium line on polar and subpolar glaciers. *Zeitschrift für Gletscherkunde und Glazialgeologie*, 19(1):1–25.

Hutchinson, M. F. (1989). A new procedure for gridding elevation and stream line data with automatic removal of spurious pits. *Journal of Hydrology*, 106:211–232.

IPCC (2001). Third Assessment Report of Working Group I of the Intergovernmental Panel on Climate Change. Technical report, WMO/UNEP. In press.

Konzelmann, T. and Braithwaite, R. J. (1995). Variations of ablation, albedo and energy balance at the margin of the Greenland ice sheet, Kronprins Christian Land, eastern north Greenland. *Journal of Glaciology*, 41(137):490–502.

Konzelmann, T. and Ohmura, A. (1995). Radiative fluxes and their impact on the energy balance of the Greenland ice sheet. *Journal of Glaciology*, 41(139):490–502.

Konzelmann, T., van de Wal, R., Greuell, W., Bintanja, R., Henneken, E., and Abe-Ouchi, A. (1994). Parameterization of global and longwave incoming radiation for the Greenland ice sheet. *Global and Planetary Change*, 9:143–164.

Kuhn, M. (1987). Micro–meteorological conditions for snow melt. *Journal of Glaciology*, 33(113):263–272.

La Casinière, A. (1974). Heat exchange over a melting snow surface. *Journal of Glaciology*, 13(67):55–72.

Lachenbruch, A. and Brewer, M. (1959). Dissipation of the temperature effect of drilling a well in Arctic Alaska. *U.S. Geological Survey Bulletin*, 1083-C:73–109.

Laternser, M. (1992). Firntemperaturmessungen in den Schweizer Alpen. Master's thesis, ETH Zürich.

Lehning, M., Bartlet, P., Brown, B., Russi, T., Stöckli, U., and Zimmerli, M. (1999). Snowpack model calculations for avalanche warning based upon a network of weather and snow stations. *Cold Regions Science and Technology*, 30(1-3):145–157.

Ling, C. (1985). A note on the density distribution of dry snow. *Journal of Glaciology*, 31(108):194–195.

Lliboutry, L., Briat, M., Creseveur, M., and Pourchet, M. (1976). 15 m deep temperatures in the glaciers of Mont Blanc (French Alps). *Journal of Glaciology*, 16(74):197–203.

Lowe, P. (1976). An approximating polynominal for the computation of saturation vapor pressure. *Journal of Applied Meteorology*, 16:100–103.

Lüthi, M. (2000). Rheology of cold firn and dynamics of a polythermal ice stream: Studies on Colle Gnifetti and Jakobshavns Isbræ. Mitteilung 165, Versuchsanstalt für Wasserbau, Hydrologie und Glaziologie der ETH Zürich, Gloriastrasse 37-39, ETH-Zentrum, CH-8092 Zürich. pp. 212.

Lüthi, M. and Funk, M. (1997). Wie stabil ist der Hängegletscher am Eiger. *Spektrum der Wissenschaft*, 5:21–24.

Lütschg, M. (2000). Räumliche Verbreitung der oberflächennahen Firntemperaturen im Monte Rosa Massiv und deren Zusammenhang mit den Klimavariablen. Master's thesis, ETH Zürich. Unpublished.

MacAyeal, D. R., Firestone, J., and Waddington, E. (1991). Paleothermometry by control methods. *Journal of Glaciology*, 37(127):326–338.

Male, D. (1980). The seasonal snowcover. In Colbeck, S., editor, *Dynamics of snow and ice masses*, pages 305–395. Academic Press.

Martin, S. (1975). Wind regimes and heat exchange on Glacier de Saint-Sorlin. *Journal of Glaciology*, 14(70):91–105.

Medici, F. and Rybach, L. (1995). *Geothermal Map of Switzerland 1995 (Heat Flow Density).* Studentendruckerei, Zürich.

Meier, M. F. (1984). Contribution of small glaciers to global sea level. *Science*, 226(4681):1418–21.

Mitchell, A. R. and Griffiths, D. F. (1987). *The finite difference method in partial differential equations.* John Wiley and Sons.

Monin, A. and Obukhov, A. (1956). Fundamentale Gesetzmässigkeiten der turbulenten Vermischung in der bodennahen Schicht der Atmosphäre. In *Statistische Theorie der Turbulenz*, pages 199–226, Berlin. Akademie Verlag.

Monterin, U. (1941). Il Monte Rosa. *Bolletino del Comitato Glaciologico Italiano*, 21.

Moore, C. (1986). Frequency response corrections for eddy correlation systems. *Boundary-Layer Meteorology*, 37:17–35.

Moore, I., Gallant, J., and Guerra, L. (1993a). Modelling the spatial variability of hydrological processes using GIS. *IAHS*, 211:161–169. Application of Geographic Information Systems in Hydrology and Water Resources.

Moore, I., Norton, T., and Williams, J. (1993b). Modelling environmental heteorogenity in forested landscapes. *Journal of Hydrology*, 150:717–747.

Morris, E. (1989). Turbulent transfer over snow and ice. *Journal of Hydrology*, 105:205–223.

Morton, K. W. (1980). Stability of finite difference approximations to a diffusion-convection equation. *International Journal of Numerical Methods England*, 15:677–683.

Müller, F. (1962). Zonation in the accumulation area of the Glaciers of Axel Heiberg Island, N.W.T. Canada. *Journal of Glaciology*, 4:302–313.

Obukhov, A. (1946). Turbulence in the thermally inhomogeneous atmosphere. *Trudy Instituta Teoreticheskoyi Geofiziki*, 1:95–115.

Ødegård, R., Hagen, J., and Hamran, S.-E. (1997). Comparison of radio-echo sounding (30-1000 MHz) and high-resolution borehole-temperature measurements at Finsterwalderbreen, southern Spitsbergen, Svalbard. *Annals of Glaciology*, 24:262–267.

Ødegård, R., Hamran, S.-E., Bø, P., Etzelmüller, B., Vatne, G., and Sollid, J. (1992). Thermal regime of a valley glacier, Erikbreen, northern Spitsbergen. *Polar Research*, 11(2):69–79.

Oerlemans, J. (1992). Climate sensitivity of glaciers in southern Norway: Application of an energy–balance model to Nigardsbreen, Hellstugubreen and Alfotbreen. *Journal of Glaciology*, 38(129):223–232.

Oerlemans, J. (2001). Analysis of a three-year meteorological record from the ablation zone of the Morteratschgletscher, Switzerland: energy and mass balance. *Journal of Glaciology*. In press.

Oeschger, H., Schotterer, U., Stauffer, B., Haeberli, W., and Röthlisberger, H. (1977). First results from Alpine core drilling projects. *Zeitschrift für Gletscherkunde und Glazialgeologie*, 13(1-2):193–208.

Ohmura, A. (1982). Objective criteria for rejecting data for Bowen ratio flux calculations. *Journal of Applied Meteorology*, 21:595–598.

Ohmura, A. (1984). Comparative energy balance study for arctic tundra, sea surface, glaciers and boreal forests. *GeoJournal*, 8(3):221–228.

Ohmura, A., Konzelmann, T., Rotach, M., Forrer, J., Wild, M., Abe-Ouchi, A., and Toritani, H. (1994). Energy balance for the Greenland ice sheet by observation and model computation. In Jones, H., Davies, T., Ohmura, A., and Morris, E., editors, *Snow and ice covers: Interaction with the atmosphere and ecosystems*, IAHS Publication No. 223, pages 85–94, IAHS.

Oke, T. R. (1987). *Boundary layer climates*. Routledge, second edition.

Paterson, W. S. B. (1994). *The Physics of Glaciers*. Pergamon, New York, third edition.

Philipona, R., Fröhlich, C., and Betz, C. (1995). Characterization of pyrgeometers and the accuracy of atmospheric long-wave radiation measurements. *Journal of Applied Optics*, 34(9):1598–1605.

Plüss, C. (1997). The energy balance over an Alpine snowcover. Zürcher Geographische Schriften 65, ETH Zürich. pp. 115.

Preunkert, S., Wagenbach, D., Legrand, M., and Vincent, C. (2000). Col du Dôme (Mt Blanc Massif, French Alps) suitability for ice-core studies in relation with past atmospheric chemistry over europe. *Tellus*, 52B:993–1012.

Ritz, C. (1989). Interpretation of the temperature profile measured at Vostok, East Antarctica. *Annals of Glaciology*, 12:138–144.

Robin, G. (1955). Ice movement and temperature distribution in glaciers and ice sheets. *Journal of Glaciology*, 2(18):523–532.

Robin, G. (1983). *The climatic record in polar ice sheets*. Cambridge University Press, first edition.

Rossi, G., Johnston, P., and Maggi, V. (2000a). ALPCLIM project: Reconstruction of the monthly values of solar radiation incident over the Lys Glacier surface (Monte Rosa-Western Italian Alps). In *26th Int. Conference on Alpine Meteorology - Innsbruck 11th September 2000*. ICAM.

Rossi, G., Johnston, P., and Maggi, V. (2000b). Project ALPCLIM: Résultats de l'observation météorologique dans le site de Colle du Lys (4250 mètres). In *Réunion Annuelle Société Hydrotechnique de France, Section Glaciologie. Grenoble 1er Mars 2000.* Société Hydrotechnique de France.

Rossi, G., Novo, A., Maggi, V., Orombelli, G., and Smiraglia, C. (1998). Carottage profond sur le glacier du Lys (Monte Rosa): résultats préliminaires. *La Houille Blanche*, 5/6:22–25.

Salamatin, A., Lipenkov, V., and Blinov, K. (1994). Vostok (Antarctica) climate record time-scale deduced from the analysis of a borehole-temperature profile. *Annals of Glaciology*, 20:207–214.

Schmid, H. (1997). Experimental design for flux measurements: matching scales of observations and fluxes. *Agricultural and Forest Meteorology*, 87:179–200.

Shumskii, P. A. (1964). *Principles of Structural Glaciology. Translation D. Kraus.* Dover Publications Inc., Dover, New York, first edition.

Smiraglia, C., Maggi, V., Rossi, G., and Johnston, P. (2000). Preliminary results of two ice core drillings on Monte Rosa (Colle Gnifetti and Colle del Lys), Italian Alps. *Geografia Fisica Dinamica Quat.*, 23(2):165–172.

Stull, R. (1988). *An introduction to boundary layer meteorology.* Kluwer Academic Publishers.

Suter, S. (1993). Dépouillement des sondages radar au Col du Dôme, massif du Mont-Blanc (F), du 1er au 5 juin 1993. Travail de stage pratique au VAW, EPF Zürich, responsabilité: M. Funk et W. Haeberli (unpublished).

Suter, S. (1995). Die Verbreitung kalter Firn- und Eisregionen im Alpengebiet. Master's thesis, ETH Zürich.

Suter, S., Laternser, M., Haeberli, W., Hoelzle, M., and Frauenfelder, R. (2001). Cold firn and ice of high-altitude glaciers in the Alps: Measurements and distribution modelling. *Journal of Glaciology*, 47(156):85–96.

Sverdrup, H. (1936). The eddy conductivity of the air over a smooth snowfield. *Geofys. Publ.*, 11:1–69.

Vallot, J. (1893). Recherches scientifiques dans le tunnel du Mont-Blanc. *Annales de l'Observatoire Météorologique, Physique et Glaciaire du Mont-Blanc*, 1:131–143.

Vallot, J. (1913). Valeur et variation de la température profonde du glacier, au Mont Blanc. *Comptes Rendus Hebdomadaires des Séances de l'Académie des Sciences*, 156(20):1575–1578.

van de Waal, R., Oerlemans, J., and van der Hage, J. (1992). A study of ablation variations on the tongue of Hintereisferner, Austrian Alps. *Journal of Glaciology*, 38(130):319–324.

Vincent, C., Vallon, M., Pinglot, J., Funk, M., and Reynaud, L. (1997). Snow accumulation and ice flow at Dôme du Goûter (4300 m), Mont Blanc, French Alps. *Journal of Glaciology*, 43(145):513–521.

Vonder Mühll, D. and Funk, M. (1995). Gletscherdickenmessungen mittels Radar auf dem Grenzgletscher, Monte Rosa Massiv. Internal Report, VAW, ETH Zürich. Unpublished.

Wagenbach, D. (1989). Environmental records in Alpine glaciers. In Oeschger, H. and Langway, C. C., editors, *The Environmental Record in Glaciers and Ice Sheets*, pages 69–83. John Wiley & Sons limited.

Wagner, H. P. (1979). Strahlungshaushaltsuntersuchungen an einem Ostalpengletscher während der Hauptablationsperiode. Teil I: Kurzwellige Strahlung. *Archiv für Meteorologie, Geophysik und Bioklimatologie*, 27:297–324.

Wagner, H. P. (1980). Strahlungshaushaltsuntersuchungen an einem Ostalpengletscher während der Hauptablationsperiode. Teil II: Langwellige Strahlung und Strahlungsbilanz. *Archiv für Meteorologie, Geophysik und Bioklimatologie*, 28:41–62.

Wagner, S. (1996). Dreidimensionale Modellierung zweier Gletscher und Deformationsanalyse von eisreichem Permafrost. Mitteilung 146, Versuchsanstalt für Wasserbau, Hydrologie und Glaziologie der ETH Zürich, Gloriastrasse 37-39, ETH-Zentrum, CH-8092 Zürich. pp. 135.

Wahba, G. (1990). Spline models for observational data. *CBMS-NSF Regional Conference Series in Applied Mathematics*. Philadelphia: Soc. Ind. Appl. Maths.

Warren, S. (1982). Optical properties of snow. *Reviews of Geophysics and Space Physics*, 20(1):67–89.

Wegmann, M. (1998). Frostdynamik in hochalpinen Felswänden, am Beispiel der Region Jungfraujoch–Aletsch. Mitteilung 161, Versuchsanstalt für Wasserbau, Hydrologie und Glaziologie der ETH Zürich, Gloriastrasse 37-39, ETH-Zentrum, CH-8092 Zürich. pp. 144.

West, R., Winebrenner, D., Tsang, L., and Rott, H. (1996). Microwave emission from density-stratified Antarctic firn at 6 cm wavelength. *Journal of Glaciology*, 42(140):63–76.

Wilson, W. (1941). An outline of the thermodynamics of snowmelt. *Transactions of the American Geophysical Union*, 22:182–195.

Zotikov, I. (1986). *The thermophysics of glaciers*. D. Reidel Publishing Company, Dordrecht, Holland.

Seite Leer /
Blank leaf

Curriculum Vitae

Person:

Name:	Suter
First Name:	Stephan
Date of birth:	April 25, 1969
Native town:	CH-Muri AG
Family status:	unmarried
Nationality:	Swiss

Education:

1976–1981	Primary school in Dottikon and Villmergen AG
1981–1985	'Bezirksschule' in Wohlen AG
1985–1989	High School ('Kantonsschule') in Wohlen AG with emphasis on modern languages

University Studies:

1990–1995	Studies of Earth Science at the Swiss Federal Institute of Technology (ETH) Zürich with a degree in Natural Science
1995–1996	Lectures and practical courses in the area of didactics and pedagogy at ETH Zürich
1998–2001	PhD thesis at the Laboratory of Hydraulics, Hydrology and Glaciology (VAW) at ETH Zürich in the framework of the EU-Project ALPCLIM

Professional Experience:

1989–1990	Part-time job at the Swiss Post (former PTT) in Wohlen and Villmergen (AG)
1995–1997	Employment as a research assistant at the Laboratory of Hydraulics, Hydrology and Glaciology (VAW) at ETH Zürich and at the Physical Geography Department of the Institute of Geography at the University of Zürich within the World Glacier Monitoring Service and the Glaciological Commission of the Swiss Academy of Sciences (Swiss Glacier Monitoring Program)
1996–2000	Teaching at a professional school ('Berufsschule') in Brugg (mathematics and physics) and at a high school ('Kantonsschule') in Wohlen (geography)

Seite Leer /
Blank leaf

Acknowledgements

O give thanks unto the LORD,
for he is good:
for his mercy endureth for ever.

Ps. 107,1

Many many people and institutions have contributed in o so different ways to the successful conclusion of this study in leading and supervising me, in helping me in the sometimes very strenuous field work on 'top of Europe', in giving me support in instrumental setup, data supply, -analysis and -interpretation and computational problems and – above all – in being colleagues and friends.
First of all, my thanks go to Prof. Dr. Hans-Erwin Minor for giving me the possibility to do this thesis at the Laboratory of Hydraulics, Hydrology and Glaciology (VAW) at ETH Zürich and for being a kind 'Doktorvater' and Dr. Martin Funk for his support within the Section of Glaciology. Prof. Dr. Atsumu Ohmura (Institute for Atmospheric and Climate Science (IAC), ETH Zürich) and Prof. Dr. Michael Kuhn (Institute for Meteorology and Geophysics, University of Innsbruck, A) were not only willing to be co-examiners for my thesis, but they also gave me important scientific support, which is gratefully acknowledged.
Besides being a careful and helpful supervisor of my PhD, Dr. Martin Hoelzle was even more a steady motivator and supporter of my work right from the beginning. Thank you, Martin, for the great and unforgettable time in science and friendship!
The present study was carried out in the framework of the EU-Project ALPCLIM (Environmental and Climate Records from High-Elevation Alpine Glaciers) and would not have been possible without the financial support of the European Union (ENV4-CT97-0639), the Swiss Bundesamt für Bildung und Wissenschaft (BBW Nr. 97.0349-1), the Laboratory of Hydraulics, Hydrology and Glaciology (VAW) at ETH Zürich and the Institute for Atmospheric and Climate Science (IAC) at ETH Zürich.
A lot of people helped me during the frequent and extensive field works under sometimes very beautiful, but at times also very difficult conditions: Gudfinna Adalgeirsdottir, Urs H. Fischer, Christian Hauck, Martin Hoelzle, Michael Iten, Gwendolyn Leysinger Vieli, Josef Luthiger, Martina Lütschg, Rolf Meier, Matthias Meinck, Peter Oberholzer, Mélanie Raymond, Michael Schnellmann, Thomas Schuler, Monika Weber (ETH Zürich); Patrick Hager, Eric Lutz, Aurel Schwerzmann, Catherine Stocker-Mittaz (University of Zürich); Karin Grust (Freiburg i. Br., D); Fredy Biner, Richard Lehner, Gabriel Willisch (Zermatt); Hansueli Gubler (ALPUG, Davos); Raphaël Blanchard, Marc Delmotte, Bruno Jourdain, Susanne Preunkert, Matthieu Tournoud, Christian Vincent (LGGE, Grenoble, F); Michael Huke, Lothar Keck, Urs Ruth, Martin Schock, Andreas Stanzick (University of Heidelberg, D); Olaf Eisen and Uwe Nixdorf (AWI, Bremerhaven, D).
Additionally, field operations were logistically supported by Air Zermatt (Zermatt), the Matterhorn- and Gornergratbahnen (Zermatt), LGGE (Grenoble, F) and Chamonix Mont-Blanc Hélicoptère CMBH (Argentière, F).

The important technical help with instruments and measurements provided by Josef Luthiger, Karl Schroff, Hanspeter Hächler, Cornelius Senn, Daniel Gubser, Georg Meier and Thomas Wyder (ETH Zürich); Hansueli Gubler (ALPUG, Davos); Rolf Philipona and Remo Venturi (WRC, Davos) was highly appreciated. Especially Josef Luthiger and Karl Schroff gave me a continuous and enthusiastic support without which the measurements under very difficult conditions would never have been possible.
Valuable data sets, digital elevation models and software were made available by Giancarlo Rossi (Noale, I); Rolf Philipona (WRC, Davos); the Swiss Meteorological Institute (MeteoSchweiz, Zürich); Hermann Bösch, Martin Lüthi and Matthias Meinck (VAW, ETH Zürich); Matthias Rotach (IAC, ETH Zürich); Lothar Keck (University of Heidelberg, D); Susanne Preunkert (LGGE, Grenoble, F); Reinhard Böhm and Inge Auer (ZAMG, Vienna, A); Urs Wild and Urs Marti (Swiss Federal Office of Topography, Wabern). Their help is sincerely acknowledged.
In everyday's life, computers became an indispensable working tool and I would like to thank Andreas Bauder and Martin Lüthi for their occasional computer support. Many lively, encouraging and interesting discussions were the result of sharing the office with Christian Hauck (in the rare moments, when he was physically present...) and of being next door to Daniel Vonder Mühll. Thank you both!
I am indebted to Dietmar Wagenbach and Lothar Keck (University of Heidelberg, D); Christian Vincent and Susanne Preunkert (LGGE, Grenoble, F); Reinhard Böhm and Inge Auer (ZAMG,Vienna, A); Giancarlo Rossi (Noale, I); Regula Frauenfelder, Wilfried Haeberli, Andreas Kääb, Catherine Stocker-Mittaz (University of Zürich); Stephan Wagner (Ebnat-Kappel); G. Hilmar Gudmundsson, Urs H. Fischer, Martin Funk, Martin Lüthi and Thomas Schuler (VAW, ETH Zürich) for many helpful scientific and also non-scientific discussions. I greatly enjoyed the coffee breaks at the 'Arvenstübli' and the delicious sweets! Thanks to all, who contributed to the nice atmosphere and especially to Bruno Nedela, who was always there when a hand was needed!
Non seulement Mélanie Raymond a accepté de traduire le résumé, mais elle a aussi contribué à approfondir mes connaissances du français et était prête à s'évader de temps en temps avec moi. Merci Mélanie!

Last but not least, my deepest thanks go to my parents and many dear friends, who always carried me through.